Università degli Studi di Milano-Bicocca
Facoltà di Scienze Matematiche, Fisiche e Naturali
Dipartimento di Scienza dei Materiali

Ph. D. School of Materials Science

XXIV cycle

Surface and Interface Effects on the Stability of SiGe Nanoislands

Doctorate Thesis of :
Daniele Scopece
(055188)

Supervisor: Prof. Leonida Miglio

Dean of the Doctorate: Prof. Gian Paolo Brivio

January 2012

"It is not knowledge,
but the act of learning,
not possession
but the act of getting there,
which grants the greatest enjoyment..."
Carl Friedrich Gauss

To my parents,
friends,
colleagues
and those all that have substained and supported me
in these years of studies.

Outline

Deposition of Ge upon Si substrates is the prototype of the mechanism called Stranski-Krastanov growth, i.e. the self-assembled formation of 3D islands, following the formation of a thin, 2D Wetting Layer.

As is shown in Chapter 1, the nucleation of these islands is random and non-uniform when the deposition is performed upon the standard Si(001) substrate.

Deposition of SiGe on different substrates of Si can lead, however, to a high degree of uniformity. Some examples are described in Chapters 3 and 4.

The aim of this thesis is to supply a quantitative analysis for some peculiar phenomena concerning island nucleation that occurs on these non-standard substrates.

This is performed through the evaluation of the internal energy of the island (including also effects on the substrate) as discussed at length in Chapter 2, where the elastic, surface and edge energy contributions are described, focusing particular attention to the second one, that turns out to be quite complicated.

Particular attention is devoted to the island nucleation on stepped substrates of Si (Chapter 4). An in-depth analysis of the formation of faceting upon the substrate Si(1 1 10) is carried out in Chapter 5, whereas Chapter 6 deals with the transition from the faceting to three-dimensional islands on this peculiar system.

Conclusions are drawn in Chapter 7.

Appendices A and B contain some additional information regarding the elastic field and the description of surfaces.
In Appendix C an analysis of the strained surface energy is carried out.
In Appendix D some preliminary work performed during the PhD period on other important surfaces for the SiGe system is discussed.

Finally at page 203 a Curriculum Vitæ is reported.

Contents

List of Figures

List of Tables

List of Acronyms

In alphabetic order:

AC As Cut = bulk-like, unreconstructed surface

AR Aspect Ratio = height / square root of base of nanostructures

BL Bi-Layer

CET Classical Elasticity Theory

CP Chemical Potentials

CVD Chemical Vapour Deposition

DFT Density Functional Theory

DVL Dimer Vacancy Line

ECS Equilibrium Crystal Structure

FEM Finite Element Method

FM Frank Van der Merve growth mode of self-assembled nanostructures

FP Facet Plot

GGA Generalized Gradient Approximation

ISK Inverse Stranski-Krastanov

LDA Local Density Approximation

LET Linear Elasticity Theory

MBE Molecular Beam Epitaxy

ML Mono-Layer

MP Monkhorst-Pack way to create a meshes in k-space

PBC Periodic Boundary Conditions

PF Perfect Faceting = condition of faceting of a surface (e.g. 1,1,10) where all the islands have the same size and no WL is present

RHEED Reflection High Energy Electron Diffraction

RS Rebonded Step = the most stable reconstruction of Ge(105)

SE Surface Energy

SK Stranski-Krastanow growth mode of self-assembled nanostructures

SOM Surface Orientiation Map

TD Thermo-Dynamics = Total energy calculations

USPP Ultra Soft PseudoPotential

VW Volmer-Weber growth mode of self-assembled nanostructures

WL Wetting Layer (pseudomorphic planar growth of the epilayer)

WS Weighted Slope (see section 2.4.3)

XC eXchange-Correlation contributions

List of Symbols used

ϵ_{ij} = Component ij of strain field tensor
C_{ijkh} = Component ijkh of the stiffness constants tensor
C_{ij} = Component ij of the stiffness constants tensor in the .... notation
ρ = Elastic energy density
γ = Surface energy density
Γ = Edge energy density
$\alpha \equiv AR$ = Aspect Ratio = height of island / square root of base area
θ = co-latitude angle
φ = azimuth angle or inclination of ripples on (1 1 10)
n_j = vector of direction: n_3 is along z direction
n_{jk} = k-th component of the vector n_j
D_b = Double step B-type
N_{Ge} = number of Ge atoms in the simulation cell
N_{Si} = number of Si atoms in the simulation cell
F = relaxation factor = $-\frac{\rho_{isl}-\rho_{WL}}{\rho_{WL}}$

1

State of the Art

"Standing on the shoulders of giants"
Bernard of Chartres

1.1 Introduction

Even though the first transistor was made of germanium, in modern technology the role of silicon is undoubtely the dominant one, thanks to its well-established and cheap set of processes. In the last few decades the scaling down predicted by the Moore's law in Si technology has been fulfilled, yet the top-down approaches for the size of nanometer (10^{-9} m) length are ineffective to shrink the size of any device (as the Field Effect Transistor, FET). Due to the fatigue of keeping the reliable top-down approach alive, researchers has been driving importance to bottom-up approaches where Silicon can still be the main actor. This is the reason why SiGe heteroepitaxial self-assembled nanostructures have attracted a considerable interest in the development of new electrical and optical devices.

Besides of these application-driven needs, SiGe systems can be considered the prototypical systems of the self-assembly phenomena and the concepts developed from the analysis of this system can be extended and used to understand more complex situations like the partially polar III-V compounds (like InAs/GaAs) or II-VI ones.

In this chapter, some basic concepts and discoveries concerning the growth of SiGe islands on Si substrates are briefly reviewed and summarized.

1.2 Heteroepitaxy in a nutshell

Epitaxy is defined as a controlled phase transition that leads to a single crystalline solid [1]. In this process a material, called epilayer, is deposited onto a crystalline solid, called substrate, of a given structure. In epitaxy the crystallographic orientation is determined by the exposed surface of the substrate. If the epilayer and the substrate are of the same material such process is called *homoepitaxy*. In contrast, when atoms of material A grow on a material B the process is called *heteroepitaxy* and the epilayer adopts the in-plane lattice parameter of the substrate. If A has different lattice parameter than B, elastic energy is stored in the epilayer. In heteroepitaxy three growth modes are observed [2]: Frank Van der Merve (FM), Volmer-Weber (VW) and Stranski-Krastanow (SK) mode. The three mode, sketched in Fig.1.1, can be described as layer by layer two dimensional growth, island growth and layer by layer (Wetting Layer,WL) plus island growth respectively.

The growth mode is mainly governed by surface energies and by lattice mismatch.

In lattice matched systems (A and B have the same lattice constant) the growth mode is governed by surface energy only. Let us call γ_{epi} the surface epilayer energy, γ_{int} the energy of the interface between A and B and γ_{sub} the surface substrate energy. If $\gamma_{epi}+\gamma_{int} < \gamma_{sub}$, the deposited material wets the substrate, and the growth proceeds in the FM mode. A change in $\gamma_{epi} + \gamma_{int}$ alone may drive a transition to the FM to VW growth mode: the epilayer either wets the substrate or does not.

In lattice mismatched systems there is an additional possibility. In case of systems with small interface energy but large lattice mismatch, SK growth mode is favored. Initial growth is layer by layer, but because a thicker layer has large elastic energy, islands are formed to relax the strain.

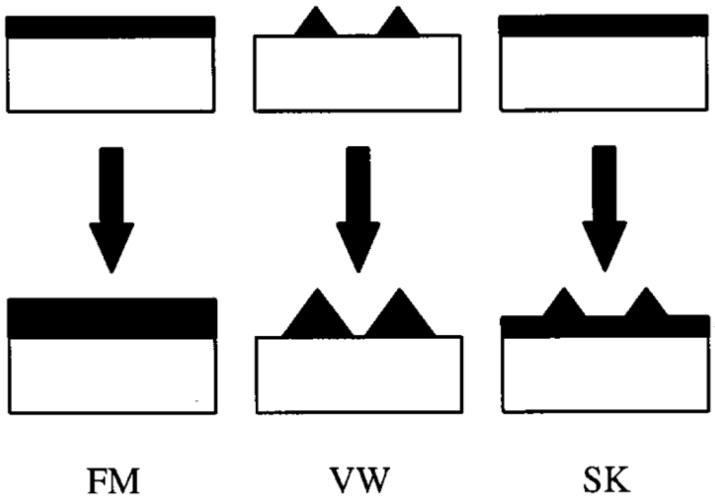

FIGURE 1.1: The three growth mode of heteroepitaxy: FM=Frank van der Merve, SK=Stranski-Krastanov, VW=Volmer-Weber.

1.3 Ge/Si island formation: elastic relaxation

Germanium and silicon are group IV semiconductor and they both have a diamond lattice with lattice constant along the [100] direction equal to $a_{Si} = 5.432\mathring{A}$ and $a_{Ge} = 5.658\mathring{A}$ [3]. Thus, Ge/Si is a mismatched system, where the difference in lattice parameter accounts for about 4%.
From a chemical point of view, Ge and Si are very similar. Alloying is favored and $Si_{1-x}Ge_x$ (x is the Ge content) alloys are fully miscible in the whole composition range for temperatures used in heteroepitaxy[1]. By tuning the Ge content x, the lattice mismatch between the alloy and the substrate varies from 0% to 4%.

The surface energy $Si_{1-x}Ge_x$ is lower than the surface energy of Si, and their interface energy is small, so the Ge content x is a key parameter in determining the heteroepitaxial growth mode of SiGe alloys on Si. The initial growth occurs layer by layer, then three-dimensional islands are formed to relieve the elastic energy stored in the system (elastic relaxation). The evolution of this system upon increasing deposition and different conditions (typically flux and substrate temperature) in the MBE or CVD growth chamber has clarified the path followed by the system [4, 5].

The substrate evolve from a Si terminated one to a Ge-terminated since the dangling bond of Ge are less energetic. Further, the WL evolve through a 2xN-DVL reconstruction to a MxN patch pattern [6, 7, 8]. Deformed in the pseudomorphic structure, the wetting layer stores elastic energy that will find paths to be released. By increasing the amount of deposited material (typically after $\sim$ 3MLs [4]), because of the high lattice mismatch, the elastic energy stored in the lattice is sufficient to nucleate 3D nanostructures, called ***quantum dots*** or ***islands***, arising from the substrate in a bottom-up, self-assembled fashion. As will be shown in section 2.4 at page 39, Ge-on-Si quantum dots represent a more effective route towards elastic relaxation with respect to a flat film, at the cost of an extra surface energy exposed and these driving forces are playing in the further evolution of islands in shape.

Islands are typically described by a parameter called *Aspect Ratio* (AR) defined as the ratio of height of island over the square root of the base surface:

$$AR \equiv \frac{h}{\sqrt{B}}$$

As reported in Figure 1.2-[a,b], the islands evolve increasing the value of the AR since a higher aspect ratio *typically*[2] allows a better strain relieve.

The observed islands are reported in Figure 1.2-[c-f].
The first islands to appear are unfacetted, low-aspect-ratio nanostructures, called pre-pyramids [9], PP in panel [c]. The nucleation barrier to nucleate such structures is zero [10], which accounts for its actual experimental observation. At later stages of growth, those structures transform into fully-3D faceted islands, with the shape of a truncated pyramid [11], TP in panel [c]. Before the transition to a full-3D structure, it was shown the stability

[1] ranging from $\sim 550^\circ$ to $\sim 800^\circ$
[2] but with some cautions and limitations, see discussion at sec.2.4.3 at page 50

of intermediate, metastable shapes of Ge elongated "huts" [12, 13], particularly visible under specific growth conditions, like temperatures in the range 400-550°C, panel [d].

Raising the temperature can lead to evolution of steeper and steeper islands.
When the growth temperature is $\sim 600 - 720$°C, a bimodal distribution of square base pyramids ($AR = 0.1$) and rounded islands called "domes" ($AR \simeq 0.2$) are observed [14, 15], panel [e].
In the range $\sim 720 - 800$°C "barn-shaped" islands with $AR \simeq 0.3$ appear [16] (B in panel [c]), and recently a even steeper island with $AR \simeq 0.4$ has been reported if the temperature is raised to ~ 900°C ("Cupola" islands) [17].

Evidently Ge islands exposes defined crystallographic facets among all the possible available; this already implies that there must be facets with higher and others with lower surface energy, so that Ge islands, among all the possible ones, have shapes such that they preferentially expose the lowest-energetic facets. A detailed morphological analysis is reported in the next section.

1.4 Morphological analysis: Facets

Every island shape just outlined is characterized by a well-defined set of facets that are experimentally revealed via a slope analysis leading to a "facet plot" (FP)[3] (Fig.1.2-[f]) [19] that has allowed to identify a small number of stable facets for each island species.
The pre-pyramids and pyramids are made of shallow ($\sim 11°$) {105} facets. At every step of the evolution, new steeper facets are added at the bottom of the island [17] with a mechanism based on step-bunching starting from the facets formed in the previous stage [20], as is the case of the transition dome in Fig.1.2-[c].
In the domes the {113} and {15 3 23} facets are added [19]; in the barns {20 4 23}, {23 4 20} and {111} appear [16]; finally in the cupola {322}, {715} and {12 3 5} [17]. Depending on the experimental conditions, the tip of the island can be cut by a (001) facet.

This analysis refers to the case of Si(001) substrate, however the same family facets are observed to appear if the Ge deposition is performed on different orientation of substrates [21, 22, 23], although the geometry of islands is different because of the constraint due to the substrate. This suggests that while the appearance of steeper facets is driven by the reduction of the strain energy, the orientation of these facets that actually appear (determining the island's morphology) is governed by the energetics of a small number of facets. Moreover, since it happens even on III-V compound like InAs/GaAs [24], this may be true under a general pespective.

The stability of different facets of Si and Ge has been assessed experimentally and divided into two categories [25]:

- 'major': a stable surface that does not consist of nanofacets of any other stable surfaces (typically flat surfaces)

[3] also called Surface Orientation Map, SOM

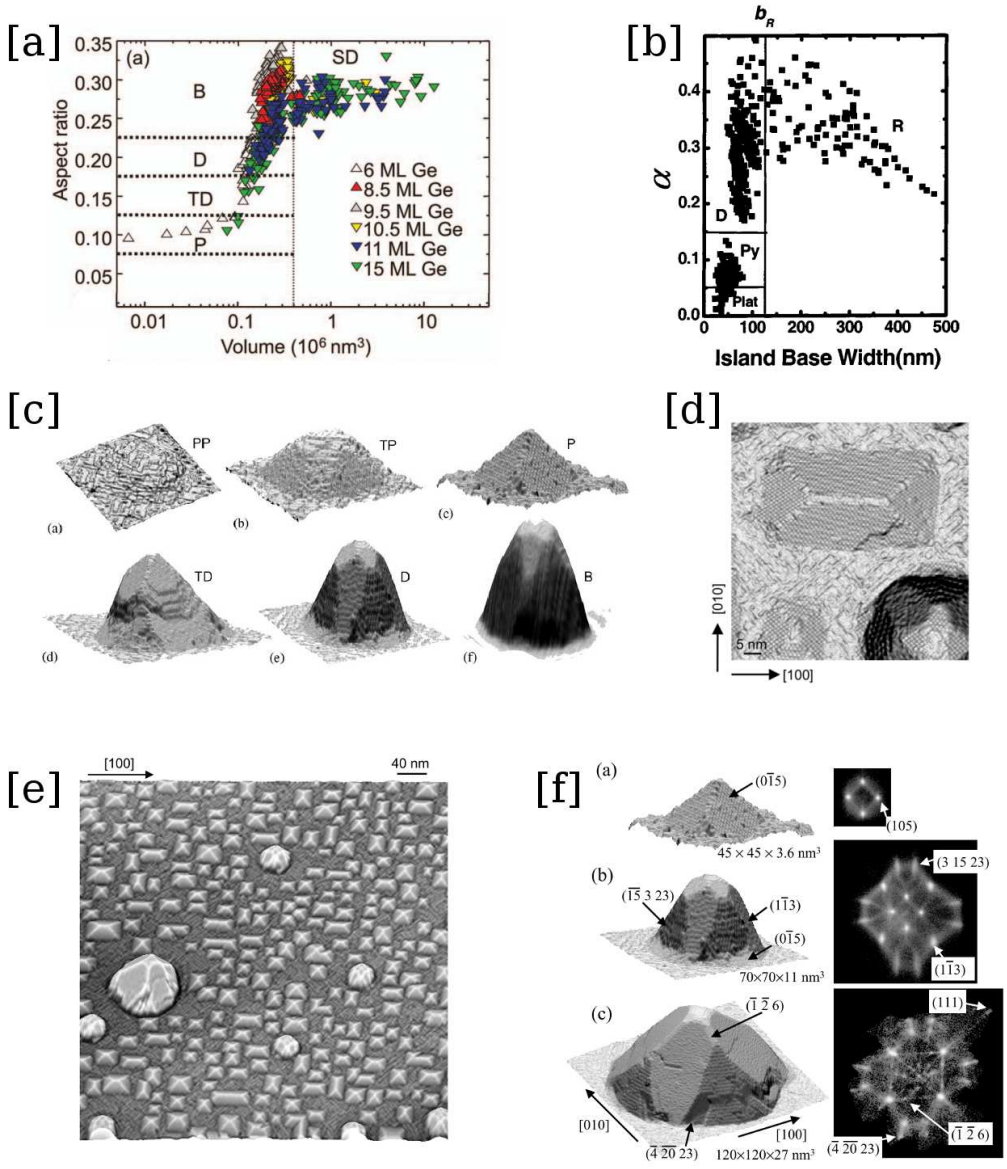

FIGURE 1.2: Ge/Si(001) nanoislands. Evolution of the islands AR as a function of their volume [a] (from Ref.[16]) and base [b] (from Ref.[18]). "SD" and "R" denote the SuperDomes or Relaxed, dislocated islands, see sec.1.6. [c] shows a 3D view of the islands: from top left to bottom right mound, pre-pyramid, pyramid, transition dome, dome, barn. [d] shows an enlarged view of a hut cluster and a dome. [e] shows a large scale image. [f] shows a 3D view of pyramid, dome and dislocated (relaxed) dome and their Facet Plot that allows to identify the facets. [c-f] are taken from Ref.[5]

- 'minor': a stable surface consisting of nanofacets of one or more major surfaces

Some studies on Si and Ge unstrained are reported in Ref.[26]. Here it is shown that the (105) surface is not a stable facet for Ge, an apparent contradiction to its early observation. This is easily explained considering that the facets on Ge/Si islands are compressively strained and literature results [27] show that the (105) surface is stabilized by compressive strain.

As is costumary, in this thesis we will present the orientation-dependent properties of crystals (among which surface energies and stability) by using the concept of the **"Stereographic Triangle"**, that will be first presented and rapidly explained in sec.2.4.2 at page 40 and used in sec.4.1 at page 83.

1.5 Intermixing

The creation of islands from a WL requires adatoms to have enough mobility on the surfaces, having their energy provided by the temperature of the substrate itself. At the same time, high temperature triggers a high intermixing between Si and Ge, with the consequent that the Ge concentration both in the WL and in islands hardly reaches 100%. Photoluminescence experiments [28] have confirmed this holds for the WL and quantitative similar results have been obtained via dedicated atomistic simulations, also with a Monte Carlo approach [29] of allowed Ge-Si chemical mixing during Ge layer-by-layer deposition.

Altough even at temperature equal to 700°C, the Ge concentration in a layer-by-layer growth can exceed 80% [28], this is not true for 3D islands.
The typical concentration for domes grown at 700°C is $\sim 40\%$ [30], whereas it lowers to $\sim 20 - 30\%$ for T=720°C [31].

Apart from a higher mobility and possibility of exchange Si-Ge at surfaces, a well-understood mechanism in which islands become Si-rich is described as follows. The pyramid-to-dome shape transition is accompanied by the formation of trenches surrounding the island [32, 33]. Trenches dig into the Si substrate, thus representing a fresh source of Si at that stage of growth. Ge islands start to incorporate Si and intermixing phenomenon takes place. The driving force towards Si incorporation is the entropy of mixing that leads to alloy Si and Ge. By lowering the Ge content the local lattice parameter of a $Si_{1-x}Ge_x$ alloy comes closer to the Si bulk decreasing the lattice mismatch. The compositional profile of the SiGe island is clearly affected by the intermixing phenomenon. The intermixing of the deposited Ge, with Si popping up from the substrate, which has been shown to decrease the Ge content with increasing growth temperatures, both in CVD and MBE [34] growths.

One experimental technique successfully applied to study the composition profiles inside island is etching [35]. By the use of a chemical solvent (the etchant), islands can be selectively removed over the substrate, allowing for the study of the reaction of the islands upon attack with a solution able to remove SiGe alloy, but not pure Si. In particular, wet chemical etching with a 30% solution of hydrogen peroxide (H_2O_2) selectively removes $Si_{1-x}Ge_x$ alloys with compositions having $x > 0.65$ (i.e. Ge-rich material). At this stage, etching is thus useful to explore the 65% Ge isocompositional profile inside islands, which

is already enough to get into some details of the anisotropic island Ge concentration. Recent experiments, carried out with etchants able to remove material up to the complete dissolution of the islands, were carried out assisted by atomic force microscopy (AFM) scan of the partially etched island at every etching step [36]. Known the etchant composition selectivity at every etching step, it is finally possible to reconstruct a cross-sectional map of the Ge content.

The maps come already very useful to get the first insights of the actual Ge distribution inside islands (domes). The general features are here listed. First of all, a Ge-rich core is clearly present at the top of the island. Second, Si-rich areas are visible at the island corners, which can be explained as the accumulation of material driven by strain by intermixing, during the trenches excavation, as mentioned above. Finally, even if it cannot be inferred from the maps of Fig.1.3, it is expected a pure-Ge layer at the very free island surface. This happens because of the reduced surface tension of Ge with respect to Si: the energy of a dangling bond, in fact, is 0.96 eV for Ge and 1.15 eV for Si from Tersoff potential. This effect is called "surface segregation"[4] and consists in the tendency of material to expose Ge to a greater extent than Si. This effect has thus strong influence especially when Si is deposited on Ge, where now surface segregation becomes a direct driving force towards intermixing.

Recent simulations [37, 38] show that the experimentally revealed profile distribution is the one minimizing the elastic energy: the Ge atoms are preferentially located at the more relaxed top of the island, the Si atoms at the bottom. This is a proof that intermixing phenomena represent an alternative path to the minimization of elastic energy. Indeed, if it is not triggered because of the not-high-enough temperature, some extended defects are created to relieve strain (see sec.1.6 below).

It is noteworthy to say that intermixing can play a non-negligible role in the transition of shape of islands. Indeed the {20 4 23} and {23 4 20} are stable facets of Si but not of Ge, and indeed these facets appear when the temperature is high enough (see discussion above), that favours intermixing.

The role played by silicon in islands stability has been established also from the 'reversal evolution', where a dome covered by a capping layer of Si trasforms back into a pyramid and amorphous mound [39].

As intuitive, typically the higher the temperature, the lower the average Ge concentration in the island. Further on Si(001) the evolution to steeper islands is one-way, the lower Ge content being present in the steeper islands [40] (because of the high temperature necessary to create it).

An important counter-example that proves the importance of considering the detailed geometry and Ge content in the islands for the estimation of their stability has been studied in the present work and is reported in Chapter 3.

[4] and the top Ge layer is called "Floating Layer"

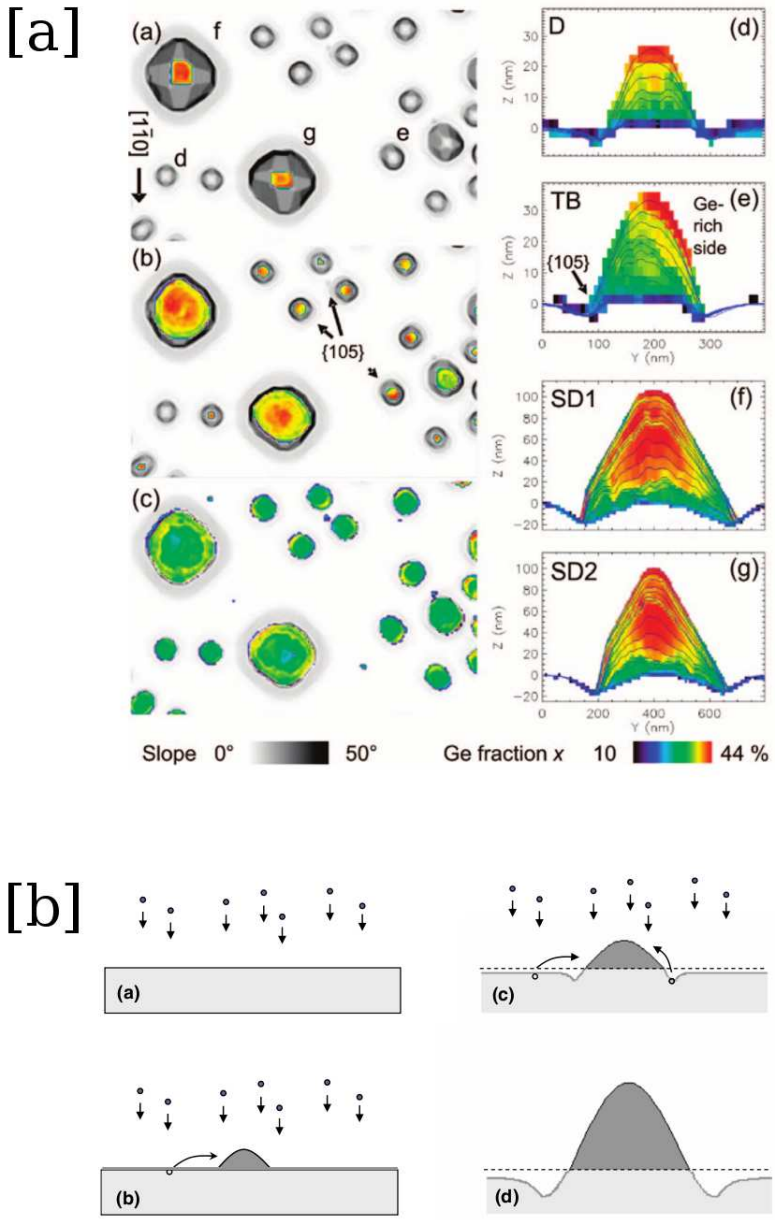

FIGURE 1.3: [a] Intermixing profiles in islands on Si(001) as determined by etching techniques, from Ref.[36]. Since the nucleation is random on the surface the Ge profile may be asymmetric as in (e) due to some ripening phenomena occurring between neighbouring islands. D, TB, SD stands for Dome, Transtion Barn and SuperDome (i.e. dislocated). [b] shows the creation of the trenches triggered by the strain compression due to the island and the silicon spilling out from them (c), thus increasing Si concentration in the island. Reproduced form Ref.[33].

1.6 Plasticity

As stated, both the transition to steeper islands and the intermixing have the aim to reduce the elastic budget stored in the island. An alternative route to these is the onset of a plastic relaxation through the formation of extended crystallographic defects (dislocations) in the islands.

Under peculiar experimental conditions of deposition flux and temperature, the domes become dislocated before transforming into barns. Since these defected islands can relieve strain at a higher degree, they attract adatoms from the surface and enlarge in size, a reason why they are also called "superdomes" [12]. Examples of dislocated domes are reported in Fig.1.3-[a] and 1.2-[e,f], where it is evident that the presence of the line defect alters the island growth, making it asymmetric since atoms prefer to be located in the nearby of the dislocation.

Evidences [17] show that the higher the temperature, the fewer dislocated islands on the sample, suggesting that alloying and dislocation onset are competitive mechanisms.

Since dislocations are detrimental for both electronic and optical properties of nanostructures, a great effort is being devoted in literature to the comprehension of their dynamics and energetics.

In this thesis, we will deal just with coherent islands, neglecting the dislocated ones.

2

Modeling the shape and energy of nanostructures

"Divide et impera" (Divide and conquer)
Latin quote

In this chapter we describe in details the method we adopt to model the nanostructures and to assess their energy.

After discussing the multiscale description of the internal energy of the nanoislands adopted in literature, we define and explain the concept of Wulff solid to model the island shapes.

The basics of atomistic (both *ab initio* and semiempirical) approach and continuum ones are described.

Afterwards the volumetric contribution is described focusing on the anisotropy of the WL. We critically analyze the criterion of the Aspect Ratio for elastic relaxation and show its incompleteness.

An extensive analysis of the way to model surface energies via slab geometries with novel solutions is presented along with its analytic dependence on both Ge epilayer thickness and strain. The need to use the proper strained chemical potential is discussed and proven in Appendix C.

Finally we present the possible nucleation regimes coming out from a different balance between the energy contributions.

2.1 Multiscale modeling of formation energy of nanostructures

Following previous studies we may break the net formation energy of a three-dimensional nanostructure into volumetric (elastic), surface and edge energy contributions [30, 41]. Further we may take the early-stage WL as a reference of energy writing the formation

energy of an isolated island as:

$$\Delta E = E_{isl} - E_{WL} = \Delta E_{vol} + \Delta E_{surf} + \Delta E_{edge} \tag{2.1}$$

The **volumetric energy** is written as

$$\Delta E_{vol} = V \cdot (\rho_{isl} - \rho_{WL}) = V \cdot \rho_{WL} \cdot \left(\frac{\rho_{isl} - \rho_{WL}}{\rho_{WL}} \right) \equiv -V \cdot \rho_{WL} \cdot F \tag{2.2}$$

where the energy of a fixed amount of material in a WL or island configuration is compared and therefore V is the volume of the island that is imposed to be the same as a certain amount of material in the WL; ρ are the elastic energy density of island and WL.
F is the "relaxation factor" quantifying the percentage of strain energy relaxed by the 3D island. Since $\rho_{isl} < \rho_{WL}$ a minus sign is necessary to make F a positive quantity. When $\widetilde{F} \to 0$, the island relaxes very little, when $\widetilde{F} \to 100\%$ it means that $\rho_{isl} = 0$ and the island is perfectly relaxed. The description and quantification of ρ is reported below in section 2.4 where for its computation both atomistic and continuum approaches have been used.

The **surface energy** term must take into account the exposed facets of the island S_i and the area of the WL covered by this B_{cov}, each with the relative surface energy density per unit area γ:

$$\Delta E_{surf} = \sum_{i}^{exposed} S_i \cdot \gamma_i - B_{cov} \cdot \gamma_{WL} \tag{2.3}$$

The surface energy densities γ and their complexity due to the strong dependence on the atomistic details of the surface are described in sec.2.5, where their estimation is achieved just via atomistic approaches. Since this data are typically combined with strain results from continuum approach, this method is called "Multiscale".

The **edges** between adjacent facets of a nanoislands represent a discontinuity of the solid where bonds are broken, they therefore have an energy cost per unit length Γ. Thus, the edge energy term becomes:

$$\Delta E_{edge} = \sum_{j} L_j \cdot \Gamma_j \tag{2.4}$$

where L_j are the lengths of the different edges. Since edges between different facets can in principle have different energies, different values of Γ_j are required. The estimation of the edge energies is not trivial, since they depends not only on the geometries of facets and their reconstruction but also on the way the facets join to each other. A way to estimate it is either via atomistic simulations of idealized geometries [42] or via a combination of theoretical modeling with experimental findings, the latter being a result of this thesis and described in Chapter 5.

It is customary to use eqn.(2.1) with the aim to predict the variation of an island shape when it grows self-similarly, i.e. when the shape is not altered [43]. Since in enlarging the island the ratios surface-to-volume and edge-extension-to-volume change, it

is a common habit to define adimensional quantities called "geometrical factors" β that remain unchanged with the volume as follows:

$$\beta_i^{exp} = \frac{S_i}{V^{2/3}}; \quad \beta_{cov} = \frac{B_{cov}}{V^{2/3}}; \quad \beta_i^{edge} = \frac{L_i}{V^{1/3}} \tag{2.5}$$

That, substituted in the previous relation, turn the internal formation energy into:

$$\begin{aligned} \Delta E &= -V \cdot \rho_{WL} \cdot F + \\ &+ V^{2/3} \cdot \left(\sum_i^{exp} \beta_i^{exp} \cdot \gamma_i - \beta_{cov} \cdot \gamma_{WL} \right) + \\ &+ V^{1/3} \cdot \sum_j \beta_j^{edge} \cdot \Gamma_j \end{aligned} \tag{2.6}$$

This equation can also be expressed as a function of a length characteristic and easy-to-measure of the island b, such as the diameter or the base length of a pyramid or dome. In such a case we can use other parameters K:

$$V \equiv K_V \cdot b^3 \tag{2.7}$$

$$S_i \equiv K_{Si} \cdot b^2 = \beta_i \cdot V^{2/3} \Rightarrow K_{Si} = \beta_i \cdot K_V^{2/3} \tag{2.8}$$

$$B \equiv K_B \cdot b^2 = \beta_{cov} \cdot V^{2/3} \Rightarrow K_B = \beta_{cov} \cdot K_V^{2/3} \tag{2.9}$$

$$L_j \equiv K_j^{edge} \cdot b = \beta_j^{edge} \cdot V^{1/3} \Rightarrow K_j^{edge} = \beta_j^{edge} \cdot K_V^{1/3} \tag{2.10}$$

Hence the equation becomes

$$\frac{\Delta E}{b} = -b^2 \cdot K_V \cdot \rho_{WL} \cdot F + \tag{2.11}$$

$$+ b \cdot \left(\sum_i^{exposed} K_{Si} \cdot \gamma_i - K_{cov} \cdot \gamma_{WL} \right) + \tag{2.12}$$

$$+ \sum_j K_j^{edge} \cdot \Gamma_j \tag{2.13}$$

From these results it is evident that the role of edge energy has a vanishing contribution for large enough volumes, and in literature it is typically neglected. An important counter-example studied in this thesis is the case of ripples on Si(1 1 10) that is described in Chapter 5.

Quantifying this energy ΔE in a way as much accurate as possible is the main goal of this thesis. It is noteworthy to mention that the energy described involves just internal contribution, with no temperature and entropy contribution included. The hypotesis underlying the use of this equation is the thermodynamical equilibrium, i.e. the *kinetic* accessibility (and stability) of the minimum energy state.

The different nucleation regimes coming from the balance of volume and surface contributions are described in sec.2.6, afterwards a full discussion of the two terms is performed.

2.2 Nanoislands as Wulff solids

The first step to the simulation of any system is to find a mathematical model and description of the system itself.

As seen in the previous chapter, the self-assembled SK nanostructures are geometrical solids laying on a substrate. The first ones observed (the pyramids) are extremely simple but the next ones observed (domes and barn) appear rather complex and generally they cannot be described as platonic truncated solids. Finding the geometry of nanoislands is analogous to finding the equilibrium crystal shape (ECS) of a growing crystal. In the growing process the system will seek the shape that minimizes the total surface energy subject to the constraint of fixed volume (i.e. amount of material). This question amounts to a problem in affine geometry that was first solved by Wulff [44, 45]. In the case of strained nanostructures we are dealing with, the geometries can be described as the convex envelope of more than one pyramids (as shown later) and the Wulff solid is the interior envelope of the family of planes [44, 46].

The basic idea is the following and is sketched in Figure 2.1.
Suppose the solid is composed of a bunch of different facets, such as the {105}, {113} or any other. Suppose that each i-th surface, whose normal is n_i, is laying at a certain distance w_i from a fixed point called Wulff point [47]. The Wulff solid is made by the space containing the Wulff point delimited by the surfaces nearest to the Wulff point itself. As shown in the example of Figure 2.1-(a,b) where the Wulff point is the point O, depending on the relative values of w_i, some facets might not be present in the Wulff construction. Indeed, the higher the value of w, the further away the surface, the smaller the relative facet (as if w was a surface energy, as discussed below).

In order to create a solid on a surface (as is the case of our nanostructures), we set the w value of the surface being the substrate to zero in such a way the Wulff point lays at the base of the solid itself and the w_i's of the experimentally-observed exposed surfaces are tuned 'empirically' to reproduce the desidered geometry. The typical geometries of dome and barn observed on Si(001) are reproduced in Fig.2.1-(c-f) with the parameters reported in Tab.2.1.

From these examples some features of the Wulff construction can be deduced.
First of all the mechanism of Wulff construction creates a solid with the steeper facets at the bottom and the shallower at the top (panels c,d), that is definitely the shape observed on the experimental islands (see Chapter 1).
Secondly, the ratio between different facets (i.e. the shape of the island) is a function just of the relative ratio of the w, and not of their absolute values: the same shape is formed if all the w's are multiplied by a constant factor.
Further, the relative extension of the facets depends on the orientation and w values of all the other facets.
Finally, the shape is highly sensitive to the substrate itself (panels g,h).

This shows that if the facets present on the nanostructures are just the few ones with low energy, then a modification of shape should be expected in changing the substrate as predicted by the Wulff construction. This is what is observed (see discussion in Chapter 1) and in some circumstances the solid cannot even close (as is the case described

in Chapter 4). Although the overall solid is the intersection of several pyramids each of which made of a single family of facets (as depicted in Figure 2.1-c,d), and although the geometrical values for pyramids are analytically derivable, the geometrical properties of the islands β are not *a priori* predictable and must be determined case by case.

Quantity	Pyramid	Dome	Barn
w(105)	10.0	9.6	9.8
w(113)	∞	10.2	10.2
w(15,3,23)	∞	12.3	11.9
w(001)	∞	9.2	9.5
w(111)	∞	∞	14.8
w(23,4,20)	∞	∞	14.8
w(20,4,23)	∞	∞	13.2
Aspect Ratio	0.10	0.23	0.28
β_{exp}	9.846	5.193	4.460
β_{cov}	9.655	4.574	3.544
$\beta_{exp} - \beta_{cov}$	0.191	0.619	0.916
β_{exp}^{edge}	8.876	15.452	22.806
β_{cov}^{edge}	12.429	7.722	6.798

TABLE 2.1: Geometrical parameters of realistic island shapes on (001) substrate. The w are the surface energies that enter the Wulff construction: ∞ means that the surface is not included in the solid. The β are the geometrical factors defined in eqn.(2.5). The edges are divided into covered (if they all lie in the substrate plane) and exposed (if at least one point of the segment is out of the substrate plane).

As for the surface energies, it is noteworthy to remind something about the physical interpretation of the Wulff construction.
In an abstract space the fact to include in the solid the portion of space nearest to the Wulff point is equivalent to minimize the quantity

$$\sum_i w_i \cdot S_i$$

that can be seen as the total surface energy if the w_i are the surface energy densities.
This interpretation is not valid in a strained nanostructures like the ones we are studying, because the strain energy accumulated inside the island[1] is an energy term that is not taken into account in this interpretation. Additionally, the surface energies of any facet are highly sensitive to the strain state they are subject to[2], so in a strained nanostructure the w_i's are distinct objects from the actual surface energies of the facets in the island γ_i. However, when no strain is present, the Wulff solid may be used backward to deduce the surface energies of different facets [47]. In these respects the Wulff solid is also the Equilibrium Crystal Structure (ECS) of the system [48].

[1] see sec.2.4
[2] see sec.2.5 and Chapter 5

With this in mind, these models are employed to quantify the elastic relaxation of realistic island shapes in a Finite Element Method approach (as described below) and finally to get the effective surface energy of their facets in a multiscale approach (see below).

2.3 Computational approaches

Here some details on the methods used in this work are summarized to allow the reproducibility of data.

2.3.1 Tersoff potential

A way to handle interatomic interactions in a solid is through semiempirical potentials, that employ ad-hoc analytical expressions to model the interatomic interactions. One potential that is known to work for group IV systems (like Si and Ge) is Tersoff potential [49, 50] where also a three-body term is introduced to better describe the diamond lattice. This potential allows to accurately reproduce the strain field [51].

The potential has been implemented into a hand-made software written in fortran90. In all the calculations the system has been relaxed through a Steepest Descent algorithm, the maximum allowed force being 10^{-6} eV/Å in modulus.

2.3.2 DFT-LDA

In literature several studies of surface energy values are addressed with the use of quantum mechanical calculations based on density function theory (DFT).

In our calculations, we use the planewave-pseudopotential code VASP [52, 53]. Electron-core interactions are modelled with ultra soft pseudopotential (USPP) [54], and exchange and correlation effects are described using the local density approximation (LDA) of Ceperley and Alder [55] as parametrized by Perdew and Zunger [56]. Previous results for GeSi systems [57] show that the LDA approximation used here gives results in good agreement with calculations using the generalized gradient approximation (GGA) for exchange-correlation effects.

In order to build a fully consistent set of surface energies, for all calculations the planewave cutoff energy is set to 355 eV for both Si and Ge atoms, and a vacuum region between slabs of twice the Si diamond cubic lattice constant ($\sim$ 11 Å) is used in the calculation cells. Eigenvalues were computed on a Monkhorst-Pack grid of special k points, the density of which has always been checked to guarantee the convergence. The atomic positions are optimized via a conjugate gradient algorithm, with relaxed structures identified when the maximum residual force fell below 5 meV/Å.

2.3.3 FEM

The elasticity theory is a classical problem of partial differential equations [58], thus, it can be solved in a continuum approach using a finite element method (FEM), that can be syntetically described with the following points. First of all it is worth recalling the

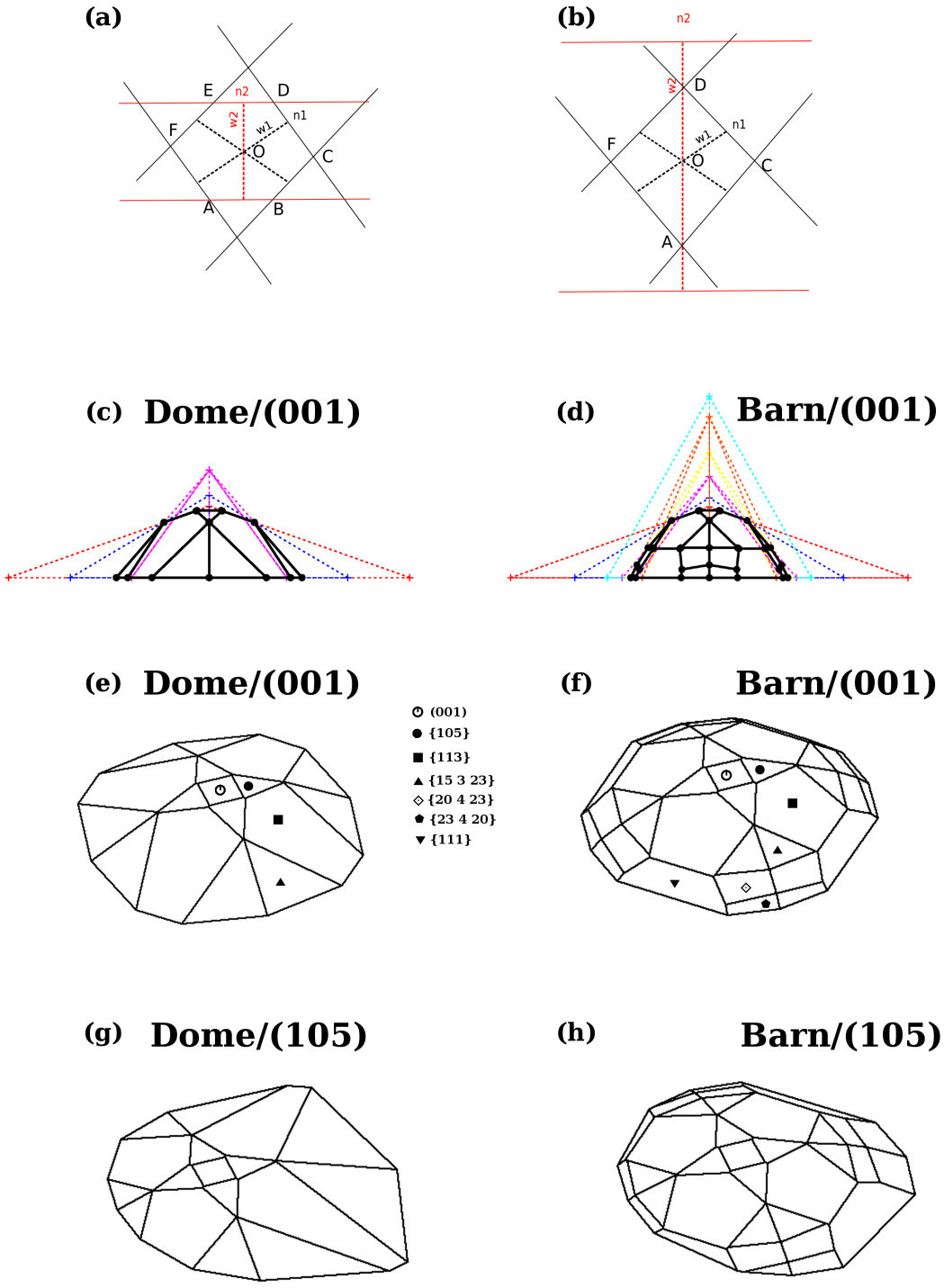

FIGURE 2.1: Wulff solids of nanoislands: Top row = 2D simple case with 2 w's (black and red), point O being the Wulff point. In (a) the Wulff construction is the area containing O and delimited by points ABCDEF. In (b) the w of the red line is too long and its facets are missing in the construction ACDF. (c) and (d) show the construction of the envelope (black lines) of dome and barn on (001) with the parameters of Tab.2.1 with all the pyramids (dashed lines). (e) and (f) are perspective view of (c) and (d) respectively with the facets families highlighted. (g) and (h) show the same solids when the substrate is not 001 but 105 to show the change in shape. All the figures are made with a software in fortran90 written on purpose.

elastic problem which finds in Finite Elements its numerical way of solution. The linear elasticity theory used here is the generalization to three dimensions of the Hooke's law of a spring. In this formulation the deformation is described by the symmetric strain tensor ϵ_{ij}, the diagonal components describing the compression or dilation on the three cartesian axes whereas the off-diagonal components describing a deformation in space. The forces are described by the stress tensor σ_{ij} and they are linked to the deformations through the stiffness tensor C_{ijkh} as:

$$\sigma_{ij} = C_{ijkh} \cdot \epsilon_{kh} \tag{2.14}$$

As discussed in Appendix A, symmetries can simplify the problem by using also the Voigt notation [58].

Our systems consist in a free (uncapped) island laying on a WL or substrate and the problem to solve for the displacement field u when no external forces apart the mismatch is applied is the following:

$$\begin{cases} -\sum_{j=1}^{3} \partial_j \sigma_{ij} = 0 & inside \quad \Omega \\ \sum_{j=1}^{3} \sigma_{ij}(u) n_j = 0 & on \quad \Gamma_N \\ u_i = 0 & on \quad \Gamma_D \end{cases} \tag{2.15}$$

where Ω is the region where the solution is found (the SiGe island and the WL or substrate underneath), Γ_N are the Neuman boundary conditions that impose equal to zero the force normal to the surface (that we apply to the borders of the substrate) and Γ_D are the Diriclet boundary conditions that impose no displacement for points on the boundary (i.e. fixed boundary, that we apply to the bottom of the cell). The exposed facets of both the island and the substrate/WL are free to relax.

The initial condition (stress of the island) is introduced thorugh the use of Eshelby's Theory of inclusions [58]: the initial stress is computed from an eigenstrain that due to the strain induced by the lattice mismatch between the epilayer and the substrate:

$$\epsilon_m = \frac{a_{sub} - a_{epi}}{a_{epi}} \tag{2.16}$$

The solution of (2.15) is computed on every node of a properly-created grid and from this is possible to calculate the displacement field u at each node, and the elastic properties of the system (stress, strain and elastic energy).

Once the displacement field u is computed, the elastic energy density stored in a deformed solid is given by:

$$\rho \equiv \frac{1}{2} \cdot C_{ijkh} \cdot \epsilon_{ij} \cdot \epsilon_{kh} \tag{2.17}$$

$$= \frac{1}{2} C_{11}(\epsilon_{xx}^2 + \epsilon_{yy}^2 + \epsilon_{zz}^2) + \frac{1}{2} C_{44}(\epsilon_{yz}^2 + \epsilon_{zx}^2 + \epsilon_{xy}^2) + $$

$$+ C_{12}(\epsilon_{xx}\epsilon_{yy} + \epsilon_{yy}\epsilon_{zz} + \epsilon_{xx}\epsilon_{zz}) \tag{2.18}$$

Where eqn.(2.18) hold in the case of cubic materials [59] and it is this quantity that enters the energy balance.

The results showed in this thesis are obtained using the commercial FEM code Comsol Multiphysics.

2.4 Elastic field

Here we discuss the properties of the elastic field.

2.4.1 Bulk properties

The elasticity theory describes the deformation with respect to the unstrained bulk, hence the first step to obtain the strain field of a system is the assessment of its bulk properties.

Since the interatomic interactions are different for different potentials, it is fundamental to use the equilibrium values for the potential employed to be consistent. The equilibrium lattice constant of a bulk material can be obtained by taking the value giving the minimum energy per atom. An example of this obtained by Tersoff potential for Ge is sketched in Fig.2.2. The minimum energy value of the lattice constant is the equilibrium lattice constant and the corresponding value of energy is the "chemical potential" μ, whose modulus is the cohesive energy of the system. Its asymmetry from the minimum is due to non-linearity terms that cannot be described by the elasticity theory. This trend is well-described by the Birch-Murnaghan equation [60, 61] and allows to extract some elastic constant as well [62]. On the other hand, the elastic constants can be extracted by properly straining a bulk cell [63].

The bulk properties for all the parametrization adopted are reported in Tab.2.2, where the elastic constants given by Tersoff potential are compatible with the ones found by other authors with the same potential [64].

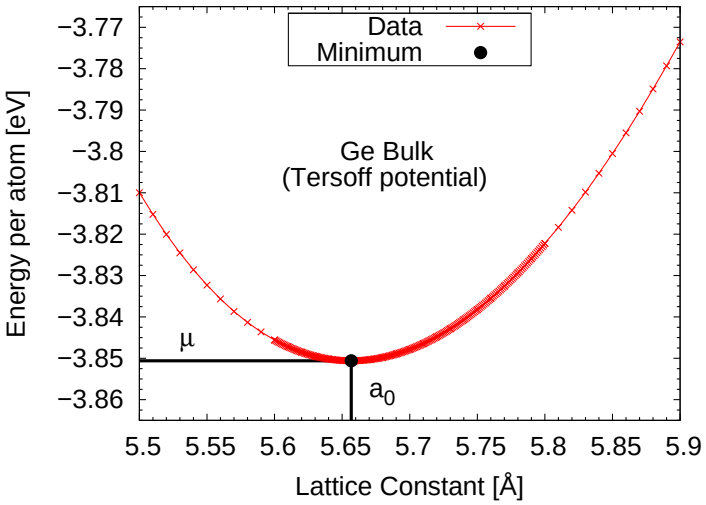

FIGURE 2.2: Example of energy per atom for different lattice constant in the case of a Ge bulk described by Tersoff potential.

Material	Potential	a_0 [Å]	C_{11} [GPa]	C_{12} [GPa]	C_{44} [GPa]	μ [eV/atom]
Ge	Exp	5.658	128.35	48.23	66.66	X
	Tersoff	5.6567	138.441	44.449	66.813	-3.85060
	DFT-LDA	5.624	121.6	46.5	64.3	-5.199221
Si	Exp	5.432	165.78	63.94	79.62	X
	Tersoff	5.4320	142.541	75.392	69.012	-4.62959
	DFT-LDA	5.390	160.2	62.1	76.2	-5.976782

TABLE 2.2: Elastic constants for all the potential used in this work and the chemical potential of Bulk materials. The experimental constants 'EXP' are taken from Ref.[3].

2.4.2 WL: the role of anisotropy and non-linearity

The elastic energy of a WL, ρ_{WL}, plays a fundamental role in the stability of nanoislands in eqn (2.2). Additionally, a biaxially-strained GeSi/Si WL can increase the charge carrier mobility in high-speed transistors, an effect that already reached the stage of application [65] and therefore has a relevance on its own.

Unlike the 3D islands, the elastic energy of a biaxially-strained WL can be computed analytically inside the LET (linear elasticity theory)[3], therefore this system can also be used as a test for the role played by non-harmonic terms by comparing analytic results with atomistic approaches. At the same time the anisotropic behaviour is analyzed showing a strong directional-dependent relaxation that must be taken into account when dealing with the nucleation of islands on substrates different from (001) along with the distorted shape of the domes.

Additionally, as is proven thoroughly in Appendix C at page 165, giving the correct energy to a strained bulk is also of fundamental importance to avoid non-sensical results for surface energies.

ρ of a strained WL in LET

The elastic energy of a WL can be deduced analytically in several ways [66]. Here we employ the direct definition of elastic energy.

The definition of elastic energy density for a generic system is:

$$\rho = \frac{1}{2} \cdot C_{ij,kh} \cdot \epsilon_{ij} \cdot \epsilon_{kh} \tag{2.19}$$

In the case of a WL strained in the direction x of $\epsilon_{xx} = \epsilon_1$, along direction y of $\epsilon_{yy} = \epsilon_2$ and free to relax along the direction z to minimize its energy reaching a deformation state of $\epsilon_{zz} = \epsilon_3$, the system cannot undergo any deformation in shape, since the only stresses are applied along the facets of the parallelepiped. Therefore, all the off-diagonal components will be zero:

$$\epsilon_{ij} = 0 \quad \text{if } i \neq j$$

[3] see Appendix A

Further, the strain in the plane $\epsilon_{xx}, \epsilon_{yy}$ are fixed by the external conditions (the adaptation to the substrate lattice), the only unknown variable, therefore, being the strain along the free surface z ϵ_{zz}. Since no stress is applied to this surface we have:

$$\sigma_{33} = C_{33ij} \cdot \epsilon_{ij} = 0$$

After expressing the stiffness constants in Voigt notation this expression can be solved for ϵ_{zz} getting the value:

$$\epsilon^*_{zz} = -\frac{C_{13} \cdot \epsilon_{xx} + C_{23} \cdot \epsilon_{yy}}{C_{33}} \tag{2.20}$$

$$= -\frac{C_{13} + C_{23}}{C_{33}} \cdot \epsilon \tag{2.21}$$

Where the latter equation is for the biaxial strain situation: $\epsilon_{xx} = \epsilon_{yy} = \epsilon$.
Note that the strain relaxation has opposite sign with respect to the strain applied in the plane and typically a different value. This is named **Poisson effect** and the ratio ϵ_{zz}/ϵ Poisson ratio. Giving the correct value of ϵ_{zz} plays a fundamental role in assessing the correct values of the surface energies (see Appendix C).

From this, the elastic energy for a WL free in the direction 3 turns into:

$$\rho = \frac{1}{2} C_{ij,kh} \epsilon_{ij} \epsilon_{kh} = \frac{1}{2} C_{ii,kk} \epsilon_{ii} \epsilon_{kk} \equiv \frac{1}{2} C_{ik} \epsilon_i \epsilon_k \tag{2.22}$$

$$= \frac{1}{2} \left[C_{ii} \epsilon_i^2 + 2C_{12} \epsilon_1 \epsilon_2 + 2C_{13} \epsilon_1 \epsilon_3 + 2C_{23} \epsilon_2 \epsilon_3 \right] \tag{2.23}$$

$$= \frac{1}{2} \epsilon_1^2 \cdot \left(C_{11} - \frac{C_{13}^2}{C_{33}} \right) + \frac{1}{2} \epsilon_2^2 \cdot \left(C_{22} - \frac{C_{23}^2}{C_{33}} \right) +$$

$$+ \epsilon_1 \cdot \epsilon_2 \cdot \left(C_{12} - \frac{C_{13} \cdot C_{23}}{C_{33}} \right) \tag{2.24}$$

$$= \epsilon^2 \cdot \frac{1}{2} \cdot \left[C_{11} + C_{22} + 2 \cdot C_{12} - \frac{(C_{13} + C_{23})^2}{C_{33}} \right] \tag{2.25}$$

where the last equation is for the biaxial strain case $\epsilon_{xx} = \epsilon_{yy} \equiv \epsilon$.

In all these equations the stiffness tensor is expressed in a general form.
Indeed, from the way the elastic constants are defined [63, 67, 68], they refer to the case where the cartesian axes are along the axis of the cubic cell: i.e. x//[100], y//[010], z//[001]. If this is the case, the stiffness tensor is the one reported in Appendix A and we have

$$C_{13} = C_{23} = C_{12} \quad ; C_{33} = C_{22} = C_{11}$$

Hence in the case of a biaxial strain we get:

$$\epsilon^*_{zz}(001) = -\epsilon \cdot \frac{2 \cdot C_{12}}{C_{11}} \tag{2.26}$$

$$\rho_{WL}(001) = \epsilon^2 \cdot \left[C_{11} + C_{12} - 2\frac{C_{12}^2}{C_{11}} \right] \tag{2.27}$$

Where is evident that the elastic energy density is a quadratic function in the deformation, and the theory is an harmonic one[4].

[4]Hence the name Linear Elasticity Theory

For general directions, eqns (2.24,2.25) are still valid, provided that the stiffness tensor is referred to the proper directions. Indeed, the elastic energy of a biaxially-strained WL in the case of a general direction $z//(n_1, n_2, n_3)$ can be deduced by properly rotating the stiffness tensor.

For sake of simplicity we consider directly the case of a biaxial strain and since the strain applied is isotropic on the xy plane in this case, any couple of mutually-orthogonal directions can be taken as x and y normal to the z axis. The chosen directions are:

$$\begin{cases} z &= [n_1, n_2, n_3] \\ x &= [n_2, -n_1, 0] \\ y &= z \wedge x = [n_1 \cdot n_3, n_2 \cdot n_3, -(n_1^2 + n_2^2)] \end{cases} \tag{2.28}$$

All the subsequent results called "LET" are obtained by numerically rotating the stiffness tensor and using eqn (2.25).

Atomistic Approach

In the case of atomistic approaches, no expression for the energy as a function of strain is strictly needed, rather the chemical potential μ of the atoms can be extracted directly from the energy of the strained cell and since it is a bulk every atom has the same energy. In any case, the strain along z is *a priori* unknown and is determined as follows.
As is the case of continuum approach, here we suppose the strain ϵ_{xx} and ϵ_{yy} to be fixed and known and the system will relax till the energy reaches a local minimum given these conditions, the only variable being the strain along z. By imposing to the cell different ϵ_{zz} values, this minimum is found for a value of the strain ϵ^*_{zz} as sketched in Figure 2.3 for the simple case of z//(001).
For a generic direction it is mandatory to find a way to minimize the number of atoms needed in the cell, since the computational cost and time is proportional to a power of the number of atoms, a parameter particularly relevant in the case of an *ab initio* analysis used in this work. For this reason, a conventional, cubic, 8-atoms, unit cell is exploited, that is distorted in such a way to reproduce the proper strain.

The chemical potential μ can be linked to the elastic energy density ρ by considering the latter as the additional energy per unit of UN-strained volume taking the unstrained condition as a reference:

$$\rho = (\mu - \mu_{unstr}) \cdot \frac{N}{V_0} \tag{2.29}$$

where μ is the energy per atom in the strained condition, μ_{unstr} is the energy per atom in an UNstrained solid that are reported in Table 2.2, N/V_0 is the density of atoms in an UNstrained solid. In the case of a diamond lattice (as Si, Ge and their alloys) the density is:

$$\frac{N}{V_0} = \frac{8}{a_0^3} \tag{2.30}$$

where a_0 is the lattice constant of the material in an unstrained bulk.

All the results are reported in the next subsection.

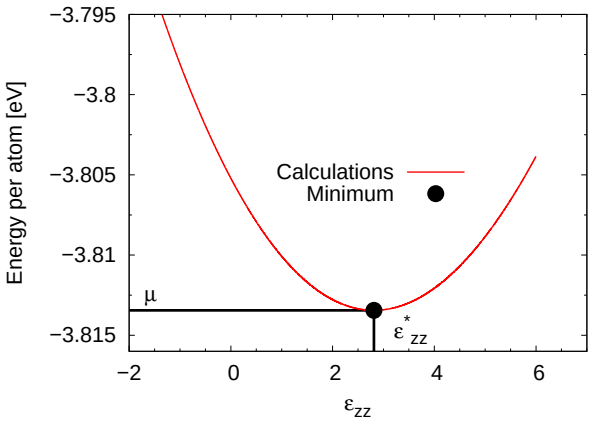

FIGURE 2.3: Method to find μ and ϵ^*_{zz}. Tersoff potential trend for the energy per atom of a WL of Ge(001) strained biaxially at -4% for different strain imposed along z ϵ_{zz}. The non-parabolic trend due to non-linear effects is evident. The minimum energy is μ and the strain at which this happens is the Poisson-effect-due value ϵ^*_{zz}. In the case of DFT-LDA just some points are computed and the minimum is found with a interpolation with a third degree polynomial function around the estimated minimum (not shown).

Results

In this subsection the results for $\mu, \rho, \epsilon^*_{zz}$ are presented.
After showing the method of the stereographic triangle to visualize directional-dependent results, an extensive comparison is made between Tersoff potential results and the LET approach in order to show non-linearity effects.
An analysis of the anisotropy is performed for both experimental elastic constants in LET, Tersoff potential and DFT-LDA approach.

Visualization:
The visualization of physical property as a function of the direction is typically made in polar coordinates on a sphere [66]. However, by exploiting the symmetries of cubic crystals the independent directions to analyze are the ones inside the so-called **"stereographic triangle"** [69][5]. This triangle is a portion of the full sphere of directions and one of the possible and simplest way to represent it is as follows.
The directions laying inside it are the ones with the Miller indexes (n_1, n_2, n_3) satisfying the following criteria:

$$\begin{cases} n_1 & \leq & n_3 \\ n_2 & \leq & n_1 \\ 0 \leq n_2 & \leq & n_1 \leq n_3 \end{cases} \tag{2.31}$$

From these the values of the variable in the entire sphere of directions can be determined, so the stereographic triangle is a convenient 2D representation of direction-dependent properties in cubic crystals.

[5] see sec.1.4 at page 24

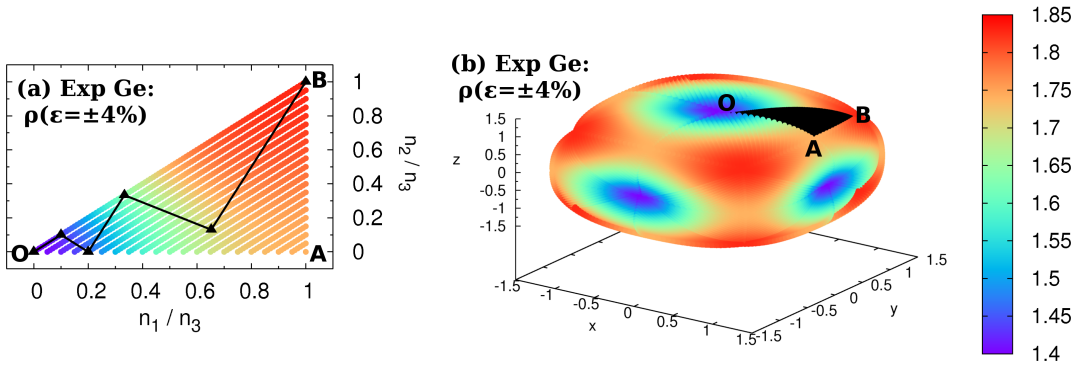

FIGURE 2.4: Anisotropy of ρ for a WL biaxially strained at $\epsilon = \pm 4\%$ in the plane (n_1, n_2, n_3) analyzed with the experimental elastic constants in a LET approach. (a) stereographic triangle with the direction highlighted from O to B: (001), (1 1 10), (105), (113), (15 3 23), (111). (b) 3D polar representation with a colour scale. The region in black is the region covered by the stereographic triangle in panel (a). The units of ρ are meV/Å^3.

Elastic energy density:
An example of the use of the stereographic triangle is reported in Figure 2.4, where the elastic energy density ρ of a WL biaxially strained at $\epsilon = \pm 4\%$ is reported as obtained by LET using experimental constants for germanium. Panel (a) shows the values inside the stereographic triangles with a colour scale. The black points from O to B highlight the directions: (001), (1 1 10), (105), (113), (15 3 23) and (111). Panel (b) shows the same results in a 3D polar representation where the region covered by the stereographic triangle is represented in black. The same colour scale is used for clarity. As evident the elastic energy density is highly anisotropic: it ranges from 1.4 meV/Å^3 for the case of (001) to 1.85 meV/Å^3 for the case of (111), giving rise to a 3D shape already reported in literature [66], that highlights the {001} directions are 'soft' ones in Ge (and Si) systems [70].

Since LET is used, the elastic energy density is quadratic in the in-plane-strain (see equation (2.25)), so the same energy is for both $\epsilon = -4\%$ and $\epsilon = +4\%$.
This is not the case if any atomistic approach is used. Indeed Figure 2.5 shows that the values for μ and ρ of a Ge WL subject to a in-plane-strain equal to -4% (panel a) or +4% (panel b) as computed by Tersoff potential are different to each other: 1.6 and 1.4 meV/Å^3 for (001) respectively. Further, they both differ from the results of LET with Tersoff potential (panel c). This is a clear effect of non-linearity. Indeed panel (d) shows the trend of μ (left y axis) and ρ (right y axis) as a function of ϵ for the directions highlighted by the black points in the other panels. The curve is clearly not symmetric with respect to $\epsilon = 0$ and it resembles a Lennard-Jones potential. Panel (e) focuses on the values for $\epsilon = -4\%$. Panel (f) reports the same quantity obtained with a DFT-LDA approach.

From the results it is evident that the non-linear effects might play a role in modifying the value of the elastic energy density (particularly for high strain values). Further they also show the necessity to compute the elastic energy case by case, taking into account the

direction under analysis since the anisotropy may modify the elastic energy considerably (consider the differences between panel (e) and (f)).
As for the anisotropy, the LET may get different values yet it preserves the general trends of ρ with the direction, indeed panel (c) resembles in tone both (a) and (b).

Strain zz:
Fig. 2.6 shows the results of ϵ^*_{zz} in the same cases as Fig. 2.5.

Panels (a) and (b) shows Tersoff potential results for the case of $\epsilon = -4\%$ and $+4\%$, respectively. Some changes in the color gradations are revealable.

The trend of ϵ^*_{zz} vs ϵ is a line in LET, but from the analysis with the in-plane-strain of panel (c), we see that this is a rather good approximation just for small absolute strain values, whereas some non-linear contributions (dependent on the surface) are evident.

A comparison of the actual values for Tersoff potential (panel d) and for DFT-LDA (panel e) shows that a detailed computation case by case is needed, since some variation are observed: for instance the relative values of (113) and (15 3 23) are inverted in the two atomistic approaches.

Conclusions

In this simple case it is evident that the anisotropic response cannot be ignored for a quantitative analysis. Indeed if the elastic constants are imposed to be isotropic all the directions have the same energy as the (001), leading to a maximum error in the elastic energy equal to:

$$\frac{\rho(001) - \rho(111)}{\rho(111)} \simeq \frac{1.4 - 1.85}{1.85} \simeq -24.32\% \tag{2.32}$$

in the case of experimental constants used in LET, a quantity that is considerable compared to the degree of relaxation of a 3D island (see next section).

As for the non-linearity effects, here it has been shown that the LET (and the FEM analysis used for that) can lead to results compatible with the atomistic treatments provided the strain is not too high, for the case of strain $\sim -4\%$ being acceptable. Yet for a quantitative comparison a correction to the LET must be introduced and this will be explained in Chapter 5.

Additionally, the elastic response must be computed in every case separately since every potential (Tersoff or DFT-LDA) can give slightly different values but in each treatment everything must be consistent with the other elements.

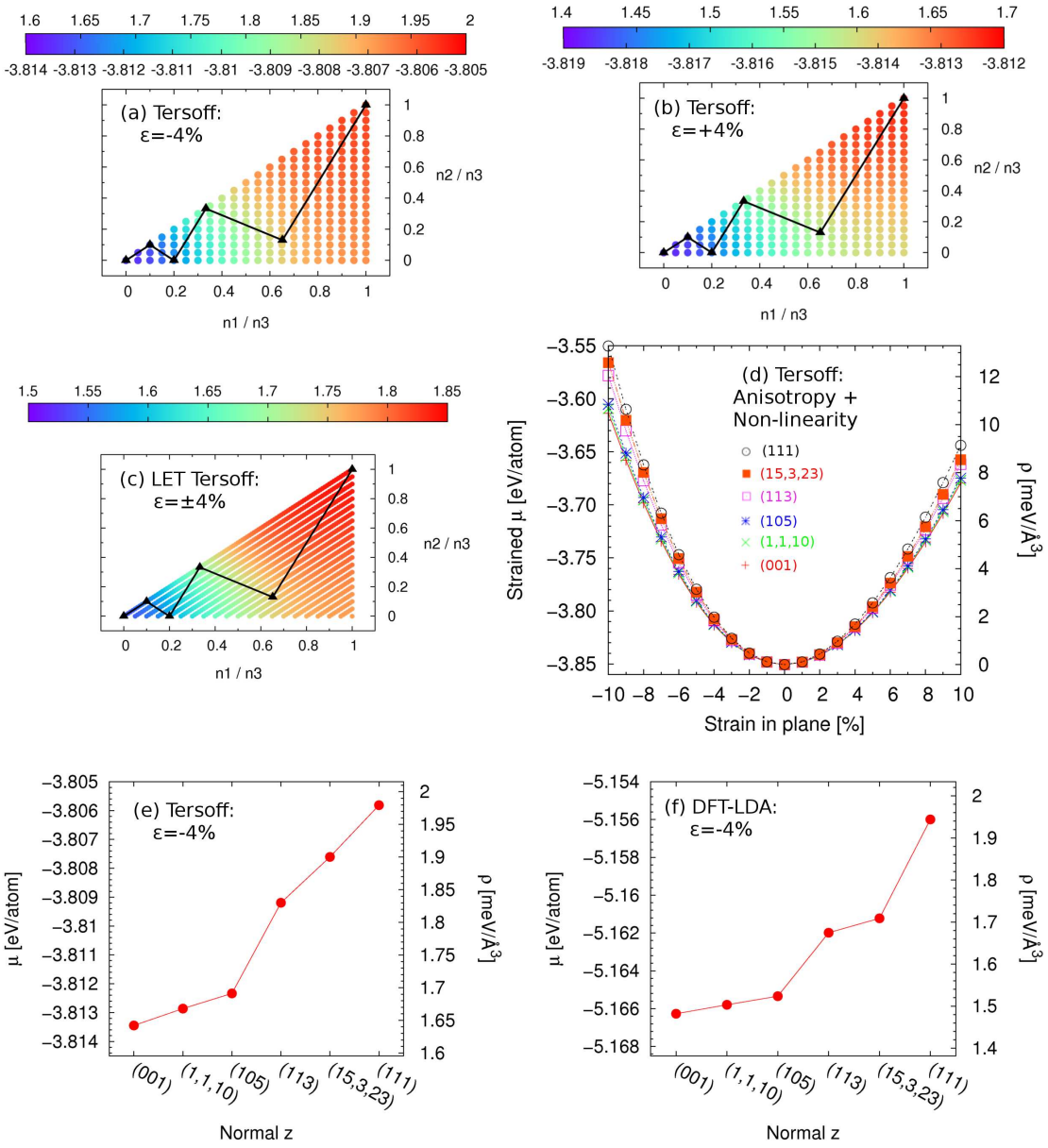

FIGURE 2.5: Anisotropy of ρ (values at the top of the scale in meV/Å^3) and μ (values below the scale in eV/atom) for a WL biaxially strained at $\epsilon = -4\%$ (a) and $\epsilon = +4\%$ (b) analyzed with the Tersoff potential. In this case the values in the two cases are different and differ also from the results given by LET with tersoff elastic constants (c). This is an effect of the non-linearities, i.e. non perfect parabolic shape of the chemical potential with strain (d). In all the triangles the black points are the same as in Fig.2.4-(a) and their values for (a) are reported in (e). Panel (f) reports the values for DFT-LDA at $\epsilon = -4\%$ for comparison.

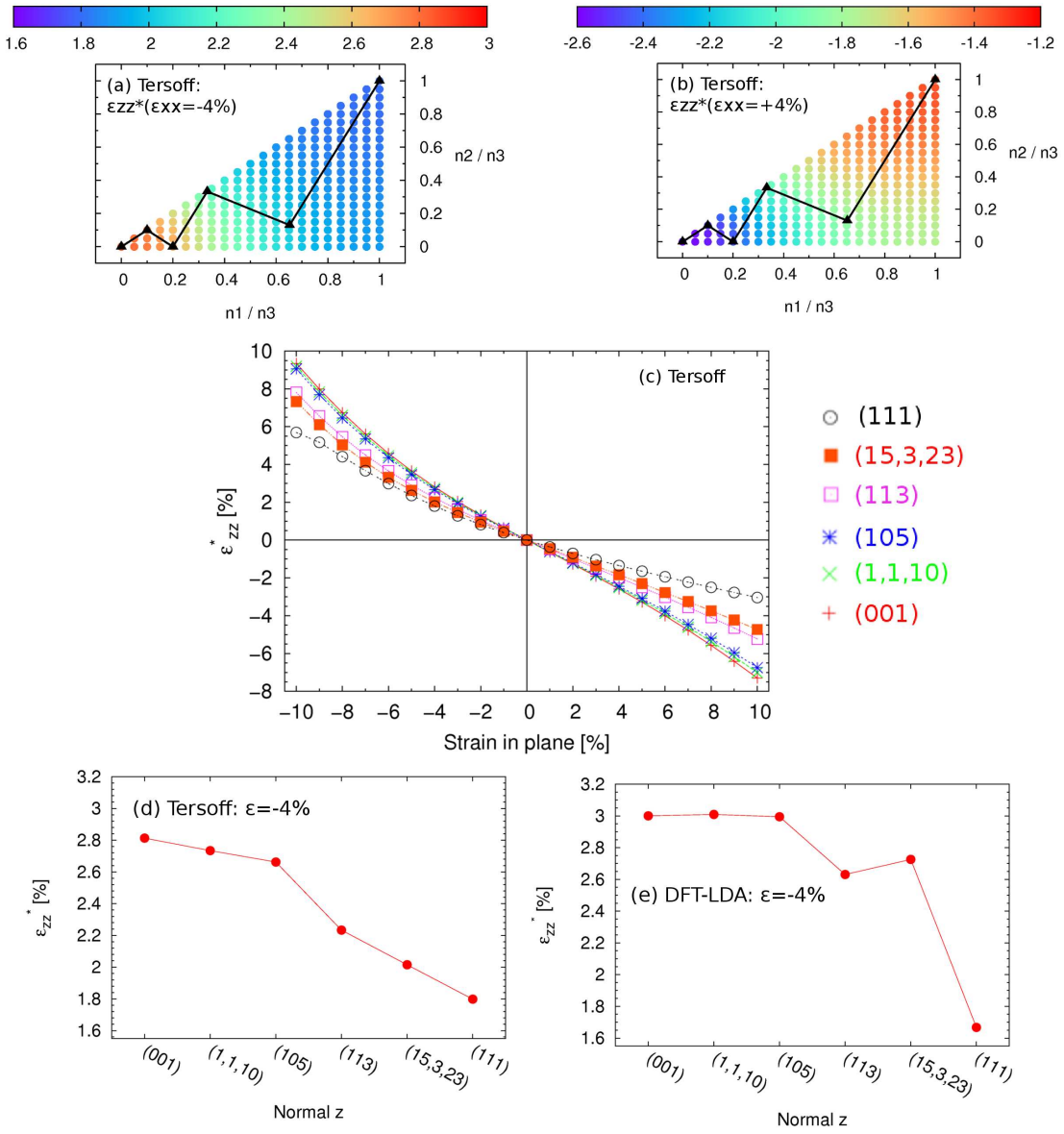

FIGURE 2.6: Anisotropy and non-linearity on ϵ^*_{zz} (in %) analyzed with atomistic potentials. Tersoff potential results for $\epsilon = -4\%$ (a) and $+4\%$ (b) are reported. In (c) the non-linear trend with strain is evident for the directions highlighted in the triangles. Panels (d) and (e) show the values for $\epsilon = -4\%$ for Tersoff and DFT-LDA approaches respectively. It is noteworthy that the relative values of (113) and (15 3 23) are inverted in the two panels, showing the necessity of a detailed computation for each situation.

2.4.3 Islands and the Aspect Ratio role revisited

In this section, the elastic field of an island is described as obtained from the continuum approach. After outlining the general feature of relaxation, a detailed check of the degree of relaxation for numerous islands of different shapes is performed, leading to some interesting outcomes.

General feature of 3D relaxation

Contrary to the WL situation, analytical expressions for the strain field in a 3D structure are not known, hence the only possible approach is the FEM one. Obviously nanoislands are much more complex than a flat WL, with a consequent great variety of features of the non-homogeneous strain field. The results for the shapes of pyramid, dome and barn are reported in Fig.2.7 for the ideal case of 100% Ge islands atop of Si(001) in absence of any WL underneath.

As is the case of the WL, the strain field is influenced by the free surfaces that tends to expand outwards, but in addition to that even the edges are centers for strain relieve (see panels d-e) since atoms can experience more degrees of freedom in these regions. As evident, the islands are more relaxed at their top (see panels a,b,d), a reason why the Ge atoms tends to accumulate in this region in intermixed islands (see sec.1.5). Contrary to the WL, the off-diagonal components of strain are non-zero (panels c,e) showing that a deformation of the shape of island is taking place.

The non-homogeneous expansion of the island causes the deformation of substrate with some compressive lobes at the bottom lateral borders of the island and an expansive lobe below the center of the island (see panel b). This lobes compress the WL under the island to a different extent depending on the island-to-WL size ratio: an effect that makes the analysis as a function of volumes non self-similar.
The trend of the elastic energy density per unit Ge volume (the stressor) as a function of the ratio island-height-to-WL-height is reported in Fig.2.8 for the simple case of a 2D 100% Ge island where periodic boundary conditions (PBC) are applied in the plane. The elastic energy density changes continuously from the one of the WL (1.4 meV/Å^3) to the one of the island on Si ($\sim$1.3 meV/Å^3) with the growing of the island size. Considering that the result for the ratio of height equal to ~ 6 is just negligibly different from the one of the island alone and that the typical WL thickness in Ge/Si SK island is $\sim 3ML$, we can infer that this effect can be neglected if the island is $\simeq 6 \cdot 3ML \cdot 0.14nm/ML \simeq 2.52$ nm heigh or larger. Since domes and barns are typically higher than ~ 5 nm [71], this effect can be neglected, but it can be relevant for shallower and smaller islands like pyramids or huts[6].

It is noteworthy to see that the elastic energy density must be trated carefully in the stability equations, in a different manner as treated here. This is discussed in Chapter 5.

The values of the elastic energy density ρ are analyzed and reported in the next subsection.

[6] as will be shown in chapter 5

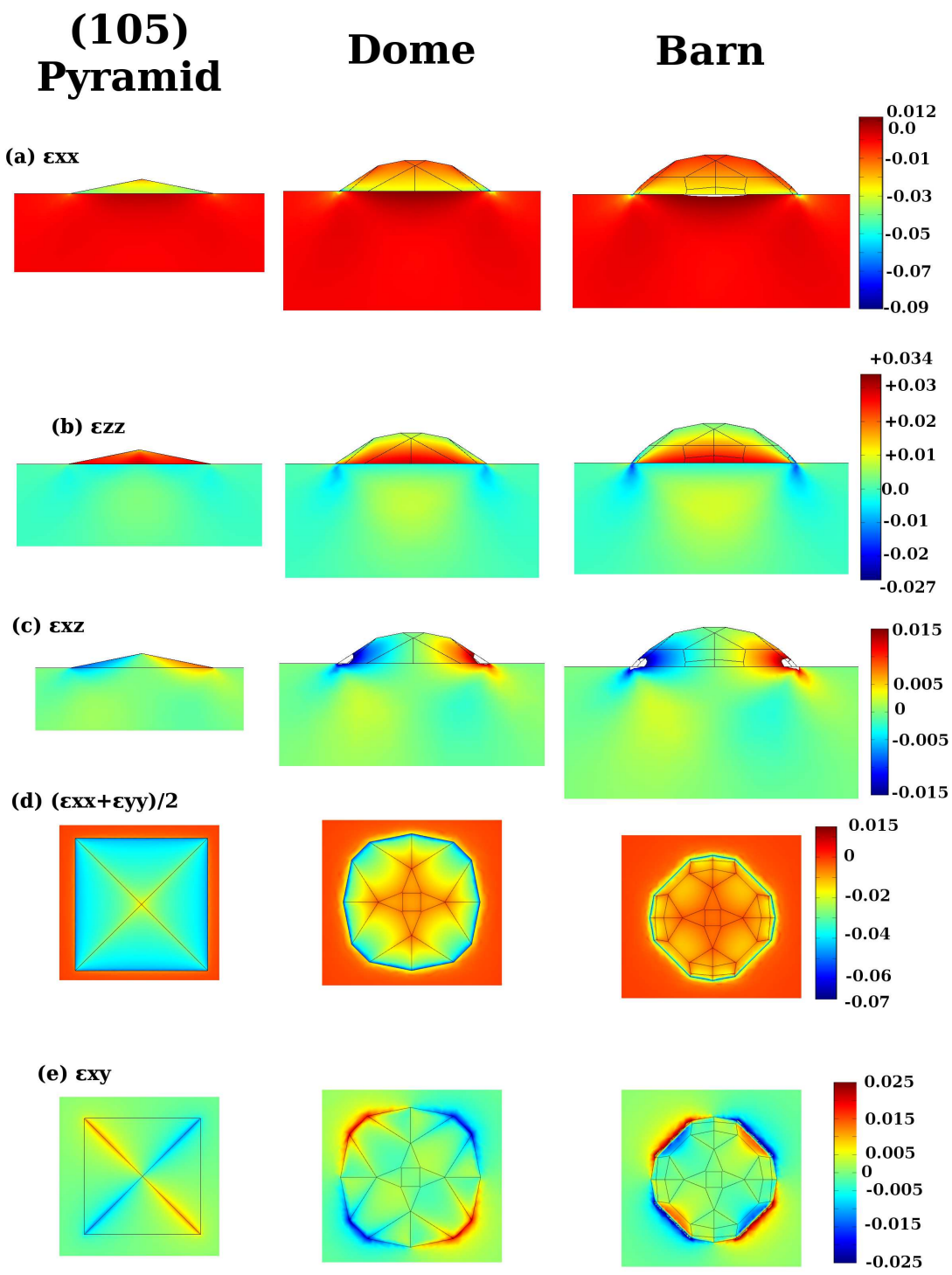

FIGURE 2.7: Strain field components in 100% Ge 3D islands on Si(001) as obtained from FEM with experimental elastic constants.

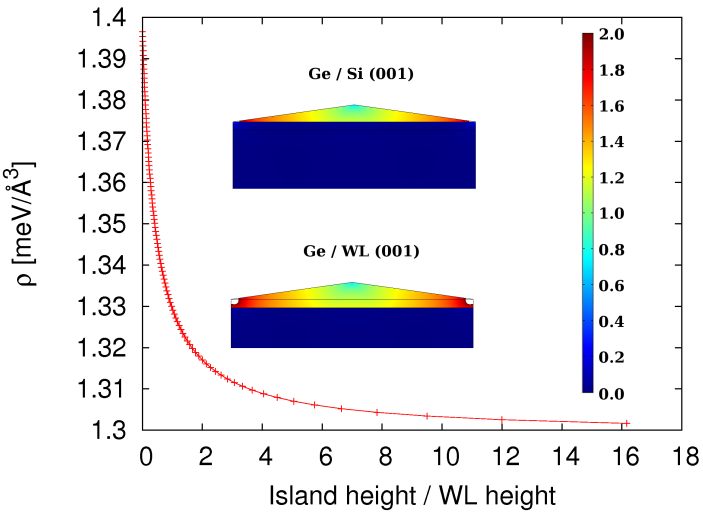

FIGURE 2.8: Effect of WL under the island on the elastic energy for the case of a shallow 2D island. The value of ρ is per unit volume of Ge in the cell. The colour maps show the values of the elastic energy.

Is *really* the steeper the more relaxed?

In the previous section we have highlighted some general properties of the strain field in the nanostructures. We have also shown that the steeper island has a lower elastic energy density. Although this is a general statement in literature and it is an argument generally adopted to explain the shape evolution of strained nanoisland as their volume increases [72], no detailed analysis of this has been performed so far.

Here we perform a careful check of this trend "The steeper, the more relaxed".

To fix the ideas, we focus our attention on nanostructures on Si(001) with the same surface families as dome ({105}, {113} and {15 3 23}) yet without the top (001) surface to simplify the treatment. In a Wulff construction, the relative extension of these facets (i.e. the island shape) is governed not by the absolute values but rather by their ratio. Hence, in the case of three facets any geometry is determined by the two coordinates of w:

$$\left(\frac{w(113)}{w(105)}, \frac{w(15\ 3\ 23)}{w(105)}\right) \tag{2.33}$$

The values of the Aspect Ratio (AR) obtained for any geometry can therefore be represented in a 3D graph[7] as Figure 2.9 shows. As already stated in section 2.2, the area of a facet is roughly inversely proportional to the value of w, hence, when the w value of the surface is smaller enough than the others, the outcoming island is a pyramid with this family alone, leading to the *plateaux* in the figure. For some other regions of this space, just two families are actually present, whereas all the three families appear in a small region (highlighted with larger dots in the figure). We focus on the case of this latter region, where it is evident that there is continuum of AR values from 0.10 (mostly 105

[7] it is for this purpose that we have neglected the top (001) facet in the dome

facets) to ∼0.30 (mostly 15 3 23 facets, when all the w have the same value).

It is remarkable that the same value of AR can be obtained with different combinations of the w factors, and therefore with different geometrical features of the islands (see geometries (d,e) in Fig.2.9).

Elastic energy and AR:
In order to have some statistics, we take both the domes just defined with all the families of facets and the 'experimental' islands analyzed in sec.2.2 at page 34. The elastic energy is computed in a FEM approach paying attention to have the same mesh density in all the islands, checking also the variation with the mesh density to ensure the convergence. For sake of simplicity the domes are 100% Ge and are laying directly on the Si substrate without any WL. The reported data are shown in Figure 2.10 as a function of the Aspect Ratio (red points) computed with experimental anisotropic elastic constants for both Si and Ge. The relaxation factors F defined in sec.2.1 (page 31) are reported on the right y axis.

The gross trend seems to validate the criterion of the AR, yet if it was 100% correct, one should expect a very narrow line. Instead, a rather broad dispersion is revealed in the interval of AR$\in [0.20 : 0.25]$ where some cases show an opposite result: the higher the aspect ratio, the *higher* the elastic energy density. This is the case of panel (b) of figure 2.10, where the points relative to domes (d) and (e) of Figure 2.9 are highlighted. This shows that the actual relaxation state of the island cannot be described properly by the Aspect Ratio, but rather it depends on the details of the geometry.

This is thoroughly proven by a comparison with the other islands reported in the same figure. The result for the {113} pyramid is out of the line of the domes. If the experimental dome 'Dome exp' seems to be inside the red curve, the experimental barn is completely out of it, with a better strain relieve than domes with the same AR. This proves that additional facets may vary the elastic response heavily. One last point is the relax of the truncated {15 3 23} pyramid (green points), that are, again, out of the curve of red points.

The same calculations have been performed with Tersoff elastic constants and by changing the isotropic factor A[8] in the experimental constants (not shown) and the shape of the trend has not changed, meaning that this is not an artifact given by the anisotropy, particularly because all the shapes are roughly symmetric (the vertical axis passing through the center is a symmetry one).

All these points together show that the AR is not a proper variable to describe strain.

Other geometric parameters:
Since the AR is ruled out as the only parameter describing the elastic relaxation, a reasonable question is whether another one can be proper for this purpose. This geometric parameter is expected to be a general one, able to sort the degree of elastic relaxation for ANY geometry, from the slightly different domes up to the difference between pyramids and barn.

Since the relaxation is due mainly to the free surfaces one candidate can be the geo-

[8] see appendix A

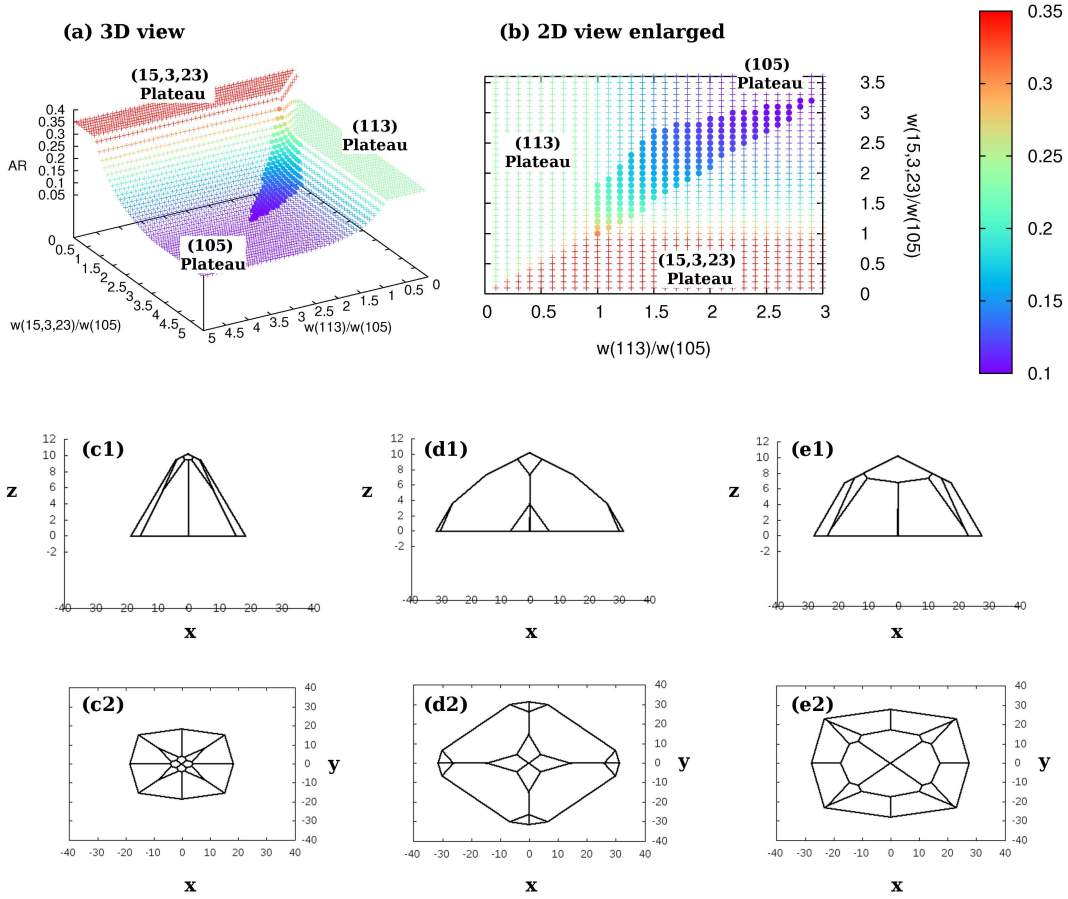

FIGURE 2.9: (a) 3D and (b) 2D plot of aspect ratio of the domes with {105}, {113} and {15 3 23} facets on (001) substrate as a function of the ratio of the ws with colorscale. Smaller dots are islands where at least one family of facets is missing. Larger dots represent the region where all the families are present and that is analyzed here. The plateaux in AR are the region where a single family is present, i.e. a pyramid.
(c,d,e) show some Wulff plots of the domes (1=side view, 2=top view).
(c): AR = 0.3033, w(113)/w(105) = w(15 3 23)/w(105) = 1. This is the maximum AR obtained for this set of facets.
(d): AR = 0.2028, w(113)/w(105) = 1.1, w(15 3 23)/w(105) = 1.7.
(e): AR = 0.2022, w(113)/w(105) = 1.4, w(15 3 23)/w(105) = 1.5.
(d) and (e) show that a close AR can be obtained with very different geometries, that give very different relaxation energy (see below).

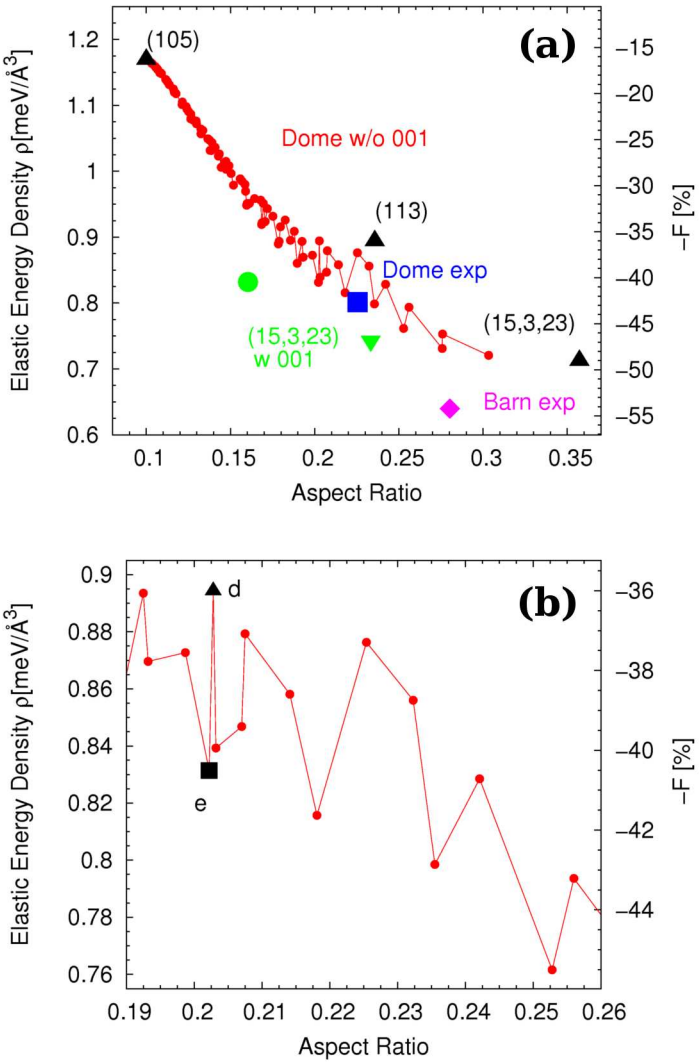

FIGURE 2.10: (a) Elastic energy density as a function of the Aspect Ratio of the 100% Ge domes without the (001) facet of Figure 2.9 (red points) compared with the values for pure pyramids (black upward triangles), the dome and barn shown in sec.2.2 (blue rectangle and purple diamond respectively) and a couple of {15 3 23} pyramids truncated by a (001) facet at different heights. The non-monotonic trend for the domes at AR∼0.2-0.25 is evident. Further the values of the truncated pyramids are completely out of the trend of the domes. The energies are computed within the FEM using the experimental anisotropic constants. The right y axis shows the value of the relaxation factor F. In (b) a focus on the AR is shown reporting the point relative to the domes of Figure 2.9 (d,e).

metrical factors βs. In particular, the total exposed geometrical factor:

$$\beta_{exp} = \sum_{i}^{exposed} \beta_i = \sum_{i}^{exposed} \frac{S_i}{V^{2/3}} \tag{2.34}$$

From the values reported in Tab.2.1 at page 35 we can argue that another candidate parameter could be the difference of the total exposed geometrical factors with the covered one:

$$\beta_{exp} - \beta_{cov} \tag{2.35}$$

Panels (a)-(d) of Figure 2.11 shows the value of the AR and the elastic relaxation as a function of this parameters. As evident, the AR is not a 1-to-1 function of these parameters, showing again that the AR is just a gross description of the island shapes. The dispersion in the elastic energy density is lower than the one for AR, yet not enough.

Another possibility can be taken as the following. By considering that the steepest the facets of the island, the higher the degree of relaxation, another possibility could be to consider the inclination of the exposed facets averaged over all of them:

$$\tan\theta \equiv \frac{\sum_i^{exposed} \beta_i \cdot \tan\theta_i}{\sum_i^{exposed} \beta_i} \tag{2.36}$$

where θ_i is the angle formed by the i-th facet with the substrate (in this case the 001 surface).

The analyses for this variable are reported in Panel (e) and (f). In this case the dispersion is still present, yet much lower and the points seem to belong to a line. However this treatment seems not be a general one, since the barn seems to be out of the prolongation of the trend all the others belong to.

Conclusions:

The results of the analysis carried out here lead to the conclusion that the criterion of the AR for the elastic relaxation is not valid in general, though it can have a validation for the experimentally observed structures such as the pyramid, dome and barn, hence it has not been misused in literature if limited to these cases. Yet, more than some counter-examples have been found in the detailed analysis just carried out.

The use of other parameters, such as the geometrical factors and the average slope can help in giving a trend but it is not precise enough.

This proves the high sensibility to the geometry of the island and the relative position and extension of the facets. Therefore when dealing with an island its precise geometry must be described, for instance by giving the parameters w's of the Wulff construction in order to uniquely identify the shape. Due to this high sensitivity on the geometry, the use of a continuum approach, reliable and fast, taking the detailed geometry into account is mandatory.

Since the elastic relaxation of the islands alone cannot neither describe nor predict the experimentally-observed geometries of the nanostructures, this can be explained by considering the energy of the facets to assess the configuration with lower energy. Another contribution might be the kinetic evolution of the islands, but this is not considered here since we make the hypotesis that the islands are at the thermodynamic equilibrium in a minimum energy configuration.

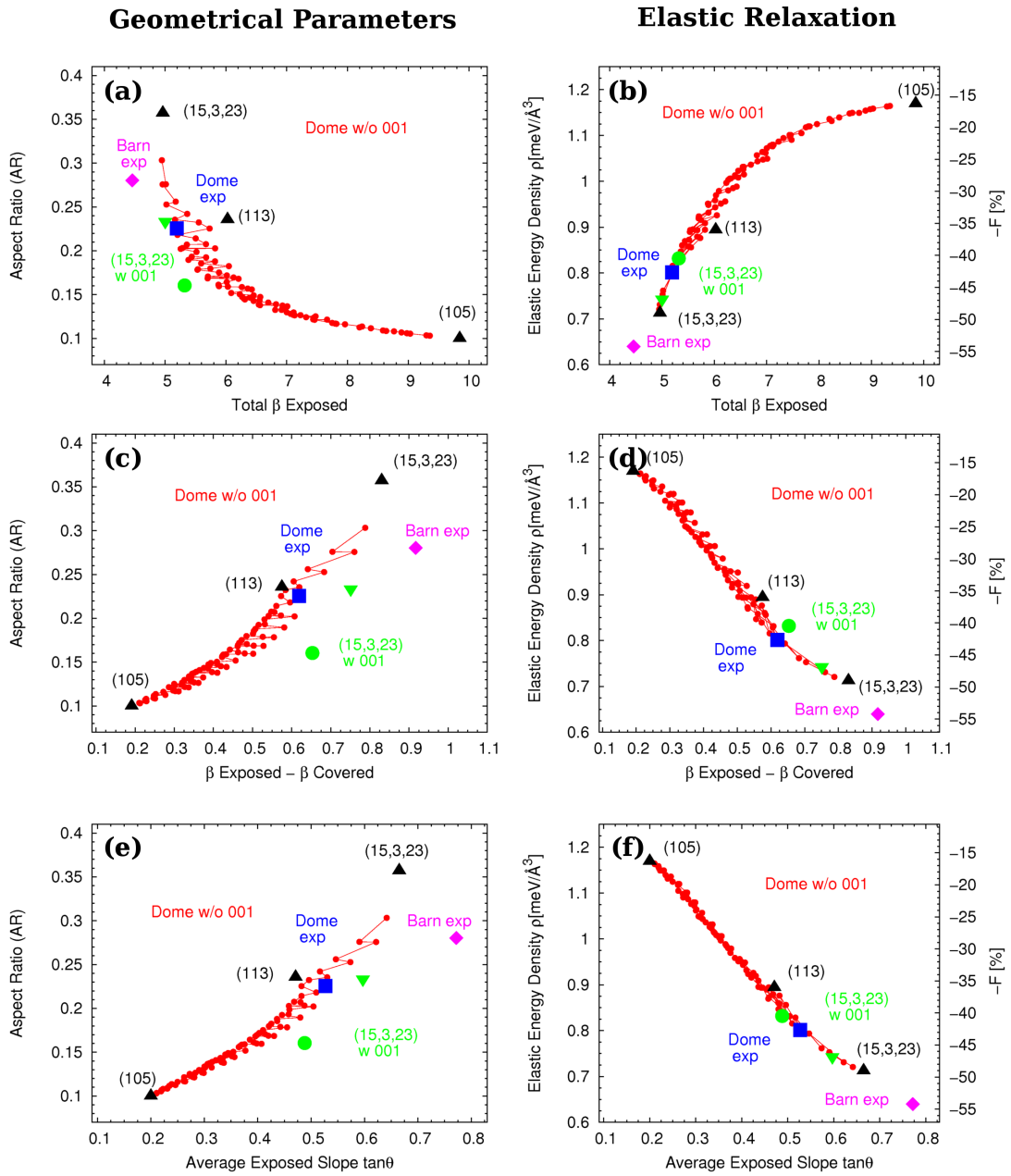

FIGURE 2.11: Variation of the AR (left column) and the elastic energy density (right column) as a function of other variables for the description of the elastic energy density in nanoislands. (a,b) = the geometrical factor of the exposed surface β_{exp}; (c,d) = the geometrical factor of the extra surface $\beta_{exp} - \beta_{cov}$; (e,f) = the average slope $\tan\theta$. In all cases the dispersion is lower than the AR case, but in no situation all the points lie on a single curve.

2.5 Surface energy: Theory and Method

The second contribution to the formation energy of eqn.(2.1) comes from the surface energy densities γ. Here we define these quantities and describe a general procedure to build the cells along with some analytical properties. We also highlight and discuss its dependence on macroscopic parameters.

2.5.1 Definition and functional dependence

In a *gedank* experiment a surface along a given direction n is created from an infinite bulk by cutting the bonds along that direction and moving the two half-bulks far apart (Fig.2.12-(a)). The atoms on the first few layers on the surface thus experience a different force field caused by this lack of neighbours, with a consequent relaxation along the direction normal to the surface (that we define to be z). Along with this phenomenon, called "Relaxation"[44], the atoms adopt a different geometry with respect to the one they would have in a bulk due to their extremely reactive dangling bonds causing a different "Reconstruction" of the surface. This is extremely relevant in semiconductor surfaces heavily influencing both the energetic stability of the interested surface and its kinetic properties such as its diffusion constants [73].

The surface energy density γ is the energy provided to the system to create a unit area of such a surface and it depends on the energy of the broken bonds, hence it is a genuinely atomistic property of solids and a continuum approach is thus unfeasible.
From an inspection of the large amount of data available in literature, we can explicit the macroscopic variables influencing its value:

$$\boxed{\gamma = \gamma(n, \Theta, \epsilon_{ij}, N_{epi})} \tag{2.37}$$

Here n is the normal to the surface specifying its Miller indexes, Θ is the reconstruction it adopts, ϵ_{ij} is its strain state and N_{epi} is the epilayer thickness (useful in case of Ge/Si system at different coverage). The contribution of each term is described in the following subsections.

2.5.2 Anisotropic geometries of surfaces and the Slab Method

The atoms in a solid occupy fixed positions in the Bravais lattice according to their peculiar symmetry space group. It is therefore obvious that the relative position in space and number of the broken bonds vary with the direction of the surface analyzed. The anisotropy of solid surface have a direct experimental proof in the growing of small crystallites [47, 74, 75], where the surfaces that have lower energy are growing at a higher rate than the more energetic ones.

An infinite bulk is reproduced by the replication through periodic boundary conditions (PBC) of a properly-built cell. A practical way to get the surface geometry for given lattice symmetry and direction of the cut is by constructing this cell where, let us say, the direction n_3 of the basic vector is the direction analyzed n and the directions n_1 and n_2 lies in the plane (n_3) and are non-collinear. The basic vectors l_1, l_2, l_3 along these directions are

found in the way sketched in Fig.2.12-(b) and here briefly summarized. After resolving a 'big enough' cell in planes whose normal is n_3 (thin red lines), vectors l_1 and l_2 are searched in these planes such that the vectors connect two atoms (blue lines). This is a necessary condition to have PBC in the plane xy, but to ensure PBC another atom MUST be found in the position $2 \cdot l_1$ AND $2 \cdot l_2$ (blue dashed lines). The same holds for direction z (vector l_3).

If in the cell so obtained the PBC along n_3 are omitted by introducing some vacuum along this direction, we get a slab exposing an infinite[9] n_3 plane on both sides. This kind of cell is the one widely adopted for actual calculations of γ in the **"Slab Method"** framework [76, 77]. In this approach the total energy of the cell is given by:

$$E^{TOT} = \sum_{i=1}^{N} \mu_i \cdot N_i + 2A \cdot \gamma \tag{2.38}$$

where μ_i is the reference chemical potential of the atom of species i in the bulk (that must be computed separately), A is the area of the cell spanned by the vectors l_1, l_2 and γ is the surface energy density of the top and bottom surface in the simple case in which they are identical.

Several papers are present in literature [27, 76, 78, 79, 80] dealing with and using surface slabs in their calculations, though none of them has ever conducted a systematic analysis to deduce general rules for their geometrical parameters, such as:

- the directions of the basic vectors (with their Miller indexes) n_1, n_2, n_3
- the length l_j of these vectors
- N_{layer} = the number of layers along n_3 direction determining the thickness of the cell
- T_3 = the distance between two adjacent layers in the direction n_3:

$$T_3 = \frac{l_3}{N_{layer}} = \text{length along direction 3 / number of layers}$$

- N^{AT}_{plane} = number of atoms in a single n_3 plane, that are relevant to reproduce a given reconstruction in the plane, see below
- N_{TOT} = total number of atoms in the cell (that is, the computational cost of the calculation)

Here we aim to **fill this lack of knowledge and to fix the nomenclature**.
By performing a systematical analysis on several directions in a **1-species, unitary lattice constant diamond crystal**, some of which are reported in Table 2.3, we can infer the following properties for a generic direction $n_j = [n_{j1}, n_{j2}, n_{j3}]$ where the n_{jk} are integer numbers prime with each other.

[9] thanks to the PBC along n_1, n_2

1. The length l_j is an integer fraction of the length of n_j:

$$l_j = \frac{\sqrt{n_{j1}^2 + n_{j2}^2 + n_{j3}^2}}{f_j} = \frac{|n_j|}{f_j} \quad \left(f_j \in \mathbb{N}^+, f_j \geq 1\right) \tag{2.39}$$

   Where the factors f_j are given by

$$f_j \;=\; \begin{cases} 1 & \text{if } \sum_i n_{ji} = \text{ODD} \\ 2 & \text{if } \sum_i n_{ji} = \text{EVEN} \end{cases} \tag{2.40}$$

2. The distance T_j between a lattice plane and the nearest one may not be fixed in a diamond crystal. Whenever all the three indexes are odd an alternation of distances is observed: T-3T-T-3T.... We call such surfaces "Type O" (odd) and in literature the units is defined as the BI-Layer (BL) (Fig.2.12-(d)) [80]. On the contrary, when at least one index is even the distance is kept constant from a plane to the next one. We call such surfaces "Type E" (even) and the units are the monolayers (ML). In the table in the case of type O surface (113 and 15 3 23) N_{layer} represents the number of the layers the cell would have IF all layers are present. Therefore, because of the "missing layers" (Fig.2.12-(d)), the actual number of layers WITH atoms are $N_{layer}/2$, as can be deduced by a comparison between N_{layer} and N_{TOT}^{AT} in the table.

3. The smallest cell with $n_1 \perp n_2$ can be much larger than the case of general (non-collinear) directions (as shown in the table for the case of 15 3 23). Additionally, the directions n_1 and n_2 are not unique: a different search can lead to different directions, but conserving the area in the plane and the angles between the two vectors (this is the reason why the 15 3 23 ORTHO has different directions w.r.t. the free case).

4. The thickness of 1 ML and the areal density of atoms in 1 ML $\widetilde{d}_j = N_j/A$ on the plane n_j is given by the following ($N_j = N_{layer}$):

$$T_j \;=\; \frac{l_j}{N_j} = \frac{|n_j|}{f_j} \cdot \frac{1}{N_j} = \frac{f_j}{|n_j|} \cdot \frac{1}{4} \tag{2.41}$$

$$\widetilde{d}_j \;=\; 8 \cdot K_j \cdot T_j = 2 \cdot K_j \cdot \frac{f_j}{|n_j|} \tag{2.42}$$

   Where the factor K_j takes into account the different density of atoms in the type O and E surfaces:

$$K_j \;=\; \begin{cases} 1 & \text{if } n_j = \text{Type E surface} \\ 2 & \text{if } n_j = \text{Type O surface} \end{cases} \tag{2.43}$$

After obtaining the geometry of the bulk-like slab it must be handled and modified according to the requirements of the calculation, in particular focusing on the vacuum space, the cell thickness, its area and the position of fixed atoms layers in order to make the calculation feasible (particularly in DFT approach). The tricks adopted in this thesis, along with the consequent modification of eqn.(2.38), are discussed at length in Chap.5.

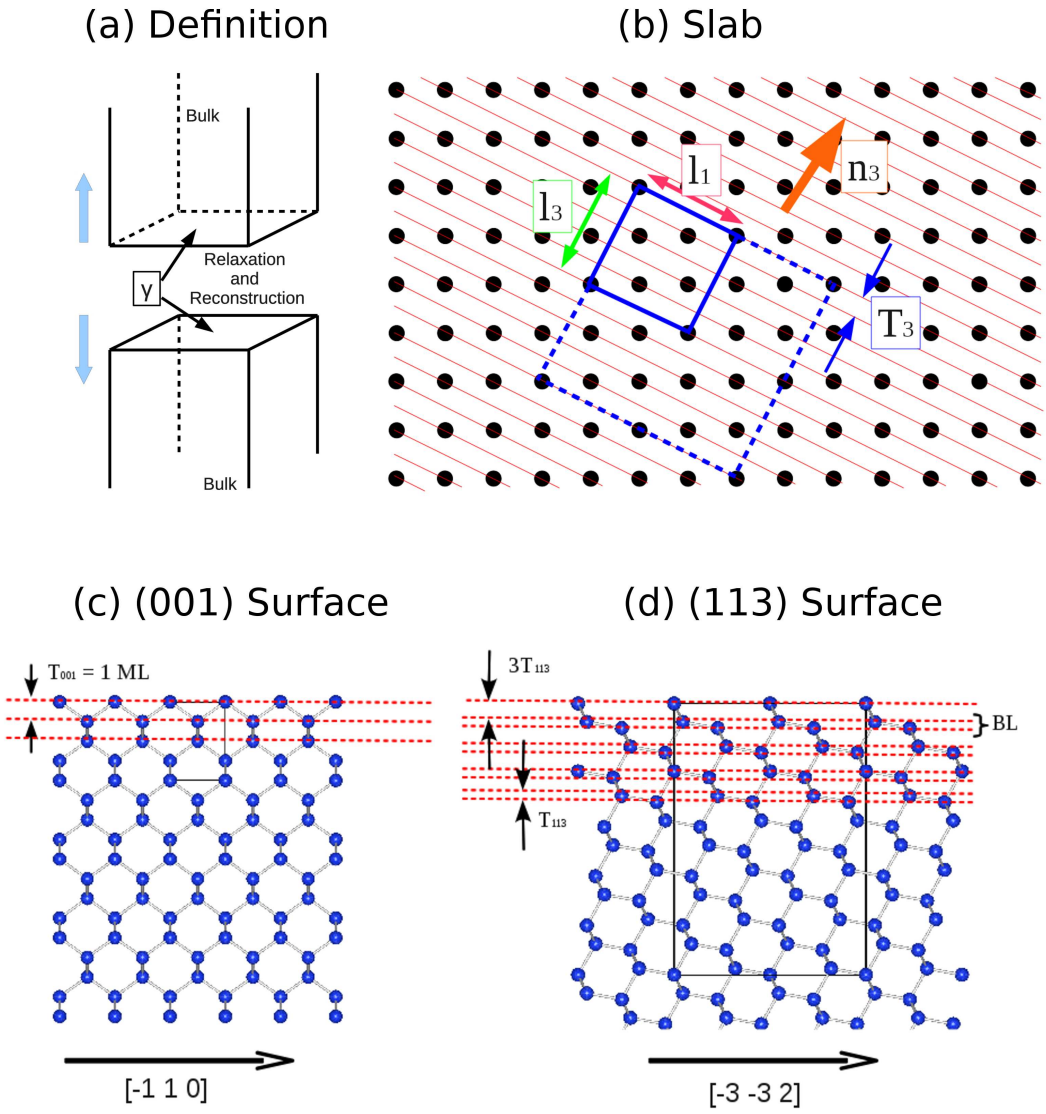

FIGURE 2.12: (a) Definition of the surface energy density γ from a *gedank* experiment where an inifnite bulk is cut and the two halves pushed apart. (b) Sketch of the method and geometric properties to determine the cell exposing the facet n_3 and therefore creating the slab used in the calculation of γ. Atoms are resolved in n_3 planes by the red thin lines distant T_3 from the next one. l_1 and l_3 are the base vector of the cell (thick blue lines) and the dashed blue lines are the borders of the double cell used to check the correcteness of the PBC. Vector l_2 penentrates in the page. (c,d) Real slabs of Si(001) and Si(113)-ORTHO respectively. The unit cell is highlighted by black lines. Planes are red dashed lines and the distances $T(n)$ are indicated by black arrows. The (001) is a 'type E' surface and all the Ts are the same, whereas the (113) is a 'type O' surface where the succession T-3T-T-3T... is highlighted and the unit of BL is also shown. We refer to this structure as the 'missing layers' since it is as if two layers are missing between one BL and the new one.

n_3	n_1	n_2	f_3	f_1	f_2	N_{layer}	N^{AT}_{plane}	N^{AT}_{TOT}	$n_1 \perp n_2$?	NOTES
(0, 0, 1)	[-1, -1, 0]	[-1, 1, 0]	1	2	2	4	1	4	YES	
(1,1,10)	[-1, 1, 0]	[-5, -5, 1]	2	2	1	102	2	204	YES	
(1, 0, 5)	[0, -1, 0]	[-5, 0, 1]	2	1	2	26	2	52	YES	
(1, 1, 3)	[-1, 1, 0]	[-1, -2, 1]	1	2	2	44	1	22	NO	d-3d-d-3d
(1, 1, 3)ORTHO	[-1,1,0]	[-3, -3, 2]	1	2	2	44	2	44	YES*	d-3d-d-3d
(15, 3, 23)	[1, -5, 0]	[4, 3, -3]	1	2	2	3052	1	1526	NO	d-3d-d-3d
(15, 3, 23)ORTHO	[2, 13, -3]	[44, -13, -27]	1	2	2	3052	26	39676	YES*	d-3d-d-3d
(1,1,1)	[0, 1, -1]	[1, 0, -1]	1	2	2	12	1	6	NO	3d-d-3d-d
(1,1,1)ORTHO	[0, -1, 1]	[-2, 1, 1]	1	2	2	12	2	12	YES*	3d-d-3d-d

TABLE 2.3: Slab properties of some important SiGe surfaces, where the lattice constant is set to unity. See description in sec.2.5.2. Here ORTHO means that the direction n_2 is required to be orthogonal to n_1 (YES*). This shows that the smallest cell can be non-orthorombic. NOTES specifies when the 'missing layers' are present (type O surfaces). Here the Miller indeces are divided by commas to make them more easily readable.

2.5.3 The fundamental role of the reconstruction

The properties of the surfaces outlined above are valid for as-cut (AC), i.e. unreconstructed, surfaces. In fact, however, an AC surface has never been observed in literature in a typical MBE or CVD experiment conducted on Si and Ge, since the surface atoms tend to rearrange to minimize the overall energy. Therefore, in semiconductor physics the quest and understanding of the most stable reconstruction for a fixed direction of cut is a relevant matter and still an open question that challenges both experimentalists and theoreticians. The typical experimental technique that has been adopted to observe the reconstruction is the Scanning Tunneling Microscopy (STM) either with filled and empty states [81, 82]. In particular, the surface energy is a quantity that cannot be determined from experiments (at least its absolute value), therefore theory plays a dominant role in the assessment of the relative stability of the different models that experiments propose.

In SiGe systems an extremely wide variety and peculiarities of reconstructions is observed for each surface.

The wide zoology and complessity of the topic can be catched from an inspection of Fig.2.13, collecting literature data. Each facet has its own peculiarities in the observed reconstruction (panel a) including elements such as interstitial [80, 83, 84], dimers, trimers or pentamers and combination of these. In addition to that, several differences can be found by moving slightly away from the major facet (panel b). In this case the periodicity of the repeated cell can increase with respect to the one of the unreconstructed surface, this increase being specified by the numbers such as MxN (as is the case of 113 surface where the cell is 3x2 [83]). Moreover, the basic cell can also appear rotated wrt the AC one.

Further, the geometry of surfaces can be complicated by the presence of steps and its possible rebonding states [85, 86]. This topic is treated at length in Chapter 4 in this thesis.

Even the reconstruction of a major surface can be subject to changes if other parameters are playing a role, such the epilayer thickness. One example of this is the (001) surface evolution when Ge is deposited onto Si [6, 8, 87]. In this case the WL evolves from a missing dimer line (DVL–dimer vacancy line) to a system with missing dimer row (DRV–dimer row vacancy) to the creation of a MxN pattern [6].

The observed reconstruction is highly dependent on the other parameters, such as the coverage of the epilayer [6] or the strain state [88][10].

For this reason the typical theoretical praxis is to compute the surface energy for a given reconstruction under several conditions of coverage and strain and to eventually compare the stability for different reconstructions [76]. In this way the reconstruction of the strained Ge(105) facet was identified to be the one depicted in panel d (bottom part) and called Rebonded-Step (RS) that in this thesis will be re-computed in a more detailed fashion in Chapter 5.

It is worth mentioning that intermixing is also playing a role [6]. In more complicated situations, like the III-V compounds, another variable is the balance of the internal pressure of the different species in the growth chamber [89].

[10] along with the experimental growth conditions

Even though some general computational methods, like the genetic algorithm [90], have been invented to search for the reconstruction corresponding to the global minimum of energy, the experimental observation still remains the major font of information.

Since different reconstructions can have a different value of energy, in the computation of the formation energy of nanostructures it is important to adopt the geometry of the observed reconstruction for both the facets and the WL surface, as will be shown in Chapter 5 in this thesis.

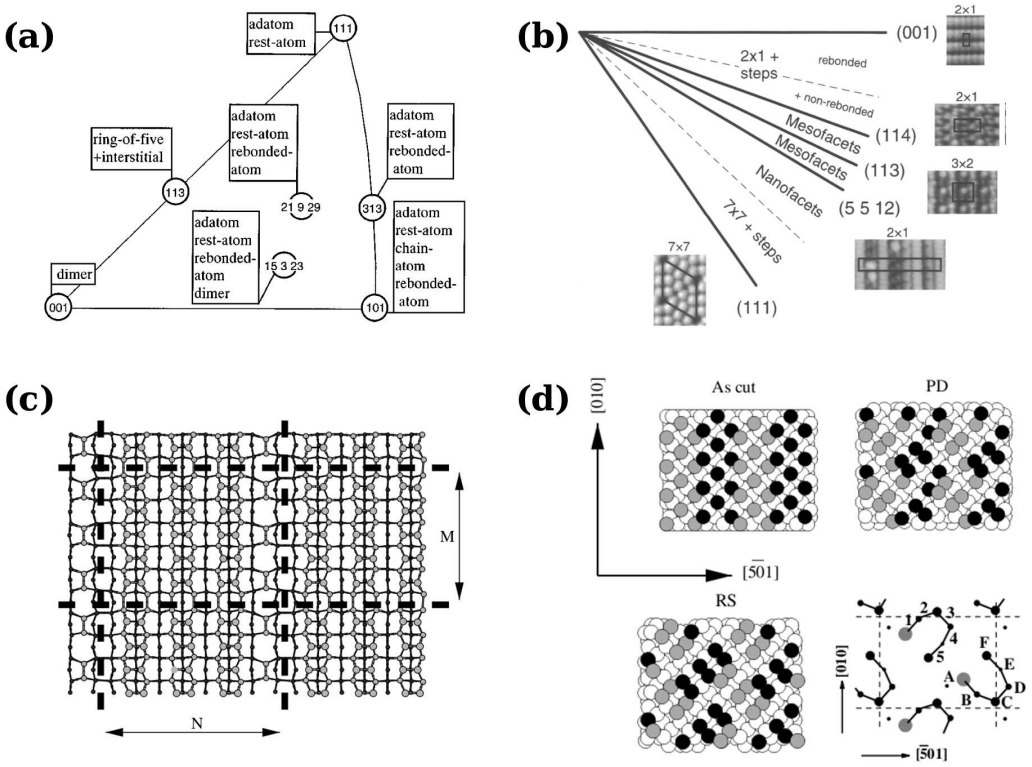

FIGURE 2.13: Examples of reconstructions on SiGe surfaces. (a) Revealed features of different Ge surfaces in the stereographic triangle, from Ref.[25]. (b) Peculiar features of the line connecting (001) and (111) for Si, from Ref.[91]. The important topic of the steps is discussed in Chapter 4. (c) (001)-MxN reconstruction of Ge/Si from Ref.[7]. (d) Different reconstructions of Ge/Si(105), from Ref.[27].

2.5.4 Dependence on strain

Although several papers have addressed the dependence on strain of the surface energy (SE) [27, 77], none[11] has ever underlined the general trend expected, so here we address this issue.

The surface energy is a measure of the strength of the bonds at the surface to be broken in creating the surface. A qualitative trend of $\gamma(\epsilon_{ij})$ can be deduced by following this definition.
The energy of pair interaction along any direction as a function of the distance of the atoms has the shape outlined in Figure 2.14. The vertical distance between the points on the curve and the zero energy (i.e. atoms at an infinite distance) is a measure of the energy to give the system to break the bonds, i.e. the surface energy if the direction taken is the z one. In the case of no external strain the atoms will be located at the distance of the minimum (l^*) and the strength of their bond is the position of the minimum. The strength of the bond in this position is the maximum possible and a high energy must be supplied to the system to break them and eventually creating a surface. This point has the maximum SE value. If either a compressive (or tensile) strain is applied to the surface in the xy plane, the atoms along z direction move apart to the distance $l_2 > l^*$ (or $l_1 < l^*$) because of the Poisson effect (see sec.2.4.2, page 40). In these cases a lower energy is necessary to create a surface, so a lower SE is expected.

In the case of real surfaces the peculiar many-body interaction of the atoms, the relaxation and the reconstruction have the effect to deviate the maximum of γ from the case of zero applied strain to a certain value of strain ϵ^*_{ij}. The position of this point, therefore, depends critically on the normal considered n_3 and with the reconstruction Θ.

This shows that for a fixed n_3, Θ, N_{epi} holds:

1. $\gamma(\epsilon_{ij})$ is a function with a single MAXIMUM at the certain strain state ϵ^*_{ij}
2. $\gamma(\epsilon_{ij}) \to 0$ if $(\epsilon_{ij} \gg \epsilon^*_{ij})$ or $(\epsilon_{ij} \ll \epsilon^*_{ij})$

In this interpretation the variation in surface energy is due entirely to mechanical strain effects, and assumes that possible electronic contributions are second order, as noted in Ref. [92]. Additionally, this shows that trend of γ is the opposite of the trend of μ with strain (compare sec.2.4.2) as evident from eqn (2.38) after expliciting γ.

The strained surface energy density can be referred to the unit area of the deformed or un-deformed surface. In the former convention (called Eulerian [77]) the area of the surface can be ideally measured by a ruler. The latter is called Lagrangian [27].

From results in literature [27], strain can heavily modify the value of the SE. Considering that the strain field in nanostructures is highly non-homogenous and the WL is biaxially strained at the lattice constant of Si, this dependence must be taken into account for the quantification of the surface energies entering eqn.(2.1).

In this thesis (chapter 5), the analysis with strain is performed with a 1-species cell (typically Ge) whose strain is applied in the plane xy and strain is expressed with respect to the bulk lattice constant. The strain is applied along the two orthogonal directions x

[11] to our knowledge

and y independently, the length of cell along these direction being modified according to the relation:

$$l_{ii} \rightarrow l_{ii} \cdot (1 + \epsilon_{ii}) \tag{2.44}$$

The strain applied along z, instead, is the one obtained by bulk calculations governed by the Poisson effect (see sec.2.4.2).

Intuitively, the reference for a strained surface must be the strained bulk, consequently the chemical potential μ in eqn.(2.1) must be the one strained in x and y and Poisson-corrected in z. This is thoruoghly proven in Appendix C.

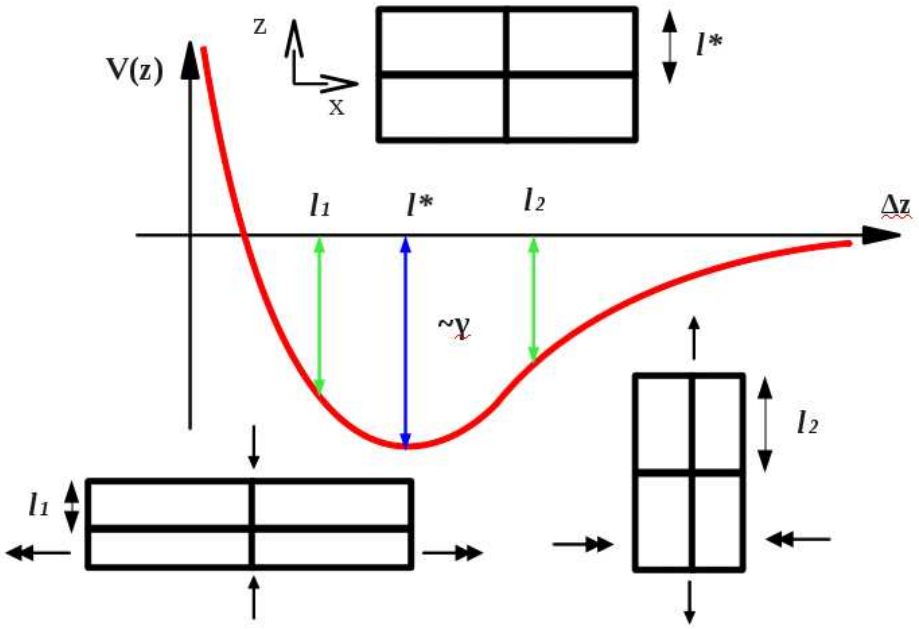

FIGURE 2.14: Explanation of trend of γ with strain. Lennard-Jones-type curve of the potential energy between adjacent layers along z direction as a function of their distance. There exists a certain distance l^* that stabilizes the surface most (top sketch of the cells). If the surface is dilated in the plane, it will be compressed along z for the Poisson effect (bottom left sketch) and viceversa (bottom right sketch). In both cases the surface is destabilized. The surface energy γ is a measure of the distance of each point of the red curve from the zero potential energy. Therefore γ as a funciton of strain has a maximum value. This suggests also that gamma might have a non-symmetric trend from the maximum value.

2.5.5 Dependence on epilayer thickness and convention

As the case of the Ge WL on Si(001) shows, the reconstruction changes as a function of the coverage of the epilayer. Published results [76, 93] show that this can be explained as a dependence of the surface energy on the epilayer thickness causing a monotonic decrease with the increase of the Ge overlayer thickness.

As reported in literature [94], this is a general effect due to the wetting factor that decreases in both directions away from the Ge-Si interface. For semiconductors, an exponential function is determined as the best fit for this decay [94, 95]. Since our interest is mostly on Ge/Si surfaces, and since Ge has typically a lower SE than Si, in this work we model γ as a function of overlayer thickness according to:

$$\gamma(N) = (\gamma_0 - \gamma_\infty) \cdot e^{-B \cdot N} + \gamma_\infty \tag{2.45}$$

Where N is the number of Ge (001) MLs (as obtained from the conversion described by eqn(2.48) below), γ_0 and γ_∞ are the surface energy values of pure Si (N=0) and of pure compressed Ge, and B is a parameter with units of (001) ML^{-1}.

This trend is the one expected for Ge/Si cells when all the other parameters in eqn (2.37) are fixed. In particular, here the strain ϵ_{ij} is a fixed quantity because the Si substrate is fixed at its own lattice constant.

This trend can also be used as a check to deduce the correct chemical potential μ to use in eqn (2.38) as described in Appendix C.

In Chapter 5, the surface energies of (105) and (1 1 10) are computed as a function of Ge coverage and, since this trend is not fullfilled by the results obtained via the Tersoff potential, we deduce that this is not proper for this kind of analysis and an ab initio approach is mandatory.

In comparing the surface energies for different directions as a function of the overlayer thickness a general definition of coverage is needed. In theoretical praxis, coverage is defined as the normal distance between the topmost (external) layer of epilayer and the first layer underneath of substrate atoms. In Ge/Si heteroepitaxy[12] the coverage is typically expressed in terms of (001)MLs. This has its origin in the experimental habit to reveal the thickness of the epilayer from the RHEED peaks measured on a Si(001) sample put in the growth chamber along with the sample to study. It is, therefore, useful to deduce a relation between the number of layers to convert into epilayer in a general direction that have the same thickness as 1 ML (001).
Calling D_3 the deposited MLs along direction n_3 and D_{001} the number of (001) MLs of the same thickness, the equality of material implies that

$$D_3 \cdot T_3 = D_{001} \cdot T_{001} \tag{2.46}$$

Hence,

$$\frac{D_3}{D_{001}} = \frac{T_{001}}{T_3} = \frac{|n_3|}{f_3} \tag{2.47}$$

[12] but also in III-V compounds

Some example of the conversion are given below:

$$1 \text{ ML } (001) = \begin{cases} \sqrt{26}/2 & \text{MLs } (105) & \simeq 2.550 & \text{MLs } (105) \\ \sqrt{11} & \text{MLs } (113) & \simeq 3.317 & \text{MLs } (113) \\ \sqrt{102}/2 & \text{MLs } (1\ 1\ 10) & \simeq 5.050 & \text{MLs } (1\ 1\ 10) \\ \sqrt{763} & \text{MLs } (15\ 3\ 23) & \simeq 27.622 & \text{MLs } (15\ 3\ 23) \end{cases} \tag{2.48}$$

In applying these relations the presence of the missing layers for Type O surfaces must be taken in mind (compare Fig.2.12-(d), page 59).

2.6 Nucleation Regimes

In a field of research like the self-assembly of SiGe nanoisland, the experiments are getting more and more detailed and controlled. Likewise, the theoretical models must include more details in the treatment in order to be able to follow and explain the experimental discoveries.

The internal energy outlined in section 2.5.2 (page 56) is a very simple and widely adopted one [43]. In the past, it has been used to correctly explain the nucleation mechanism underlying the Ge/Si deposition, predicting the onset of steeper islands (dome) at a later stage of deposition than the shallower one (pyramids) [96], as sketched in Fig.2.15.

However, it has been shown recently [30] that a highly-controlled deposition and annealing procedure can lead to an apparent violation of this thermodynamical ordering. This violation is completely explained by taking into account the role played by the WL in the mechanism of island formation. Indeed the hypotesis underlying the use of the equation is the constantness of the WL surface energy before and after the island nucleation, condition that we have seen not be strictly valid for the first few MLs of coverage.

The generalization of the energy expression (and the limitations of the previous one) is obtained by considering Figure 2.16.
Taking the initial condition as a N-MLs thick WL of area A, we have two possibilities for an additional ML of the deposited Ge:

1. The additional material can form one additional ML of the WL, leading to the final thickness of (N+1)-ML (panel a)

2. The additional material can rearrange and create a 3D island atop the N-ML thick WL (panel b)

The total energy of condition 1 is:

$$E_{WL} = V \cdot \rho_{WL} + A \cdot \gamma(N+1) \tag{2.49}$$

where the volume V is the amount of additional material (in this case 1 ML of Ge).
The total energy of condition 2 is:

$$E_{isl} = V \cdot \rho_{isl} + (A - B) \cdot \gamma(N) + S \cdot \gamma_S + L \cdot \Gamma \tag{2.50}$$

where the exposed area of the WL is the original area A minus the area covered by the island B and the thickness of the WL is N ML's in this case. The contribution $S \cdot \gamma_S$ takes into account the exposed facets of the island and $L \cdot \Gamma$ the edge terms.

The island will be energetically favoured to form if $E_{isl} - E_{WL} < 0$, otherwise a layer-by-layer growth is preferred. The difference is therefore:

$$\begin{aligned} \Delta E &= E_{isl} - E_{WL} = \\ &= V \cdot (\rho_{isl} - \rho_{WL}) + S \cdot \gamma_S - B \cdot \gamma(N) + L \cdot \Gamma + \\ &+ A \cdot [\gamma(N) - \gamma(N+1)] \end{aligned} \tag{2.51}$$

From this it is straighforward to obtain the simple expression if $\gamma(N) = \gamma(N+1)$, a condition that is the underlying hypotesis of that use. The area A involved in the transition

is obtained by considering that the volume V of the island must come form 1 ML of the WL:

$$V = A \cdot h_1$$

where h_1 is the height of 1 ML of the WL.
Hence the additional contribution is a volume-scaling one:

$$\begin{aligned} \Delta E &= V \cdot \left[\rho_{isl} - \rho_{WL} + \frac{\gamma(N) - \gamma(N+1)}{h_1} \right] + \\ &+ S \cdot \gamma_S - B \cdot \gamma(N) + L \cdot \Gamma \end{aligned} \tag{2.52}$$

The volumetric contribution can be written in terms of an *effective* elastic energy of the WL given by:

$$\rho_{eff} = \rho_{WL} - \frac{\gamma(N) - \gamma(N+1)}{h_1} < \rho_{WL} \tag{2.53}$$

where the inequality holds for Ge/Si systems since $\gamma(N) > \gamma(N+1)$.
Therefore the concavity of the trend is given by the effective volumetric term:

$$\Delta E_{vol}^{eff} = V \cdot [\rho_{isl} - \rho_{eff}]$$

that, depending on the values of N and the trend of γ, can be reduced in module wrt $\rho_{isl} - \rho_{WL}$ or even made positive, leading to a growth condition called 'Inverse Stranski-Krastanov' [30] where the energy curves bend upward with the consequent that the islands have a preferential size not tending to grow indefinitely. Neglecting this term for the early deposition can lead to gross mistakes.

Since a 3D island relaxes strain better than a 2D WL, the elastic term $(\rho_{isl} - \rho_{WL}) < 0$, so for large enough volumes this dominates and $\Delta E < 0$, leading to a higher stability of the island. By contrast, the surface term is *typically* a cost[13] (positive contribution) both because of the extra surface exposed with respect to the one covered and because of different values of the surface energies γ_i's. The edge term is always a cost for an island, whose contribution being relevant for small volumes.

Accidentally, this statement can be corrected in the following way. If we neglect the edge term contribution, from the balance between the elastic and surface terms of the **generalized** expression we can get **three different nucleation regimes** sketched in Fig.2.16-(c):

1. Stranski-Krastanov (SK) regime if $\Delta E_{vol}^{eff} < 0$ and $\Delta E_{sup} > 0$
2. Barrierless (BL) regime if $\Delta E_{vol}^{eff} < 0$ and $\Delta E_{sup} < 0$
3. Inverse-Stranski-Krastanov (ISK) regime if $\Delta E_{vol}^{eff} > 0$ and $\Delta E_{sup} < 0$

The **SK regime** is the typically obtained when the dependence on overalyer thickness of γ is neglected or when the difference $\gamma(N) - \gamma(N+1)$ is negligible in comparison to the difference in elastic energy densities. In this case the elastic relaxation is a term favouring 3D nucleation whereas the balance between exposed surfaces and covered ones

[13] an important counter-example is the case of Ge growth on Si(1 1 10), Chap.5

is a barrier that the increasing elastic budget with volume can overcome. Since *typically* the steeper islands (blue line in Figure 2.15) expose a higher surface, they have an extra initial cost, but they also relax strain better leading to a higher negative derivative, making them more favourable for higher volumes (as is the case of the pyramid-to-dome transition [20]). Hence in this case the expected succession is: WL, shallow island, steeper islands (red curve in Fig.2.16). In the case of alloys the elastic relaxation is smaller (since the misfit is smaller) and islands' volume are expected to be larger[14].

The **BL regime** favours the islanding at a very low volumes, since the exposed facets have such a low energy with respect to the WL that it compensates the extra surface exposed.

The **ISK regime** is the one raising from the explicit dependence of γ_{WL} to N. In this case for a fixed N, the volumetric energy ΔE_{vol}^{eff} is destabilizing the islands, with the net effect that the 3D nanostructures have a *preferential* volume and they do not show the tendency to grow. This is the reason why it is called *Inverse*. This stable volume depends on the value of N and an evolution of the islands size can be observed by increasing the coverage (as discussed in Chapter 5). Moreover, in such cases, under a detailed control of growth conditions, the steeper islands can be observed BEFORE the shallower one, thanks to coarsening effects [30].

Finally, it is noteworthy that for a detailed analysis the elastic energy stored in the condition with the island ρ_{isl} is not a self-similar quantity with the volume V of the island, since the WL underneath makes a perturbation to the elastic field dependent on the island-height to WL-height ratio[15].

[14] see results concerning the nucleation of domes on Si(1 1 10) in Chap.6

[15] see discussion at section 2.4.3 at page 48 and Chapters 3,5 for the importance of taking the detailed geometry into account

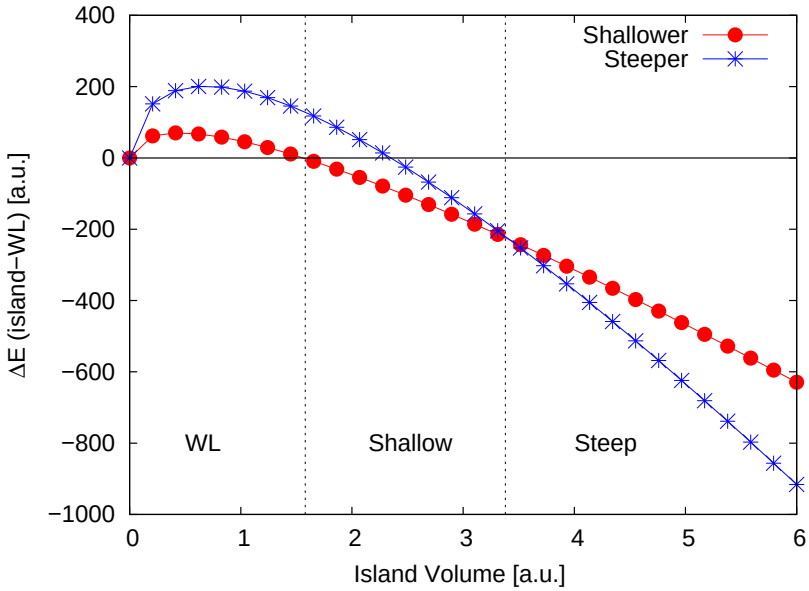

FIGURE 2.15: Example of trend of ΔE vs volume using eqn (2.1) in the SK regime. The steeper island exposes more surface, that is a cost, yet it relaxes better, so at higher volumes it is more stable. The succession observed is: WL, shallow island, steeper island.

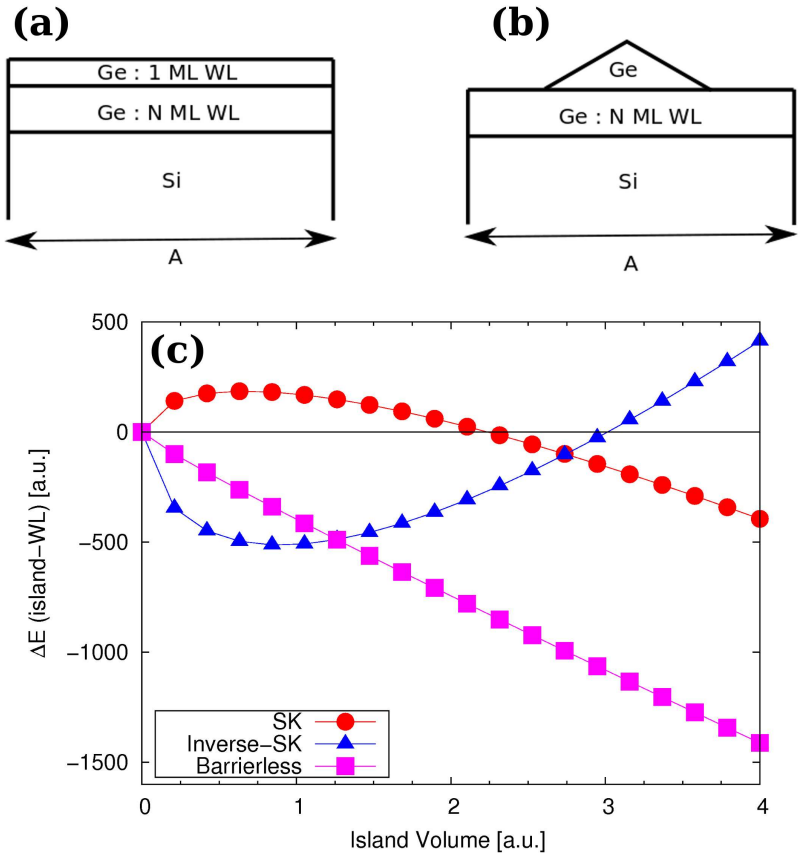

FIGURE 2.16: Generalization of the energy balance to take the $\gamma_{WL}(N)$ dependence into account. (a) Sketch of the condition where the additional material is creating a 1-ML-thick WL upon the existing N-ML-thick WL. (b) Sketch of the condition where the additional material is creating a 3D island atop the existing N-ML-thick WL. (c) Nucleations regimes.

2.7 Summary and conclusions

In short in this chapter we have:

- described the division of the internal energy of nanostructures into volume, surface and edge contribution
- described the concept of the Wulff solid and shown that the shape of nanoislands on any substrate orientation can be described with this mathematical concept
- highlighted the computational approaches adopted in this thesis: Tersoff and DFT-LDA for surface energies with atomistic approaches and FEM method for the elastic energy density
- described the elastic field of the strained objects involved:
  - Wetting Layer: where we showed the importance of the anisotropy in the elastic response
  - 3D nanoislands: describing the general features of their elastic elastic field (free surfaces and compression of the substrate)
  - 3D nanoislands: analyzing their degree of relaxation in details we showed that the Aspect Ratio is not a proper parameter to describe the "Steepness" of the islands themselves, suggesting its definition in terms of the average slope
- described the simulation of the surface energy
  - by expliciting the dependence of γ on the other parameters of the system (strain, epilayer thickness etc.)
  - by showing a general method to determine a slab exposing any direction and the slab geometric properties
  - by showing the role played by the reconstructions in semiconductor physics
  - by studying in details the dependence of γ on the strain the facet is subject to, and by proving with simple arguments that it must have a maximum with strain
  - by studying in details the dependence of γ on the epilayer thickness
- showed what types of different nucleation regimes exist depending on the balance between the energy terms

In the next chapters we will exploit all these methods to evaluate the internal energy ΔE for the systems under analysis.

3

Patterned substrates and intermixing: Shape Oscillations

"In the struggle for survival,
the fittest win out at the expense of their rivals
because they succeed in adapting themselves
best to their environment."
Charles Darwin

In this chapter, the estimation of the internal energy of Ge/Si(001) nanoislands is used as a tool to understand the formation and evolution of domes and barns in a real situation of potential technological interest in a patterned substrate. This modeling allows to understand the fundamental role played in the system of self-assembled islands by the intermixing and the importance of properly taking the balance between elastic and surface energy into account in the theoretical approach.

The case of study is a joint work of our group with experimental colleagues [97] showing an unexpected evolution of islands onto a pit-patterned substrate with respect to the one on flat. The peculiarities of the nucleation and growth of nanoislands on patterned substrate are also highlighted.

3.1 Uniformity and site-controlled nucleation of islands: the patterned substrates

Ge/Si(001) islands not only represent the stereotypical system for the formation of the self-assembled nanoislands, but also may cover important roles in technology. They can have possible applications in electronic [98, 99] and optoelectronic devices [100]. As an example, strained Si channels on top of buried, coherent SiGe islands may be used for field effect transistors with enhanced electron mobility [98]. For such an application and several others, both spatially and morphologically ordered island ensembles are required [101]. None of these criteria are, however, satisfied by the nucleation on flat Si(001) surface

[32]. In the last few years, on the contrary, patterned substrates have been acquiring a growing interest because of their capability to accomplish with both of them [100, 101, 102]. The pattern adopted in these works is a 2D arrays of holes ("pits") obtained by optical lithography and selective ion etching [101]. The phenomenology in this system is rather complex and involve a faceting of the cylindrical holes (driven by the Si buffer layer), and its deformation into a {105} inverted pyramid upon Ge deposition.

It is an evidence that the pits act as preferential sites for the island formation [103, 104] defining also equally sized capture zones for the deposited Ge, so that different islands form and grow simultaneously after the completion of a wetting layer. As a consequence, coarsening due to material exchange among islands with dissimilar sizes [105][1] is largely suppressed [101]. This has also the intriguing effect to make visible the different stages of evolution of islands being able to discern the transition forms (like the transition pyramids and domes) much more clearly than the random nucleation on unpatterned substrates allow [101]. This has also allowed to be distinguish the steps of the evolution of the facets of the barn, as discussed in the next section.

In addition, the rate of Ge accumulated within a capture zone determined by the pits can be precisely controlled by changing the Ge flux or the pit period [101]. This is important, since Ge-rich islands with high aspect ratio are needed as efficient stressors for strained-silicon transistors [98].

As alredy explained in Chapter 1, on both planar and patterned substrates, by increasing the amount of deposited Ge at relatively high growth temperatures, 3D islands evolve from pyramids into domes, and eventually into steeper barns [101, 106]. This sequence corresponds to a monotonic increase of the aspect ratio, driven by a progressive strain release with island steepness [105].

With further Ge deposition, the strain energy is eventually released by plastic relaxation. Plastically relaxed islands display a "cyclic" growth, accompanied by "oscillations" of the island shape after the introduction of each new dislocation [107]. As the growth on pit-patterned substrates has been found to delay the onset of plastic relaxation by lowering the critical elastic budget in the island, it is reasonable to expect aspect ratios beyond the one of barns, as happens on planar substrates, though for higher temperatures [17].

3.2 Experimental evidences of "shape oscillations"

Experiments reveal that the nucleation and growth in a pit-patterned substrate may take a different path from the one on flat.

Indeed, such a desirable result of increasing aspect ratio may be hindered by unexpected shape oscillations during Ge deposition, which nevertheless allow the islands to keep growing in size without plastic relaxation. We observe that with increasing Ge deposition domes transform into barns, then back into domes, and subsequently again into barns, and so on.

The samples were grown by solid-source molecular beam epitaxy on 2D pit-patterned Si(001) substrates with periods of 500 and 900 nm. The pit depth and width were about

[1] also called Ostwald ripening

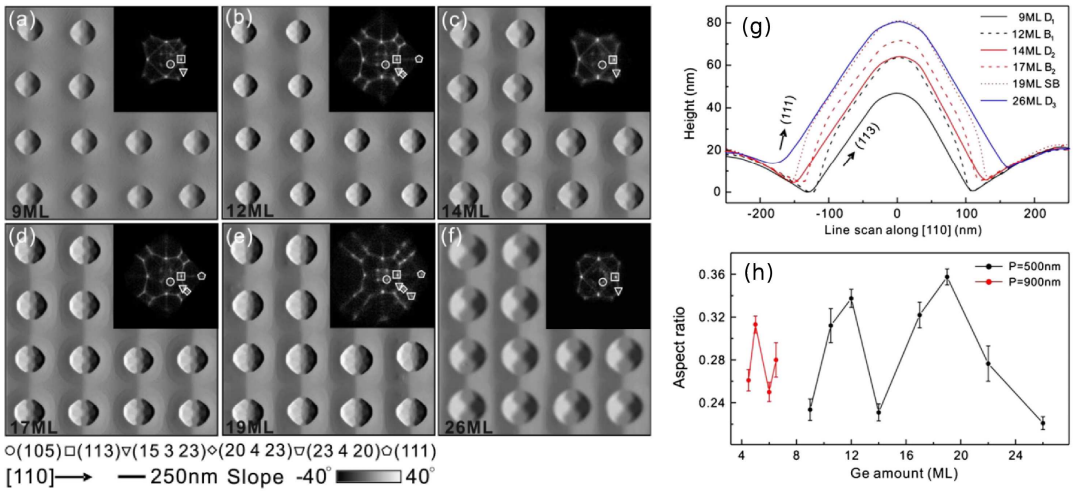

FIGURE 3.1: Experiments of Shape Oscillations in pits. Left: AFM images of islands obtained after deposition of 9 (a), 12 (b), 14 (c), 17 (d), 19 (e), and 26 ML Ge (f) on pit-patterned substrates with a period of 500 nm at 720°C. The gray scale represents the first derivative along the horizontal axis, and the insets show surface orientation maps with different symbols marking different facets. Right: (g) AFM line scans passing through island centers along [110] direction for islands shown in panels (a–f). (h) Island aspect ratio as a function of deposited amount of Ge for pit-patterned substrates with periods 500 and 900 nm, respectively.

65 and 350 nm, respectively. Above 45 nm of Si buffer, different amounts of Ge [from 6 to 26 monolayers (ML)] were deposited at a substrate temperature of 720°C and at a rate of 0.03 Å/s. After growth, the samples were cooled to room temperature for AFM imaging. Figures 3.1(a)-(f) show AFM images of a sample series obtained after deposition of 9, 12, 14, 17, 19, and 26 ML Ge, respectively, for a pit period of 500 nm.

For all investigated Ge coverages from 9 to 26 ML, 2D ordered arrays of islands with homogeneous shape are observed. Before 12 ML Ge, the island evolution follows the same path as on the flat surface: {105} pyramids (6 ML), domes bounded by {105}, {113}, and {15 3 23} facets (9 ML) and steeper {111} and {20 4 23} facets appear after 12 ML, characteristic for barns. The corresponding surface orientation maps (SOM, see, e.g., Ref.[36]) are plotted in the insets of Figs.3.1(a) and (b), respectively. In all cases, a highly uniform array of island that coherently evolve in size, shape and composition is observed.

Based on previous results [107, 106], one would expect the transition to even steeper morphologies or dislocation formation with further deposition of Ge. Surprisingly, we find here that after 14 ML Ge barns transform back into domes [see SOM in the inset of Fig.3.1(c)]. After 17 ML Ge, the steeper facets reappear again [inset of Fig.3.1-(d)] and the domes evolve into barns. At 19 ML Ge, barn-shaped islands with additional {23 4 20} facets are observed, as illustrated by the SOM in the inset of Fig.3.1-(e). We denominate this kind of islands as 'steep barns' (SB). This demonstrate that the observed barn on flat surfaces is actually the result of two successive introductions of steep facets, where the {23 4 20} appear at a later stage, as was speculated in Ref.[16]. By continuing the Ge

deposition, the SBs transform back to barns (not shown) which, for 26 ML Ge, transform for a second time back to domes, as shown in Fig.3.1-(f).

It is important to note that such a sequence of transformations occurs without dislocation introduction, as proven by TEM investigations. To distinguish the domes and barns at different stages, we denominate the first appearing domes and barns as D_1 and B_1, the second domes and barns as D_2 and B_2, and so on. These morphologies are further illustrated by AFM line scans passing through the island centers along the $[\bar{1}10]$ direction [Fig.3.1-(g)], which clearly show the appearance and disappearance of steep {111} facets. When domes transform to barns, the island base width stays almost constant but their height increases. When barns transform back into domes, the island base width increases while the height stays almost the same.

Figure 3.1-(h) displays the island aspect ratio as a function of the Ge amount for growth on patterned substrates with a period of 500 nm and for a period of 900 nm under the same growth conditions. For the larger pit period, only one shape oscillation is observed while dislocated islands appear with further Ge deposition, showing that the number of oscillations before plastic relaxation depends on the pattern period.

3.3 Measured role of intermixing

Several works [35] highlight the role played by intermixing in the evolution of islands as another channel to relieve strain apart from the ones outlined in sec.2.4.3. For this reason we focus our attention on the Ge distribution inside the islands. We determine the 3D composition profiles at different evolution stages by a nanotomography approach based on atomic force microscopy (AFM) and selective wet chemical etching [36], and by x-ray diffraction (XRD) measurements. This analysis clearly shows that the level of intermixing between deposited Ge and Si from the substrate is not constant throughout the deposition in spite of a constant Ge flux and that intermixing leads to Ge distributions in the islands which are more complex than in islands grown on planar substrates.

More precisely, at constant Ge supply rate, the rate of Ge incorporated into islands depends linearly on the capture zone area [101]. Therefore, we expect the Ge incorporation rate for islands on substrates with a pit period of 900 nm to be by a factor of about[2] 3.2 larger than the corresponding value for a pit period of 500 nm. The larger local Ge flux leads to reduced intermixing, and correspondingly to a higher Ge content. The higher strain associated with the larger Ge content results in an earlier onset of plastic relaxation [108], as happens for islands on flat substrates for moderate temperatures. The critical role of composition explains why only one shape oscillation is observed for island growth on substrates with the 900 nm period and possibly also why no shape oscillations were reported for island growth performed at lower temperatures [101]. In order to obtain a more detailed understanding of this effect, we investigated the Ge composition evolution from D_1 to D_3 by nanotomography [36].

Figures 3.2(a)–(d) show AFM line scans obtained at different steps of etching and the extracted cross-sectional Ge distributions on (110) planes passing through the centers of

[2]$=(900/500)^2 = 1.8^2$

D_1, B_1, D_2, and B_2 islands, respectively[3].

The first dome D_1 shows a composition profile for which the Ge fraction increases rather monotonically along the growth direction, consistent with XRD results for domes grown on patterned substrates. However, the first barn B_1 shows some deviation from this commonly observed trend: we see in fact a relatively Ge-poor region sandwiched between a Ge-rich top shell and the bottom core [SO-Fig. 3(b)]. This behavior becomes more pronounced for the D_2 and B_2 islands. Our XRD measurements further confirm these observations and support the accuracy of the nanotomography results.

As shown in Fig.3.2-(e), corresponding to the shape oscillations in the sample with pit period of 500 nm, the average Ge content also follows an oscillatory behavior. The average Ge content increases from D_1 to B_1, and it drops by more than 4% when B_1 transforms back to D_2 before increasing again when D_2 evolves to B_2 and SB. Finally, the evolution of SB into D_3 is again accompanied by a decrease in Ge fraction by more than 6%.

We also note that the average Ge content of D_2 and B_2 is lower than that of D_1 and B_1, respectively, indicating that the ratio between Si and Ge incorporation rates is not constant during the Ge deposition process. The average incorporation rates of Si and Ge, calculated from the measured Ge composition distributions, are shown in Fig.3.2-(f). From the plot we see that the Si incorporation rate in the process leading from B_1 to D_2 is $\sim$3 times higher than the one for the process from D_1 to B_1. These values indicate that the B_1-to-D_2 shape transformation is associated with a larger Si-Ge intermixing. The same phenomenon is observed for the SB-to-D_3 transition, and its possible origin is discussed later on.

On the other hand, the Ge incorporation rates remain rather constant and close to the expected nominal rate. The latter [see horizontal dashed line in Fig.3.2-(f)] is estimated from the nominal deposition flux and pattern size, assuming a constant amount of Ge in the wetting layer.

3.4 Confirmation from modeling

Total energy calculations for different island shapes with realistic volumes show that the shape oscillations can be well explained as due to oscillations of the average Ge content in SiGe islands with increasing size.

To fix the idea we focus on the Barn-to-Dome transition with the shape outlined in Fig.3.3-(a).
Following the experimental data, a barn of composition x is modeled as sitting on an inverted, {105} pyramid[4] (fixed composition, 10% in Ge), so that the barn base perimeter is tangential to the square base of the inverted pyramid[5] (see Fig.3.3-(b)).

If we now transform the barn into a dome of equal V and x, but larger in base and smaller in height, the dome base will move upwards and an additional layer of composition x will be added on top of the base of the inverted pyramid (still at 10% in Ge). Despite the

[3]For the sake of simplicity, results for SB and D_3 are not shown
[4]whose inclination is 11°
[5]that determines, in turn, the filling of the pit

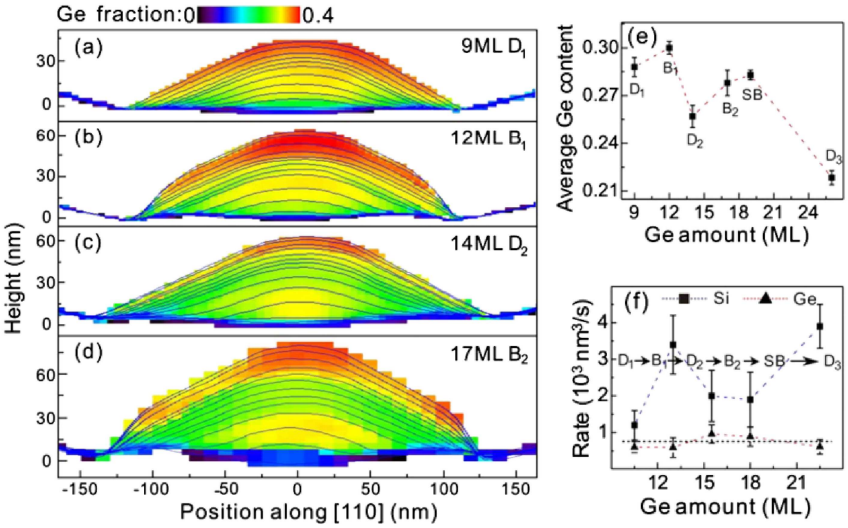

FIGURE 3.2: (a)–(d) Cross-sectional Ge distributions along [110] direction of the sample with pit period of 500 nm passing through the island centers for the first dome D_1 (a), first barn B_1 (b), second dome D_2 (c), and second barn B_2 (d) obtained by selective etching. (e) Average Ge content as a function of deposited Ge amount for D_1, B_1, D_2, B_2, steep barn (SB), and third dome (D_3); the dotted line is a guide for the eye. (f) Calculated Si and Ge incorporation rates at different stages of Ge deposition; the dashed line shows the nominal Ge incorporation rate.

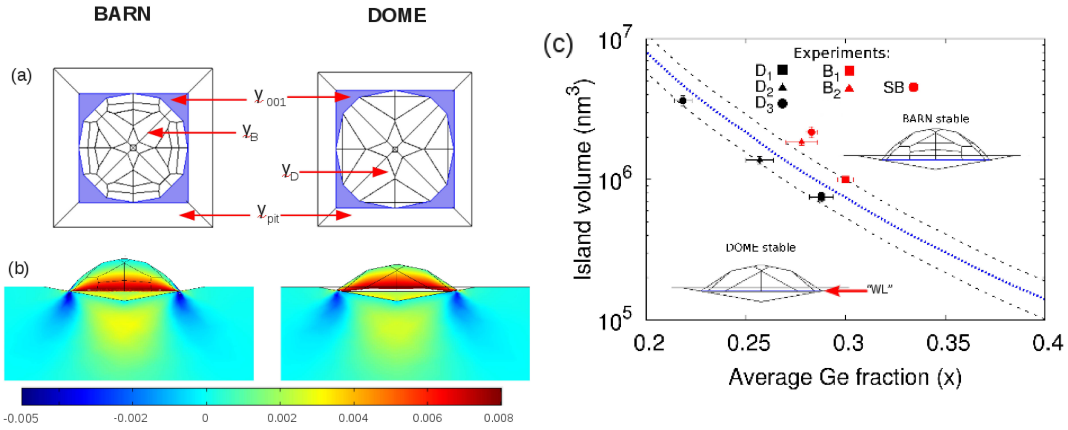

FIGURE 3.3: Modeling of shape oscillations. (a) Top view of the Barn (left) and Dome (right) used in the calculation where the surface energies contribution are highlighted. (b) Color map of ϵ_{zz} for the two cases in the case of x(island)=0.30 and x(pit)=0.10. (c) Morphological stability diagram for domes and barns, depending on volume and composition, as calculated by the finite element method. The dotted blue line is the predicted domain boundary and the dashed black lines are our maximum estimated error in the surface energies (see text). Experimental values are shown by black (D, domes) and red (B, barns; SB, steep barns) points, along with their experimental error bars.

presence of the pit geometry that makes the analysis slightly more complex, the energetic balance between the two islands is analogous to the flat-substrate case [30]: steeper islands better relax the elastic-energy density, $\rho_B(x) < \rho_D(x)$, whereas shallower islands allow for a lower surface energy because of their lower surface exposed.

By making the hypotesis that the dome and barn are at equilibrium when they are at the same average Ge concentration, we can take the energy difference between the two configurations as[6]:

$$\Delta E_{BD} = E_B - E_D = V \cdot [\rho_B(x) - \rho_D(x)] + V^{2/3} \cdot [E_S] \tag{3.1}$$

By setting this to zero, we obtain for each volume V_{crit} the average composition x_{crit} at the border of the stability domains for domes and barns.

Here E_S includes all the differences in surface terms of the two configurations, including the exposed surfaces of the island $\gamma_{D/B}$, the exposed surface of the pit filling γ_{001} and the tilted surface of the pit γ_{pit} as explained in Fig.3.3-(a).

In this case the volume of eqn.(3.1) is the volume of the entire stressor, i.e. island (+WL in the case of the dome) and the pit filling. To compare the results of the nanotomography, the volume of the island alone must be extracted. This is straightforwardly done if eqn.(3.1) is supposed to hold in the case of a self-similar growth of the system (both island and pit). Within the simulated geometry the corrective factor is:

$$1 + \frac{V_{pit}}{V_{isl}} \simeq 1.257$$

The volumetric elastic-energy terms ρ were evaluated by the finite element method, following the procedure described in Ref.[30] where ab initio elastic constants and a correction to describe non-linearity effects are employed. In the simulated systems, the Ge concentration in the island is homogeneous and set equal to the measured average value.

Following the results of Ref.[30], we set the surface energy of the exposed surfaces of both the dome and barn $\gamma_B = \gamma_D$ to be 65 meV/Å^2, whereas the surface energy of the top inverted pyramid to 60.5 meV/Å^2.

The pit sidewalls are {105} faceted [109], and are characterized by the high energy contribution of the trenches at the island base perimeter (see Fig.3.3-(b)) which are totally unknown. Based on ab initio calculations of the surface energy with strain [76] and reasonable estimations, we set the effective value for the surface energy of the pit sidewalls to be 62.5 meV/Å^2. However, this is the least known quantity: in order to give a reasonable error bar to our prediction, we varied it between 60.0 meV/Å^2, corresponding to the average surface energy density for {105} facets in a pyramid, and 65.0 meV/Å^2, corresponding to the best estimate for the surface energy of the dome and the barn [30].

In Fig.3.3-(c) we display the morphological stability diagram for barns and domes with a blue dotted line sharing the two domains corresponding to the solutions of $\Delta E_{BD} = 0$. The critical volume as a function of the Ge concentration as a trend

$$V_{crit} \sim \left(\frac{1}{x_{crit}}\right)^6$$

[6] where the edge terms are neglected

that is straightforwadly obtained from (3.1) considering that the surface energy is independent on the Ge contration (due to the Ge floating layer [6]) and that the strain energy ρ scales as x^2. The black dotted lines represent the maximum error range in our estimation as obtained by varying the unknown γ_{pit} within the previously said interval.

By reporting the experimentally measured average concentrations and volumes for D_1, B_1, D_2, B_2, SB, and D_3 in the morphological phase diagram of Fig.3.3-(c), we observe that the data points for domes and barns nicely fall into their respective stability regions. We also note that the data point corresponding to the SB with additional steeper facets lies farther away from the blue dotted line compared to B_2, as expected because of its larger aspect ratio compared to B_1 and B_2. Since the experimental data points remain close to the calculated transition line, the balance between Ge flux (provided by deposition) and Si flux (provided by the substrate) determines the morphological evolution: slight fluctuations in the Ge content with increasing size can trigger the transformation of one shape into the other.

3.5 Conclusions

With the confirmation of the role played by the intermixing given by Fig.3.3-(c), our interpretation of the collective shape oscillations for coherent islands on patterned substrates is therefore the following.

First, the observation of such a phenomenon on pit-patterned substrates is easier with respect to flat substrates because the plastic relaxation is delayed. This is due to
(i) the elastic-energy relaxation provided by the shallow pit filled with a Ge-poor SiGe alloy located below the island (a purely elastic effect),
(ii) the larger availability of Si flow from the faceted pit sidewalls which do not display a homogeneous wetting layer [109], and
(iii) the effect of ordered pits in producing islands with very similar properties at all stages of growth. The latter prevents local composition and size fluctuations which are typical for growth on planar surfaces and are responsible for the occurrence of a few plastically relaxed islands even at relatively low Ge coverages [16, 19].

Second, the small variations in average concentration triggering the morphological transitions are linked to the relative fluxes of Ge and Si. The latter depends on the growth temperature and varies during Ge deposition. In particular, Fig.3.2-(f) shows that the Si flux increases considerably whenever islands reach steep morphologies. A possible explanation is that steeper islands, such as barns, are able to carve by compressive load a deeper trench at the base perimeter, expelling Si out at a higher rate than flatter islands [110]. The expelled Si within a capture zone is then readily available for intermixing with the island material and allows the islands to keep growing in size through shape oscillations and explains why the average Ge concentration is lower in the domes wrt the previous barn islands. On the contrary, evolution to flatter islands, such as domes, covers the trenches by base expansion, so that the Si flux is drastically reduced and the Ge flux incoming from the deposition can increase the Ge content in the island. This 'kinetic' explanation is consistent with the observed Ge distribution in second-generation islands that does not

correspond to the one obtained by elastic energy minimization with Monte-Carlo-FEM method [38].

In conclusion we have reported on the observation of island shape oscillations occurring during the deposition of Ge on pit-patterned Si(001) substrates. Such collective oscillations (all islands in the ensemble evolve rather simultaneously) are accompanied by a complex evolution of the Ge distribution and correlate with oscillations in the average Ge content in the islands. The latter, which are produced by a time-varying Si flux from the substrate, allow the islands to keep growing in size while avoiding plastic relaxation via efficient Si-Ge intermixing. The detailed structural information retrieved from AFM-based nanotomography and x-ray scattering measurements may allow the selection of island growth parameters for best device performance and guide the development of models describing the complex kinetic pathway determining the composition evolution of self-assembled islands.

From the point of view of modeling, these results show that thermodynamic equilibrium conditions leading to Fig.3.3 is a valuable tool to understand the energetic contributions and to explain the experimental findings. However, they also show that the actual state reached by the system is heavily influenced by kinetics and diffusion of ad-atoms on the surfaces reaching the island. This is the reason why nowadays new kinetic approaches including the thermodynamic driving forces are being studied [111, 112].

4

Stepped surfaces and Ge/Si(1 1 10)

"What saves a man is to take a step.
Then another step."
Clive Staples Lewis

In this chapter we present the important topic of the stepped (or vicinal) surfaces.

After discussing their importance in heteroepitaxy and classification, we describe some instabilities happening on these systems and the method adopted so far in literature to assess their energy.

Finally, we present the situation of the (1 1 10) surface, leading to the nucleation of Ge islands that show remarkable peculiarities with respect to the standard SK islands mentioned in Chapter 1. An in-depth analysis of this system is carried out in the next two chapters.

4.1 Stepped surfaces: importance

In diamond (and solids in general) just a limited number of surfaces are atomically flat, some examples of which are (001), (113), (111), (110) as shown in Fig.4.1-(a) [86].
The surfaces whose normal is slightly tilted from these directions are called "vicinals". They are typically characterized by high Miller indeces and consist of terraces of the flat major surface separated by steps, hence they are also called 'stepped' surfaces. In fact the steps can be regarded as the (partial) reconstruction of these surfaces themselves [91]. In the stereographic triangle they are located in the neighbourhood of the flat surface to which they are vicinal (see sec.1.4, page 24) and typically they belong to the major's 'family territory' [25, 22] (panel b of Fig.4.1). This is a practical way to determine what the flat surface consisting the terraces is.

The presence of steps cannot in fact be ignored in experiments, indeed the wafers are cut with a finite precision and even the nominally (001) surfaces are slightly miscutted of a

small angle[1]. Steps are extremely reactive regions of the surface, hence the adatoms of Ge (or Si) have a preference to aggregate in this neighbourhood and create nanoclusters (see panel c of Fig.4.1), thus being a first nucleus for nanostructures as is the case of 2D arrays or V-grooves at the nanoscale size [91, 113] in the same way as made by the holographic pits described in the previous chapter.

As for the nanostructures, the concept of steps has been widely adopted for their description. Indeed a possible approach to describe their elastic behaviour is performed by analyzing them as a superposition of steps [114, 115] and their shape evolution as due to the kinetic of these steps [116, 117] (see sec.4.2 below).

Therefore, the energy of the stepped surfaces themselves has been assigned a paramount importance for nanostructures. As an example, both for the surface energy of the substrate and the exposed facets have been analyzed to prove the barrierless nucleation of the mound (precursor to {105} pyramids, see Chapter 1) [118].

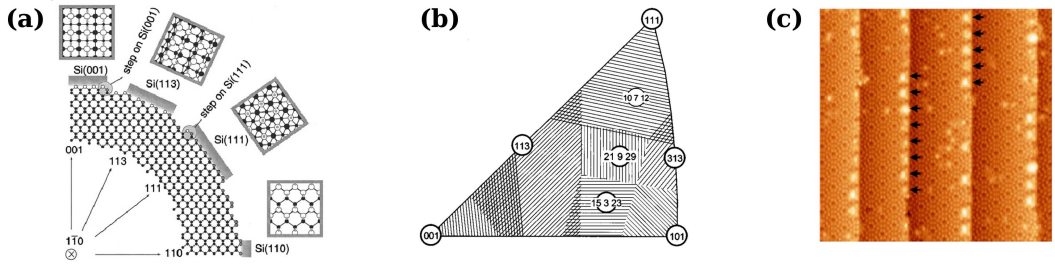

FIGURE 4.1: Generalities on stepped surfaces. (a) Position of the flat surfaces in diamond (Si) of the type (11n) and an highlight of the steps on these surfaces, reproduced form Ref.[86]. (b) Stereographic triangle for Ge showing major surfaces and their family territories, from Ref.[25]. (c) Example of preferential site nucleation on a stepped surface: upon a vicinal of Si(111) less than 0.5 MLs Ge create nanoclusters at the upper terraces of the steps (black arrow), from Ref.[86].

4.2 Vicinal surfaces: structure and instabilities

For the reasons mentioned before, in the last twenty years the structures and evolution of steps have been analyzed in details using STM studies of clean (and also passivated) surfaces.

The typical steps observed and analyzed on Si(001)[2] have an azimuth angle towards $< 110 >$ direction and a normal given by (11n) direction. Along this direction, the steps are classified in S- and D-type if they are single- or double-ML high, respectively [119]. Further, they are classified as A- or B-type depending on the direction of the dimers on the upper terraces following Fig.4.2-[a]. Since the direction of the dimer rows formed by consecutive (001) planes alternates, an S_A step must be followed by an S_B step and so on. This does not happen for double steps, where actually no D_A type step has ever

[1] for the definition of miscut and azimuth angle see Appendix B

[2] that is the typical substrate used in homo- and heteroepitaxy, as well as in the microelectronic industry

been observed, as well as a triple-height one. The border of the step can be non-bonded or rebonded depending on the dimerization of the outermost atoms [120]. The length of terraces is dictated by the miscut angle θ, but the symmetry of diamond causes the possibility of having two types of terraces of different length when n is even[3] [91].

Phenomenologically, the dynamics of stepped surface is complex and thus represents a rich field of investigation. In the simpliest case of Si homoepitaxy, the evolution of the surface can follow three paths, sketched in Fig.4.2-[c,d,e]. The incoming adatoms may attach to the border elongating all the terraces at the same rate (Step-Flow process), or some terraces may elongate faster than others with a consequent shrinking of some terraces and accumulation of steps in a narrow region (Step-Bunching) that can lead to the formation of the "rippled-structure" shown in Fig.4.2-[d] [122], or the terraces may grow rough profiles (Step-Meandering). It is an evidence that A- and B-type steps evolve differently: S_A steps have a straight profile but the upper terraces is shorter than the ones of S_B, on the contrary S_B type steps are rough with larger terraces (Fig.4.2-[c]) [122, 121, 123].

The most adopted approach for studying surface dynamics is the Kinetic Monte Carlo (KMC) [122], where the detailed energetic barriers are modeled following different flavours (the Burton-Cabrera-Frank model, the introduction of Ehrlich-Schoebel barrier sketched in Fig.4.2-[b] and the Asaro-Tiller-Grinfeld instability are just some examples [86]). All of these effective models can be made more systematic if the Potential Energy Surface (PES) of adatoms is analyzed directly within a DFT approach [124].

The complex of all phenomena that alters the geometry and structure of the system is cathegorized under the name of **"Instability"**. The evolution just mentioned are defined as "kinetic" (or growth) instabilities [122, 125, 126, 127]. These instabilities may eventually modify the mobility of adatoms causing some 'exotic' effects [128].

The case of heteroepitaxy is further complicated by the presence of instabilities linked to the long-ranged strain, and the effective dynamics is a balance between the two terms [127, 129].

The phenomenon of step-bunching has also been invoked to explain and model the pyramid-to-dome transition in SiGe heteroepitaxy [130].

4.3 Vicinal surfaces: energy

The dynamical phenomena can be regarded as the path leading to the thermodynamic minimum. Therefore, assessing the energetic stability of all types of steps as a function of the terrace length (such as the experimental evidence regarding Si homoepitaxy shown in Fig.4.2-[b] [86]), temperature and strain is a matter that involves much effort in literature with the aim of predicting the geometry expected and its evolution. In particular, these variables can be coupled requiring a more complex analysis [123] (Fig.4.3-(a)). Additionally, the energy of the stepped surfaces can heavily influence the ECS at both zero and finite temperature [126] as well as the stability of islands [10].

Ideally we can divide the surface energy of a stepped surface with miscut angle θ into a

[3] compare the discussion in the next chapter for the case of (1 1 10)

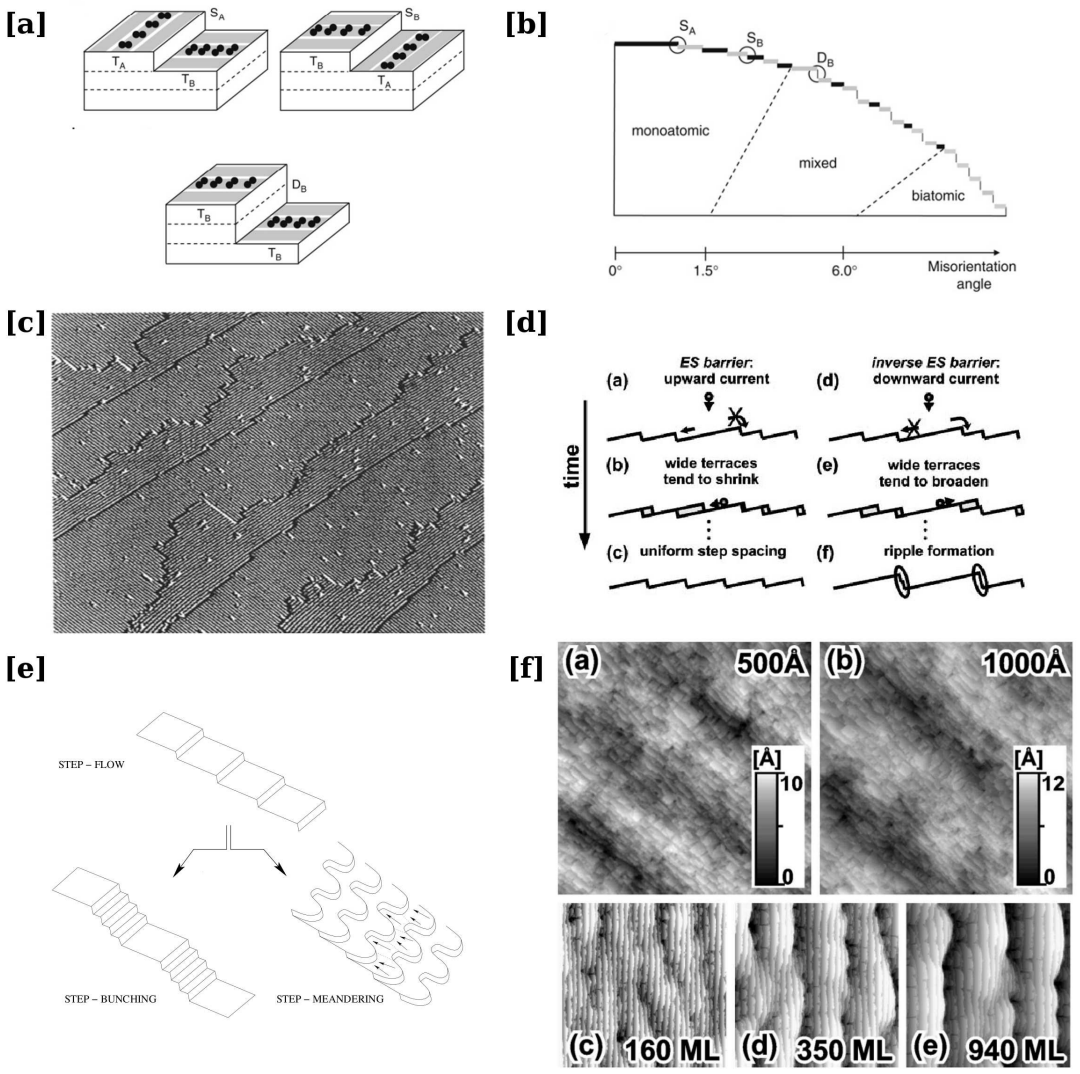

FIGURE 4.2: Structure and instabilities on vicinal surfaces. Structure of the steps S_A, S_B and D_B [a] and the observed ones for Si(001) at different miscuts [b] (reproduced from [86]). [c] Experimental image on a miscutted surface 0.5° off along [110] direction Si(001). Straight steps are S_A, the rough ones S_B. (full image reproduced from Ref.[121]). [d] Examples of the kinetic instabilities happening on a stepped surfaces (from Ref.[122]). [e] Evolution of the surface as an effect of the instabilities. [f] The 'rippled surface' as a result of the step bunching process in the case of Si(001). Top row are experimental 600nm x 600nm AFM images, lower row are results from KMC simulation, reproduced form Ref.[122].

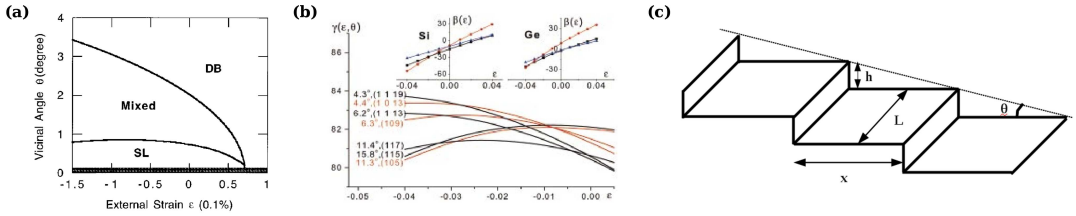

FIGURE 4.3: (a) Calculated phase diagram for strain and vicinal angles, from Ref.[123]. (b) Surface energy of various vicinal surfaces as a function of biaxial strain as obtained from Tersoff potential, from Ref.[118]. (c) Model for the calculation of the stepped surface energy in function of the energy of the flat ones, leading to the relation used in Ref.[131].

contribution coming from the flat terraces and the step. Taking Fig.4.3-(c) as a reference, we can define the *stepped* surface energy density γ_{step} per unit area of the tilted surface $\widetilde{A}$, γ_0 the energy density per unit area of the terrace A, Γ the edge energy per unit length L. In this case it holds that:

$$h = x \cdot \tan\theta; \quad d = \sqrt{x^2 + h^2} = x \cdot \sec\theta; \quad \widetilde{A} = L \cdot d = (L \cdot x) \cdot \sec\theta = A \cdot \sec\theta$$

Hence we get

$$\gamma_{step} = \frac{\gamma_0 \cdot A}{\widetilde{A}} + \frac{\Gamma \cdot L}{\widetilde{A}} = \gamma_0 \cdot \cos\theta + \frac{\Gamma}{h} \cdot \sin\theta \tag{4.1}$$

that is the same relation used in Ref.[131]. Some authors, though, modify this equation by further expliciting the different contributions (such as the dipolar interaction energy)[118].

If elasticity theory can describe effects such as the long-ranged step-step interactions, monopole and dipole contributions in a continuum approach [117], the other contributions arising from the instabilities mentioned in the previous section have a clear atomistic origin, thus requiring a purely atomistic approach. The praxis is to study the energy of the stepped surface for different geometries and reconstruction and report either γ_{step} [118] or use eqn.(4.1) along with the energy of the flat surface γ_0 at the same strain state to give the mere value of the step formation energy Γ [132]. Incidentally, the trend of γ_{step} with strain reported in Ref.[118] (and reproduced in Fig.4.3-b) clearly shows that they have a maximum as deduced in this thesis in sec.2.5.4 (page 63) from general arguments.

The concern for vicinal surfaces is to give an estimation of the energy for different geometries of terrace length, strain, epilayer thickness and temperature. Since the unit cell for vicinal surfaces is extremely large (see some examples in Tab.2.3 at page 60), so far they have been analyzed just with (semi)empirical potentials, neglecting to check the results inside a purely *ab initio* treatment[4].

Unfortunately, as pointed out in Ref.[133], the usage of different potential makes the definite estimation of step energies strenuous and not univocal. However, different potentials like the Extended Brenner and Stillinger-Weber [133] agree in finding *negative* step formation energies for Si(001) unstrained. The same result was found some years before

[4]this is performed by us showing some unexpected results, see chapter 5

in Ref.[132] where it was shown that a *compressive* strain largely reduce the formation energy. This is reasonable since the steps allow a partial relieve of the strain itself, implying that the creation of steps on compressed surfaces should be expected. A discussion of this result and a comparison with our DFT outcomes is performed in the next chapter.

Some other authors assign to the vicinal surfaces continuum values that can consistently reproduce the Wulff solid of the islands [10].

The computation of the step free energy can attempt to explain the observation of the single or double step on Si(001) reported in Ref.[86] with peculiar methods, as discussed at length in Ref.[120].

It is mention-worth that, regardless of the apparent simplicity with which the vicinal surface energies are computed, the explanation of the observed reality may be more complex because of the requirement to involve several competing ingredients. An example of this is the variation of the surface energy on the miscut angle $d\gamma_{step}/d\theta$. In Ref.[118] it is computed to be highly negative, but the addition of the experimentally-observed Dimer Vacancy Lines (DVL) on the terraces reduces the magnitude of the change in energy leading to a rather flat $\gamma(\theta)$ [134], that is actually consistent with the observed WL roughness in typical Ge/Si(001) experiments.

4.4 The case of Ge/Si(1 1 10): a path to faceting

In this section we highlight the peculiar phenomenology observed upon deposition of Ge on Si(1 1 10) surface taken from literature results, the outcomes of our work being reported in the next two chapters.

4.4.1 Experimental evidences and importance

In the previous chapter we highlighted the importance of having an homogeneous and ordered nucleation of islands for both application purposes and pure studies. Apart from the $\sim$ 200 nm-wide pits already described [109], a number of other options are adopted such as stripe-patterned substrates [135, 136] (see Fig.4.4), V-grooves [137] and laser-textured substrates leading to large scale pits ($\sim 3\mu m$) [138].

For this reason the detailed evolution of these structures has been object of intense studies in the last few years. In several systems, the spontaneous onset of ripple-like structures elongated along the [110] direction were observed on large scale pits (Fig.4.5-(a)). The same objects were observed on stripe-patterned substrates (panel b), where the more detailed analysis reported in Fig.4.5-b allowed to determine that they are composed of {105} facets and the Si substrate upon which they formed is the Si(1 1 10) created by its instabilities upon the Si buffer deposition [135]. The applicability of these '105-ripples' as a proper template for dot ordering was actually already proven earlier in Ref.[139], where a SiGe layer was deposited upon a $\sim 10^\circ$ off (001) surface to create the ripples followed by a pure Ge deposition leading to an ordered dot nucleation, see Fig.4.5-(c).

It is important to notice that notwithstanding the same adopted name, these structures are not the same as the ones obtained by Si homoepitaxy reported in Fig.4.2 discussed before. Indeed their elongation direction is perpendicular to the step edges underneath

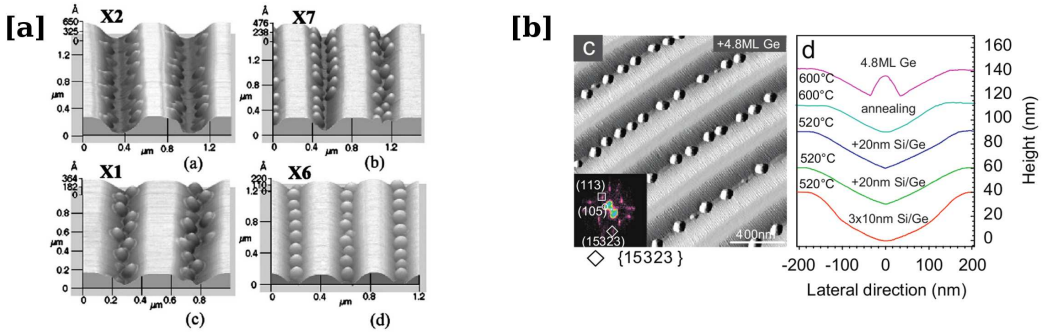

FIGURE 4.4: Stripe-patterned substrate to control island nucleation.[a] AFM images of Ge deposited on a stripe-patterned Si substrate for different sample from Ref.[136]. [b] STM image and profile sketch of deposition of pure Ge on a stripe-patterned substrate after this was covered for some SiGe ML, from Ref.[137]. In [b] the elongated structure on the sidewall of the stripes are the {105} ripples we are dealing with in this thesis.

(see Fig.4.6), evidence that they are not created by a step bunching process [129]. Moreover, they are observed when Ge (or a low diluted alloy with Si) is deposited. From an in-depth analysis of several vicinal surfaces to (001) [129], the formation of these and similar structures is explained in terms of formation of {105} facets, which develop in SiGe/Si systems. In Ref.[129] it is proposes the explanation that the observed morphology on vicinals surfaces for SiGe/Si systems is therefore dictated by the frustrated shape of equilibrium nanocrystals, see Fig.4.6-(a), that is equivalent to the concept of the Wulff solid laying on a tilted substrate discussed in sec.2.2 at page 34. This idea was confirmed by successive observations [23, 140].

With this interpretation, the elongated ripples on Si(1 1 10) are the degenerate version of the pyramids, since the direction of the edge between the facets (105) and (015) lies parallel to the plane (1 1 10), with the consequence that the solid cannot close if the sole {105} facets are available, see Fig.4.6-(b).

What is remarkable is that on Si(1 1 10) a very high degree of coherence is observed leading to a structure that very nicely resembles the ideal class of periodically faceted surfaces [141] that ideally can be exploited as the recently-hot-topic of "in-plane" Nano Wires with appealing optoelectronic properties.

4.4.2 Geometry and evolution

The discussion about the various kinetic effects in this chapter suggests their importance in stepped surfaces. Hence, the microscopic processes happening at the early stages of Ge growth on the Si(1 1 10) surface leading to the ripple formation have been studied in detail in P. D. Szkutnik *et al* in 2007 [143], with the experimental observation reported in Fig.4.7 and here resumed.

As can be determined by the stereographic triangle reported in Fig.2.4 at page 44, the

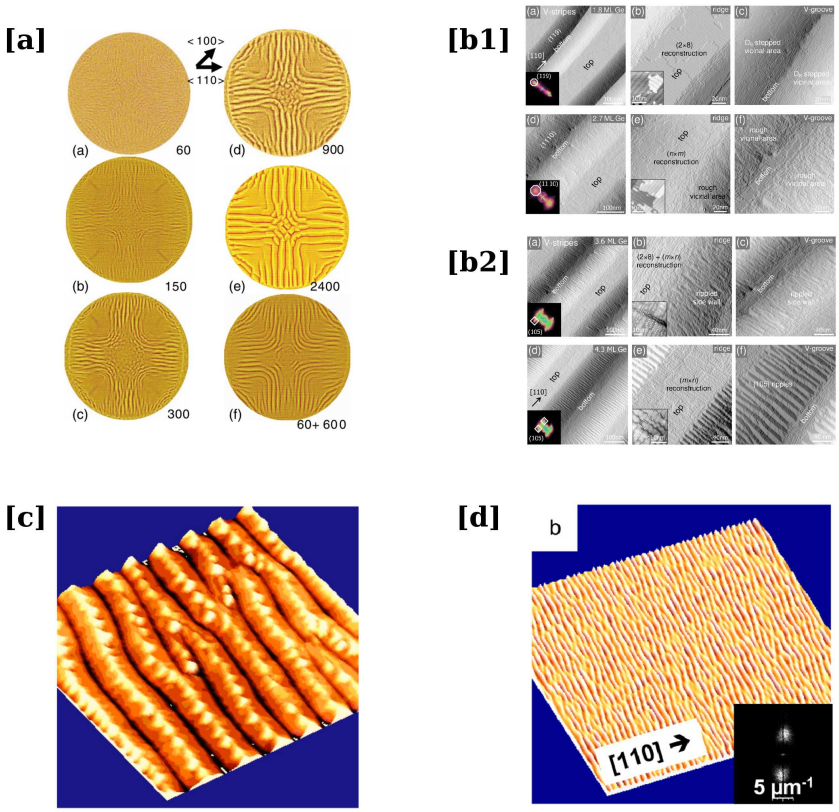

FIGURE 4.5: Evidences of Ge "ripples" in literature. [a] Ripple formation on laser-textured pits at different stages of deposition, from Ref.[138]. Evolution of Si stripes upon deposition of Si [b1], where the (1 1 10) is formed, and overgrowth of Ge [b2], where ripples are formed, from Ref.[135]. [c] Overgrowth of Ge on Ge_xSi_{1-x} ripples: the bright spots are domes nucleated at specific sites, from Ref.[139]. [d] Large scale deposition of 30% Ge on Si(1 1 10), from Ref.[86].

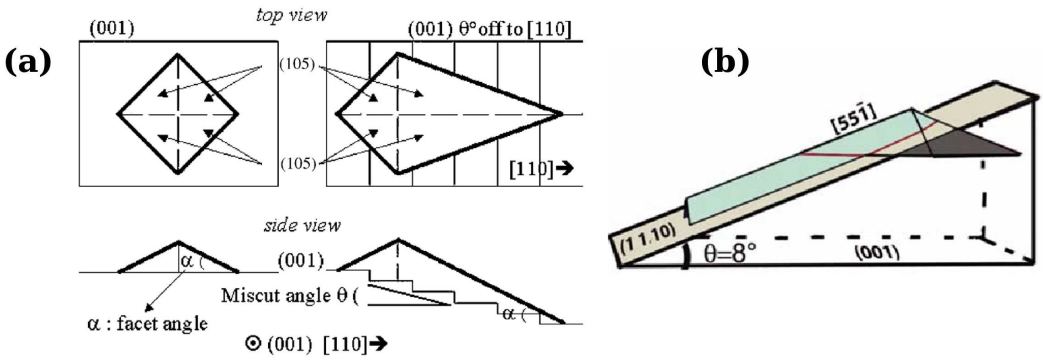

FIGURE 4.6: Explanation of {105} ripples as a degenerate pyramid. (a) General structure of a pyramid on a (11n) surface, from Ref.[142] and on the (1 1 10) surface when the pyramid cannot close, from Ref.[140]

(1 1 10) direction is a surface vicinal to (001), the azimuth direction being [110] and whose miscut angle is $\sim 8.04°$ (see the relations reported in Appendix B). From the experimental stability diagram reported in Fig.4.2-[b], in this case the Si surface is composed of Db steps alone, separating terraces whose *average*[5] length is equal to 1.9 nm.

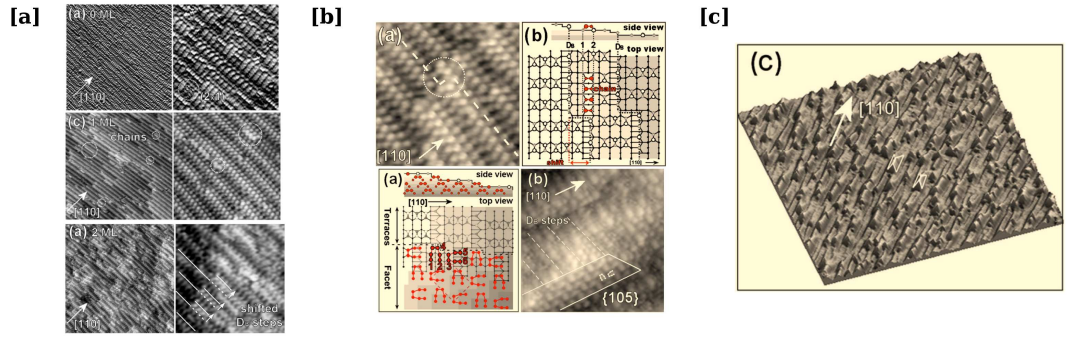

FIGURE 4.7: Microscopic processes of Ge/Si(1 1 10) leading to {105} facets, reproduced from Ref.[143]. [a] Evolution of the Si surface upon deposition of 0 (top), 1 (middle) and 2 (bottom) MLs Ge. [b] Model of the movement of steps triggered by the formation of adatoms chain (top) and formation of the (105)-RS reconstruction from the dimers of terraces (bottom). [c] STM view of the sample after 6 ML Ge. In this case short {105} ripples are formed.

Deposition of pure Ge is performed in a MBE chamber at 600°C with a flux of ~ 0.75 ML/min upon the thermally-annealed Si substrate, where no Si buffer is deposited to suppress kinetic step bunching. For this reason, the initial reconstruction is compatible with the ideal one with Db steps (panel a-top). At submonolayer Ge coverage the reconstruction on the terraces turns from 2x1 (dimers) to p(2x2) (alternated dimers), probably due to Ge-Si intermixing processes where Ge tends to be incorporated at the step-edge sites. Between 1 and 4 ML Ge, the step-flow mechanism is observed (panel [a]-bottom) as triggered by single addimers located at the middle of the terraces (panel [b]-top) forming zig-zag chains, that is an example of the local modification of the geometry induced by Ge atoms that was postulated in Ref.[129]. This observation allows to have a better insight in the microscopical mechanism underlying the step-flow process, an explanation that the typical simulations performed within the Kinetic Monte Carlo (KMC) [122] technique cannot provide. The dimers of the train of propagating steps eventually merge with the addimers creating the horse-shoe reconstruction of the Rebonded-Step (RS) (105) facet [81] (panel [b]-bottom). The {105} ridges form from the bottom increasing in height and joining at the top. Meanwhile the propagation of the double steps via step flow induces the elongation of the ripples themselves (panel [b]-bottom) along the miscut direction to create the non-closing degenerate pyramid mentioned before. At 6 ML coverage, the surface is covered by several terminated ripples whose length is ~ 40 nm (panel [c]).

With the growth parameters in this experiments, the island are rather short, not showing the faceting behaviour revealed in similar experiments as shown in Fig.4.8-(a)

[5] see discussion in next chapter

from Ref.[142]. In panel (b) of the same figure is reported an image taken after 18 hours annealing. They observe some not-well-defined triangular shaped islands that the authors in 2003 describe as formed by three {113} facets (panel c). This explanation is, however, controversial, since it is geometrically impossible to have just three (113) facets in a cubic lattice and this shape is inconsistent with any Wulff solid of the typical islands (domes and barns) observed on Si substrates.
We solve this puzzle in chapter 6 with the introduction and description of the "Tadpole"-shaped islands as the missing evolutionary ring between ripples and domes.

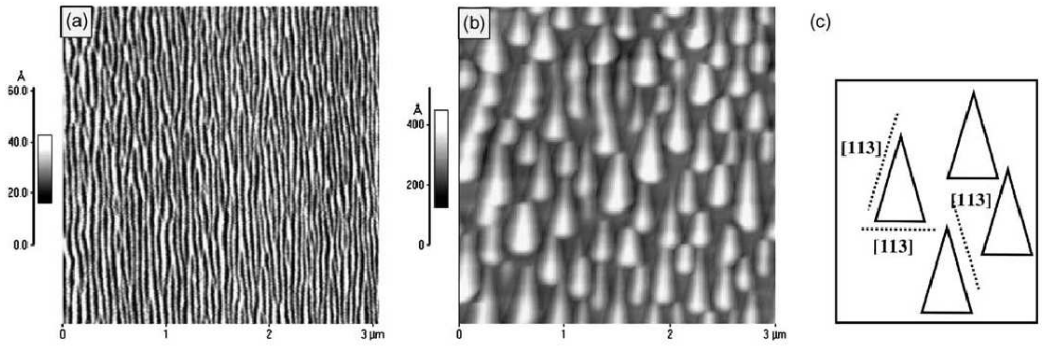

FIGURE 4.8: Evidences of elongated ripples from Berbezier et al [142]. AFM images islands obtained after the deposition of $\sim$ 17 ML of $Si_{0.7}Ge_{0.3}$. (a) as deposited, (b) after 18 hours of annealing. (c) is a controversial schematic representation of the facets of the annealed islands, that we clarify and explain in chapter 6.

4.4.3 Surface energy

Since the nucleation of {105} facets on any substrate has been shown to be due to thermodynamics and not to kinetic instabilities, the stability of the islands can be determined by the use of eqn.(2.1) at page 32. For this purpose, the energy of the (1 1 10) surface is to be assessed with a comparable accuracy as the {105} one (since it is the other surface involved in the problem). Thus, all the contributions of the Ge/Si surface must be taken into accout at the same time: reconstruction, strain, Ge epilayer thickness (if an analysis as a function of the deposition is to be performed), etc.

This analysis for the (1 1 10), however, is not present in literature, particularly if one considers that the habit in this field is to define the surfaces on the basis of the length of the terraces with the implicit hypotesis that all the terraces have the same length. However, in diamond lattice the surfaces of the type (1 1 2n) have two types of terraces [91], therefore this type of surfaces, to which the (1 1 10) under analysis belongs, has been excluded in these previous studies.

Reported in the next chapter, our calculations show the two different length can actually have relevant effects on the surface energy. Therefore the detailed analysis of this surface is performed in next chapter.

5

Ge/Si(1 1 10) early stages: surface-driven transition from SK seeds to faceting

"Once excluded the impossible, whatever remains, however improbable, must be the truth"
Sir Arthur Conan Doyle

In this chapter, we present our original results concerning the heteroepitaxy of Ge / Si(1 1 10), whose interest has been highlighted in sec.4.4 at page 88.

After showing the experimental outcomes from our collaborators, we describe in details the complex multiscale approach used to study this system.

Afterwards, the detailed computation of the surface energy both in DFT and Tersoff potential is performed. Here the so-far neglected interaction of the dimer tilting pattern and the double step is shown to be relevant in order to estimate the surface energy properly, leading to some unexpected results.

The obtained surface energies are applied to the system of ripples on Si(1 1 10) in order to quantify their onset from a rough WL. In so doing we combine our theoretical outcomes with the experimental observations and we give an estimation of the 'actual' value of the edge energy between adjacent facets, otherwise hard to compute, with some unexpected results that we rationalize.

Finally we envision a mechanism that may explain the complete faceting of the sample and quantify it.

We describe the observed transition to 3D islands upon further deposition in the next chapter.

5.1 Experimental evidences

In order to better elucidate the evolution and growth behavior of Ge on Si (1 1 10) and in particular the phase transition happening here, the experiment described in sec.4.4.2 is replicated and studied in details using in situ scanning tunneling microscopy (STM) and electron diffraction by our experimental colleagues at the Joannes Kepler University at Linz (Austria).

The growth experiments were performed in a multi-chamber molecular beam epitaxy system, allowing sequential deposition and imaging of epitaxial surfaces without exposure to ambient conditions [135]. After oxide desorption and 40 nm ($\sim$ 294 ML) Si buffer growth, Ge was deposited on Si (1 1 10) substrates at 550°C and 1.1 Å/min ($\sim$ 0.785 ML/min) in 0.5 ML increments up to a total thickness of 7 ML. Here, one ML is defined as number of atoms contained in one atomic layer of Si(001) with a thickness of 1.4 Å(=5.6Å/4). After each growth step, the samples were quenched to room temperature and imaged in situ by STM with negative sample bias around 2-4 V. Several MLs were deposited in one step for in situ reflection high energy electron diffraction (RHEED) studies and control experiments, giving essentially the same results as for the stepwise grown samples.

After buffer growth (that differs this experiments from the one described in the previous chapter by Szkutnik et al), the clean Si (1 1 10) surface displays a regular structure consisting of narrow (001) terraces separated by straight double monolayer D_B steps parallel to the $[\bar{1}10]$ direction. The terraces exhibit the typical (2x1) surface reconstruction with dimer rows perpendicular to the step edges and the D_B steps are rebonded in order to reduce the number of dangling bonds [144, 119].

Similarly to Ref.[143], upon Ge deposition, the terraces break up into short segments of varying length and shorter terrace segments are formed (showing that the Si buffer layer does not affect the main features of this system). In addition to that, the missing dimer rows of adjacent terraces start to line up along the $[55\bar{1}]$ direction. As growth proceeds, this leads to the formation of 1-2 ML deep trenches along the miscut direction as shown by the STM image at 3.6 ML Ge coverage depicted in Fig.5.1-(a).

From these structures **elongated mounds** are formed as indicated by the dashed rectangle in Fig.5.1-(a) that resembled the mounded Stranski-Krastanow seeds observed for subcritical Ge on Si(001) [11]. The elongated mounds have typical widths of 5-10 nm and lengths of 15-30 nm and their sidewalls are formed by small areas with local {105} orientation. This leads to the appearance of weak {105} facet spots in the surface orientation density map (SOM) of the STM images shown in Fig.5.1-(a) as insert.
The isolated **ripple-seeds** persist up to 4 ML coverage without much change in amplitude or size.

At a critical coverage of 4.2 ML, however, a dramatic and sudden surface transition occurs by which the whole epilayer surface is completely transformed into a **perfectly {105} facetted**, quasi-periodic ripple structure. This is demonstrated by the STM images displayed in Figs.5.1-(c) and (d) at 4.5 ML coverage. In the high resolution STM images, the sidewalls of the ripples exhibit the characteristic zig-zag structure of the rebonded-step {105} surface reconstruction [81, 145] and the surface orientation map [insert in Fig.5.1-

(d)] exhibits exclusively two sharp maxima at the {105} surface positions.

The nanoripples seamlessly cover the whole epilayer surface and the original (1 1 10) surface is nowhere exposed. The abruptness of the ripple transition is revealed by in situ RHEED experiments shown in Fig.5.2-(a), where the intensity evolution of the specular spot and of a 3D ripple spot (blue, respectively, black line) are plotted as a function of Ge coverage. The corresponding diffraction features are indicated in the corresponding RHEED patterns displayed in Figs.5.2-(b) to (d). Since the electron beam was directed perpendicular to the ripples, the diffraction pattern strongly changes upon ripple formation due to surface diffraction from the tilted ripple facets. The sudden appearance of the ripple diffraction spots at 4.2 ML coverage clearly proves that the **abrupt surface transition** is completed within a fraction of a ML. As demonstrated by the large scale STM image displayed in Fig.5.1-(d), all ripples are perfectly aligned along the $[55\bar{1}]$ miscut direction and they are remarkable uniform in size. Their height is 1.2 nm and their average width 17 nm according to statistical analysis, whereas their length well exceeds 300 nm.

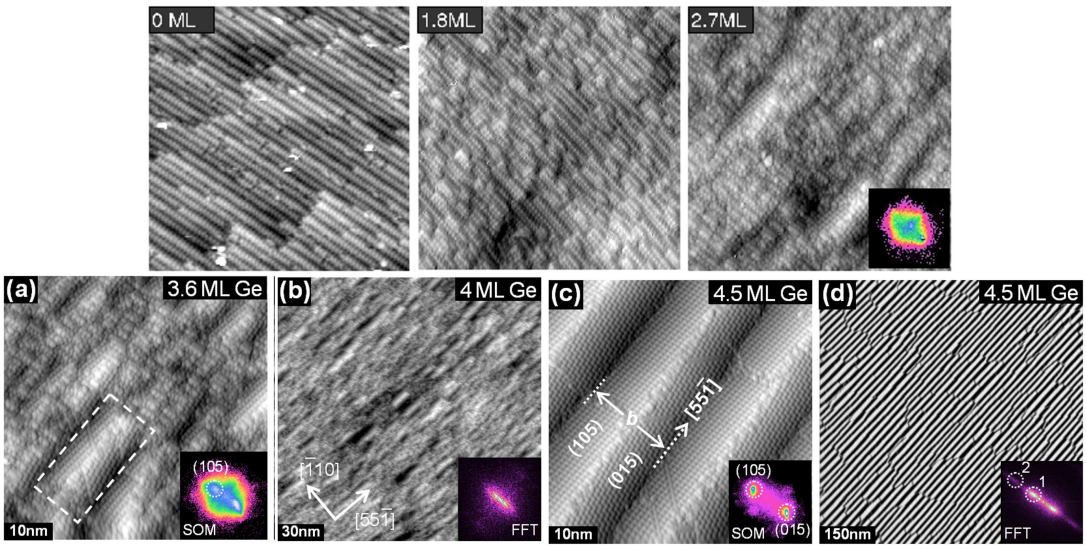

FIGURE 5.1: STM images of Ge on Si (1 1 10) deposited at 550°C recorded at coverages of (a) 3.7 ML (b) 4.0 ML and 4.5 ML for (c) and (d). Note the different scale of the images. The inserts in (a) and (c) depict the surface orientation maps (SOM) calculated from larger STM images, revealing complete {105} facetation of the Ge surface at thicknesses exceeding 4.2 ML. Only isolated mounds and pre-ripples are seen for lower coverages. The inserts in (b) and (d) show the 2D FFT power spectra of the STM images. For the perfectly facetted Ge surface at 4.5 ML, FFT satellite peaks (indicated by circles) up to the second order are observed.

The ripple transition exhibits several **remarkable features** distinguishing it from the common SK evolution observed for Ge on Si(001) [14, 30, 40, 146]. First, the ripples cover the whole epilayer surface, i.e., initial ripple seeds do not evolve into separate SK islands but the layer as a whole is transformed to a non-planar, perfectly facetted wetting layer as shown schematically in Fig.5.2-(e) and (f). Secondly, the ripples display a remarkable uniformity in size and shape, as well as an excellent lateral ordering. This is evidenced by the appearance of even second order FFT satellites in the 2D FFT power spectrum of the STM image depicted in the insert of Fig.5.1-(d). This ordered configuration with high correlation degree among the ripples is in contrast to the uncorrelated island nucleation seen for the usual SK growth mode. Whereas SK islands grown on top of the wetting layer, the ripple transition consumes most of the layer underneath the ripple-seeds and the ripples extends all the way down to the Si/Ge interface. This follows from the analysis of the ripple volume per unit area V_R/A using

$$\frac{V_R}{A} = \frac{1}{2} \cdot b \cdot \frac{hl}{bl} = \frac{1}{2}h = \frac{1}{4}b \tan\varphi \tag{5.1}$$

where the sidewall angle $\varphi = 7.97°$ is fixed to the precisely defined {105} ripple geometry on (1 1 10) surface, h being the height of the ripples, b their base. Since at the used growth temperature of 550°C only little Si/Ge intermixing occurs [147], and the ripple period of b=16.8 nm can be precisely derived from the FFT satellite spacings, we obtain the result that at 4.5 ML coverage, 4.1 ML of material is contained in the ripples, leaving less than half of a ML at the interface.
This is strictly true in the case of pure Ge ripples, but also allowing, e.g., a $\sim$ 10% intermixing, the residual WL would still only be of the order of one ML. The ripple array also display a remarkable stability upon post-growth annealing, showing no signs of coarsening, even for extended annealing cycles at 550°C (not shown).

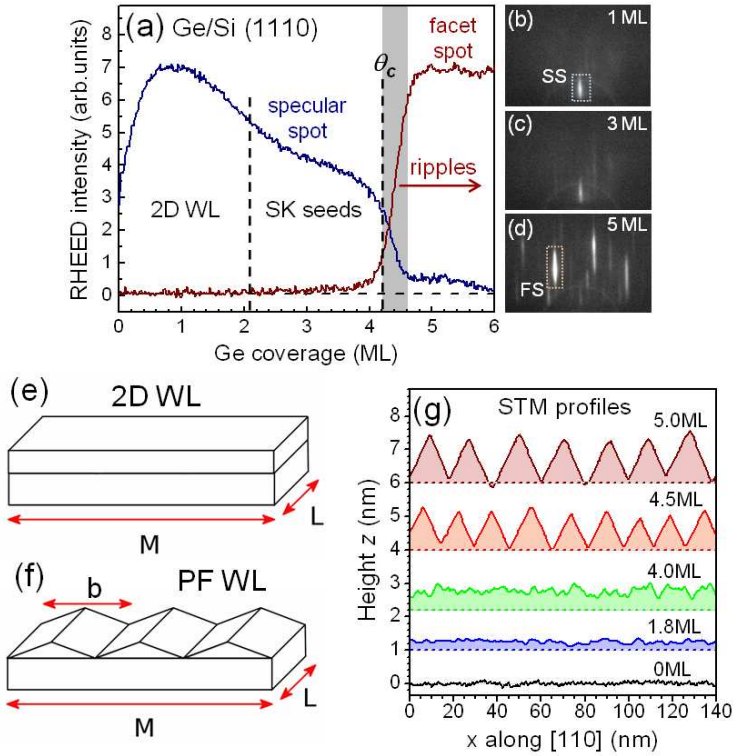

FIGURE 5.2: (a) RHEED intensity of the specular spot (SS, blue line) and a facet diffraction spot (FS, black line) plotted as a function of Ge coverage on Si (1 1 10), indicating an abrupt morphological transition at a critical coverage of 4.2 ML. RHEED patterns recorded at different coverages are shown in (b) to (d). The schematic illustration of the flat 2D wetting layer (WL) and the perfectly faceted (PF) ripple surface are shown in (e) and (f), respectively. Panel (g) shows the evolution of the surface profile along <110> as a function of Ge coverage. The shaded regions below the profiles represent the respective total Ge amount deposited in each case and the horizontal dashed lines the location of the Ge/Si heterointerface. For clarity, the profiles are offset in the vertical direction

5.2 Simulation technique: Multiscale approach

The described features above are observed during deposition. However, the atoms impinging on the surface represent an hindrance to the diffusion of the adatoms diffusing on the substrate themselves, thus reducing their mobility and diffusion length and making them unable to reach the thermodynamic equilibrium. It is therefore reasonable that the transition may happen at a lower coverage if the adatoms are given enough time and energy to diffuse on the surface. In order to check this idea, and to find the thermodynamic critical coverage, a series of small depositions with subsequent annealing are performed. In so doing, the critical coverage lowers to $\sim 3.6 - 3.8$ ML for the transition from the rough surface and the perfectly faceted one. It is this value that an energetic theory can (and should) predict.

In this respect the basic idea is to compare the energy of the different phases (finite-size ripples, perfect faceting and WL) with equation (2.1):

$$E_{system} - E_{WL} = V \cdot (\rho_{system} - \rho_{WL}) + S_{system} \cdot \gamma_{system} - B \cdot \gamma_{WL} + L \cdot \Gamma_{edge} \qquad (5.2)$$

As seen in sec.2.5.5 at page 65, the surface energies γ depend on the distance between silicon and the topmost layer of germanium:

$$\gamma(N) = (\gamma_0 - \gamma_\infty) \cdot e^{-B \cdot N} + \gamma_\infty \qquad (5.3)$$

Here N, in the case of the WL, is equivalent to the ML of coverage, and since the transition here is happening in the first few MLs, corresponding to the region of higher derivative in $\gamma(NGe)$, a precise estimation of its value is mandatory, particularly because it is this term the one giving the critical deposition we are looking for. For these reasons, the strategy we adopt is the same applied in Brehm *et al* [30], leading to eqn.(2.52) at page 68.

However, contrary to that paper, here the analysis is complicated by the reduced size of the islands we are dealing with[1]. Indeed in this case, the distance Ge-Si must be taken into account not only in the WL surface energy (as in Ref.[30]), but also in the estimation of the effective {105} surface energy, since the fraction of facet adjacent or near to the Si is non-negligible, thus influencing the energy overall.

As already discussed in sec.2.5.4, the γ is a function of the strain to which it is subject. While this dependence is already included in the simulations of the Ge/Si(1 1 10) WL, this must be taken explicitly into account for the {105} facets. Considering that the relaxation on the surface of these elongated structures is strongly anisotropic, a uniaxial strain dependence is needed, that is still missing in literature.

We aim to fill this gap of knowledge in the following way. For calculations of the strain dependence of surface energy we consider pure Ge slabs subject to biaxial or uniaxial strains. In this case μ_{Ge} is calculated for Ge compressed in x and y and Poisson corrected in z for the reasons highlighted in Appendix C. To map discrete calculations into a continuum model for the strain dependence of surface energy we fit $\gamma(\epsilon_{xx}, \epsilon_{yy})$ with a second-order polynomial. This models the variation in surface energy as due entirely to mechanical strain effects, and assumes that possible electronic contributions are second

[1] as already discussed in Ref.[30]

order, as noted in Ref. [92]. In the strain interval of interest ranging from ∼-4% (Ge compressed to the Si lattice constant) to 0%, surface energy is interpolated as [148]:

$$\begin{aligned}\gamma(\epsilon_{xx},\epsilon_{yy}) &= \gamma_0 + \tau_{xx}\cdot\epsilon_{xx} + \tau_{yy}\cdot\epsilon_{yy} + \\ &+ S_{xx}\cdot\epsilon_{xx}^2 + S_{yy}\cdot\epsilon_{yy}^2 + S_{xy}\cdot\epsilon_{xx}\cdot\epsilon_{yy}\end{aligned} \tag{5.4}$$

Here the surface energy γ is defined per unit of deformed area (i.e. is defined in the Eulerian reference frame), and τ and S are defined as the surface stress and surface elastic constants, respectively [148]. For completeness, we conduct this analysis for both (105) and (1 1 10) surfaces, as reported below.

A further complication consists in handling both the depedence on strain and NGe *at the same time*, that, to our knowledge, has not been performed before. The way we handle this is described in the next subsection.

A further complication due to the reduced size of the islands is the non-negligible role played by the WL under the islands to the strain budget in the system[2]. Therefore, the actual geometry of the system must be taken into account in the FEM analysis.

A resume of the multiscale strategy adopted is reported in the next subsection.

5.2.1 Multiscale

Our starting ingredients are:

- ρ, ϵ = elastic energy density and strain tensor of the relaxed structure as obtained by a FEM modeling
- $\gamma(\epsilon_x, \epsilon_y)$ = strain-dependent surface energy of the facets as computed from a pure Ge cell in atomistic (DFT or Tersoff) approach, fitted as given by eqn.(5.4)
- $\gamma(NGe)$ = epilayer-thickness dependent surface energy of the facets as computed from Ge/Si cell in atomistic approaches, interpolated by the exponential function (5.3)

In this section we outline how to combine all of them to accurately estimate the {105} facets contribution to the internal energy. The method is resumed in Figure 5.3.

Solving the elastic problem in FEM calculations, we get the strain tensor on every point of the mesh $\widetilde{\epsilon_{ij}}$. Let us focus on point P in the figure. This strain must be used to get the local value of the surface energy by applying eqn.(5.4), paying attention that in this equation, the strain values ϵ are the ones along the direction of the slab adopted $(\epsilon_{xx}, \epsilon_{yy})$, that not necessarily coincide with the strain along the {100} directions of the cell in the continuum calculation (that are the ones obtained by FEM) $(\widetilde{\epsilon_{ij}})$. The strain values to be used in this equation are obtained from the FEM ones simply by rotating the strain tensor [66] along the same directions of the slab of the facet used, for instance along the system of reference of each facet as shown in Fig.5.3, steps 1 and 2 in the figure.

[2] compare the results shown in sec.2.4.3 at page 48

This would be the correct surface energy value for the (105) ripple facet if the influence of the underlying Si substrate could be neglected—that is, if the height of the island surface at P was sufficiently far from the substrate. In other words, the "pure Ge (105)" surface energy extracted for point P of the ripple surface is the local value of $\gamma_\infty(105)$ as defined in Eq. (5.3). Given this connection, we re-write Eq. (5.3) for the strain and thickness dependent surface energy at the point P as:

$$\gamma(P) = [\gamma_0 - \gamma_\infty(\epsilon_P)] \cdot \exp(-B \cdot z_P) + \gamma_\infty(\epsilon_P) \ , \tag{5.5}$$

The strain state ϵ_P represents (ϵ_{xx}, ϵ_{yy}) evaluated at P.
Rigorously, the distance z_P from the silicon should be taken orthogonal to the surface considered, but, noting that the island we study are very shallow ones with an inclination angle equal to $\sim 7.97°$, here we take the vertical distance for sake of simplicity. This approximation is obviously not valid for steeper islands. Following the convention described in sec.2.5.5, this distance is expressed in units of (001) MLs.
As a simplifying assumption, the B parameter is assumed to be independent of strain state, as is taken from the fit of Eq. (5.3) to calculated atomistic results. Finally, γ_0 is set equal to the Si(105) surface energy. This is the step 3 of the figure.

This procedure is used to estimate the value of the surface energy at point P.
The effective energy of the facet to which P belongs is given by numerically integrating the energies of every point and dividing by the area of the facet considered:

$$\gamma(105)_{eff} = \frac{1}{A} \cdot \int \gamma(P) dA \tag{5.6}$$

And this is step 4 in the figure.

From this discussion, it is evident that this method is strictly valid for 100% Ge islands where no (or negligible) intermixing is happening. This hypotesis is very well fulfilled here since pure Ge is deposited at moderate low temperature and no Si from the substrate can spill out from the trenches[3] since the latter are not excavated by very shallow islands[4].

He we will adopt the hypotesis that the ripples are 100% Ge.

5.2.2 DFT and non-linear elastic field

As is shown below, Tersoff potential is not able to reproduce the smooth trend of the surface energy $\gamma(NGe)$ as the Ge thickness changes. For this reason, the used values of the surface energies will be the ab initio ones. For internal consistency, the elastic energy must be computed with the elastic constants deduced from the same parametrization, reported in Tab.2.2 at page 40, along with the misfit strain as deduced from the lattice constants reported there.

However, a comparison between elastic energy density derived from FEM with this constants for a biaxially-strained Ge(001) WL slightly differ from the ones obtained by a DFT-LDA calculation directly, see Fig.5.4, left panel.

[3] see discussion in Chapter 3

[4] compare the strain maps of Fig.2.7 at page 49 showing that the substrate in the case of the pyramid is less perturbed than the Dome or Barn case.

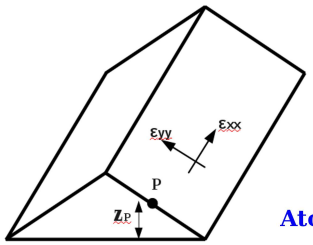

1) Rotation of strain tensor from FEM

FEM → $\widetilde{\epsilon_{ij}} \longrightarrow \epsilon_{xx}, \epsilon_{yy}$

2) Evaluation of surface energy from strain

Atomistic → $\gamma[\epsilon_{xx}(P), \epsilon_{yy}(P)] = \gamma_\infty(\epsilon_P)$

3) Value in P from distance

Extrapolation → $\gamma(P) = [\gamma_0 - \gamma_\infty(\epsilon_P)] \cdot \exp(-B \cdot z_P) + \gamma_\infty(\epsilon_P)$

4) Integration on the facet

FEM Integration → $\gamma(105)_{eff} = \frac{1}{A} \cdot \int \gamma(P) dA$

FIGURE 5.3: Multiscale method for evaluating the effective energy of (105) facets with both strain and distance dependence. See description in sec.5.2.1. z_P is the distance of point P from the Si interface, here we sketched the case of no WL under the ripple.

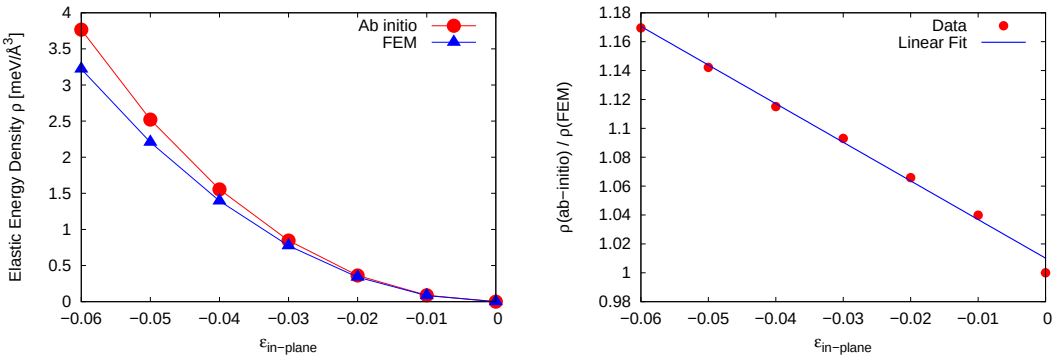

FIGURE 5.4: Studies of the elastic energy density as obtained for a biaxially strained Ge WL for DFT-LDA and FEM where the elastic constants of DFT are used. Left panel shows they differ, and this difference may be due to non-linear terms in DFT. We fit the ratio between the two values of the elastic field with eqn.(5.7), that is a good fit for $\epsilon_{in-plane} \sim -4\%$.

This discrepancy is due to non-linearity effects included in DFT, but excluded, by definition, from the continuum-based Linear Elasticity Theory of FEM.
We overcome this prolem by interpolating the two values with a polynomial function in order to get a "non-linear correction factor" for the WL. Throughout the present work, we make the ansatz that this function is valid for *every* shape and Ge concentration in the islands and the elastic energies reported are given by:

$$\rho_{non-lin} = \rho_{FEM} \cdot (a_{non-lin} \cdot \epsilon_{in-plane} + b_{non-lin}) \tag{5.7}$$

where $\epsilon_{in-plane} = 0.5 \cdot (\epsilon_{xx} + \epsilon_{yy})$ is the absolute value of the strain in plane (not %), $a_{non-lin} \simeq -2.67387$ and $b_{non-lin} \simeq 1.01013$.

5.3 Surface energy and the role of dimer tilting

In this section we compute the energies of the surfaces involved in this system.

We report the procedure and data of our estimation of the surface energies $\gamma(105)$ and $\gamma(1\ 1\ 10)$ both in DFT-LDA and Tersoff potential approach.

After describing the geometry of the reconstruction and the simulation cells to make the calculation more efficient (if not affordable at all), a careful check on the k-points density is performed leading to what we baptise "the bulk criterion".

By comparing the outcomes from DFT-LDA and Tersoff potential, we understand the non-negligible role played in stepped surfaces by the path of the dimer tilting in raising the energy of such surfaces, thus showing that the sole strain is not enough to assess the stability of surfaces when steps and dimers are present.

All the obtained data are reported in Table 5.1 at page 114.

5.3.1 Surface geometries

Here we outline the geometries of the cells adopted in the calculations.

From a general point of view, layers of atoms with **fixed atomic positions** are included in the calculation slabs in order to impose bulk coordinations within the slab and to prevent drift of the slabs in the z direction. As discussed in Ref.[148], the distance between any surface of interest and the fixed layers should be maximized to yield calculated surface energies applicable in bulk (semi-infinite) systems. Minimizing the total number of atoms in the calculation cell while maximizing this separation can be achieved with **asymetric slabs** which place fixed layers closer to the bottom surface of the slab than the top. In this construction the energy of a cell with top and bottom surface with different energies is:

$$E^{TOT} = N_{Si} \cdot \mu_{Si} + N_{Ge} \cdot \mu_{Ge} + (\gamma_T + \gamma_B) \cdot A \tag{5.8}$$

where γ_T (TOP) is the surface energy value of interest, and, as the bottom surface is present only to allow for periodic boundary conditions perpendicular to the surface, γ_B (BOTTOM) is not physically meaningful, A is the area of the surface.

Here the **chemical potentials** μ must be computed at the strain of interest considering also the Poisson relaxation (see discussion in Appendix C and sec.2.4.2). We take as the μ the minimum value of the energy per atom obtained by applying the strain in plane and changing the strain normal to the free surface. Since using the slab along the (105) and (1 1 10) surface may be very large[5], this procedure is performed on an 8-atoms conventional cell deformed in such a way that the strain tensor is the one imposed by the slab state we are considering.

The value of γ_B is computed in a separate calculation with a cell whose slab thickness is twice the distance from the bottom surface to the fixed layers in the asymetric slab, and is given as:

$$\gamma_B = \frac{E_{tot}^{sym} - N_{Si} \cdot \mu_{Si}}{2A} \tag{5.9}$$

[5] see discussion below

(105)-RS surface

The geometrical parameters of the As Cut (AC) surface can be extracted from Tab.2.3 at page 60. The reconstruction we adopt is the Rebonded-Step (RS) model, that is the established most stable one [81, 88, 145], that fits in a single AC cell in the xy plane. Our cell is reproduced in Fig.5.6 and consists of 52 (105) MLs along z direction (corresponding to the thickness of 2 AC cells) with both top and bottom surfaces reconstructed. The reconstructed cell contains 208 atoms.

Five fixed (105) MLs are located in the bottom third of the slab, i.e. the middle of the bottom AC cell, maximizing the thickness of relaxed atoms associated with the surface of interest at the top of the slab. These are coloured in green in Fig.5.6.

The bottom surface energy γ_B is computed from a symmetric cell (not shown) composed of 26 (105) layers along the z direction and reconstructed on both surfaces, where the fixed layers are kept the same as in the larger cell.

(1 1 10)-D_B surface

The (1 1 10) is the substrate in this system.

From Tab.2.3, we see that the As Cut cell contains 204 atoms.
The (1 1 10) surface is a vicinal of (001) whose miscut angle is $\sim 8.04°$. The experimental results shown in Fig.4.2-[b] predict the expected reconstruction for Si at this miscut angle to be a double step D_B. The need to create dimers on the terraces compels to double the cell size, thus reaching 408 atoms, that represent a very demanding calculation in an *ab initio* framework.

If both surfaces had to be reconstructed with the same idea as the (105), the number of atoms would double, making the calculation unaffordable. For this reason here we adopt a different geometry in order to use a single cell in z direction. In this case the bottom surface is composed of **fixed** atoms in the position of the AC cells, as shown in Fig.5.5. The reconstructed cell contains 91 (1 1 10) MLs where the bottom 13 (1 1 10) layers (equivalent to a thickness of ~ 3.5 Å) are kept fixed at their strained bulk positions. The total number of atoms is 360.

The bottom surface energy γ_B is computed independently from a symmetric cell made of 91 (1 1 10) MLs with top and bottom layers fixed at their (strained) bulk positions.

Here we use less than an integer cell along the z direction, but in sec.5.3.3 below we prove that this does not affect the results.

(001)-2xN DVL

Given that (1 1 10) surfaces are constructed of (001) terraces, we have also calculated the surface energy of the Ge on Si (001) surface ($\gamma^{(001)}_{Ge/Si}$). While the Ge and Si (001) surfaces have been widely studied with both DFT and Tersoff potential [76, 88, 93], we include calculations of the Ge on Si (001) surface to provide a fully consistent set of *ab initio* surface energy values calculated with uniform input parameters. We limit our present work to the (001) 2×8 dimer vacancy line (DVL) reconstruction, which has been shown by other authors [76, 93] as the stable structure of the Ge on Si wetting layer surface,

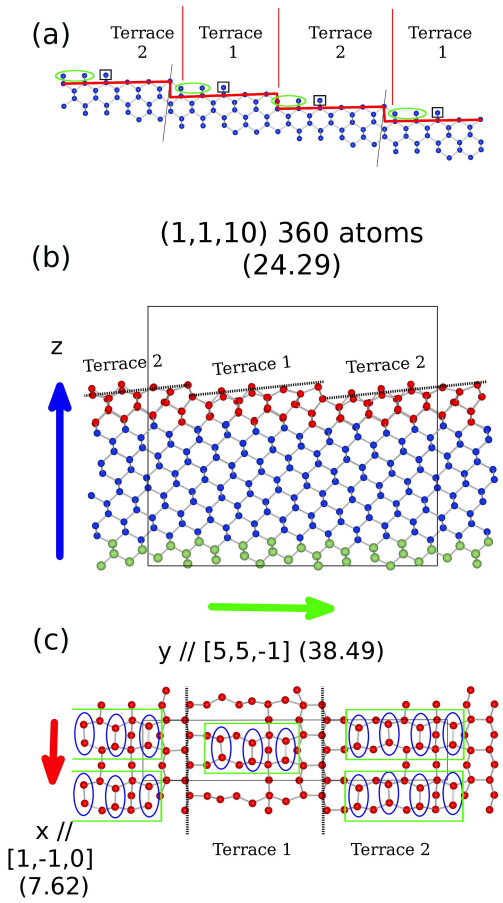

FIGURE 5.5: Geometry of (1 1 10) cell. (a) Side view of the as cut (1 1 10) surface with the Db step profile highlighted (red lines), the atoms in the green circles being rebonded to reproduce the rebonded step configuration, the atoms in the black squares being erased to create a double step. The two types of terraces are delimited by the vertical red lines. Panels (b,c) show the relaxed positions in the case of Ge/Si(1 1 10) cell with 4 ML (001) of Ge. The simulation cells is delimited by the black lines. In (c) the dotted vertical lines are at the Db step position and the dimers are encircled. In (b) instead red atoms are the Ge ones, blue atoms are Si, the Si fixed atoms are in green (light atoms). The numbers in brackets are the extension of the cells expressed in Å along x and y or the thickness of the atoms along z. The tip of z axis designate the top surface (energy γ_T), the other surface is the bottom one (energy γ_B). The figures are created by using the VESTA software [149].

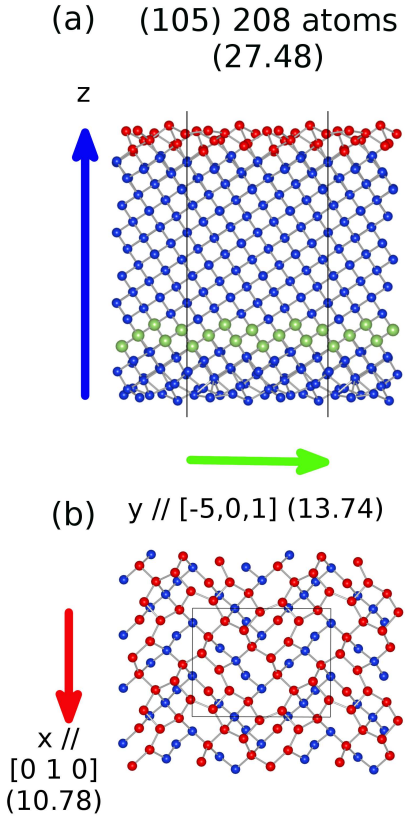

FIGURE 5.6: Geometry of the reconstructed Ge/Si(105) cell with 6 ML (105) of Ge. See Fig. 5.5 for the meaning of colors and quantity in parenthesis. (a) side view, (b) top view.

and focus our calculations on only Ge on Si slabs. The geometry of the cell for DFT calculations (not shown) is similar to that used for (1 1 10) surface calculations, and consists of an asymmetric slab with 15 (001) MLs free to relax and 5 (001) MLs at the bottom of the cell fixed in their bulk positions. Dimers are initialized in an alternating configuration similar to the tilts selected for the (1 1 10) surfaces described above (see Figure 5.12(a) for a side view), except where specifically noted.

5.3.2 Methods

The details of the simulation in the DFT-LDA approach and with Tersoff potential are the same as the reported in sec.2.3 at page 36.

The cells described in the previous subsection are the ones adopted for ab initio calculations. Since Tersoff potential is much less expensive than DFT, for Tersoff potential calculations cells with 306 or 260 layers [for (1 1 10) and (105) surfaces respectively] are used. The bottom 6 (1 1 10) and 28 (105) layers of these slabs are kept fixed, and E^{TOT} for the slabs is computed by excluding the energy of all fixed atoms. The slab thicknesses were selected to ensure that the last unfixed atoms above the fixed atoms have energies per atom equivalent to the energy per atom of bulk Ge or Si (that is, μ_{Ge} or μ_{Si}), as appropriate. While being aware that this method involves the use of very thick cells, we note that thinner slabs, similar to the *ab initio* case, could be adopted to guarantee a reasonable degree of convergence as well.

In both Tersoff and ab initio cells, the epilayer of Ge is put just on the top surface and a certain number of the topmost Si atoms (see below) are converted into Ge in order to have the desidered Ge thickness expressed in (001) MLs as described in sec.2.5.5 at page 65:

$$1 \text{ ML}(001) \simeq 5.049 \text{ ML}(1110) \simeq 2.549 \text{ ML}(105) \tag{5.10}$$

In the case of Ge/Si surfaces the chemical potential of Si is the unstrained one, whereas the one for Ge is compressed in x, y and subject to the Poisson effect along z.

The trend with strain is analyzed for pure Ge cells. In this case the applied strain includes the Poisson effect along z direction (the normal to the surface) in such a way that the fixed atoms in the cell are at the same strain state as the reference chemical potential μ computed from bulk cells.

The choice of the reciprocal space sampling is described in the next subsection.

5.3.3 k-point convergence of *ab initio* results

Accurate calculation of materials properties within the DFT framework requires a careful assessment of the convergence of calculated values with respect to input parameters. While parameters like energy cutoff for the planewave expansion of the electronic wavefunction are generally well-determined by the atom types included in the calculation, the grid of reciprocal space points over which the Kohn-Sham equations are discretely integrated depends on the geometry of the calculation cell. As we seek to compare calculations across varying cell geometries, care must be taken to assure relatively uniform convergence with

respect to k-space sampling. We have specifically explored this issue for the surfaces considered here.

Using the 8-atom diamond cubic bulk unit cell we considered Monkhorst-Pack (MP) meshes of special k points of increasing density. Meshes of 6×6×6 k-points or greater gave convergence of the total energy per atom to within 0.5 meV/atom. The 6×6×6 k-mesh is equivalent to a k-density of ~ 140 Å^3, a value we take as a baseline and call the "bulk criterion" for k-point convergence.

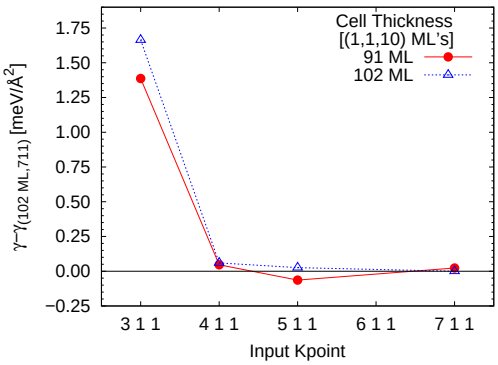

FIGURE 5.7: Convergence checks for the (1 1 10) cell as a function of thickness (91 MLs or 102 MLs of (1 1 10)) and input kpoints along x (abscissa). The values plotted are the difference of γ_T obtained for 4 MLs (001)-thick Ge epilayer and the one obtained for the best 7 1 1 kpoint, 102 MLs thickness. The values at Kpoint=4 1 1 are those predicted by the bulk criterion, and they are within 0.10 meV/Å^2 from that value.

Directly applying the bulk criterion to the (1 1 10) surface cells (see cell geometry in Fig. 5.5) implies a MP mesh of 4×1×1 k-points. Energy convergence for (1 1 10) slabs was checked by comparison with both higher and lower density k-meshes up to a 7×1×1 mesh, and by comparison 91- and 102-ML thick slabs[6] (where the 102-ML thick calculation cell is taller, and hence realizes a high k-point density in z). The results of this analysis for a 4 ML Ge epilayer-on-Si structure are reported in Figure 5.7 by plotting the deviation of the calculated value of $\gamma_{Ge/Si}^{(1110)}$ from the best converged calculation ("thick", 102 ML slab with 7×1×1 k-mesh). These results demonstrate that the 4×1×1 k-mesh as predicted by the bulk criterion converges the calculated surface energy to within 0.1 meV/Å^2. In addition, no appreciable variation is observed between the 102 and 91 ML-thick slabs, demonstrating that the 91-ML thick slab is thick enough to prevent interaction between the top and bottom surfaces.

Having validated the applicability of the bulk k-point convergence criterion on the (1 1 10) surface slabs, we apply the same criterion to both the (105) and (001) surface slabs. For the (105) calculation cells (shown in Figure 5.6), this gives a required MP k-mesh of 3×2×1. Similarly, for (001) surface slabs as considered in sec. 5.3.6 we have a required MP k-mesh of 1×4×1.

[6] corresponding to an entire AC cell

5.3.4 Calculated Surface Energies

We show first the results of DFT-LDA and then the Tersoff potential ones.

Ab Initio Results

(1 1 10)-Db Surface: The Ge and Si (1 1 10) surfaces are vicinal to the (001) surface and exhibit a miscut angle of $\sim 8.05^\circ$. Both the Ge and Si (1 1 10) surfaces consist of (001) terraces separated by atomically sharp steps, as depicted in Figure 5.5.

As a general phenomenon of $(11n)$ surfaces for even n in diamond cubic systems, alternate terraces differ in length [144]. In the case of (1 1 10) (see Fig. 5.5) Terrace 1 is ~ 1.7 nm long and has three dimers along with a rebonded step, while Terrace 2 is ~ 2.1 nm long with four dimers and a rebonded step. The detailed reconstruction adopted throughout our calculations is the one experimentally observed on silicon, where, for $\sim 8^\circ$ miscuts with respect to (001), double ML height "Db"-reconstructed steps are observed [86]. The full reconstructed calculation cell is shown in Fig. 5.5-(b,c) where the (001) surface dimers and rebond configuration of the Db steps are highlighted [85]. Note that care has been taken to construct initial atomic configurations with correct tilting of the terrace dimers, as the effect of dimer tilting significantly influences the calculated surface energies (see detailed discussion in sec. 5.3.6 below).

Figure 5.8 plots the values of $\gamma_{Ge/Si}^{(1110)}$ as a function of Ge on Si overlayer thickness for Ge on Si slabs with triangles. Given this reconstruction, the number of Ge atoms in these cells are 16, 36, 56 and 76 for a coverage of $\sim$ 1, 2, 3 and 4 ML(001) respectively. These same numbers hold for the Tersoff potential calculations reported below.

Materials parameters fit from Eq. (5.3) are reported in Table 5.1. The Ge overlayer surface energy decreases monotonically with increasing Ge thickness. This is consistent with previous results which have justified the decreasing surface energy on the basis of the lower energy of the Ge dangling bonds combined with the decreasing surface-induced elastic effects in the stiffer Si substrate [76, 150].

Figure 5.10-(c) plots the calculated values of $\gamma_{Ge}^{(1110)}$ as a function of strain state for pure Ge slabs. Biaxial compressive strain is clearly shown to stabilize the (1 1 10) surface, with $\gamma_{Ge}^{(1110)} = 66.4$ meV/Å^2 at $\epsilon_{ij} = 0\%$ (unstrained Ge) and $\gamma_{Ge}^{(1110)} = 61.3$ meV/Å^2 at a biaxially compressive strain of -4% (Ge strained to the Si lattice constant). Figure 5.10-(c) also shows that the surface lowers its energy when the Db steps are squeezed towards each other: specifically, for a fixed value of strain along the steps (here, ϵ_{xx}), the minimum (in the range analyzed) surface energy occurs at -4% strain along the direction perpendicular to the dimers (ϵ_{yy}). This results in a positive value of the surface stress τ_{yy}, as reported in Table 5.1. In contrast, for a fixed state of strain perpendicular to the dimers (ϵ_{yy}), a local maximum in surface energy is found between $\epsilon_{xx} = 0$ and -4%. The lowest calculated surface energy value occurs for $\epsilon_{xx} = 0$ and $\epsilon_{yy} = -4\%$ with $\gamma_{Ge}^{(1110)} = 60.6$ meV/Å^2.

(105)-RS Surface: The calculated values of $\gamma_{Ge/Si}^{(105)}$ as a function of Ge overlayer thickness for Ge on Si slabs are plotted as circles in Fig. 5.8. In this case the number of Ge atoms in the cells are 14, 22, 30 and 38 for a coverage of $\sim$ 1, 2, 3 and 4 ML(001)

respectively. These same values hold for the Tersoff potential calculations shown below as well.

The parameters of the fit to Eq. (5.3) are reported in Table 5.1. Compared to previous reported results of similar calculations by Liu *et al* [76, 93], we calculate a lower surface energy for Ge (105) overlayers by ~ 3 meV/Å^2. We attribute this discrepancy to differences in calculation settings, specifically: different k-mesh densities (in the plane of the surface, 1×1 versus 2×1 used here), different planewave cut-offs (163 eV versus 355 eV used here), as well as the use of thicker slabs in the present work.

Calculated values of $\gamma_{Ge}^{(105)}$ for Ge (105) surface energy as a function of applied strain are plotted in Fig. 5.10-(a). While it is clear that biaxial compressive strain strongly stabilizes the Ge (105) surface, as shown previously [88], Fig. 5.10-(a) also shows that uniaxial compressive strains also stabilize the Ge (105) surface. This is reflected in positive values of the surface stresses τ_{xx}, τ_{yy}, reported with other parameters of eqn.(5.4) in Table 5.1. In addition, it should be noted that the negative values for the surface elastic constants also contribute to a reduction in (105) surface energy under compression.

Consideration of both the (1 1 10) and (105) surface energies as a function of Ge overlayer thickness (see Fig. 5.8) shows that while the pure Si (1 1 10) and (105) surface energies are similar (90.0 vs 89.9 meV/Å^2), the (105) surface energy decreases more rapidly with increasing Ge overlayer thickness than the (1 1 10) surface energy. The present results indicate that at any non-trivial Ge overlayer thickness the (105) surface has lower absolute energy than the (1 1 10) surface. For Ge overlayer thicknesses greater than ~ 0.2 MLs, surface energy is in fact a driving force for the formation of (105) facets on (1 1 10) Si substrates. This is consistent with a number of recent experimental results showing both (i) the formation of (105) facets on (1 1 10) surfaces upon deposition of Ge [86, 129, 143, 151, 152, 153] and (ii) the stability against (105) facetting of the bare Si(1 1 10) surfaces.

(001) Surface: The calculated Ge on Si (001) surface energy is plotted in Fig. 5.8 as a function of Ge overlayer thickness. Fitting parameters for eqn.(5.3) are given in Table 5.1. The present results are quantitatively and qualitatively consistent with previous DFT calculations of Ge on Si overlayer DVL (001) surface energies [148], and show a monotonic decrease in surface energy with increasing overlayer thickness. Figure 5.8 shows that DFT predicts the (1 1 10) surface to have higher absolute energy than the (001) surface over the thickness range considered. These results are consistent with experimental observation of (001) surfaces stable against spontaneous facetting to (1 1 10).

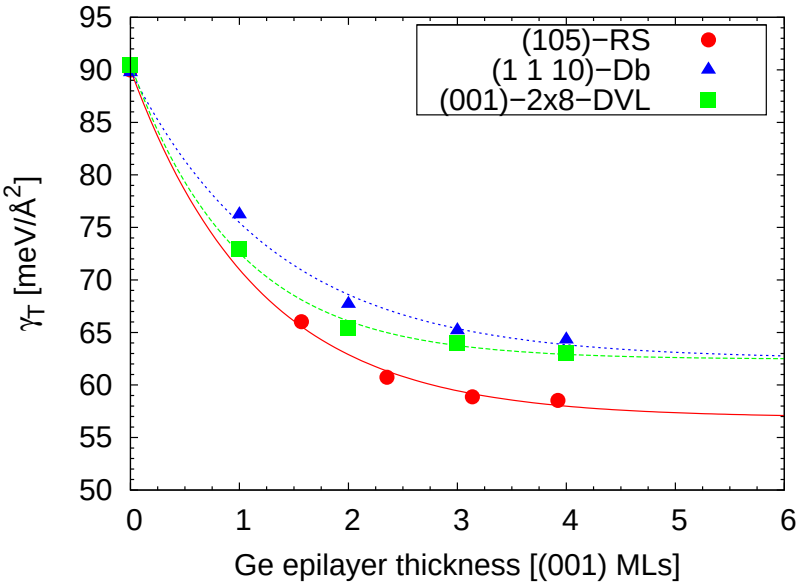

FIGURE 5.8: DFT-LDA results for γ_T(NGe), i.e. the dependence of the surface energy on the Ge epilayer thickness. Points are the direct calculations, lines the interpolation given by eqn (5.3). See discussion at Section 5.3.4.

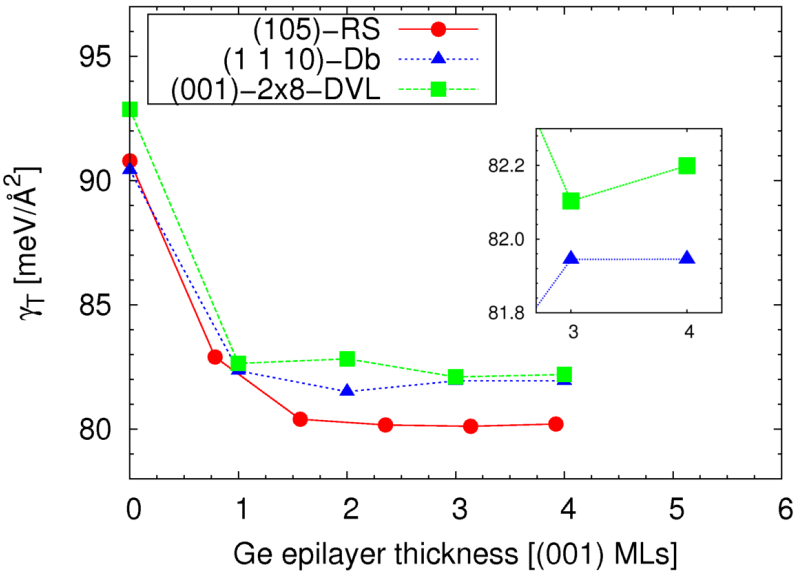

FIGURE 5.9: Tersoff potential results for γ_T as a function of the Ge epilayer thickness. The lines are just to guide the eye. Inset is a zoom at 3-4 ML Ge to show the slightly higher energy of (001) than (1 1 10). See discussion at Section 5.3.4.

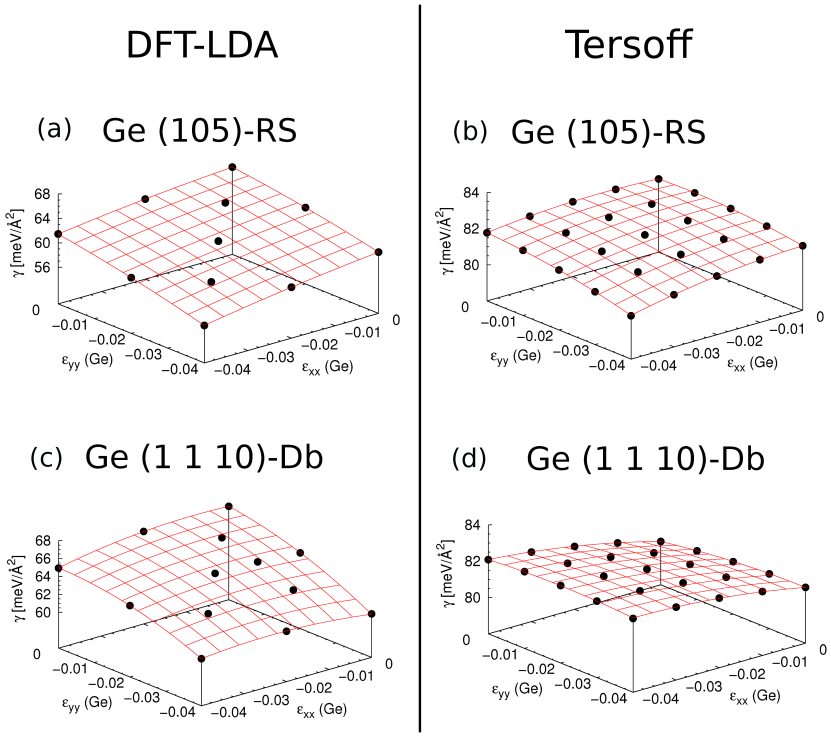

FIGURE 5.10: $\gamma_T(\epsilon_{xx}, \epsilon_{yy})$ of pure Ge cells as obtained from DFT-LDA (left) and from Tersoff potential (right). Black points are direct calculations, the red grid is the interpolation with eqn.(5.4). The strain is the one for Ge. The directions x and y are the same as in Figures 5.5 and 5.6. Here the γ are per unit deformed area. See text for details.

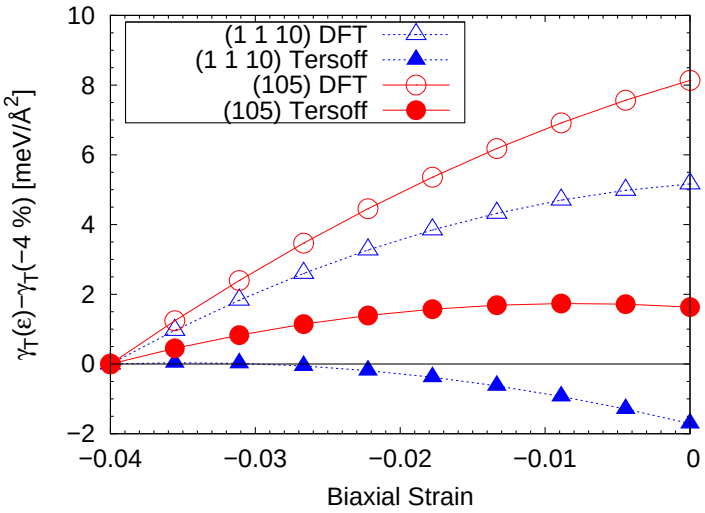

FIGURE 5.11: Biaxial strain ($\epsilon_{xx} = \epsilon_{yy}$) dependence of the surface energies as obtained by first principles approach (open symbols) and from Tersoff potential (close symbols) for both (1 1 10) surface (squares) and (105) (circles). The curves are those obtained by the fit reported in Table 5.1, the points are just sampling of the curves at a fixed interval and are aimed to guide the eye. Here the values of $\gamma_T(\epsilon)$ are plotted with respect to the value of the same curve at -4% strain in order to compare the derivative of each curve on the same scale. The relative position of the curves is therefore meaningless. For a discussion of results see Section 5.3.5.

Tersoff Potential Results

(1 1 10)-Db Surface: Figure 5.9 plots the Ge on Si surface energy as a function of overlayer thickness and shows that the Tersoff potential predicts almost no long-ranged decrease in surface energy after deposition of the first atomic layer of Ge. In addition, the Tersoff potential predicts a shallow local minimum in surface energy at an overlayer thickness of 2 (001) MLs [154].
Figure 5.10-(d) plots the Ge surface energy as a function of applied strain state as calculated with the Tersoff potential, and shows that the *unstrained* Ge (1 1 10) is predicted to have a lower surface energy (80.4 meV/Å^2) than the Ge (1 1 10) surface biaxially compressed to $\epsilon_{xx} = \epsilon_{yy} = -4\%$ (82.1 meV/Å^2 at -4%). The Tersoff potential predicts a local maximum in the Ge (1 1 10) surface energy at $\epsilon_{xx} = \epsilon_{yy} = -3.5\%$. Surface stress and surface elastic constants parameterizing eqn.(5.4) are given in Table 5.1.

(105)-RS Surface: The overlayer thickness dependent Ge (105) surface energy as calculated with the Tersoff potential is also plotted in Fig. 5.9. The Ge (105) surface energy decreases to a stable value after deposition of ~ 1.5 (001) MLs (001). Figure 5.10-(c) plots the strain-dependent Ge (105) surface energy, and, as with the Tersoff potential results for Ge (1 1 10), shows a local maximum in surface energy near $\epsilon_{xx} = \epsilon_{yy} = -1\%$. In contrast to the (1 1 10) Tersoff results, the Ge (105) surface energy for Ge biaxially compressed to the Si lattice constant is lower (80.4 meV/Å^2) than that calculated for the uncompressed state (82.1 meV/Å^2).

As is the case of first principles calculations, the pure Si value is almost degenerate as the one for (1 1 10) and the thick-Ge energies are lower than the one for (1 1 10), but the trend is not smooth, contrary to ab initio calculations.

(001) Surface: Figure 5.9 plots the Ge on Si (001) overlayer surface energy as a function of thickness as calculated from Tersoff potentials. The (001)-2x8-DVL and (1 1 10)-Db have close energies after thickness saturation is reached, but with the vicinal surface having slightly lower energy than the singular one.
The Tersoff results are consistent with previously published results using semi-empirical potentials [132, 150] on vicinal surface in Si and Ge. In these works the vicinal surfaces are found to have a lower energy than the singular (001) because the steps allow a larger strain relaxation of the biaxially compressed Ge layers. While results of Tersoff potential calculations show a lower absolute surface energy for Ge (1 1 10) overlayer surfaces with respect to (001), these results are still consistent with the absence of experimentally observed spontaneous faceting of Ge (001) overlayers to (1 1 10) because of the surface area correction accounting for the $\sim 8^\circ$ miscut of (1 1 10) relative to (001).

Parameter	DFT-LDA	Tersoff
a(Si-BULK)[Å]	5.390	5.4320
a(Ge-BULK)[Å]	5.624	5.6567
μ(Si-BULK)[eV/atom]	-5.976782	-4.62959
μ(Ge-BULK)[eV/atom]	-5.199221	-3.85060
μ(Ge/Si-1 1 10)[eV/atom]	-5.162938	-3.81370
μ(Ge/Si-105)[eV/atom]	-5.162474	-3.81318
μ(Ge/Si-001)[eV/atom]	-5.163430	-3.81397
γ Ge/Si(1 1 10) vs NGe	$\gamma_\infty \simeq 62.463$	X
	$B \simeq 0.75$	X
	$\gamma_0 \simeq 89.93$	X
γ Ge/Si(105) vs NGe	$\gamma_\infty \simeq 56.90$	X
	$B \simeq 0.85$	X
	$\gamma_0 \simeq 90.03$	X
γ Ge/Si(001) vs NGe	$\gamma_\infty \simeq 62.44$	X
	$B \simeq 1.02$	X
	$\gamma_0 \simeq 90.55$	X
γ Ge(1 1 10) vs strain	$\gamma_0 \simeq 66.428$	80.39
	$\tau_{xx} \simeq -24.765$	-66.389
	$\tau_{yy} \simeq 55.081$	-33.850
	$S_{xx} \simeq -1534.85$	-595.67
	$S_{yy} \simeq -2127.37$	-415.31
	$S_{xy} \simeq 1191.64$	-427.42
γ Ge(105) vs strain	$\gamma_0 \simeq 64.281$	82.05
	$\tau_{xx} \simeq 46.070$	-16.834
	$\tau_{yy} \simeq 72.195$	-9.898
	$S_{xx} \simeq -624.74$	-597.29
	$S_{yy} \simeq -850.99$	-547.89
	$S_{xy} \simeq -651.72$	-542.53

TABLE 5.1: All the parameters used and obtained in this work. The results of the interpolation of Figures 5.8 and 5.10 are reported both for dependence on strain and on deposition. It is noteworthy to remember that the values of surface energies as a function of strain for pure Ge cells and that the strain is referred to the Ge bulk lattice parameter, whereas in the case of Ge/Si surface as a function of NGe the germanium is strained according to the lattice mismatch with Si (i.e. $\sim 4\%$). Here strain is expressed in absolute numbers (not %). The different values of the μ along the directions analyzed reveal the slight difference due to the anisotropic elastic behaviour (constants) of the materials.

5.3.5 Comparison of *ab initio* and semiempirical results

Given the computational difficulty of treating arbitrary surface orientations in a fully *ab initio* context, semiempirical potentials, particularly the Tersoff potential, have been widely applied to calculate surface energies in the Ge/Si system. Even so, semiempirical potentials are known not to accurately address all physical effects that may influence surface energy and surface structure. This has been previously explored in terms of the electron transfer effects leading to sp^2 and sp^3 configured surface atoms and the resulting dimer tilting in (001)-based Ge and Si surfaces [155, 156, 157]. The present set of DFT and Tersoff potential results for (105), (1 1 10) and (001) Ge and Ge on Si overlayer surfaces provides an excellent dataset within which to compare the predictions of DFT and Tersoff potential calculations for surface energies in the Ge/Si system. As shown below, such comparison is instructive to highlight deviations due to electronic effects [88].

Comparison of the DFT and Tersoff predicted strain-dependent surface energies for pure Ge (105) and (1 1 10) surfaces (see Fig. 5.10) reveals a number of differences. While both DFT and Tersoff potential predict smooth variations in surface energy with applied strain, DFT predicts a significantly greater stabilization of both the Ge (1 1 10) and (105) surfaces with the application of compressive strain. This can be highlighted by considering surface energy as a function of biaxial strain alone, as plotted in Fig. 5.11. Of particular note is that while DFT predicts the zero strain state (Ge lattice constant) as the strain state at which both the (1 1 10) and (105) Ge surface have local maxima in surface energy, as noted above Tersoff potential calculations predict local maxima in surface energy at $\sim -3.5\%$ and $\sim -1\%$ biaxial strain for (105) and (1 1 10) surfaces, respectively. Moreover, Tersoff potential predicts that the zero strain state is in fact the local minimum in surface energy over the range of strain considered for the (1 1 10) Ge surface.

In addition, as discussed above, DFT calculations show a smooth exponential decrease in Ge surface energy with increasing Ge overlayer thickness for all considered surface orientations, suggesting the decay of a long-ranged interaction effect. This is in contrast with the results of Tersoff calculations, which suggest a rapid convergence to thick film behavior with deposition of the first 1-3 atomic layers. In the case of (1 1 10) surface, the appearance of a shallow local minimum in the Ge surface energy at $\sim$2 MLs of Ge is also in contrast to the monotonic relaxation of surface energy predicted by DFT calculations. In addition, while the bare Si (1 1 10) surface energies are quantitatively similar for DFT and Tersoff calculations, the relaxation of surface energy [that is, the value of B in eqn.(5.3)] is much greater in DFT-based results. This leads to DFT calculated surface energies for Ge (1 1 10) for thick Ge overlayers of $\sim$20 meV/Å^2 lower than Tersoff calculated values.

This same difference between first principles and Tersoff values at convergence is found in the trend of the (105) surface. Similarly to the case of (1 1 10) surface, also in this case the value of pure Si surfaces is comparable to the ab initio one, but for the (105) no local minimum is found. In both Tersoff and first principle results the value at convergence for the (105) is lower than the (1 1 10) one.

Finally we note that DFT calculations predict that Ge (1 1 10) overlayers have higher absolute surface energy than both Ge (001)-2x8-DVL and (105)-RS overlayers throughout the Ge deposition range analyzed. This is in contrast to the Tersoff potential results (see

Fig. 5.9), which predict that Ge (1 1 10) overlayers have lower absolute surface energy than the Ge (001)-2 $\times$ 8 DVL.

5.3.6 Role of Dimer Tilting

There is growing interest in continuum level models of nanostructure stability in heterogeneous systems. Such models generally balance changes in net surface energy against changes in strain energy. In order to yield accurate predictions of nanostructure stability, calculated surface energies employed in these models must exhibit at least qualitatively accurate relative values of surface energy among the various surfaces present in the nanostructure(s) of interest. The above comparison between DFT and Tersoff potential results for (1 1 10), (105) and (001) Ge and Ge on Si surfaces suggests that care should be taken when employing surface energies calculated using Tersoff potential and other semimepirical approaches [132] alone. This is particularly relevant with respect to the qualitatively different predictions for the magnitude and nature of the relaxation of surface energy with increasing overlayer thickness—particularly for the Ge on Si (105) surface. In addition, as the Tersoff potential is widely used to study stepped or vicinal surfaces in the Ge/Si system, the qualitatively different predictions of the relative stability of (1 1 10) and (001) Ge overlayers is also of particular importance.

In an effort to assess this last difference—that DFT predicts the (1 1 10) surface to have higher absolute energy than the (001) surface in contrast to current and previous Tersoff results—we have considered the potential role of experimentally observed (and DFT-predicted) tilted dimers on (001) surfaces.
Previous DFT calculations [148] predict that correct arrangements of alternating dimer tilts on (001) surface reduces the Si and/or Ge surface energy by ~ 2 meV/Å^2–a significant amount when comparing the (1 1 10) and (001) surface energies (see Figs. 5.8 and 5.10). Given that DFT predicts that the RS (105) is stable with respect to the (1 1 10) by $\sim$ 4 meV/Å^2 while Tersoff calculations predict that (1 1 10) is stable for thin enough films ($\leq$3 MLs), an error in surface energy due to treatment of tilt patterns on (001) terraces of (1 1 10) surfaces could be important.

As noted above, all (11n) vicinal surfaces in diamond cubic lattices with even n and terraces separated by double-height steps necessarily have inequivalent terraces. For the (1 1 10) surface, one terrace has 4 dimers and the second has 3 dimers. As dimer tilts have been shown to alternate along the rows of dimers, the terrace with an odd number of dimers cannot complete a tilt pattern. Moreover, the presence of rebonded steps likely influences the tilting of both the first and last dimers on each terrace. As dimer tilts are only predicted in DFT calculations, we hypothesize that step interference with dimer tilt patterns will represent a penalty against the (1 1 10) surface energy in DFT calculations that is absent in Tersoff calculations. Assuming equivalent treatment of other strain effects, and a second-order nature to all other electronic effects, this hypothesis would imply that Tersoff calculated (1 1 10) surfaces would be lower in energy relative to (001) surface energies than equivalent DFT calculated (1 1 10) vs (001) calculations. That is

$$\gamma_{(001)}^{Tersoff} - \gamma_{(1\ 1\ 10)}^{Tersoff} = \gamma_{(001)}^{DFT} - \gamma_{(1\ 1\ 10)}^{DFT} + \Delta_{Tilt}^{DFT} \tag{5.11}$$

for Δ_{Tilt}^{DFT} a positive value (energy penalty). Hence, a large enough Δ_{Tilt}^{DFT} could result in differing predictions for the relative stability of the (1 1 10) and (001) surfaces—e.g., as observed here for Ge on Si overlayers.

To directly address the hypothesis that dimer tilt patterns can play a key role in determining relative surface stability, and, in fact, explain the differing predictions for (1 1 10) versus (001) stability in the present work, we have used DFT to compare surfaces with tilted and un-tilted dimers. Results reported above were calculated using cells initially constructed with alternating dimer tilts and which retain alternating tilts upon structural relaxation.

In contrast, cells constructed with symmetric (flat) dimers relax to a local (but not global) energy minimum that retains flat dimers, as shown in Figure 5.12-(c) and (d). Comparison of the surface energy of tilted and un-tilted (1 1 10) and (001) Ge on Si surfaces shows that the predicted relative surface stability is *reversed* depending on the state of dimer tilts.

In the case of a 3 ML Ge overlayer, the (001) and (1 1 10) surfaces have surface energies of 64.0 and 65.2 meV/Å^2, respectively, if dimer tilting is allowed [structures in Figs. 5.12-(a) and (b)] and 71.2 and 67.42 meV/Å^2 if dimer tilting is *not* allowed [structures in Figs.5.12-(c) and (d)]. The un-tilted dimer DFT results are therefore consistent with the predictions of Tersoff potential, which, like other semi-empirical potentials, does not predict tilted dimer (001) reconstructions.

These results demonstrate that correct dimer tilt patterns are an essential factor in determining the relative stability of different surface orientations and structures. Such effects are likely at play on any Ge or Si surface that exhibits dimer bonds, and hence the potential for mixed arrangements of sp^2 and sp^3 configured surface atoms. Such surfaces include, e.g., surfaces vicinal to (001) and "rebonded step" structures like Ge (105).

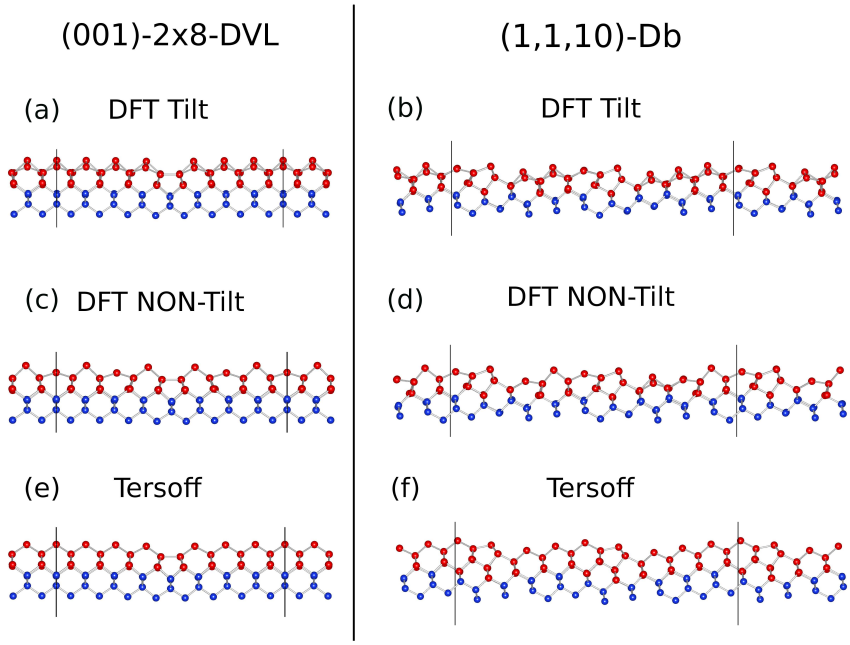

FIGURE 5.12: Relaxed side views of (001) and (1 1 10) surfaces with 3 ML(001) Ge deposited on it when tilting is allowed or not compared with the outcome of Tersoff potential. The repeated cell is delimited by the black vertical lines. See Section 5.3.6 for details.

5.4 Perfect faceting simplified

With these needed surface energies at hand, we can compare the energy of the two extremal situations sketched in Fig.5.13-(a): a WL and a perfect {105} faceting with no WL under the ripples, and for that purpose, we need to asses the effective surface energy of the (105) facets as explained in sec.5.2.1 as follows.

Leveraging the DFT calculated surface energies reported above, we first evaluate the in-plane components of the strain tensor, ϵ_{xx} and ϵ_{yy}, for the case of perfect {105} faceting on (1 1 10) (see Fig. 5.13) using elasticity theory solved using Finite Element Method (FEM) calculations. Since the ripples are infinite in the y direction (we use a 2D model) as defined in Fig. 5.13-(a), $\epsilon_{yy} \simeq -0.04$. The FEM calculated dependence of ϵ_{xx} on the position P along the ripple facets given in Fig 5.13-(b). Given the local ϵ_{xx} and ϵ_{yy} values, we can extract a local pure Ge (105) surface energy value from eqn.(5.4) as fit to calculated DFT surface energies as shown graphically in Fig. 5.13-(c). The curve as a function of epilayer thickness (i.e. distance from the Si substrate) that crosses this $\gamma_\infty(105)$ value is drawn in panel (d) in green.

Using the above procedure we have calculated the net surface energy of a perfectly facetted Ge {105} ripple structure on a Si(1 1 10) substrate and that of a flat Ge on Si(1 1 10) wetting layer with the same Ge volume. Figure 5.14 compares these net surface energies as a function of ripple width as expressed by base size. Note that these results show that surface energy alone is a driving force for the formation of Ge {105} ripples at all non-vanishingl ripple widths.

Following previous studies we may break the net formation energy of a three-dimensional nanostructure into volumetric (elastic energy), surface and edge energy contributions [30, 41]:

$$\Delta\text{E(PF-WL)} = \Delta E_{el} + \Delta E_S + \Delta E_{ed} \tag{5.12}$$

Simple geometrical arguments lead to the following relations for the three contributions in the case of perfectly facetted {105} ripples on (1 1 10):

$$\Delta E_{el} = LM \cdot \frac{h_R}{2} \cdot (\rho_R - \rho_t) \tag{5.13}$$

$$\Delta E_S = LM \cdot (\sec\varphi \cdot \gamma_R - \gamma_{WL}) \tag{5.14}$$

$$\Delta E_{ed} = LM \cdot \left(\frac{\Gamma_R}{b}\right) \tag{5.15}$$

Here LM is the total surface area covered in ripples with base widths b and height h_R (see Fig.5.13-(a)). The pure Ge ripples lie directly atop a Si(1 1 10) substrate. The elastic energy density of a uniform, flat, tetragonally strained WL is ρ_t, and ρ_R is the elastic energy density of Ge in a perfectly facetted ripple configuration. The angle between the ripple facet and the substrate is given by φ, and is 7.97° for (105) ripples on (1 1 10). Γ_R is the edge energy density *per ripple*.

As both the elastic energy density and net surface energy are both driving forces for the formation of ripple facetting, a positive value of Γ_R is required to reproduce the experimentally observed onset of ripple formation with finite Ge overlayer deposition. As

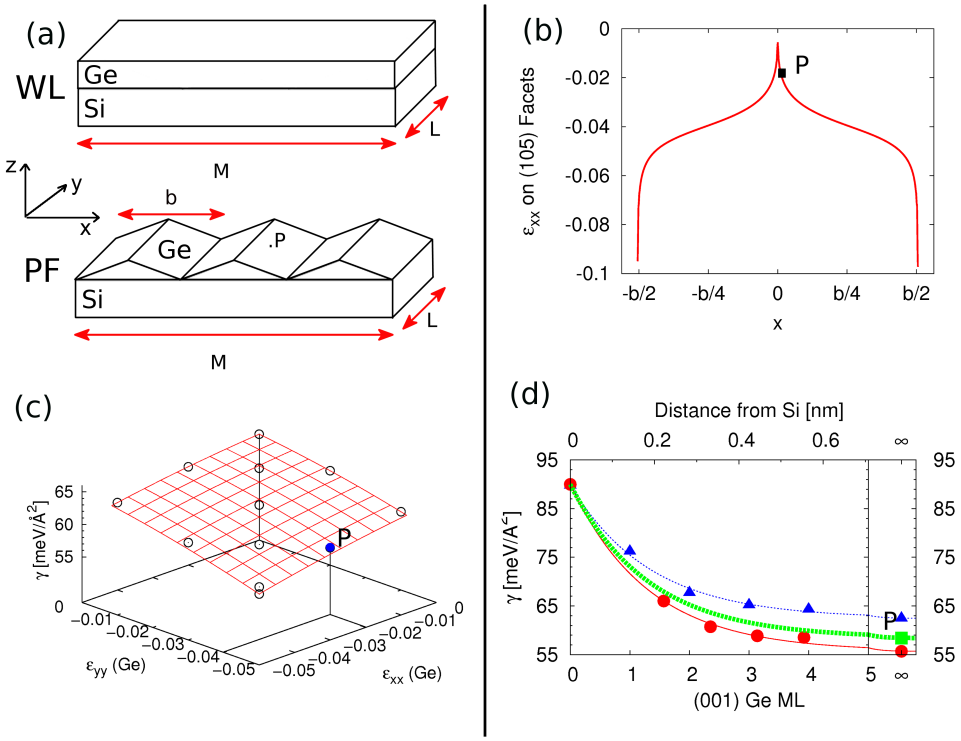

FIGURE 5.13: Multiscale approach to merge strain-dependent and Ge-thickness dependent surface energies discussed in sec.5.2.1. (a) Sketch of the systems whose stability is compared. A flat Wetting Layer (WL) is compared with a Perfect Faceting (PF) made up of pure Ge (105) adjacent ripples laying directly on the Si substrate. (b,c,d) Method used to model the strain and the deposition dependence of $\gamma(105)$ on ripples at the same time. (b) strain along x on a (105) facet in a PF. (c) From this strain, the corresponding value of γ_∞ is deduced from the uniaxial dependence of $\gamma(105)$. (d) Trends with the numbers of Ge ML's. Blue triangles are (1 1 10)-Db, red circles are (105) from slab calculations, the green line is the trend estrapolated from the point P (green square).

described in detail in the next section, based on experimental evidence we estimate Γ_R as ~ 370 meV/Å. Figure 5.15 shows $\Delta E\,(PF - WL)\,/(LM)$ as a function of Ge deposition in an interval of Γ_R of $\pm 10\%$ of this estimated value. The transition deposition nicely reproduce the experimental evidence as discussed at length in the next section where we also propose a kinetic path leading to the ripple formation.

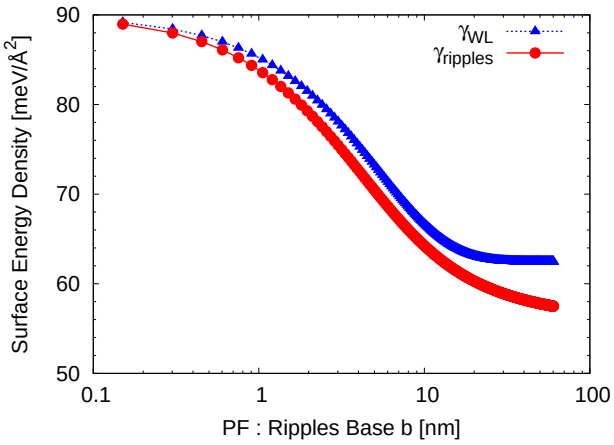

FIGURE 5.14: Effective (105) surface energies of ripples in a PF as compared with the (1 1 10)-WL as a function of the ripples base. In this case the base is linked to the Ge deposition as shown in Figure 5.8 top x-axis.

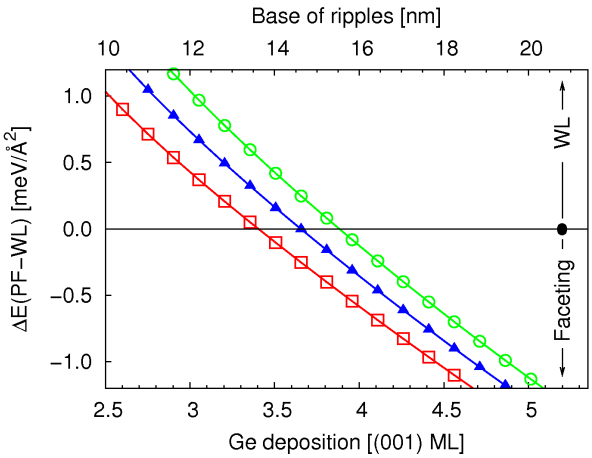

FIGURE 5.15: Stability of Perfect Faceting with respect to a flat Wetting Layer as a function of the Ge deposition. estimated through eqn (5.12). Central curve is for $\Gamma_R = 370$ meV/Å, the external ones for a variation of $\pm 10\%$ of this value. In the lower part the PF has lower energy, in the upper part the WL is stable.

5.5 Elongation of SK seeds and the 'actual' edge energy density

The previous section compares the energy of the initial and final situation experimentally observed where we put the unknown value of the edge energy density Γ of the order of ~ 370 meV/Å^2.

However in so doing we are neglecting the first stages of formation of isolated islands, like the one shown in Fig.5.1-(a). These islands form randomly on the substrate, have a finite extension and lay atop of a non-vanishing WL, qualities that make them similar to the typical Stranski-Krastanow islands on other substrates, such as the Si(001).

In this section we compute the stability of these isolated islands as a function of their parameters (WL thickness underneath and their base size). This detailed computation allows to extrapolate the unknown edge energy density Γ by comparing the theoretical outcomes with the experimental observations. This value turns out to be too high in comparison with previous estimations, however we also rationalize our result.

5.5.1 Model

Even though the SK seeds observed have a finite extension, they are rather elongated. Further, since a {105} pyramid cannot close on this substrate[7], it is not clear how to close these islands[8]. We simplify the treatment by considering an extremely-long ripple of length L and base b laying atop of a N ML(001)-thick WL, by adopting the 2D model sketched in Fig.5.16.

Our aim is to deduce the conditions (N and b) at which additional material prefers to attach to an existing ripple to make it elongate rather than creating WL. This condition is actually mathematically equivalent to compare the energy of the ripple condition and the same amount of material distributed on the substrate creating an additional layer of WL.

The corresponding total energy difference between these two configurations is calculated taking volumetric, surface and edge energy costs into account:

$$\Delta E_{TOT} = \Delta E_{vol} + \Delta E_{surf} + \Delta E_{edge} \tag{5.16}$$

Following the same reasoning as in sec.2.6, we can write the volumetric energy term per unit length as:

$$\frac{\Delta E_{vol}}{L} = \frac{b^2 \tan\varphi}{4} \cdot \left(\rho_R - \rho_{WL} + \frac{\gamma_{WL}^{1110}(N) - \gamma_{WL}^{1110}(N+1)}{h_{WL}} \right) \tag{5.17}$$

which contains:

1. the differences in elastic energy densities $\rho_R - \rho_{WL}$ between the ripple and the biaxially strained WL

[7] see discussion in sec.4.4.2, page 89

[8] although some evidences reveal some (001) facets, as discussed in sec.6.3 below

2. the energy cost for adding one ML on top of the WL instead of covering its Nth ML surface by the basal area of a ripple, expressed by the difference in γ_{WL}^{1110}, as described in sec.2.6 at page 67

The surface energy term can be written as

$$\frac{\Delta E_{surf}}{L} = b \cdot \left(\sec\varphi \cdot \gamma_R^{105} - \gamma_{WL}^{1110}(N)\right) \tag{5.18}$$

where γ_R^{105} is the effective surface energy of the $\{105\}$ ripple facets.

Finally, the edge energy term is given by

$$\frac{\Delta E_{edge}}{L} = 3\Gamma \tag{5.19}$$

where 3Γ is the triple edge energy at the top and two basal ripple facet intersections, that represent a discontinuity in the surfaces.

In simulating this system, a FEM calculation for each couple of variables (b,N) is needed. This holds not only to compute the effective surface energy of the $\{105\}$ facets with a numerical integration as shown in sec.5.2.1 by taking the distance of the WL into account, but also for the elastic term. Indeed, it was already shown in sec.2.4.3 at page 48 that, when the islands lay atop of a WL whose heigth is non-negligible in comparison to theirs, the elastic relaxation is non self-similar as a function of the islands' size. Since we have to look for small bases ($\sim 10nm$), we need to model each real situation inside our FEM code.

The elastic energy density in eqn.(5.17) are multiplied by the volume (in two dimensions, the area) of the ripple alone, since it is the energy of this system we are comparing to the WL. However, in assessing these energies, we need to take into account the compressive lobes the ripple is creating in the WL underneath as well.

One way to correctly estimate the term $\rho_R - \rho_{WL}$ is by comparing the total elastic energy W of the two cells sketched in Fig.5.16-(b). In this case we substract from the total elastic energy of the cell with the WL and ripple, the energy of a cell without the island, but with the same amount of WL. This difference accounts for the role played by the presence of the island. If we divide this quantity by the volume of the island itself, we get an energy density per unit volume of the ripple account for just its presence. Mathematically we can write it as:

$$\begin{aligned} \rho_R &= \frac{W_{R+WL} - W_{WL}}{V_R} = \frac{(V_R + V_{WL}) \cdot \rho_{Ge} - V_{WL} \cdot \rho_{WL}}{V_R} \\ &= \rho_{Ge} + \frac{V_{WL}}{V_R} \cdot (\rho_{Ge} - \rho_{WL}) \end{aligned} \tag{5.20}$$

where ρ_{Ge} is the elastic energy density per unit of stressor (Ge) in the cell with the island.

In the calculation we have fixed the cell size to 100 nm and the WL elastic energy is computed to be equal to[9] 1.624 meV/Å^3. In Fig.5.16-(c) the values of the difference

[9]Reminder: we are using ab initio elastic constants and non linear corrections here, so its value is different from the 1.4 meV/Å^3 for experimental elastic constants

$\rho_R - \rho_{WL}$ is reported for the case of M=100 nm and for different values of N.

The other term entering the volume contribution is the difference in WL surface energy divided by the thickness of 1 ML (001). This quantity is independent of the ripple base b and the ab initio results reported in the previous sections give the results:

$$\frac{\gamma_{WL}^{1110}(N) - \gamma_{WL}^{1110}(N+1)}{h_{WL}} \simeq \begin{cases} 4.889 \text{ meV/Å}^3 & (N=1) \\ 2.310 \text{ meV/Å}^3 & (N=2) \\ 1.412 \text{ meV/Å}^3 & (N=3) \\ 0.516 \text{ meV/Å}^3 & (N=4) \end{cases} \tag{5.21}$$

Comparing these values with the ones of $\Delta\rho$ in Fig.5.16-(c), we see that the former are $\sim$1 order of magnitude larger than the latter. This shows that the term in b^2 (giving the curvature of the curves) is actually dominated by surface energy terms. Consequently, the coefficient of b^2 is positive, leading to what we have called an Inverse Stranski-Krastanow in sec.2.6.

Also the pure surface energy term depend on the ripple base b and N via the effective 105 surface energy, where the distance from Si is the sum of the height of the point considered and the WL thickness underneath. The trend of the effective surface energy multiplied by the constant $\sec\varphi \simeq 1.0097$ is reported in Fig.5.16-(d), from which it is evident that the term ΔE_{surf} is negative, thus favouring the elongation and nucleation of the ripple.

5.5.2 Total energy and extrapolation of edge energy density

Once all the contributions have been estimated as in the previous subsection, we can put them together to predict the stability of the ripple.

The only missing term is the edge energy 3 Γ, whose an ab initio estimation is neither present, nor feasible. Typically this term is neglected in SK islands on other substrates like the (001) since the islands are growing self-similarly and the edge contribution to the total energy scales as $\sim V^{1/3}$, becoming negligibly small with respect to the volume and surface contributions for the typical volumes observed ($\sim 10^6\ nm^3$). However, in the ripples the edges extent is as long as the ripple itself, being thus far from negligible. But fortunately in this system its contribution is a constant, therefore we can evaluate the difference

$$\begin{aligned} \frac{\Delta E_{TOT}}{L} - 3\Gamma &= \frac{b^2 \tan\varphi}{4} \cdot \left[\rho_R - \rho_{WL} + \frac{\gamma_{WL}^{1110}(N) - \gamma_{WL}^{1110}(N+1)}{h_{WL}}\right] + \\ &+ b \cdot \left[\sec\varphi \cdot \gamma_R^{105} - \gamma_{WL}^{1110}(N)\right] \end{aligned} \tag{5.22}$$

for different values of N and b as reported in Fig.5.17 (left y axis values).

It is evident that in this system the trend of the energy is the same as the Inverse SK regime discussed in sec.2.6 at page 67.

As evident, the points at bases of some nm are at negative values of energy. This means that not only the the volumetric term but also the surface one pushes to create a ripple instead of a WL, contrary to what happens for SK islands like domes on (001). This

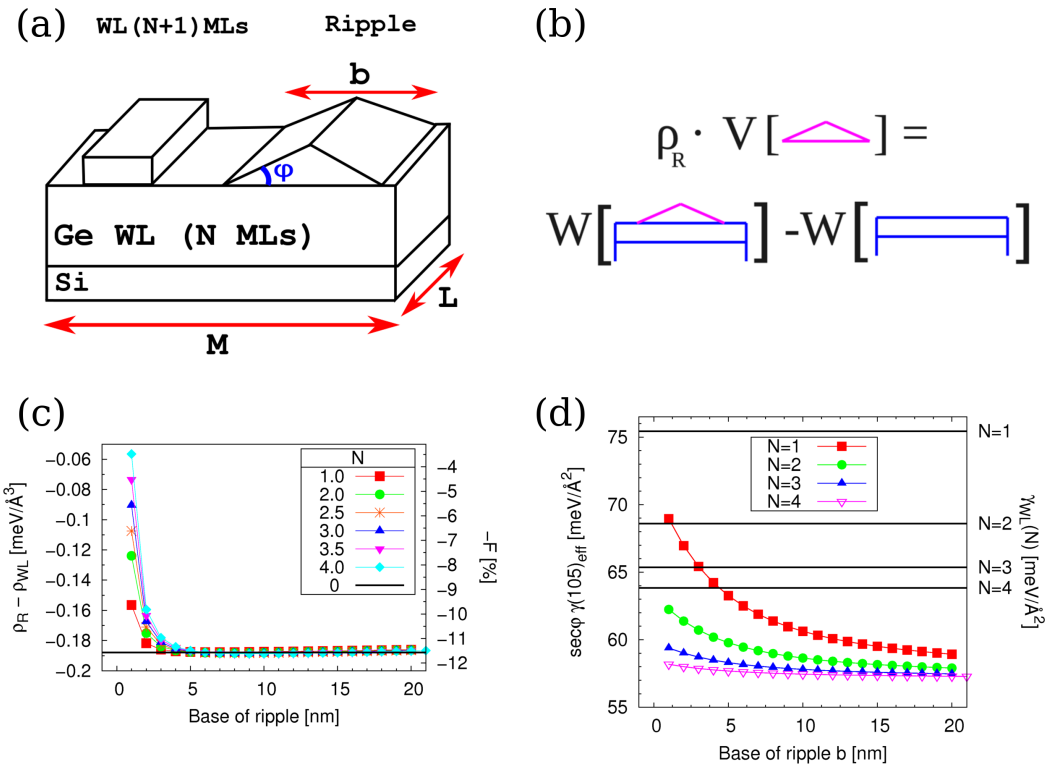

FIGURE 5.16: (a) Geometry of the model of the isolated SK seeds on Si(1 1 10) used in the calculation. We compare the energy of the ripple atop a N-ML thick WL (right) with the one of a (N+1)-ML thick WL (left). (b) Sketch of the method used to compute the elastic energy density per unit volume of the island ρ_R leading to eqn.(5.20). (c) Difference $\Delta\rho$ for different Ns for a fixed substrate of M=100 nm. (d) Surface energy contribution of the (105) surface $\sec\varphi\cdot\gamma(105)_{eff}$ (left y axis and coloured lines) compared to the values of $\gamma_{1110}(N)$ for various N (black horizontal lines). As evident, the (105) surface energy is much lower than the energy of the covered WL, so that $\Delta E_{Surf} < 0$, that is a driving force for ripple nucleation and elongation.

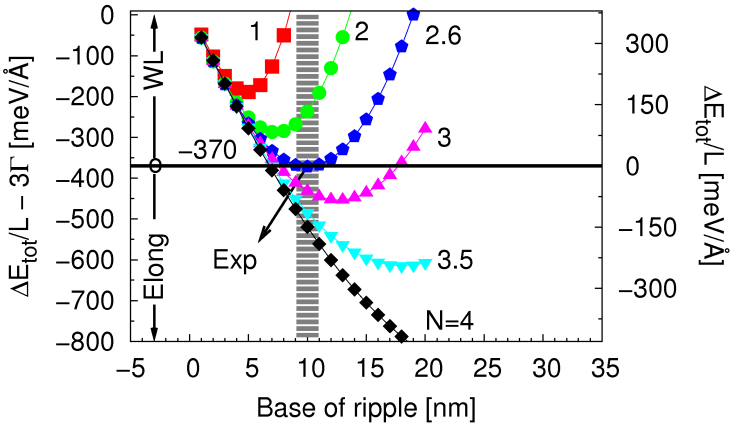

FIGURE 5.17: Energy difference $\Delta E_{TOT}/L - 3\Gamma = \Delta E_{vol}/L + \Delta E_{surf}/L$ calculated using Eqs.(5.17) and (5.18) between an infinitely long {105} facetted ripple on a N ML thick WL and the N+1 ML thick 2D WL with the same volume plotted as a function of ripple base b at different coverages N (left axis). The horizontal line represents the value of $E_{edge}/L = 3\Gamma = 370$ meV/Å obtained by comparison with experiments (vertical shaded bar). The right hand axis shows the total energy $\Delta E_{TOT}/L$ of the system using this value.

happens because the (1 1 10) surface energy is so high that the system prefers to cover it with a much less expensive surface as the (105).

Putting apart the problem that for a tiny island this method of dividing the energy into volumetric, surface and edge contribution is not valid anymore since there are just a few atoms with "bulk" properties, we can deduce that for small bases the sole opposing factor to the creation of the ripple lies in the edge term 3 Γ. Hence, we can take the experimental input of the observation of the first ripples and deduce backward from this an estimation of the value of the edge term needed to reproduce this observation.

The extrapolation of the values of b and N from experiments is not an easy task. Both because there are just a few measurements made for carefully-annealed samples we are aiming at simulating[10] and because the experimentally determined coverage D is not easily linked to the WL thickness under the ripples. Furthermore, in experiments a number of nearby ripples are observed, in contrast to the simplified model we are using here.

A careful analysis estimates the material stored in the ripples as ~ 1 ML and the base b of the first finite-sized ripples is ~ 10 nm observed at a deposition equal to ~ 3.6 ML.

If we make the assumption that the ripples, when observed, are of finite extension because at equilibrium with the WL and the adatoms have just a small gain in energy in forming an elongated ripple, then we can put

$$\Delta E_{TOT} = 0 \text{ (Ripples in equilibrium with the WL)}$$

Hence, the value of the horizontal cross of the base band represent the value of -3Γ. Further, if we suppose that the ripples lie on the minima of the curves since all of them have roughly the same base, then we deduce that the edge energy amounts to approximately:

$$\boxed{3\Gamma \sim 370 \text{ meV/Å}} \tag{5.23}$$

The total energy value and the stability region of the ripple and WL in the case of $3\Gamma = 370$ meV/Å is reported in Fig.5.17.

[10] see discussion at sec.5.2

5.5.3 Rationalization of the edge energy found

The edge energy just deduced is more than one order of magnitude higher than the one estimated by the use of Tersoff potential in literature studies on similar objects [42], see Fig.5.18-(a), that predicts $\Gamma \sim 10$ meV/Å. However in that study particular care has been used to properly rebond the atoms on the edges in order to minimize the number of dangling bonds. In this way the built edges are extremely sharp and ordered.

On the contrary, the top edges of the ripples we are considering are extremely disordered and rough, with several adatoms attached to them, Fig.5.18-(b). The junction between the two {105} facets resembles the tile on a roof, i.e. it has a certain, non-negligible extension.

This observation helps to explain the high value of the edge energy we find. Indeed, we model the ripple as sketched in Fig.5.18-(c,right sketch): pure (105)-RS facets with ideal, infinitely-sharp edges at the top. Instead, the actual ripple structure includes perfect (105)-RS facets at the bottom of the ripple itself, an edge at the top, but in between the two regions is an extended (~ 3 nm wide) surface with disordered structure, whose surface energy is unknown (Fig.5.18-(c,left sketch)). In our modeling, therefore, we are attributing to a linear energy (the edge one) also a contribution from this disordered surface.

From the STM images, it appears that just the top edge is rough, whereas the two bottom ones are rather sharp, suggesting that the value found can be entirely attributed to the top edge. This anomaly can be explained as a consequence of the ripple formation, indeed experimental results [143] show that the {105} facets form from the bottom and join at the top, creating a rough junction. The very same mechanism and a very similar edge structure are observed for the {105} pyramids on Si(001) [5], Fig.5.18-(d).

This observation suggests that the edge energy found here may have a valency in other Ge/Si islands, not only limited to the ripple case. In this way, we exploited the peculiarities of the ripples (extended edges) to deduce this so-far unknown value and can apply it to other systems.

From these observations we can also give an estimation of the unknown energy of the disordered surface adjacent to the edge, as follows. Taking the model depicted in Fig.5.18-(c) as a reference, we have:

- B = base of the ripple
- b = base of the triangle at the top of the ripple that has a higher surface energy
- γ_1 = standard surface energy of the well-rebonded reconstruction (105)-RS
- γ_2 = higher surface energy in the upper triangle $\gamma_2 > \gamma_1$
- $\varphi \simeq 7.97°$ = inclination of ripples
- Γ_{ideal} = the 'standard' edge energy (if the reconstruction is good enough, well done) ~ 10 meV/Å
- Γ_{eff} = the effective edge energy to be attributed to the edge if the surface energy is supposed to be γ_1 on the whole surface

In the two cases we have the following energy:

$$E_1 = (B-b)\cdot\sec\theta\cdot\gamma_1 + b\cdot\sec\theta\cdot\gamma_2 + \Gamma_{ideal} \quad (5.24)$$

$$E_2 = B\cdot\sec\theta\cdot\gamma_1 + \Gamma_{eff} \quad (5.25)$$

By imposing $E_1 = E_2$, we get:

$$\boxed{\Gamma_{eff} = \Gamma_{ideal} + b\cdot\sec\varphi\cdot(\gamma_2-\gamma_1)} \quad (5.26)$$

We can give an estimation of the extra energy of the disordered surface with repsect to the ordered one as:

$$\gamma_2-\gamma_1 = \frac{\Gamma_{eff}-\Gamma_{ideal}}{b\cdot\sec\varphi} \simeq \frac{(370-10)meV/\mathring{A}}{30\mathring{A}\cdot 1.009} \simeq 12 \text{ meV/Å}^2 \quad (5.27)$$

where the base of the disordered region b is estimated from the images to be ~ 3 nm.

This difference in γ is not an unreasonable number considering that the difference in energy between the RS reconstruction and the (very ordered) PD is ~ 8 meV/Å^2 at a strain -4% [88].

5.5.4 Alloy and a surface-driven nucleation regime

The results reported above refer to the case where both the WL and the ripples are made of pure Ge.

As already stated, this is a reasonable assumption in this shallow islands grown at low temperature, as directly measured in literature results [158, 159]. However here we check what happens if a small amount of intermixing is introduced.

In handling intermixed systems the method used so far is not strictly appliable anymore. Indeed in an intermixed system the Si and Ge atoms are expected to mix together even at the surface, apart from the very top layer where a pure Ge "floating layer" is observed and predicted[11]. Since performing ab initio simulations for every level of intermixing is an extremely demanding task, here we adopt an approximate approach.

Exploiting the existence of the floating layer, we make the hypothesis that the surface energies are the same as the one obtained from the pure Ge case, whereas the only term influenced by the concentration is the difference $\rho_R - \rho_{WL}$ where both the WL and the ripple are assumed to have an equal content of Ge. Reasonably, this approach is approximately valid for rather high Ge content, as is expected to be our case.

The results for the Ge content equal to 80% and 60% are reported in Fig.5.19.
As evident, the values change slightly but the trends remains the same as well as the position of the minimum pf the curve N=2.6 ML. The trend is preserved because the only parameters that change in this treatment is the $\Delta\rho$. This difference for the alloy is smaller than the pure Ge case. Since, as stated before, the volumetric term (the coefficient of b^2) is dominated by $\Delta\gamma^{1110}_{WL}$ rather than the $\Delta\rho$, where the latter is roughly one order of magnitude smaller than the former. Thus the variation due to the alloy is minimal.

[11] see Chapter 1

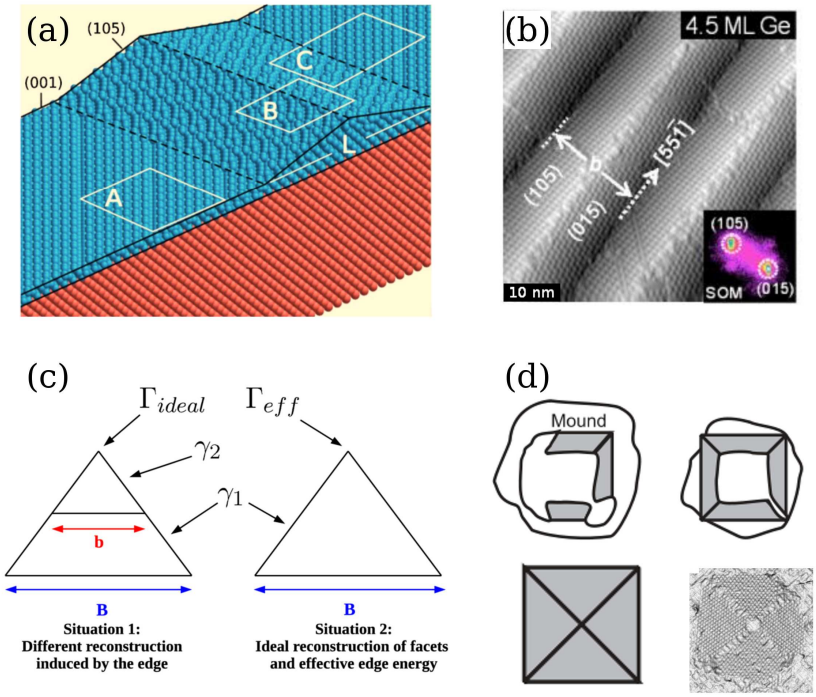

FIGURE 5.18: Rationalization of the edge energy value. (a) Structure simulated in Ref.[42] there analyzed with Tersoff potential, where the energy of the very ordered edge is found to be $\sim$ 10 meV/Å. (b) STM image of our ripples, showing a disordered structure of the top edge, very different from the one simulated in (a). (c) Models to explain the high value of the edge energy we find, since we include in our idealized model of situation 2, the surface contribution as skecthed in the situation 1. (d) Models and STM image of the formation of a {105} pyramid on Si(001), taken from Ref.[5]. Here it is shown that the pyramids (as our ripples) are formed from the bottom and the facets join at the top. The disordered structure of the edges on the pyramid resembles the one found in the ripples, suggesting that the edge energy we find may be valid even in standard SK islands.

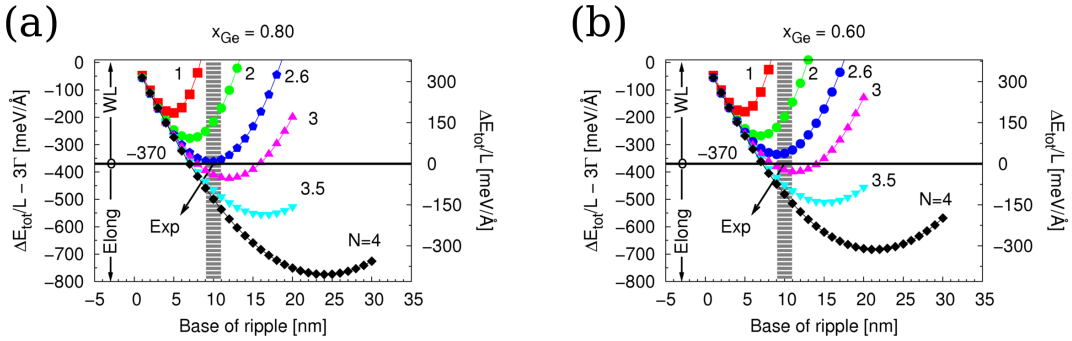

FIGURE 5.19: SK seeds: Alloys. Ge 80% (a) and 60% (b). The effect of alloying in our treatment is just to lift the curves slightly but does not modify their shape, nor the estimation of 3Γ.

For this reason this transition could be called a "surface-driven nucleation regime", as the title of this chapter suggests.

Our estimation of the edge term 3Γ is practically unaltered even in the case of an alloy.

5.6 Dynamical path to perfect faceting: the Wave Model

So far we have analyzed the energetics of a single ripple atop of a N-ML thick WL, we still have to explain (or at least model) a path leading to the formation of the observed faceting.

Thanks to its stability upon annealing, we are allowed to make the hypothesis that the faceting is at least a local minimum in the internal energy of the system. Thus, we describe the kinetic path leading to the faceting as a minimization of energy.

As evident from RHEED data of Fig.5.2, the transition from unfaceted to faceted substrate happens abruptly. This urges to look for a path involving just local rearrangement of material, since longer diffusion length would require longer relaxation times. This local rearrangement should, however, allow the observed uniformity on a long scale.

From our DFT results, we already know that the (105) surface energy is much smaller than the (1 1 10) one. This suggests that the driving force for this transition must be the covering of the (1 1 10) surface with some (105) facets. By taking Fig.5.20-(a) as a reference, we can imagine a wave-like lateral ripple multiplication process in which from each isolated ripple studied in the previous sections, secondary satellite ripples are created by downward excavation of the wetting layer at the ripple edges. The resulting lateral motion of material rapidly transforms the 2D film to a completely {105} facetted WL.

This calculation is performed by taking two cells 100 nm wide and comparing the volumetric, surface and edge energies in the case of the first generation satellites of different sizes with respect to the case of no satellite, where the volume of Ge is the same in both cells, since the satellites are made with the material extracted from the WL.

The difference in energy between the condition with satellites (middle condition in panel a) and the one without satellites (top condition in panel a) is shown in Fig.5.20-(b) as a function of the measurable satellite base b_2 for the case of the base of the precursor $b_1 = 10$ nm for the edge energy $3\Gamma = 370$ meV/Å. Here the edge energy is the sole factor opposing the formation of satellites, since a triangle shaped structure also relaxes strain better than a flat WL. The edge energy is opposing the satellite formation because the satellites creates additional edges wrt to case of no satellites, but since their number is independent on the base b_2, it causes just a rigid upward shift of the curves.

Here the curve corresponding to the value of N for the isolated ripple formation (N=2.6 ML) crosses the value $\Delta E = 0$ in its minimum. This means that the two conditions of elongation of the isolated ripple and the formation of the wave are **almost concomitant**, a fact that is consistent with the experimental observations, since no infinitely-elongated isolated ripple is observed before the onset of the faceting.

The reason why these curves have a minimum, i.e. they bend upwards for a certain b_2 on, lays in the surface term alone. Indeed the excavation of the WL responsible for the satellites growth makes the facets of the ripples nearer and nearer to the Si substrate, thus

increasing their surface energy. This has also the effect that the values of b_2 corresponding to the minima of the curves is independent on the value of the precursor's base b (not shown).

It is noteworthy to see that the residual WL thickness under the ripple[12] when the system reaches the condition correspondent to the minimum is less than 1 ML, as experiments reveal. Further, the base b_2 of the minimum corresponds to the measured one even for the samples at higher deposition. For instance, for a transformed material of N = 4.5 ML we see that the system smoothly evolves to satellite ripples with preferred base $b_2 \sim 15$ nm leaving a residual WL thickness of 0.75 ML underneath.

The fact that the preferred base b_2 is independent of the precursor's base guarantees a very high degree of uniformity in the satellites, being insensitive to oscillations in the size of the precursor due, e.g., to thermal fluctuations. This also allows to have satellites of the same base b_2 for the second and any further generation of satellites themselves, till the entire substrate is faceted (Fig.5.20-(a, bottom)).

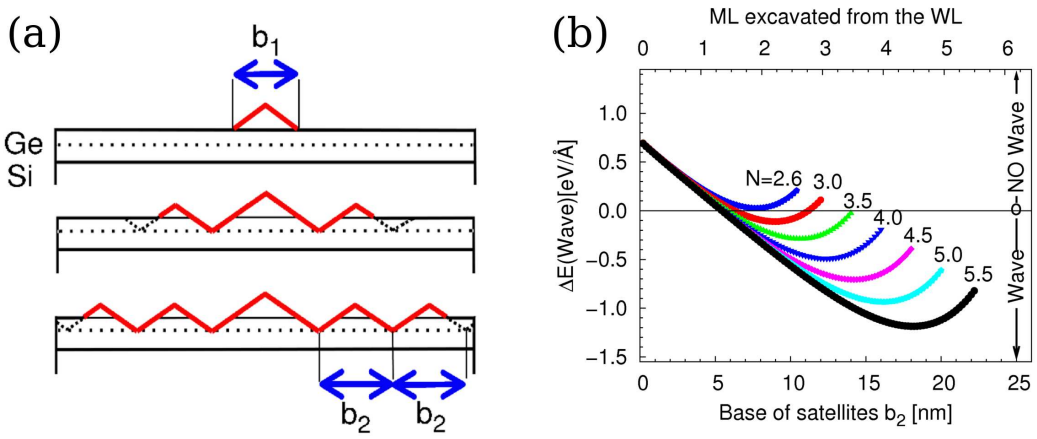

FIGURE 5.20: (a) Wave propagation mechanism starting from an isolated ripple (top) on a WL, creating first two asymmetric satellites (middle) with satellite base b_2, finally leading to full faceting (bottom). (b) Energy difference between the configurations of the single ripple $b_1 = 10$ nm (as experimentally observed) and the ripple with two satellite ripples as a function of the final satellite base b_2 for the different values of N and $3\Gamma = 370$ meV/Å.

[12] deducible from the values of the upper scale in Fig.5.20-(b)

5.7 Summary and conclusions

Summarizing, in this chapter we have:

- deduced the uniaxial strain dependence of the (105)-RS surface in both Tersoff potential and DFT-LDA approach
- depicted a method to deduce the value of the surface energy from the strain field computed in FEM
- proven that the interaction of the dimer tilting pattern with the double steps play a non-negligible role in the surface energy, raising the value one would obtain from an analysis involving the strain field alone, showing thus that an ab initio treatment is needed (from the results of 1 1 10 surface)
- deduced (and proven) the smooth decrease of the surface energy with increasing thickness of the Ge epilayer
- depicted a method to merge the trend with strain and epilayer thickness together in a multiscale method
- described a method to compute the elastic energy density properly in a non-self-similar growth model (ripple + WL)
- obtained the energy of "actual" edges Γ that is ~ 1 order of magnitude higher than expected from simple calculations because of the disordered geometry of the edge and discussed about its extension to other systems than the hereby analyzed ripples
- obtained and described a nucleation regime governed mostly by the surface energy term rather than the volumetric ones
- depicted and quantified a model for the formation of faceting starting from an isolated ripple involving just local rearrangement of material (the "wave model") leading to results in accordance with experiments

In conclusion, our experimental and theoretical results suggests that the facetted film corresponds to a new type of wetting layer rather than a SK configuration. Therefore, the usual monotone evolution of SK seeds to 3D islands during the initial deposition stages is strongly altered on the vicinal (1 1 10) surface. Such an anomaly should be present also in other systems whenever peculiar shallow facets displaying geometric degeneracy and low surface energy densities compared to the substrate are present.

Eventually, at higher coverages and temperatures, a transition to islands with steeper side facets (analogous to the domes on 001 substrate) will occur, as the energetics for larger islands is dominated by elastic effects.

This transition is described in the next chapter.

6

Ge/Si(1 1 10): Elastic-driven transition from faceting to dome

"Evolution is the key"
adapted from
Herbert Spencer & Charles Darwin

In this chapter we study the observed phase transition on Si(1 1 10) from the faceted structure described in the previous chapter to steeper islands, analogous to the transition from pyramids to domes. We study that for differently diluted SiGe alloy $Si_{1-x}Ge_x$.

We describe the experimental observations and the stability phase diagram found. After presenting a global transition model and its results, we highlight its shortcomings.

A more detailed model involving a transition involving an intermediate-step island that we call "Tadpole" or "Fish" is described after a careful experimental observation of the transition.

All the results reported here are obtained with our collaboration with experimental groups in Linz, Austria.

6.1 Further deposition: annealing-driven transition to domes

As explained in chapter 1, upon increasing deposition of Ge the islands undergo a shape deformation from shallow slopes (the case of pyramids on 001 substrates) to steeper ones (domes on 001) where the larger amount of extra-surface allows a better strain relaxation.

Since the ripples observed on Si(1 1 10) are the degenerate version of the pyramids, the same evolution should be expected here.

However the experimental conditions are crucial in determining the actual possibility of transition. An example of this is reported in Ref.[160], where up to 1250 ML of a 20% Ge alloy are deposited onto the Si(1 1 10) at 650°C at a rate of 0.012 nm/sec $\simeq$ 5.14 ML/min and the faceted structure is preserved with a thick WL underneath if annealing is not performed. Even though an explanation in terms of the stability of the concave

intersection can be called out due to the strain-dependent (105) surface energy [160], here the role of the kinetic limitations during growth is the predominant one [160].

Urged by this reasoning, new measurements are performed after annealing the samples. In particular, Si (1 1 10) substrates were cut into 9×9 mm^2 pieces, and prepared for solid source molecular beam epitaxy (MBE) by device-grade chemical pre-cleaning with a final HF treatment. The samples were then immediately introduced into either an MBE system equipped with e-beam evaporators for Si and Ge, or into a multi-chamber Si/Ge STM system, the latter being equipped with a Si e-beam evaporator, a Ge effusion cell and an STM.

A 40 nm thick Si buffer was then grown at 450-520°C, followed by mild annealing at 600°C for 5 minutes. This procedure results in flat surfaces free of step bunches or surface defects. $Si_{1-x}Ge_x$ layers with compositions of x = 0.2, 0.25, 0.3 were then deposited with growth rates of 0.1 – 0.2 nm/min (0.71–1.43 ML/min) at a substrate temperature of 650°C. The samples then underwent to an additional in-situ annealing step at the growth temperature for 15 min before being transferred to a scanning probe microscope. This measure ensures close-to-equilibrium conditions, that is the only one the energetic approach we are going to develop can predict.

The surface obtained after annealing for low Ge concentration (x= 25% and 30% Ge) are shown in Fig.6.1-(a-f). In these images the surface seems to transit from a faceted one to a perfect array of domes. This confirms that when the kinetic limitations can be overcome by thermal energy supply, the thermodynamically stable islands are the steep domes. This means that the ripples are as stable as the pyramids on 001, but their geometry is an hindrance to the diffusion of adatoms and evolution of limited-sized islands as domes from such elonged structures.

A systematic analysis is carried out on this transition with the aim to draw the phase diagram as a function of the Ge concentration. For completeness, even higher Ge concentration (50% and 100% Ge) are analyzed in Fig.6.1-(g-m). The resulting diagram is reported in Fig.6.2, which is extracted from the experiments as a function of the Ge concentration x.

As evident, the pure ripple and island phase regions are separated by a coexistence area that enlarges for smaller Ge content. This effect can be due to kinetic effects as well, since the diffusion on a Si-rich surface is slower because of the more rigid Ge-Si bond with respect to the Si-Si one[1].

[1] see chapter 1

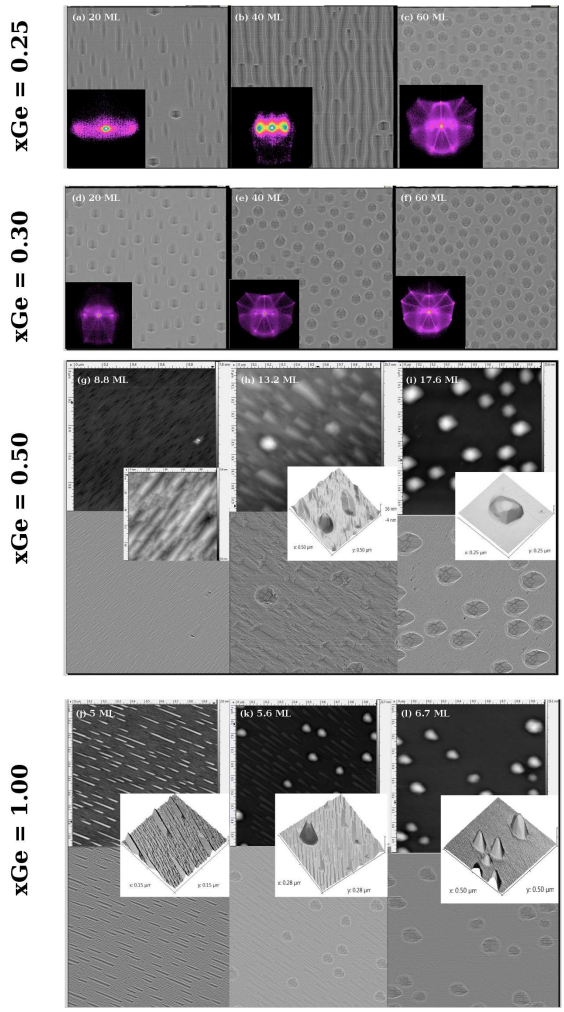

FIGURE 6.1: Onset of Domes: annealed samples. xGe = 0.25 and 0.30: AFM images 5x5 μm^2, laplacian view and surface orientation map. xGe = 0.50 and 1.00: STM images 1x1 μm^2, top view, laplacian view and 3D rendering. (Courtesy of Dr. Gang Chen and prof. Springholz, Joannes Kepler University, Linz)

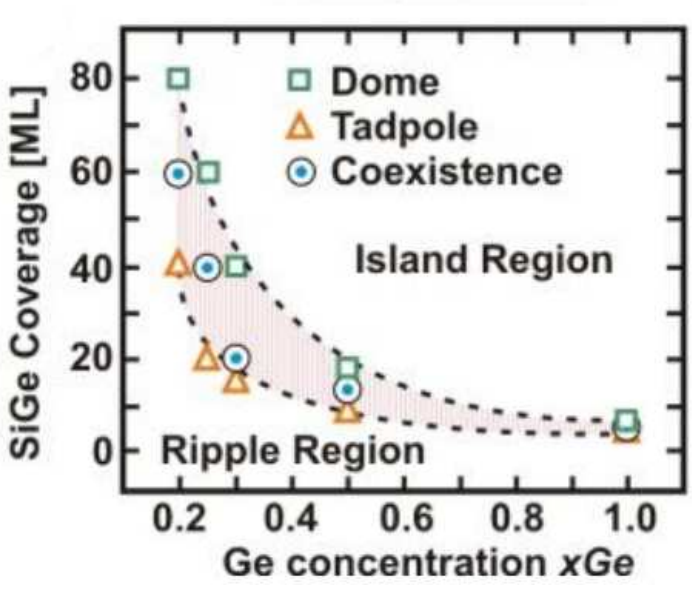

FIGURE 6.2: Onset of Domes: Experimentally-determined phase diagram.

6.2 Tiling of domes simplified: the χ model

In an effort to support the experimental phase diagram in Fig.6.2 with total energy calculations, we can attempt to create a model mimicking this system as a transition between a complete {105} faceting of the WL to an ordered nucleation of domes.

6.2.1 Idea and model

In order to predict the transition coverage we take into consideration a substrate of width M and length L and let us suppose the total deposition to be D. Let us make the additional hypotesis that all the deposited material is either in the ripples or in the dome and let us consider the amount of material stored in the WL in the dome configuration to be negligible.

Our model simplifies the geometry as depicted in Fig.6.3-(a), and consists in:
Situation 1: a perfect faceting situation of identical n_r ripples of base b and length L
Situation 2: a covering of the substrate of identical n_d domes nucleated equidistantly, each of which has a volume V_d, exposed surface S_d and covered surface B_d.

Ripples geometry

If we make the assumption that all the ripples have the same base, we have

$$b = \frac{M}{n_r} \tag{6.1}$$

By indicating as V_r, S_r, B_r and L the volume, 105 surface exposed and the area covered and the top edge length by a SINGLE ripple respectively, we can express them as follows:

$$V_r = \frac{b^2}{4} \cdot \tan\varphi \cdot L = \frac{b}{4} \cdot \tan\varphi \cdot \frac{LM}{n_r} \tag{6.2}$$

$$S_r = b \cdot \sec\varphi \cdot L = \frac{LM}{n_r} \cdot \sec\varphi \tag{6.3}$$

$$B_r = b \cdot L = \frac{LM}{n_r} \tag{6.4}$$

$$L = L \tag{6.5}$$

The total volume of the ripples in this area must reproduce all the deposited material.

$$LM \cdot D = n_r \cdot V_r \implies b = \frac{4}{\tan\varphi} \cdot D \tag{6.6}$$

So the geometrical quantities can be expressed as:

$$V_r = \frac{LM}{n_r} \cdot D \tag{6.7}$$

$$S_r = b \cdot \sec\varphi \cdot L = \frac{LM}{n_r} \cdot \sec\varphi \tag{6.8}$$

$$B_r = b \cdot L = \frac{LM}{n_r} \tag{6.9}$$

As already discussed in sec.5.4 at page 119, the total amount of exposed surface $S_r \cdot n_r$ is independent of the coverage if a defect-free faceting is created.

Ripple energy

The energy per ripple of situation 1, therefore, reads as:

$$\frac{E_r}{n_r} = V_r\rho_r + S_r\gamma_{105} + \Gamma L \tag{6.10}$$

$$= \frac{LM}{n_r}\cdot D\cdot\rho_r + \frac{LM}{n_r}\cdot\sec\varphi\cdot\gamma_{105} + \Gamma\cdot L \tag{6.11}$$

From which we get the energy per unit surface

$$\frac{E_r}{LM} = D\cdot\rho_r + \sec\varphi\cdot\gamma_{105} + \frac{\Gamma}{b} \tag{6.12}$$

$$= D\cdot\rho_r + \sec\varphi\cdot\gamma_{105} + \frac{\tan\varphi}{4D}\cdot\Gamma \tag{6.13}$$

Where in the latter equation the base of the ripples has been expressed as:

$$h_r = \frac{b}{2}\cdot\tan\theta = 2D \rightarrow b = \frac{4D}{\tan\theta} \tag{6.14}$$

that holds in the case of NO WL under the ripples themselves in which case the ripples height h_r is exactly two times the deposition.

Dome geometry

For the situation of the domes, it is convenient to define a "filling factor" χ_d defined as the ratio between the area of the exposed WL in the cell (A in a single repeated cell) to the area of the substrate covered by the domes (B_d in a single repeated cell):

$$\chi_d \equiv \frac{B_{free-WL-Domes}}{B_{covered-WL-Domes}} = \frac{LM - n_d\cdot B_d}{n_d\cdot B_d} = \frac{A}{B_d} = \frac{LM}{n_d\cdot B_d} - 1 \tag{6.15}$$

This quantity χ_d can be directly determined from the experiments (AFM measurements) and represent a measure of the island vicinity as:
$\chi \rightarrow 0 \Longleftrightarrow$ neighbouring islands touching each other
$\chi \rightarrow \infty \Longleftrightarrow$ almost isolated islands.

Let us introduce the geometrical factors that describe the geometry of a single dome:

$$V_d \equiv V_d \tag{6.16}$$

$$S_d \equiv \beta_{exp-s-d}\cdot V_d^{2/3} \tag{6.17}$$

$$B_d \equiv \beta_{cov-s-d}\cdot V_d^{2/3} \tag{6.18}$$

$$\lambda_d \equiv \beta_{edge-exp-dome}\cdot V_d^{1/3} \tag{6.19}$$

where the λ_d is the length of the total exposed edges of the dome, making the hypothesis that the edges at the base contribute negligibly to the energy, as was the case of the pure Ge ripples discussed in the previous chapter.

The total volume of the domes must reproduce the total deposition:

$$LM\cdot D = n_d\cdot V_d \Longrightarrow V_d^{1/3} = \beta_{cov-s-d}\cdot(1+\chi_d)\cdot D \tag{6.20}$$

where eqn.(6.15) has been used.

The number of tiles n_d (a priori unknown) can be expressed in terms of the dome base B_d by imposing that the total area is the substrate one:

$$\begin{aligned} n_d \cdot (A + B_d) &= LM \qquad (6.21) \\ \Longrightarrow & \\ n_d &= \frac{LM}{A + B_d} = \frac{LM}{B_d} \cdot \frac{1}{1 + \chi_d} = \frac{LM}{\beta_{cov} \cdot V_d^{2/3}} \cdot \frac{1}{1 + \chi_d} \qquad (6.22) \end{aligned}$$

Dome energy

From eqn.(6.15) we get the following:

$$\frac{B_{freeWLdomes}}{n_d} = \chi_d \cdot B_d \qquad (6.23)$$

So we get the total energy per unit of tile is:

$$\begin{aligned} \frac{E_d}{n_d} &= V_d \cdot \rho_d + S_d \gamma_d + \frac{B_{freeWLdomes}}{n_d} \cdot \gamma_{WL} + \lambda_d \cdot \Gamma_{dome} \\ &= V_d \cdot \rho_d + B_d \cdot \left(\frac{S_d}{B_d} \cdot \gamma_d + \frac{B_{freeWLdomes}}{n_d \cdot B_d} \cdot \gamma_{WL} \right) + \beta_{edge,exp,d} \cdot V_d^{1/3} \cdot \Gamma_d \\ &= V_d \cdot \rho_d + B_d \cdot \left(\frac{S_d}{B_d} \cdot \gamma_d + \chi_d \cdot \gamma_{WL} \right) + \beta_{edge,exp,d} \cdot V_d^{1/3} \cdot \Gamma_d \\ &= V_d \cdot \rho_d + \beta_{cov-s-d} \cdot V_d^{2/3} \cdot \left(\frac{S_d}{B_d} \cdot \gamma_d + \chi_d \cdot \gamma_{WL} \right) + \beta_{edge,exp,d} \cdot V_d^{1/3} \cdot \Gamma_d \\ &\equiv V_d \cdot \rho_d + \beta_{cov-s-d} \cdot V_d^{2/3} \cdot \widetilde{\gamma}_d + \beta_{edge,exp,d} \cdot V_d^{1/3} \cdot \Gamma_d \end{aligned}$$

By using also eqns.(6.20) we get the energy per unit surface

$$\begin{aligned} \frac{E_d}{LM} &= D \cdot \rho_d + \beta_{cov-s-d} \cdot \frac{D}{V_d^{1/3}} \cdot \widetilde{\gamma}_d + \frac{\beta_{edge,exp,d}}{\beta_{cov}} \cdot \frac{1}{V_d^{1/3}} \cdot \frac{1}{1 + \chi_d} \cdot \Gamma_d \\ &= D \cdot \rho_d + \beta_{cov-s-d} \cdot \frac{D}{\beta_{cov-s-d} \cdot (1 + \chi_d) \cdot D} \cdot \widetilde{\gamma}_d + \frac{\beta_{edge,exp,d}}{\beta_{cov-s-d}^2 \cdot (1 + \chi_d)^2} \cdot \frac{\Gamma_d}{D} \\ &= D \cdot \rho_d + \frac{1}{1 + \chi_d} \cdot \widetilde{\gamma}_d + \frac{\beta_{edge,exp,d}}{\beta_{cov-s-d}^2 \cdot (1 + \chi_d)^2} \cdot \frac{\Gamma_d}{D} \\ &= D \cdot \rho_d + \frac{1}{1 + \chi_d} \cdot \left(\frac{S_d}{B_d} \cdot \gamma_d + \chi_d \cdot \gamma_{WL} \right) + \frac{\beta_{edge,exp,d}}{\beta_{cov-s-d}^2 \cdot (1 + \chi_d)^2} \cdot \frac{\Gamma_d}{D} \end{aligned}$$

Energy balance

The balance of energy between situation 1 and 2 reads as:

$$\begin{aligned} \Delta E(d - r) &= D \cdot (\rho_d - \rho_r) \qquad (6.24) \\ &+ \frac{S_d / B_d}{1 + \chi_d} \cdot \gamma_d - \sec\varphi \cdot \gamma_{105} + \frac{\chi_d}{1 + \chi_d} \cdot \gamma_{WL} \qquad (6.25) \\ &+ \frac{\beta_{edge,exp,d}}{\beta_{cov-s-d}^2 \cdot (1 + \chi_d)^2} \cdot \frac{\Gamma_d}{D} - \frac{\tan\varphi}{4D} \cdot \Gamma_{top,ripple} \qquad (6.26) \end{aligned}$$

By imposing this equation to be zero, the critical deposition D_{cr} at which the transition occurs can be found.

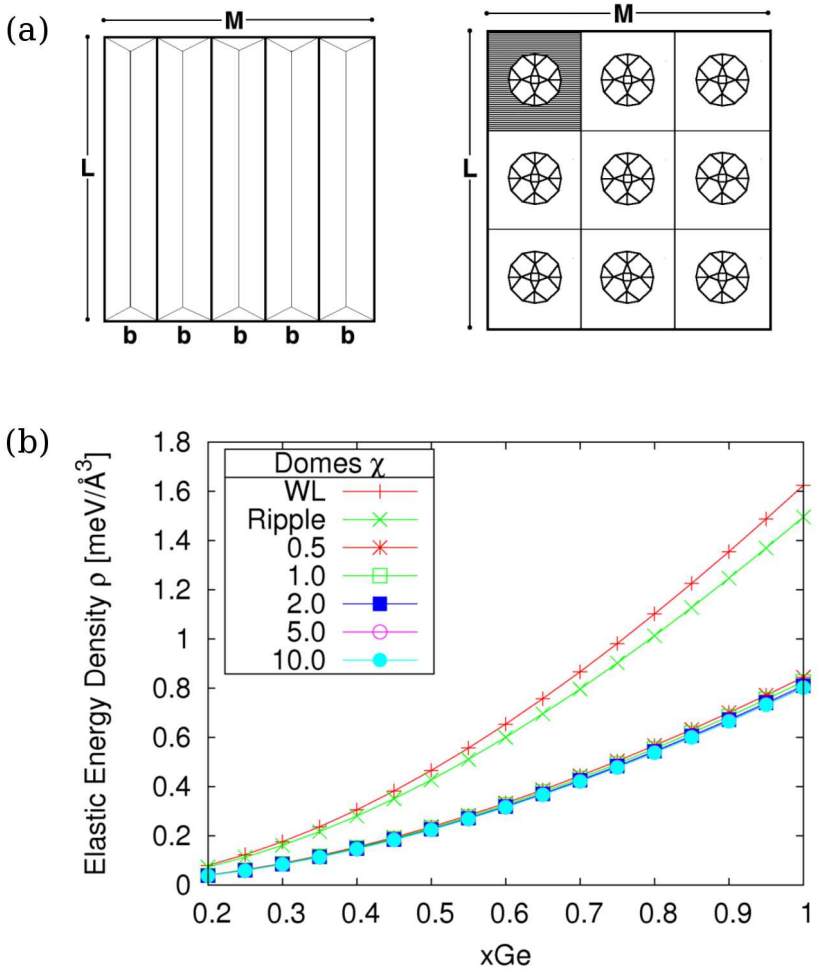

FIGURE 6.3: Onset of Domes: χ Model. (a) Sketch of the situations we are comparing: a {105} Perfect Faceting of n_r ripples of base b and an ordered onset of n_d domes. In the ratio between the black area to the aea covered by a single dome is χ_d. In (b) we report the elastic energy density of the quantity entering the calculations: WL, Ripples of (a) and domes at different χ.

6.2.2 Results and comparison with experiments

The elastic energy density of the domes ρ_d must take into account the elastic repulsion between neighbouring islands. This is performed by using the periodic boundary conditions at the cell borders.

The values of χ_d are determined by AFM images and are determined as: $\chi_d \sim 0.5$ (xGe = 20, 25 and 30%) ; $\chi_d \sim 0.8$ (xGe=50%) ; $\chi_d \sim 8$ (xGe=100%). The trend of the elastic energy density for the domes with different χ_d is reported in Fig.6.3-(b), along with the ripple in the PF situation (NO WL) and the WL itself.

The used value of the 105 surface energy is the one obtained by the perfect faceting situation where the dependence on the height is neglected since the ripples are large ones: $\gamma_r \simeq 58.41$ meV/Å^2.

The surface energy of the WL is put equal to the one of the 100% Ge (1 1 10)-Db surface obtained in the previous chapter. Different values of its thickness (and its values) are tested from N=1 to N=4 ML.

Following the result of the previous chapter, the energy Γ of the exposed edges alone is put equal to 370 meV/Å for both the ripples and the domes.

Fig.6.4 reports the values of the transition coverage obtained by using these parameters for different values of the WL surface energy (rows) and the elastic energy density for the initial ripple situation (columns). Left column refers to the case of NO WL under the ripples (i.e. Perfect Faceting) situation, the right column consider the limiting case of a thick WL under the ripples leading to an elastic energy density equal to the one of a WL. Panels (a) and (b) refer to the case of 1 ML-thick (1 1 10) WL, (c,d) the case of 4 MLs-thick (1 1 10), (e,f) to the case in which the (1 1 10) is never exposed, but rather some mini (105) ripples are formed (see experimental evidences discussed in sec.6.3 below).

As evident we have the following trends:

- the larger the value of χ_d, the more distant the domes, the lower their elastic repulsion, the lower the transition thickness (different lines inside each panel)
- the larger the elastic energy density of the initial ripple situation, the lower the transition deposition (left or right column)
- the lower the surface energy of the WL exposed, the lower the transition deposition (different rows)

Although the situations depicted in (e) and (f) seem in qualitative accordance with experimental findings, this simple model has some logical shortcomings.

First of all, here we make the implicit hypothesis that as the deposition proceeds, the periodicity[2] is increasing in such a way that all ripples have the same base (Perfect Faceting situation). The base of the ripples in this model is linked to the deposition D as:

$$D = \frac{b}{4} \cdot \tan\varphi \Longrightarrow b_{PF} = \frac{4D}{\tan\varphi} \tag{6.27}$$

[2] i.e. the ripples base

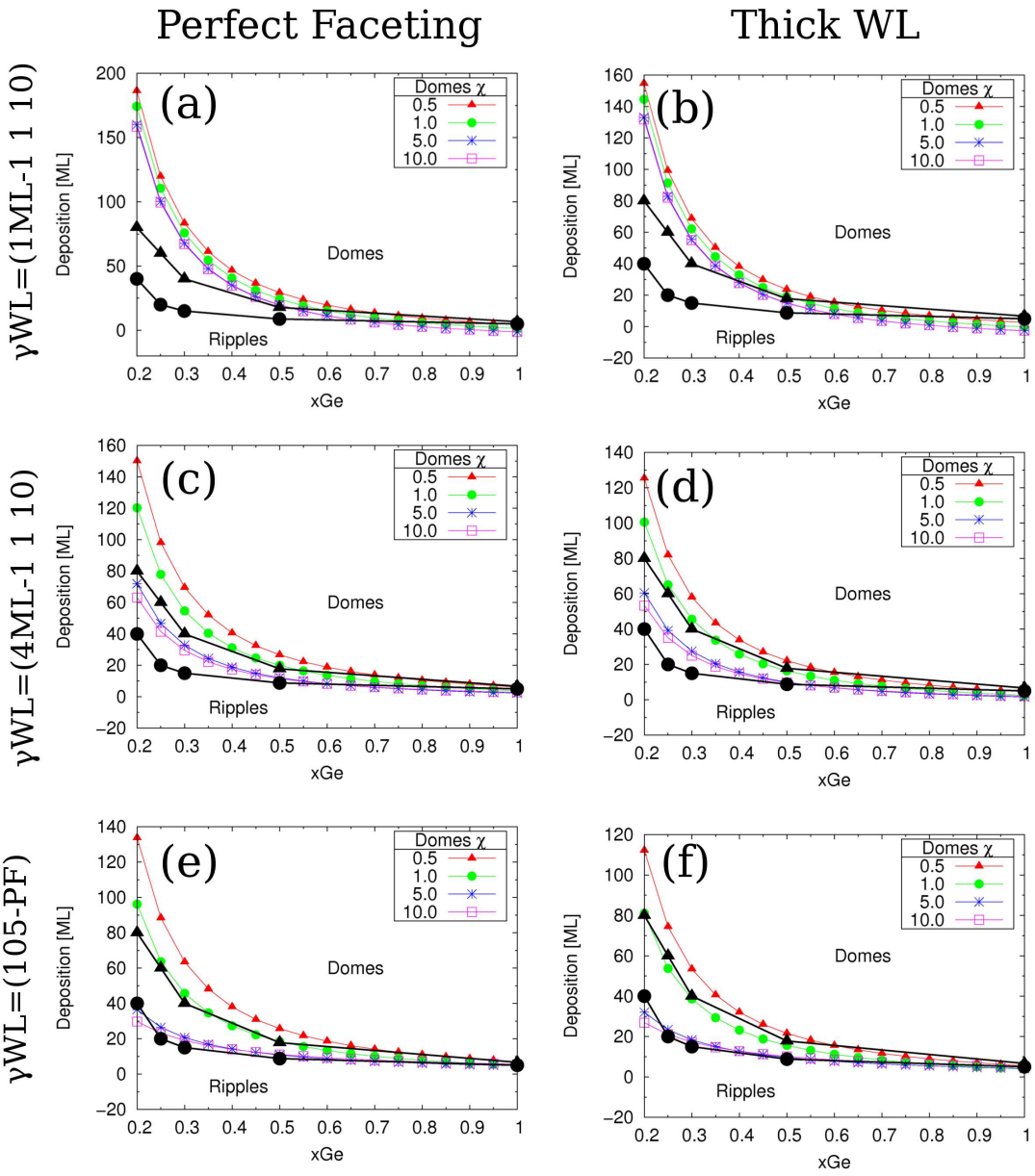

FIGURE 6.4: χ model: Results. Left column shows the case of the elastic energy density of the ripple equal to the PF situation, right column shows the case where the ripples lay atop a thick WL. From top row to bottom the surface energy of the exposed WL is set equal to: $\gamma(1ML, 1110)$, $\gamma(2ML, 1110)$, $\gamma(105 - PF)$. Γ_{edge} is set equal to 370 meV/Å for both the ripples and the domes.

A comparison between the measured base of the ripples and b_{PF} is reported in Fig.6.5 along with the measured base (diameter) of the dome. From this images we can see that:

1. the observed maximum width of the ripple is much larger than b_{PF}
2. the measured minimum base of the domes are compatible with the measured maximum base of the ripples

So our hypothesis has no experimental foundations.

Secondly, the domes are randomly distributed on the substrate, thus the value of χ_d is just an average measure of the elastic repulsion. This holds for the results coming from the use of this parameter as well.

Lastly we have to consider that on any other substrate the transition in SK deposition from an island to another with steeper facets occurs via the enlargement of the first one. This substrate cannot be an exception. This suggests that the evolution of the domes might occur from an isolated ripple, without the requirement of a long scale coherent growth of the ripples themselves.

The evolution path of the domes from an isolated ripple has been carefully analyzed, leading to the observations discussed in the next session.

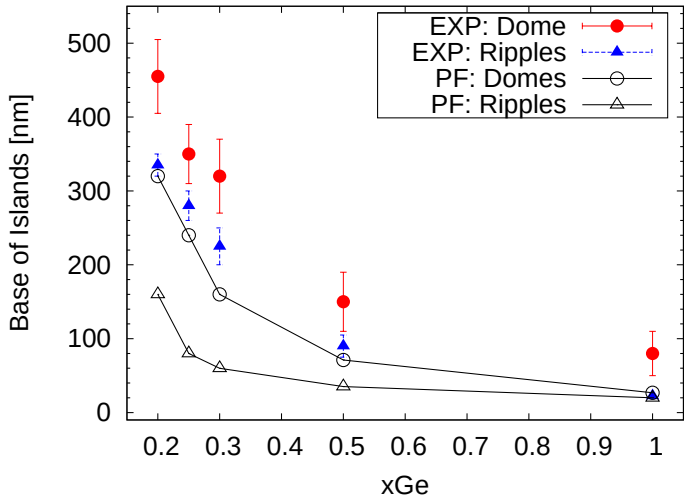

FIGURE 6.5: Onset of Domes: experimental bases vs perfect aceting hypotesis. Black lines are the expected bases of the ripples (empty triangles) or domes (empty squares) if the PF hypotesis holds obtained from the deposition using eqn.(6.27). Red and blue points represent the measured bases of the domes and of the maximum ripples width. This shows that the hypotesis that the underlying hypotesis of the χ model, i.e. that the increasing period with coverage is due to a growth of ALL ripples, is not supported by experiments. Therefore a single ripple model must be developed.

6.3 Detailed analysis of the phase transition

If on one hand the diluted alloys allow to have larger, easier-to-observe, islands, their evolution path is complicated by intermixing processes.

The STM images in Fig.6.6 show the surface morphology for different coverages of pure Ge. At Ge = 4.5 ML (panel a), a ripple-dominated surface morphology has formed, whereas at Ge = 5.5 ML (panel b), the ripple-to-island phase transition has set in with different geometries.

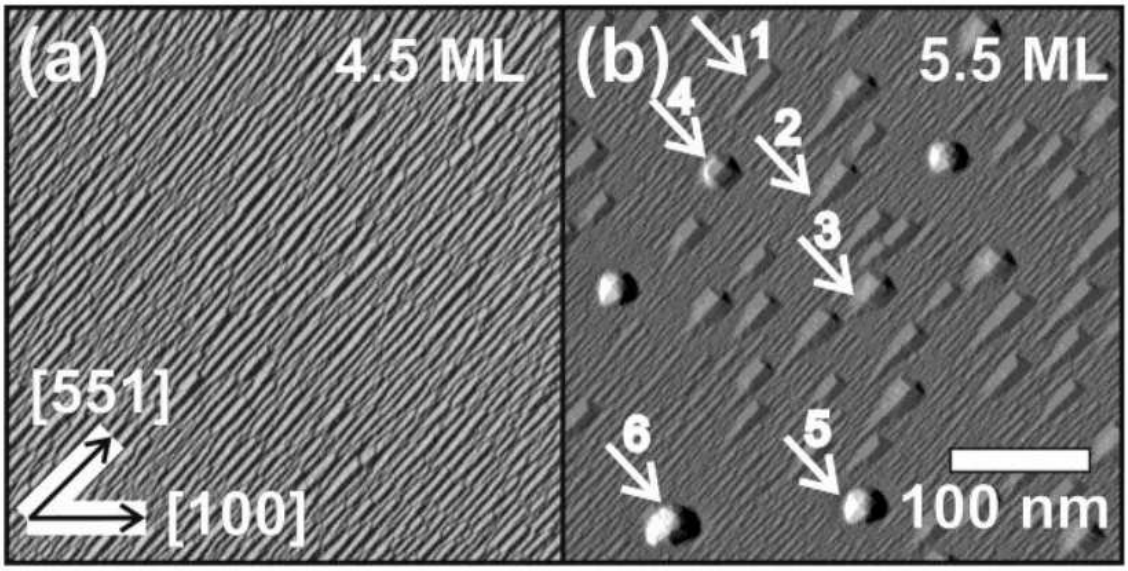

FIGURE 6.6: Differential-view STM images of the surface morphology in a 200×200 nm^2 area with different Ge coverage. (a) Ripple-dominated surface after the growth of 4.5 ML Ge; (b) Phase transition region with a complete set of evolutional stages appearing at a coverage of 5.5 ML.

In Figure 6.7 all stages of the coherent ripple-to-island evolution in the case of 100% Ge are covered by high-resolution STM images.

Starting from the perfect faceting situation described in the previous chapter, the additional material accumulates in the concave regions thus increasing the base of some ripples for a certain extension of their length on the sample and creating additional {105} facets. Reasonably this is the only way the islands can grow on a seamless faceted sample involving local diffusion of the additional material. No WL thickening under the ripples is observed that would imply a movement of material overall on the sample. For the same reason even an enlargement of the period (i.e. base) of all ripples simultaneously[3] is ruled out, since it would involve a coherent movement of ripples that can be baptised as "hut flow". The fact that a thick WL is observed for non-annealed, low Ge content samples of Ref.[160] can be attributed to Ge segregation at the surface and the phase transition of the sole topmost surface Ge-rich region.

The effect of this growth of some ripples is the formation of the ripple bifurcation shown

[3]as postulated in the χ model of the previous section

in Figure 6.7-(a) where three prism-shaped ripples meet. This point allows a partial strain relieve of the compressed ripples. Hence, ripple disruption by the formation of low-energy (001) end facets (white circle) becomes energetically favorable. Also, a step is found on the sidewall of the ripple in the center of the image (dark arrow), hinting to the mechanism for ripple broadening, as already discussed.

The images show that these enlarged ripples assume a shape resembling that of a "Tadpole" or "Fish" (white arrows #1 - #3 in Fig.6.6-(b)).

Figure 6.7-(b) shows a high resolution STM image of tadpole #1 from Figure 6.6-(b), which is already about three times wider than the initial ripples. The dark arrows show that the tail forms via the formation of step bunches on the {105}-bound body.

Therefore, we can think of the Tadpoles as composed of three parts:

- a Head that is (001)-teminated
- a Body composed of the two facets already exposed by the ripples
- a triangular-shaped Tail composed of stepped 105 facets

While the Body presents very sharp and ordered facets originated, presumably, by a single enlarged ripple, the Tail is made of the facets of the smaller ripples that are enlarging their base at a different rate, with a base growing from the extremum to the body. The conjunction between facets of different sizes creates the steps.

The next evolution stage, indicated by arrows #2 and #3 in Figure 6.6-(b), leads to the transformation of the (001)-terminated head into another set of two adjacent {105} facets (white arrows in Fig.6.7-(c,d)). In this way, the head of the tadpole develops into a tilted pyramid, because the miscut does not allow the formation of an upright {105} pyramid, as would be the case on Si(001).

The so formed {105}-terminated Head is a region that allows better strain relaxation, i.e. a region of low chemical potential for Ge, thus attracting the Ge atoms wandering around. What is observed is that when the tadpole base exceeds a certain size, the Head enlarges at the expense of the Tail that start shortening and shrinking, which is associated with pronounced step bunching in the tail region. Schematics of the two tadpole morphologies are depicted in Fig.6.7-(i) and (j), respectively.

When the head size exceeds a certain limit, the same step bunching phenomenon underlying the pyramid-to-dome transition[4] takes place, thus creating the "Dome-headed Tadpole", island # 5 in in Fig.6.6-(b). Since the dome has even lower chemical potential the process of tail and body absorption becomes more favoured with the final result to assist to a **1-Tadpole-to-1-Dome transition**.

Since the enlargement of ripples creating the domes is random on the surface (presumably driven by local surface defects), the final substrate has randomly nucleated domes sorrounded by smaller ripples, as in Fig.6.7-(e). In this case, the very dense step bunches at the tadpole perimeter have already evolved into smooth {113} and {15 3 23} facets, as confirmed by the surface orientation map shown in the inset. The resulting island structure is shown schematically in Fig.6.7-(k). Figure 6.7-(f) displays a transition stage

[4]see discussion in chapter 1

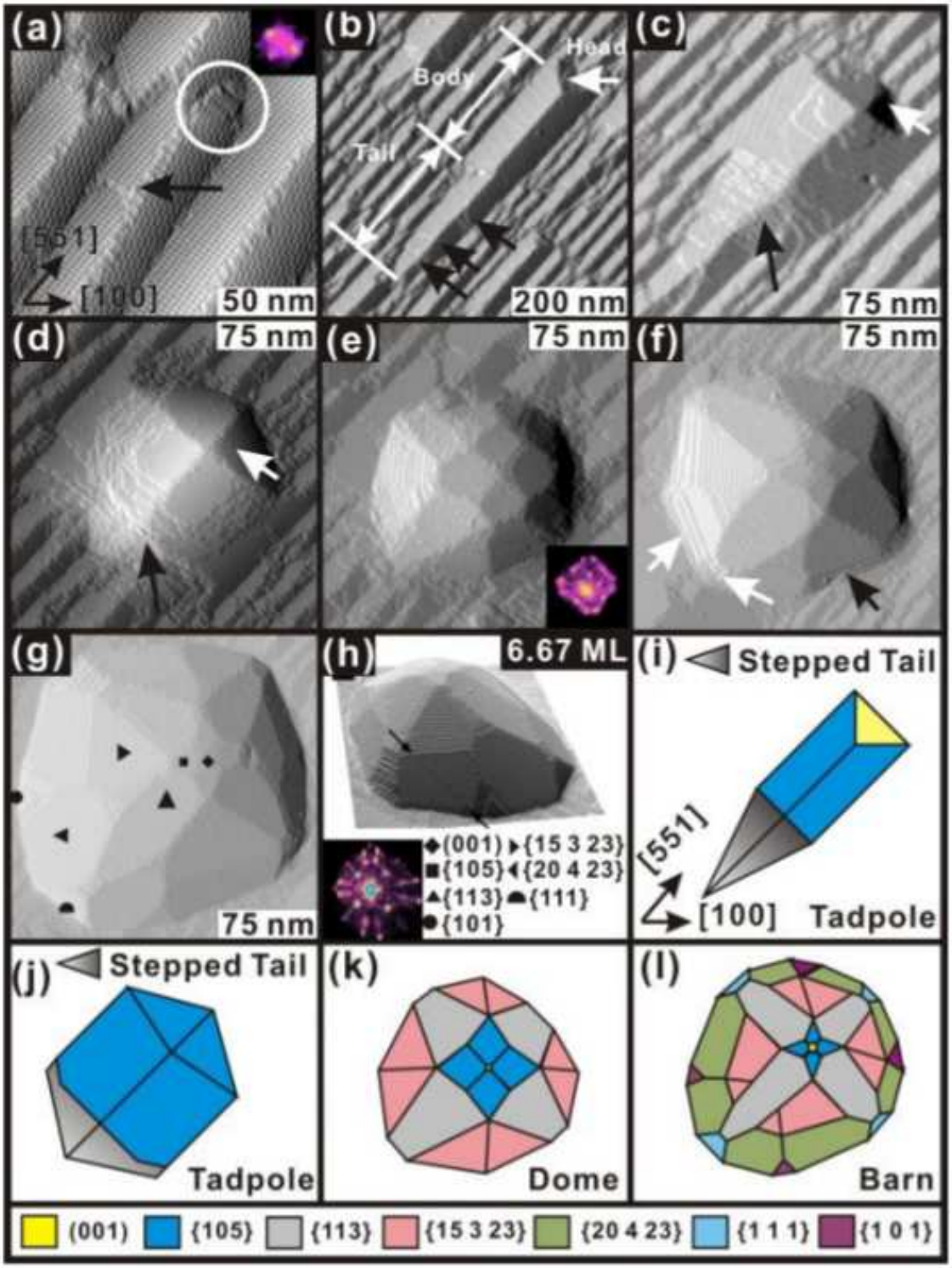

FIGURE 6.7: Differential-view, high resolution STM images of the complete morphological evolution of pure Ge samples. (a): (001)-terminated ripples; (b) and (c): tadpoles with long stepped-tails and (001)- or {105}-bound heads; (d): tadpole with 105-bound head and shrinking, highly stepped tail; (e): dome; (f): transition barn with densely steppe edges; (g) and (h): barn and its 3D view. (i)-(l): Corresponding geometrical sketches, identifying the respective facets.

between a dome and a barn, in which dense step bunches and small areas of steeper facets are seen at the perimeter of the dome (white arrows).

It is interesting to note that the shape of Tadpole with the enlarged Head resembles a triangle very similar to the one reported in Fig.4.8-(c) at page 92. This observation resolves the controversal results described in sec.4.4.2 [142] regarding the evolution of islands on these miscutted substrates without considering any unexplicable {113} facets.

It is noteworthy to see that even in the presence of the low-energy domes, the (1 1 10) surface is never exposed. This suggests that the seamless {105} faceting in this system is playing the role of the WL on other substrates. In this respect, the Tadpoles are playing the role covered by the standard {105} pyramids on other substrates.

As on the (001) substrate, the islands change morphology by adding family facets as they enlarge. Barn-shaped island forms (Fig.6.7-(g)) with a higher aspect ratio of $\simeq 0.25$. A 3D rendering and the surface orientation map of the barn are displayed in Fig.6.7-(h), revealing the steep {101}, {111}, and {20 4 23} facets with inclination angles larger than 30°. The barn structure is sketched in Fig.6.7-(l).

These results appear in contrast with others recently published [140, 161].
In these papers the authors perform similar experiments but leads to different conclusions. First of all they observe that larger ripples form by coalescence of several other smaller ripples, rather than growing from a single one. Moreover, they come to the conclusion that ripple agglomeration, and the observation of dislocated superdome clusters with preferential orientation at higher coverage, might be caused by the reduced symmetry of the elastic strain field on vicinal substrates. Our results, on the contrary, never found any indications for ripple agglomeration or dome coalescence with a preferred orientation under clean experimental conditions. Any seeming ripple or dome clustering phenomena could be identified as being due to either multiple STM-tip artefacts or substrate contaminations. Indeed, recent reports in the literature confirm the absence of ripple clustering [162].

Also, all structures in Fig.6.6-(b) are fully coherent, again in contrast to Ref.[140], where for at 4 ML already dislocated superdomes were reported. Fig.6.7, instead, clearly demonstrates a fully coherent evolution route that neither involves ripple aggregation [140] nor dome bunching [161]. As an example, Figs. 6.8-(a) and (b) show differential-view AFM images of samples with 20 and 60 ML of $Si_{0.75}Ge_{0.25}$. At 20 ML, the surface is dominated by (001)-headed tadpoles with a length of 600±200 nm. At 60 ML the surface is exclusively covered with isolated domes. At intermediate coverage, a coexistence of tadpoles and domes is observed with a similar morphology as in Fig.6.6-(b). Figure 6.8-(c) and (d) show STM images of the surface morphology for 5.0 and 6.7 ML of pure Ge. The surface of the former sample is dominated by ripples, whereas on the latter the phase transition to isolated domes is fully established. No coarsening of the domes into dislocated superdomes is observed at this coverage. Figure 6.8-(e) and (f) show 10×10 μm^2 and 2×2 μm^2 large AFM images at 7.5 ML of pure Ge, i.e. at the same coverage for which in Ref.[161] the dominance of dislocated superdomes was reported. In contrast, the morphology in Fig.6.8-(e) is dominated by coherent domes with diameters of 60±10 nm. Less than 3% of the > 400 islands in Fig.6.8-(e) are dislocated superdomes. We found an even lower percentage of coalescing domes. These are, however, randomly oriented with

no indications for the reported [161] preferential clustering orientation with respect to the miscut direction.

A zoom-in of a superdome is displayed in Fig.6.8-(f), which exhibits a clear dislocation line perpendicular to the miscut direction (dark arrow). In fact, we observed this characteristic dislocation line on many superdomes, and attribute them to the asymmetrical strain accumulated in the islands and ripples on the vicinal Si (1 1 10) substrate [160], rather than to the purported wedge defect caused by coalescence [161].

Several shallow structures in the vicinity of the superdome, including empty trenches (ET) and shrinking domes (SD), are footprints of dome-dissolution in a Ostwald ripening process [163, 164]. Thus, again the pathway to superdomes on vicinal Si(1 1 10) substrates appears to be very similar to the behavior on a Si(001) surface [165].

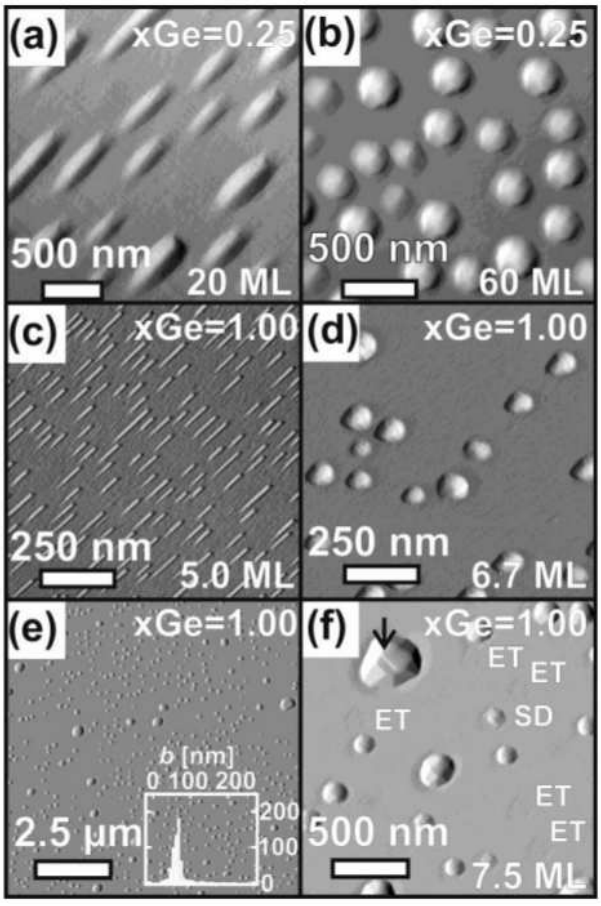

FIGURE 6.8: First derivative of AFM [(a), (b), (e), (f)] and STM [(c)-(d)] images showing the morphological evolution from ripples to islands under equilibrium growth condition for two compositions.

6.4 Single Tadpole to Dome: energetics

Starting from the observed evolution we model the onset of steeper islands as a one-to-one evolution from Tadpole to Dome. In this idea the value of the critical deposition is actually a measure of the ripple coarsening leading finally to the domes. Further, the critical deposition may depend on the experimental conditions (substrate temperature, deposition flux, time of annealing etc.), but if the transition from the large ripple to dome is governed by thermodynamics then it is the base of the former the real general and predictable parameter. Following this reasoning a TD model cannot predict a critical deposition, but rather a critical base for dome onset. In other words, what TD can predict is that domes with bases smaller than the critical one cannot be observed (or if they are, they are not thermodynamically stable). In the following we present this model.

6.4.1 Model

We want to compare the energy of the Dome with the ones of the Tadpole in order to find the transition base, measurable from experiments. The geometries of the islands are reported in Fig.6.9 and, since they are aimed at replicating the observed ones, the tadpole can be either (001)- or (105)-headed.

The energy of the tadpole (Fish, F) with respect to the flat WL is expressed as:

$$\begin{aligned} E_F - E_{WL} &= V_F \cdot (\rho_F - \rho_{WL}) \text{ [Volume]} && (6.28)\\ &+ S_H \cdot \gamma_H + S_B \cdot \gamma_B + S_T \cdot \gamma_T \text{ [Exposed surface]} && (6.29)\\ &- (B_H + B_B + B_T) \cdot \gamma_{WL,T} \text{ [Covered surface]} && (6.30)\\ &+ L_T \cdot \Gamma_T \text{ [Edge term]} && (6.31) \end{aligned}$$

where the subscripts T, H, B refer to the Tadpole Tail, Head and Body, respectively.

Similarly, the energy of the dome is:

$$\begin{aligned} E_D - E_{WL} &= V_D \cdot (\rho_D - \rho_{WL}) \text{ [Volume]} && (6.32)\\ &+ S_D \cdot \gamma_D \text{ [Exposed surface]} && (6.33)\\ &- B_D \cdot \gamma_{WL,D} \text{ [Covered surface]} && (6.34)\\ &+ L_D \cdot \Gamma_D \text{ [Edge term]} && (6.35) \end{aligned}$$

Since we are interested in a transition base, we need to express everything in terms of the base of the fish b_F and the dome b_D, where we can link to each other via:

$$\xi = \frac{b_F}{b_D} \geq 1 \Longrightarrow b_F = b_D \cdot \xi \tag{6.36}$$

and exploit the same relationships as in sec.2.1 at page 31:

$$\begin{aligned} V_D &= K_{DV} \cdot b_D^3 \text{ (Volume)} && (6.37)\\ S_D &= K_{DS} \cdot b_D^2 \text{ (Exposed Surface)} && (6.38)\\ B_D &= K_{DB} \cdot b_D^2 \text{ (Covered Surface)} && (6.39)\\ E_D &= K_{DE} \cdot b_D \text{ (Edges)} && (6.40) \end{aligned}$$

We can express the geometry of the fish as a function of its base b_F and therefore b_D. Volumes :

$$\begin{aligned} V_F &= V_H + V_B + V_T && (6.41)\\ V_H &= K_{HV} \cdot b_F^3 = K_{HV} \cdot \xi^3 \cdot b_D^3 && (6.42)\\ V_B &= K_{BV} \cdot b_F^3 = \frac{\tan\theta}{4} \cdot \left(\frac{L_B}{b_F}\right) \cdot b_F^3 = \frac{\tan\theta}{4} \cdot \left(\frac{L_B}{b_F}\right) \cdot \xi^3 \cdot b_D^3 && (6.43)\\ V_T &= K_{TV} \cdot b_F^3 = K_{TV} \cdot \xi^3 \cdot b_D^3 && (6.44) \end{aligned}$$

Exposed Surfaces :

$$\begin{aligned} S_F &= S_H + S_B + S_T && (6.45)\\ S_H &= K_{HS} \cdot b_F^2 = K_{HS} \cdot \xi^2 \cdot b_D^2 && (6.46)\\ S_B &= K_{BS} \cdot b_F^2 = K_{BS} \cdot \xi^2 \cdot b_D^2 && (6.47)\\ S_T &= K_{TS} \cdot b_F^2 = K_{TS} \cdot \xi^2 \cdot b_D^2 && (6.48) \end{aligned}$$

Covered (Buried) surfaces :

$$\begin{aligned} B_F &= B_H + B_B + B_T && (6.49)\\ B_H &= K_{HB} \cdot b_F^2 = K_{HB} \cdot \xi^2 \cdot b_D^2 && (6.50)\\ B_B &= K_{BB} \cdot b_F^2 = K_{BB} \cdot \xi^2 \cdot b_D^2 && (6.51)\\ B_T &= K_{TB} \cdot b_F^2 = K_{TB} \cdot \xi^2 \cdot b_D^2 && (6.52) \end{aligned}$$

Edges :

$$\begin{aligned} L_F &= L_H + L_B + L_T && (6.53)\\ L_H &= K_{HE} \cdot b_F = K_{HE} \cdot \xi \cdot b_D && (6.54)\\ L_B &= K_{BE} \cdot b_F = K_{BE} \cdot \xi \cdot b_D && (6.55)\\ L_T &= K_{TE} \cdot b_F = K_{TE} \cdot \xi \cdot b_D && (6.56) \end{aligned}$$

The factor $\frac{L_B}{b_F}$ (lateral aspect ratio of the body) can be determined if we make the hypothesis of negligible intermixing during the phase change. Indeed by imposing the volume of the fish to be equal to the volume of the dome, we get:

$$V_F = V_D \Longrightarrow \frac{L_B}{b_F} = \frac{4}{\tan\theta} \cdot \left(\frac{K_{DV}}{\xi^3} - K_{HV} - K_{TV}\right) \qquad (6.57)$$

so it is univocally determined.

We can make the additional reasonable hypothesis that the surface energy of the WL does not change appreciably with the different strain induced on it by the ripple or the dome ($\gamma_{WL-R} = \gamma_{WL-D}$)[5].

[5]since any surface energy depends on the strain state, compare the discussion in sec.2.5.4 at page 63

By expressing everything as a function of b_D we get the energy balance:

$$\begin{aligned}
\Delta E_{DF} &\equiv E_D - E_F && (6.58)\\
&= b_D^3 \cdot K_{DV} \cdot (\rho_D - \rho_F) && (6.59)\\
&+ b_D^2 \cdot \left\{K_{DS} \cdot \gamma_D - \xi^2 \cdot (K_{HS} \cdot \gamma_B + K_{BS} \cdot \gamma_B + K_{TS} \cdot \gamma_T)\right\} && (6.60)\\
&- b_D^2 \cdot \gamma_{WL} \cdot \left\{K_{DB} - \xi^2 \cdot (K_{HB} + K_{BB} + K_{TB})\right\} && (6.61)\\
&+ b_D \cdot \{K_{DE} \cdot \Gamma_D - (K_{HE} + K_{BE} + K_{TE}) \cdot \Gamma_F\} && (6.62)
\end{aligned}$$

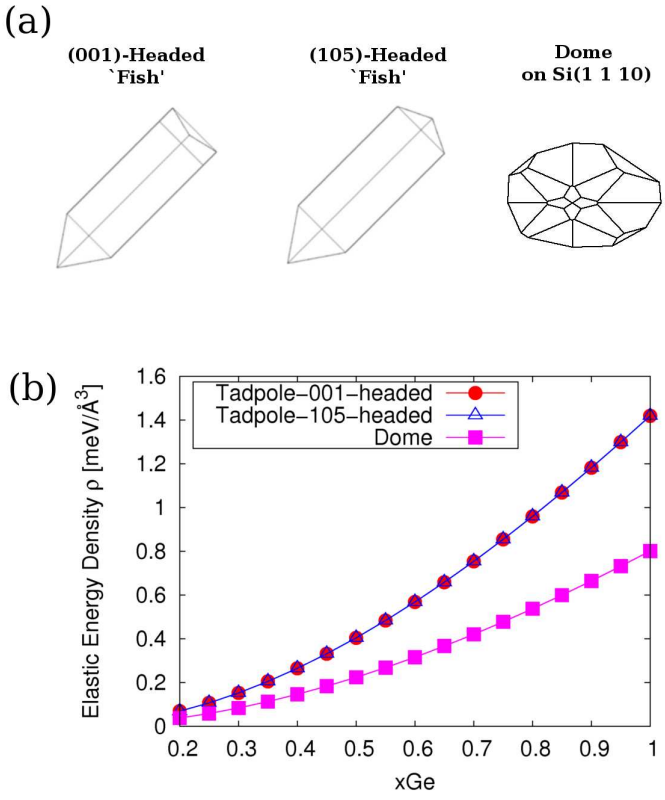

FIGURE 6.9: Single Tadpole calculation. (a) Models of the tadpoles (fishes) and the dome used in the calculation. (b) Trend of the elastic energy density for the two tadpoles and the dome as a function of the Ge content. The geometries are so elongated that the elastic energy of the two tadpoles is unaffected by the head termination but depends largely on the body and tail, that are the same for both.

6.4.2 Energy terms

The elastic energy densities ρ for the case of the tadpoles with the two terminations and the domes are reported in Fig.6.9-(b) as a function of the Ge content in the island as obtained by a FEM calculation in absence of any WL under the islands themselves. Here we adopt the same ab initio elastic constant and non-linear corrections used in the previous chapter.

The surface energy of the dome facets γ_D are imposed to be equal to 65 meV/Å^2 [30], whereas the surface energy of the (001) termination is in the range [60 : 75] meV/Å^2.

The surface energies of the {105} facets for the head and the body are computed in FEM by considering the value of the actual strain without considering the distance from the Si substrate since the experimental islands are $\geq$ 50 nm large. Given this geometry the obtained values are: $\gamma_H \simeq 57.5\ meV/\mathring{A}^2$ (for the 105-headed tadpole), $\gamma_B \simeq 56.70\ meV/\mathring{A}^2$ (for the body of the fish) and $\gamma_T \simeq 56.4\ meV/\mathring{A}^2$ (for the unincremented tail). Similarly to what done in the previous chapter, these values are obtained from the case of pure Ge islands, by making the hypotesis that the floating Ge layer at the surface compels this value to be the one of 100% Ge case.

The tail is composed of (105) facets as well, but the presence of the steps can alter their energy. For simplicity we include the effect of the steps by adding the surface energy a cost in the interval [0 : 10] meV/Å^2 to the value computed by FEM.

As done in the χ model, the WL can be treated as a (1 1 10), so to use the ab initio values. However, as discussed above, the detailed experimental analysis on 100% Ge samples reveal that a flat WL is never exposed, instead some mini-{105} ripples are always observed. This confirms our conclusion that the faceting on this system is a simil-WL. When we consider the WL to consist in mini-ripples, its surface energy is put equal to the one of the perfect faceting (58.41 meV/Å^2).

Considering the result obtained in the previous chapter, the energy of the exposed edges is put equal to 370 meV/Å for both the tadpoles and the dome.

From the experimental measurements shown in Fig.6.5, the base of the tadpole is roughly the same as the one of the dome, i.e. $\xi = 1$ and we consider this situation.

The theoretical trend should fall between the range of the dome base and the one of the ripples, this is because our b_D is the one where the domes are thermodinamically at equilibrium with the Fish.

6.4.3 Results and comparison with experiments

Figure 6.10 show the trend of the energies $E_F - E_{WL}$ and $E_D - E_{WL}$ for the case of the {105}-headed tadpole where the WL is modeled as a {105} PF for the Ge content equal to 100%, 50% and 25% Ge. The stars highlight the crossing points between the two curves (domes and tadpole). In all cases the stars are below the line of zero energy, i.e. where the WL (105-faceting) is unstable against the formation of islands.

In order to compare these results with the experiments we report these crossing points along with the experimental measurements in Fig.6.11 for different thickness of the exposed WL (rows) and for the two different tadpoles (columns). In both cases we report the data by varying the parameters $\gamma(001), \Delta\gamma_T$ in the aforementioned interval.

In any case the best agreement is achieved when the WL is treated as a {105} faceting (panels e and f), as experimentally revealed. In the case of the (001)-headed tadpole (panel e) we have the unknown variable of the (001) surface energy, but both the case of 60 and 75 meV/Å^2 is found in good agreement with experiments if the $\Delta\gamma_T$ is put equal to 10 meV/Å^2. In the case of the (105)-headed tadpole, a good agreement is also found for both extrema of $\Delta\gamma_T$ in the region xGe ≥ 0.30. It is very plausible that in the region xGe < 0.30 the hypoteses underlying this model concerning the usage of the surface energy of the 100% Ge case are no longer valid because of intermixing and kinetic limited processes, without mentioning a possible thick WL under the tadpoles due to surface segregation effects (not included in the model).

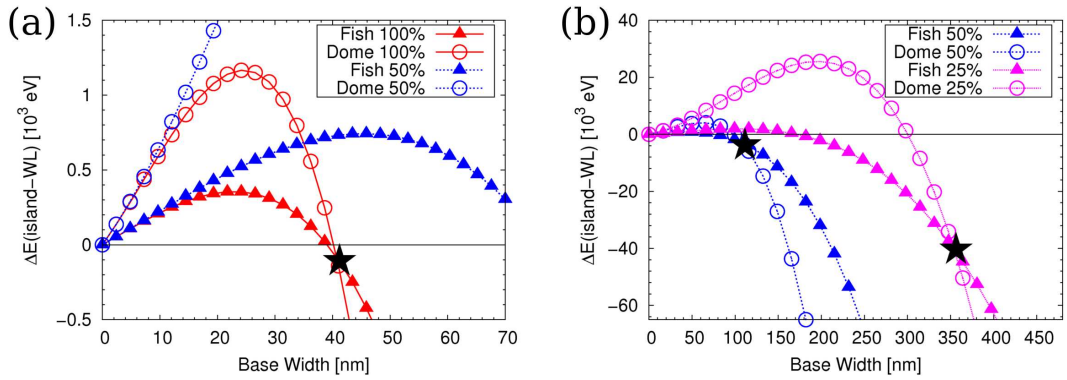

FIGURE 6.10: Tadpole-to-Dome transition: Energy curves. Trends of the energy $E_D - E_{WL}$ (empty circles) and $E_F - E_{WL}$ (full triangles) for the case of the {105}-headed tadpole and the WL is modeled as a {105} PF. The stars highlight the crossing points between the two curves.

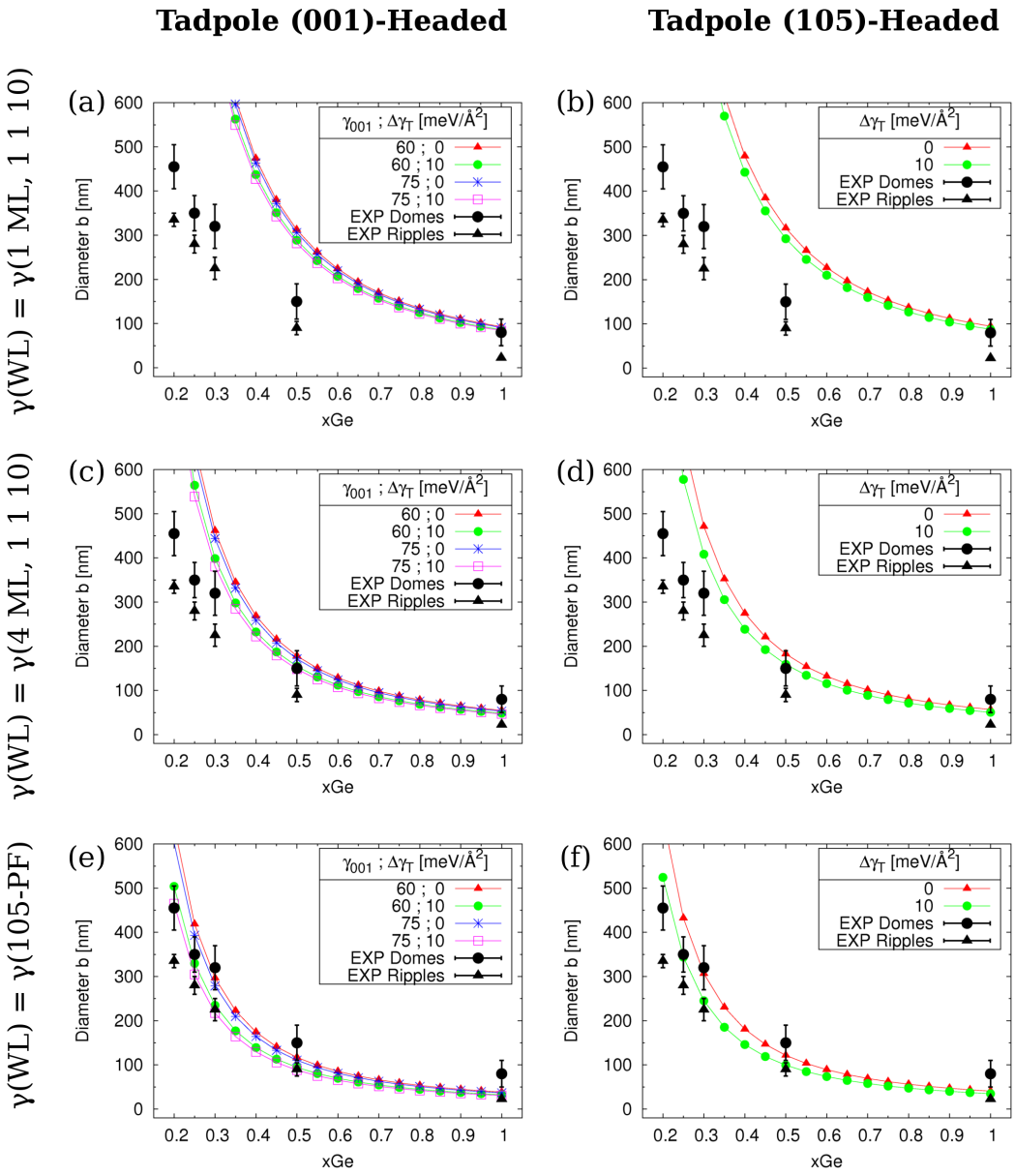

FIGURE 6.11: Results of Tadpole-to-Dome compared with the experimental energies. See discussion in sec.6.4.3.

6.5 Summary and conclusions

In this chapter we have shown the transition from the perfect faceting situation to the formation of 3D steeper islands.

We have seen the complex path leading from the breaking down of the faceting and to the developing of the domes through a "novel" island that we baptise "Tadpole" or "Fish". In this system this island is playing the role that the 105 pyramids have on other substrates (like the 001).

These detailed measurements have also allowed to identify the same facets observed on other substrates, hinting so that the shape of the islands is dictated by the surface energy of a small number of facets.

These measurements allowed to build the phase diagram of this system.

We developed a global model (the χ model) to predict these diagram, but it has some logical shortcomings. Considering, on the other hand, the transition from a single tadpole to a single dome (as observed experimentally), lead to a more reliable prediction of the critical base at which the transition occurs.

7

General conclusions and perspectives

"The scientific man does not aim at an immediate result.
He does not expect that his ideas will be readily taken up.
His duty is to lay the foundation for those who are to come,
and point the way."
Nikola Tesla

The activity of the scientific research is like a journey.
People start from a known ground and, endowed with the will to go beyond the present limits, undertake a travel. This travel may have some hardships, both conceptual and technical, and like climbing a rope or hiking a mountain, many times the road compels either to change route or to undertake considerable efforts. But once at the top of the mountain, the gain is priceless.
In the best case it can be either a new discovery that opens new fields and new perspectives on the future, or, more modestly, it can merely represents an alternative, maybe more insightful, view of some already known fields, or it allows to enjoy the known matter from a different, maybe broader, perspective.

In this thesis, we have investigated a phenomenon that has already been investigated by several groups: self-assembled nanoislands focusing on the Ge/Si prototypical case.

We have put together several ingredients sparcely present in literature, starting from the concept of the Wulff solid, the elastic field, the surface energies with their contributions, the different nucleation regimes arising from a different balance between these terms and some effects due to the presence of steps.

We have used these techniques to model the role of intermixing on patterned substrates, leading to a comparison with experiments that accounts quantitatively to the evolution pattern followed by the islands nucleated on this peculiar system.

To a larger extent we have focused our attention to the peculiar case of the islands formed on the Si(1 1 10) substrate. This substrate represents a peculiarity since here geometrical constraints prevent the {105} pyramids from forming a close solid. This has the effect to have all the islands elongated along the same direction, a geometrical factor that facilitates the complete faceting of the substrate. In chapter 5 we have shown that this faceting is compatible and explicable as a reduction of the total energy, particularly the (here dominant) surface contribution as Fig.5.8 at page 111 proves.

By following a similar reasoning in terms of the surface energy reduction, this same figure also would predict a {105} faceting on Si(001) as well. Urged by this theoretical outcomes, we performed a deep analysis of literature results on this substrate, arriving to the conclusion that here kinetic effects can play a non-negligible role and further investigations are needed.

As discussed in this thesis, the careful estimation of the energy of the nanofacets may play an important role in assessing the stability of the islands themselves. To this aim the multiscale method we have developed and described in sec.5.2 (page 98) can be improved and extended. A first relevant extension could consist in considering the facets of the dome: {113} and {15 3 23}. Considering, in particular, their dependence on the strain could help in understanding the stability of the observed shapes, since, as discussed in sec.2.4.3, the strain relaxation is not enough to predict what the precise shape of the islands is to be expected (i.e. the relative extensions of the different facets).
The same modeling could be applied to other facets appearing in the barn island as {20 4 23}, {111}, {23 4 20}.

Since we have observed the same facets appearing even in the Ge/Si(1 1 10), this analysis would have a general value on substrates other than (001).

As for the other substrates, one may ask what happens if the miscut goes beyond the 8.04° along $< 110 >$ direction, i.e. what happens if the {105} facets are not enough to make an island of finite volume. Intuitively, additional facets would form, creating a different island shape, thus a different elastic relaxation and thus different effective energy of the facets making the analysis non-trivial. This intuition is confirmed by some experimental studies where the substrate is Si(11n) with $n \sim< 10$[1]. In other cases studied in literature completely different island shape are formed, as, for instance, for Si(5 5 12) [166] (where no 105 facet appears) or on Si(113) [167].

In predicting the shape of nanoislands, we also discussed and demonstrated that the concept of the Wulff solid can be adopted to have an insight to the overall shape. And for this reason we have developed a code to handle this concept to be used as a tool.

[1] prof. Gunther Springholz, private communication

In literature some stable reconstructions of important facets have been identified, such as the one for (113) [83, 80] and even the large-scale (15 3 23) [84]. However this does not hold for any surface and indeed another rich field of research consists in the developing of global minimum research of the surface energy as, e.g. through a genetic algorithm [90].

As we have proven in this thesis, however, this search must account for the strain state of the facet, since some reconstruction may be stable if subject to a proper amount of strain (as is the case of the (105)-RS that is stable against compression).

It is noteworthy to say that, as a matter of fact, researchers have recently renovated their interest for one of the case of our study, the SiGe ripples on Si(1 1 10), not only as an example of SK growth on tilted substrate, but also to an effective, self-assembled, way to realize in-plane nanowires [162].

So our theoretical study may eventually find an application in technology.

A

Basics of Elasticity Theory

In this appendix we recall some basic concepts about elasticity theory often used in this work.

A.1 Strain tensor

Under external applied forces, any elastic medium undergoes a deformation from its equilibrium (external force-free) configuration. By denoting with **r** the position of a given point inside the medium prior of the deformation, and with **r'** its position in the deformed medium, it is possible to define the displacement field **u=r'-r** at every point. Elastic deformation is completely known when **u(r)** is known for every **r**. Given a small deformation δr, it can be written

$$u_i(\mathbf{r}+\delta\mathbf{r}) = \mathbf{u_i}(\mathbf{r}) + \frac{\partial \mathbf{u_i}(\mathbf{r})}{\partial \mathbf{x_k}} \cdot \delta \mathbf{x_k}$$

where the derivatives $\partial_k u_i$ defines the components of a rank 2 tensor γ_{ik}, which can be decomposed into a symmetric and an anti-symmetric part:

$$\epsilon_{ik} = \frac{1}{2} \cdot \left(\frac{\partial u_i}{\partial x_k} + \frac{\partial u_k}{\partial x_i} \right); \quad \omega_{ik} = \frac{1}{2} \cdot \left(\frac{\partial u_i}{\partial x_k} - \frac{\partial u_k}{\partial x_i} \right)$$

In other words, any possible deformation of the elastic body is decomposed into one rotation, described by the tensor ω_{ik}, and one distortion, which is described by ϵ_{ik}. The tensor ϵ_{ik} is the **strain tensor**. As it is clear from its definition, ϵ is symmetric: $\epsilon_{ik} = \epsilon_{ki}$.

Figure A.1 is intended to show the physical meaning of each strain tensor component. The on-diagonal components represent the relative variation of length (deformed, def) with respect to the undeformed case (l_0)

$$\epsilon_{ii} = \frac{l_{def} - l_0}{l_0}$$

In the case of hepitaxy Ge/Si the strain is:

$$\epsilon = \frac{a_{Si} - a_{Ge}}{a_{Ge}} \simeq -4.0\%$$

The off-diagonal components are proportional to the variation of the angle between adjacent axes. For instance, the variation (from 90°) of the angle between axis 1 and 2 is

$$\Delta\alpha_{12} = 2 \cdot \epsilon_{12}$$

If dV is the volume of a small portion of the solid before the deformation and dV' is the volume of the same portion after the deformation, those quantities are linked by the relation [58]

$$dV' = dV \cdot (1 + Tr(\epsilon))$$

This means that the trace of the strain tensor is the relative volume change with deformation $(dV' - dV)/dV$

Likewise the undeformed and deformed area in the plane xy (A_0 and $\widetilde{A}$, respectively) are linked by:

$$\widetilde{A} = A_0 \cdot (1 + \epsilon_{xx} + \epsilon_{yy})$$

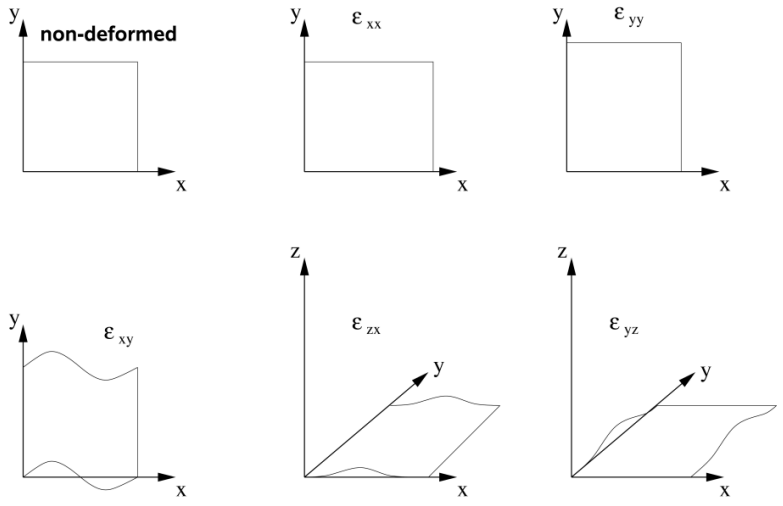

FIGURE A.1: Geometrical meaning of the strain tensor components

A.2 Stress and stiffness tensor

The elastic response of a medium under applied external forces is completely described by the stiffness tensor C_{ijkl}. This tensor links stress to strain tensor, since it holds

$$\sigma_{ij} = C_{ijkl} \cdot \epsilon_{kl}$$

The tensor C_{ijkl} have several symmetries. The symmetry of the stress tensor implies that $C_{ijkl} = C_{jikl}$, while the symmetry of the strain tensor implies $C_{ijkl} = C_{ijlk}$. Finally, from thermodynamic arguments it is possible to demonstrate that $C_{ijkl} = C_{klij}$.

Since both σ and ϵ are symmetric tensors, this means that each one has six independent coefficients.

It is thus useful to use Voigt indexes, to simplify the notation.
Making the following statements:

$$xx \to 1; yy \to 2; zz \to 3; xy \to 4; yz \to 5; xz \to 6$$

it is possible to explicit C_{ijkl} with only two indexes; this way the stress-strain relaxation can be written as

$$\begin{aligned}
\sigma_{xx} &= C_{11}\epsilon_{xx} + C_{12}\epsilon_{yy} + C_{13}\epsilon_{zz} + C_{14}\epsilon_{yz} + C_{15}\epsilon_{zx} + C_{16}\epsilon_{xy} \\
\sigma_{yy} &= C_{21}\epsilon_{xx} + C_{22}\epsilon_{yy} + C_{23}\epsilon_{zz} + C_{24}\epsilon_{yz} + C_{25}\epsilon_{zx} + C_{26}\epsilon_{xy} \\
\sigma_{zz} &= C_{31}\epsilon_{xx} + C_{32}\epsilon_{yy} + C_{33}\epsilon_{zz} + C_{34}\epsilon_{yz} + C_{35}\epsilon_{zx} + C_{36}\epsilon_{xy} \\
\sigma_{yz} &= C_{41}\epsilon_{xx} + C_{42}\epsilon_{yy} + C_{43}\epsilon_{zz} + C_{44}\epsilon_{yz} + C_{45}\epsilon_{zx} + C_{46}\epsilon_{xy} \\
\sigma_{zx} &= C_{51}\epsilon_{xx} + C_{52}\epsilon_{yy} + C_{53}\epsilon_{zz} + C_{54}\epsilon_{yz} + C_{55}\epsilon_{zx} + C_{56}\epsilon_{xy} \\
\sigma_{xy} &= C_{61}\epsilon_{xx} + C_{62}\epsilon_{yy} + C_{63}\epsilon_{zz} + C_{64}\epsilon_{yz} + C_{65}\epsilon_{zx} + C_{66}\epsilon_{xy}
\end{aligned}$$

In addition to that, the symmetry of the crystal imposes further reduction to the independent coefficient in the stiffness tensor.
Depending on the type of crystal, there are 21 independent components in the case of the triclinic crystal, 13 for the monoclinic, 9 for the orthorhombic and 3 for the cubic.

The latter ones are usually mentioned as C_{11}, C_{12}, C_{44} leading to a stiffness tensor in Voigt notation as the following:

$$C_{ij} = \left[\begin{array}{ccc|ccc} C_{11} & C_{12} & C_{12} & 0 & 0 & 0 \\ C_{12} & C_{11} & C_{12} & 0 & 0 & 0 \\ C_{12} & C_{12} & C_{11} & 0 & 0 & 0 \\ \hline 0 & 0 & 0 & C_{44} & 0 & 0 \\ 0 & 0 & 0 & 0 & C_{44} & 0 \\ 0 & 0 & 0 & 0 & 0 & C_{44} \end{array}\right] \tag{A.1}$$

Generally the crystals are anisotropic, i.e. their properties depend on the direction. In the case of cubic crystals, the behaviour is perfectly **isotropic** if the following holds:

$$C_{44} = \frac{C_{11} - C_{12}}{2} \tag{A.2}$$

The quantification of the grade of anisotropy is, therefore, the factor of anisotropy A [58]

$$A = C_{44} - \frac{C_{11} - C_{12}}{2} \tag{A.3}$$

If A=0, the system is isotropic, the larger A in modulus, the larger the anisotropy.

To deform the medium, external forces must do work, which must equal the elastic energy stored by the medium in consequence of the applied forces. The correspondent **elastic energy density** is definite as

$$\begin{aligned} \rho &\equiv \frac{1}{2} \cdot C_{ijkh} \cdot \epsilon_{ij} \cdot \epsilon_{kh} && \text{(A.4)} \\ &= \frac{1}{2} C_{11}(\epsilon_{xx}^2 + \epsilon_{yy}^2 + \epsilon_{zz}^2) + \frac{1}{2} C_{44}(\epsilon_{yz}^2 + \epsilon_{zx}^2 + \epsilon_{xy}^2) + \\ &+ C_{12}(\epsilon_{xx}\epsilon_{yy} + \epsilon_{yy}\epsilon_{zz} + \epsilon_{xx}\epsilon_{zz}) && \text{(A.5)} \end{aligned}$$

Where the latter equation holds in the case of cubic materials [59]. It is noteworthy that the relation stress-strain here adopted is a linear one (that is an anisotropic version of the Hooke's law). That is why this theory is also called Linear Elasticity Theory (LET)[1] and it is a good approximation for small strain values [59] although the real crystal can have non linear effects.

A.3 Alloys

The previous definitions are general and are valid for a GeSi alloy as well.

As discussed in Chapter 3, intermixing is a possible channel available to the system to relax strain and, further, an alloy of GeSi can be deposited directly on Si.

It is generally assumed [67, 168], that the lattice constant in an alloy is subject to the Vegard law, that implies it is the linear combination of the constants in the pure materials averaged over the concentration. A similar trend is supposed to hold for the stiffness constants. Therefore, an alloy $Si_{1-x}Ge_x$, where x is the fraction of Ge, is modeled to have a lattice constant and stiffness tensor equal to:

$$\begin{aligned} a &= a(Ge) \cdot x + a(si) \cdot (1 - x) && \text{(A.6)} \\ C_{ij} &= C_{ij}(Ge) \cdot x + C_{ij}(Si) \cdot (1 - x) && \text{(A.7)} \end{aligned}$$

[1] or Harmonic Elasticity Theory since the energy is quadratic in the deformation

B

Description of surfaces

In this appendix the convention used to describe the surfaces are reported.

B.1 Describing a general surface

In a crystal a plane is identified by the normal to the plane itself, that is a direction. A general direction in a crystal is described as sketched in Figure B.1: a versor (unitary vector) in a 3D space $\underline{n}$.

This versor can be described either in terms of the three cartesian components $[n_1, n_2, n_3]$ (panel a) [1] or in terms of the two Eulerian angles (θ, φ) (panel b).

The former (θ) is called co-latitude or, in the case of vicinal surfaces, miscut and is the angle between $\underline{n}$ and the z axis.

The latter (φ) is called longitude (or azimuth) and is the angle between the projection of $\underline{n}$ on the xy plane and the x axis.

When the indexes n_j are prime among themselves they are called Miller indexes.

Given a generic direction (n_1, n_2, n_3), the following relations hold:

$$\tan\varphi = \frac{n_2}{n_1} \tag{B.1}$$

$$\tan\theta = \frac{\sqrt{n_1^2 + n_2^2}}{n_3} \tag{B.2}$$

and the reciprocal ones:

$$n_1 = |n| \cdot \cos\varphi \cdot \sin\theta \tag{B.3}$$

$$n_2 = |n| \cdot \sin\varphi \cdot \sin\theta \tag{B.4}$$

$$n_3 = |n| \cdot \cos\theta \tag{B.5}$$

[1] an exception to this are the exagonal crystals that need 4 numbers to be fully identified but this case is not treated in this thesis

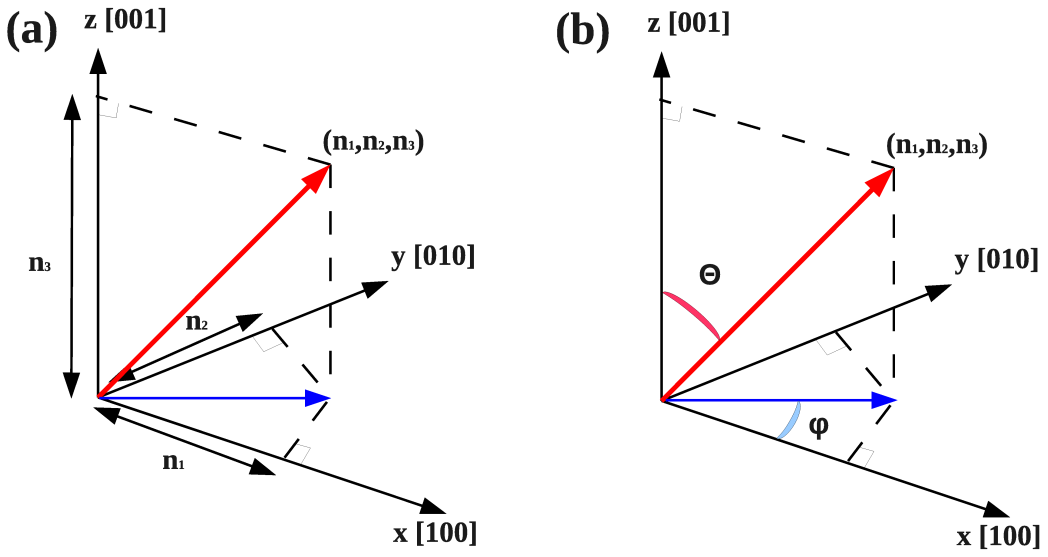

FIGURE B.1: Surface description in terms of the (a) Miller indeces of the normal or (b) the Eulerian angles. φ is the azimuth (or longitude), θ the miscut (or co-latitude).

C

Strained surface energies: What chemical potential to use?

C.1 Statement of the problem

By definition, the surface energies must describe properties of the surfaces alone, without including volume (bulk) effects.

In the slab configuration discussed in sec.2.5 at page 56, the bulk contribution is cancelled out from γ through the chemical potentials μs, therefore the concern is to give μ the proper value.

For an unstrained solid, the value to use is trivially the bulk one. But when the surface is strained isotropically or anisotropically along two directions x and y, a strain along the z (free) direction must be considered as well because of the Poisson effect (see sec.2.4.2). Since in this thesis we are dealing with relaxed surfaces, it appears natural that the chemical potential must be computed taking these two effects into account, yet this was not clear at the first attempts of such calculations and in literature some "misleading" and confusing results can be found.

Our aim here is to perform a systematic analysis of the effects on γ if chemical potentials at different strain states are used, to **prove** that the Poisson relaxation along z must be taken into account to avoid non-sensical results.

The analysis is performed for Ge and Ge/Si systems for different in-plane strains focusing not only on the case -4% (Ge/Si case) but also for higher strain up to -7% with the aim of studying the effect of higher deformation. This latter value of strain is the one for the system InAs/GaAs, that is the prototype for III-V compounds. Tersoff potential is employed as a benchmark for the simplicity and speed of calculation on a pure Ge cell. First principles results are used to study the dependence on epilayer thickness for Ge/Si cells. Last, it is shown the importance of considering anisotropy in the chemical potential as well.

C.2 Chemical potentials employed

The chemical potentials are computed by straining an 8-atoms conventional bulk cell in a proper way, as already described in sec.5.3.1 (page 103).

Let us suppose that the surface is subject to a strain along x and y equal to $(\epsilon^*_{xx}, \epsilon^*_{yy})$. The different chemical potentials are computed on a bulk cell strained along x,y,z with the strain $\mu = \mu(\epsilon_{xx}, \epsilon_{yy}, \epsilon_{zz})$ according to the following definitions.

- $\mu_0 \equiv \mu(0,0,0)\%$: the case of the **unstrained** bulk
- $\mu_S \equiv \mu(\epsilon^*_{xx}, \epsilon^*_{yy}, 0)\%$: strained situation, no Poisson effect taken into account, i.e. the bulk is strained along x and y by the external stress while it is left at its unstrained bulk position along z
- $\mu_P \equiv \mu(\epsilon^*_{xx}, \epsilon^*_{yy}, \epsilon_{zz})\%$: Poisson effect taken into account, i.e. the bulk is strained along x and y by the external stress and along z it is strained according to the Poisson effect

C.3 A simple test: Ge(001)-AC using Tersoff

The effect of the surfaces should be the same regardless of the thickness of the cell used in the calculations: the same physical effects should occur at the surface for very thick or moderately thin slabs.

This property is used as a benchmark to test the chemical potentials of the previous section.
The cell adopted is the most simple one: a pure Ge cell of the (001) unreconstructed surface (as cut, AC), where direction x is [100], y is [010], z is [001]. This is studied with Tersoff potential since it allows to analyze very thick slabs with no computational problems. All the atoms are free to relax in the cell (no atom is kept fixed), the maximum allowed force being 10^{-6} eV/Å in modulus. For simplicity the in-plane strain applied to the cell is isotropic: $\epsilon^*_{xx} = \epsilon^*_{yy} \equiv \epsilon^*$.

The chemical potentials used are plotted in Figure C.1 where different ϵ_{zz} are applied to a bulk strained along x and y. There the used values of the chemical potentials are highlighted with black points. It is evident that the difference between μ_P and μ_0 is higher for higher in-plane strain values.

In this case the chemical potential used are:

- $\mu_0 \equiv \mu(0,0,0)\% \simeq -3.85059$ eV/atom
- $\mu_S(1) \equiv \mu(-4,-4,0)\% \simeq -3.80521$ eV/atom
- $\mu_P(1) \equiv \mu(-4,-4,2.813)\% \simeq -3.81344$ eV/atom
- $\mu_S(2) \equiv \mu(-7,-7,0)\% \simeq -3.70187$ eV/atom
- $\mu_P(2) \equiv \mu(-7,-7,5.608)\% \simeq -3.73424$ eV/atom

In this case the slab is symmetric and the surface energy is given by:

$$\gamma = \frac{E^{TOT} - N_{Ge} \cdot \mu_{Ge}}{2 \cdot A} \tag{C.1}$$

Figure C.2 shows the values of the SE for different thickness of the cells in the case of $\epsilon = -4\%$ (top) or $\epsilon = -7\%$ (bottom). The following properties can be deduced:

1. if μ_P is used, the SE is very **stable** as a function of the cell thickness (up to the fourth decimal digit in this case)

2. if a $\mu < \mu_P$ is used (such as μ_0), the surface energy will monotonically **increase** for thicker cells and it will diverge

3. if a $\mu > \mu_P$ is used (such as μ_S), the surface energy will monotonically **decrease** till it becomes negative (that is physically non-sensed)

The explanation of these trends are easily found if the energy per atom is compared with these chemical potentials.

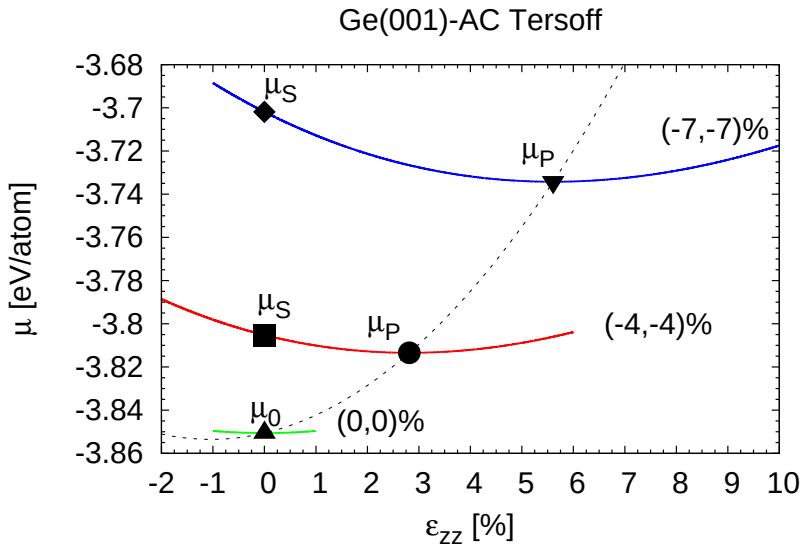

FIGURE C.1: Chemical potentials used for the case Ge(001)-AC analyzed with Tersoff potential from a strained bulk calculation. The values in parenthesis near to each curve are the strain applied along [100] and [010]. The CPs described in section C.2 are highlighted by black points. The Poisson corrected value is defined as the minimum of each curve at different ϵ_{zz}. The dotted line connecting the μ_Ps is the same line as in Fig.2.3 at page 43.

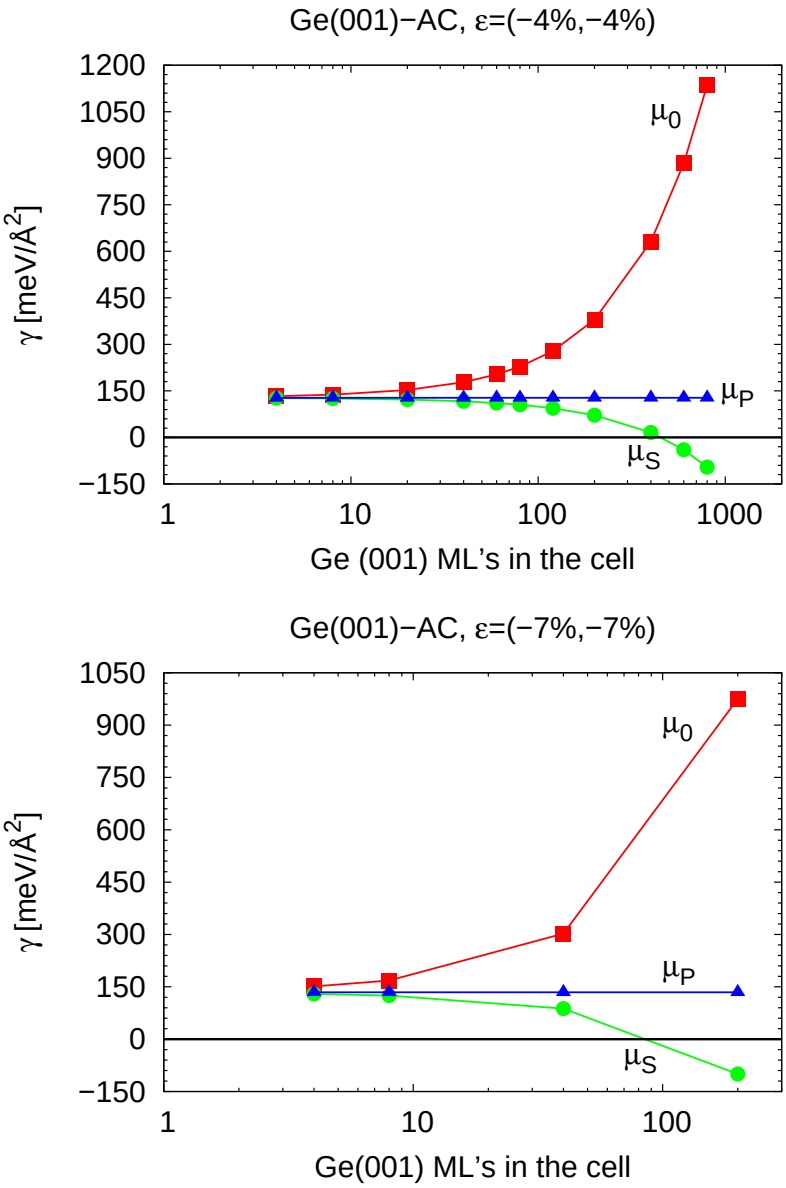

FIGURE C.2: Trend of the surface energy for Ge(001)-AC with Tersoff potential as a function of the cell thickness for different values of μ_{Ge}. TOP = case of $\epsilon = -4\%$. BOTTOM = case of $\epsilon = -7\%$. In both cases the values are very stable if the Poisson-corrected value μ_P is used, otherwise, the trend is monotonically increasing or decreasing. The derivative is higher the higher the strain applied (bottom figure). This shows that the chemical potential to use for strained surfaces is the Poisson-corrected one.

C.3.1 Explanation in terms of energy per atom

In the case of semiempirical potential the total energy E^{TOT} is simply the sum over the energy of the single atoms E_i. Since the chemical potential μ is the same for all the atoms, the surface energy can be expressed as follows:

$$\gamma = \frac{1}{2A} \cdot \sum_{i=1}^{N_{Ge}} [E_i - \mu] \tag{C.2}$$

From this we can deduce that in order to have an independence of the cell thickness (that is N_{Ge}), the atoms in the middle of the cells must have the same energy as the bulk. It is this energy to be therefore taken as a reference bulk. By comparing the energy per atom in the cells with the chemical potentials used, their difference can be highlighted.

Figure C.3 shows the energy per atom for all the cells analyzed in the case of $\epsilon = -4\%$. The top panel shows that the atoms in the central part of the cell have all the same energy regardless of the thickness. The bottom panel shows that the value μ_P coincides with these common value, while the others do not.

Therefore when a CE other than μ_P are used, the central atoms still have a contribution to the SE, leading to a monotonic trend.

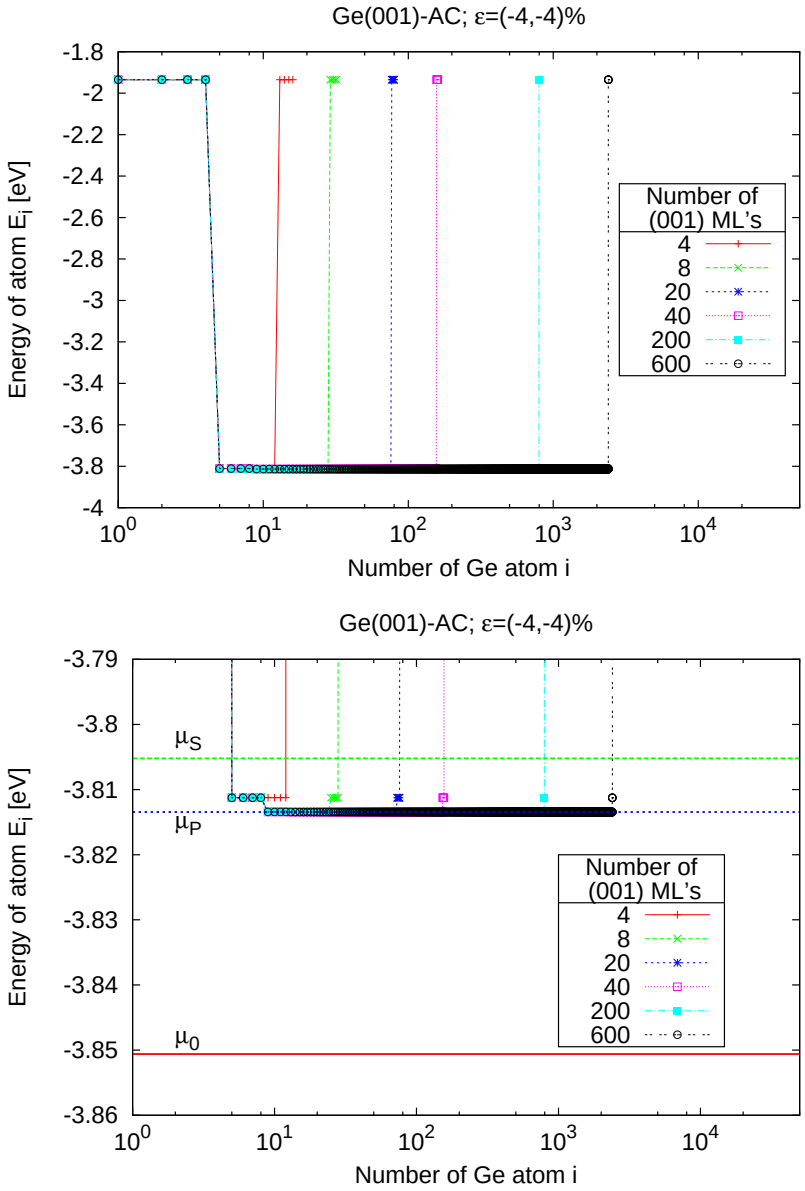

FIGURE C.3: Comparison of the chemical potentials with the energy per atom in the case of a slab Ge(001)-AC analyzed with Tersoff in the case of $\epsilon = -4\%$. The atoms are numbered from the top of cell to the bottom. TOP = large scale image showing the atoms in the central part of the cell to have all the same energy regardless of the thickness. BOTTOM = enlargement comparing the chemical potential with this energy of the central atoms.

C.4 Effects on trend with epilayer thickness

The previous analysis shows that when the Poisson corrected CP is not used as the bulk reference, some errors are introduced proportional to the number of atoms of the strained species.

In literature, the typical analysis performed is the one as a function of coverage (as performed in this work at sec.5.3.4, page 109). In this case the Ge atoms are a few, additionally the exponential trend described in sec.2.5.5 at page 65 is superimposed on the possible error due the use of an improper chemical potential. In order to have a criterion for the choice of the CP, here we explain a procedure to identify the correct trend.

The cell employed is an asymmetric one where Ge is on top and Si below (like the 1 1 10 cell studied in this thesis). Along z the cell contains 30 unit cells ($\sim$ 163 Å) and no atom is kept fixed. In increasing the Ge coverage the correct number of the topmost Si atoms are turned into Ge. The total energy of such a cell is:

$$E^{TOT} = N_{Si} \cdot \mu_{Si} + N_{Ge} \cdot \mu + A \cdot \gamma_T + A \cdot \gamma_B \tag{C.3}$$

In this case the CP of Si is its value μ_0 since no strain is applied to silicon, instead the CP for Ge is computed when strained at the lattice constant of Si. The value of interest is γ_T and γ_B is computed from a relaxed pure Si cell.

The trend with deposition in the case of Ge/Si(001)-AC analyzed with Tersoff is reported in figure C.4-(a). As equation (2.45) (page 65) suggests, at a large enough coverage the value should stabilize to a definite value γ_∞.
The only curve that fullfils this property is the one obtained with $\mu = \mu_P$.
In the case of μ_0 the trend will predict that the thicker the Ge layer the higher the SE, leading to a value $\gamma(Ge) > \gamma(Si|N_{Ge} = 0)$, that is against any known results. This increase in surface energy has been reported in some early article [169] showing that at that time a confusion of what chemical potential to use was present.
In the other case (μ_S), a monotonic decrease is observed.

In all the curves a local minimum is found at 1 ML coverage: this is a problem of Tersoff potential in dealing with the interfaces and has nothing to do with the chemical potential chosen.

To get rid of this problem, a check with DFT-LDA is done where the top surface is reconstructed as the (001)-2x8-DVL (the details of the cell and of the reconstruction are described in sec.5.3.1, page 103). A reconstructed surface in the case of ab initio calculation is needed to achieve convergence, otherwise the atoms will not find their stable positions. The results are reported in Figure C.4-(b), where it is evident that the minimum at 1 ML has disappeared.

Since eqn (2.45) is appliable with DFT-LDA data, we can use this trend as a check for the chemical potential.

Table C.1 reports the value of the reduced χ square of the fit with this equation. The case with μ_0 cannot be fitted since the trend is not monotonically decreasing. The case with μ_S has a moderately high value ($\sim$ 4), but the one with μ_P has a very low value ($\sim$ 0.5), as it should be. Therefore we can conclude that **just the Poisson corrected**

chemical potential leads to a trend with deposition that is in accordance with the theoretically expected exponential trend.

μ used	χ^2 with eqn (2.45)	χ^2 with eqn (C.9)
μ_0	does not fit	0.1919
μ_S	4.1232	0.2047
μ_P	0.5424	0.2019

TABLE C.1: Reduced χ^2 of the DFT-LDA results for Ge/Si(001)-2x8-DVL for different chemical potentials used. The second column shows the interpolation for the equation $\gamma(\mu) = (\gamma_0 - \gamma_\infty) \cdot e^{-B \cdot x} + \gamma_\infty$ i.e. the analitically expected trend for the correct values. The third column shows that the general relation found is a good trend. Just the Poisson corrected value μ_P has a good fit (low χ^2 value) for the theoretically expected trend, i.e. this is the proper CP to use.

We can also deduce an analytical trend for the general case where even a 'wrong' CP is employed.

For porpose of generality, let us consider a generic normal direction n_3. Let μ_P be the correct chemical potential to use and μ be the one used.
Since both the total energy of the cell and γ_B are the same regardless of the Ge chemical potential, from eqn (C.3) we get the deviation of the obtained SE from the correct one:

$$\gamma(\mu) - \gamma(\mu_P) = \frac{N_{Ge}}{A_0 \cdot (1+\epsilon)^2} \cdot (\mu_P - \mu) \tag{C.4}$$

Where the area A_0 is the area of the Un-strained material. Using the geometric properties discussed in sec.2.5.2 at page 56, we can express this quantity as a function of the number of (001)ML D_{001}, as is the habit in theory (see discussion at sec.2.5.5, page 65). By defining $\widetilde{A}$ as the area of the surface per unit lattice constant, a_0 as the lattice constant of the unstrained bulk and D_3 as the number of n_3 MLs, we get the following relation:

$$\begin{aligned} \frac{N_{Ge}}{A_0} &= D_3 \cdot \frac{N_3}{\widetilde{A}} \cdot \frac{1}{a_0^2} && \text{(C.5)} \\ &= \left(\frac{|n_3|}{f_3} \cdot D_{001} \right) \cdot \left(2 \cdot \frac{K_3 \cdot f_3}{|n_3|} \right) \cdot \frac{1}{a_0^2} && \text{(C.6)} \\ &= 2 \cdot K_3 \cdot D_{001} \cdot \frac{1}{a_0^2} && \text{(C.7)} \end{aligned}$$

Hence:

$$\gamma(\mu) - \gamma(\mu_P) = \frac{2 \cdot K_3 \cdot D_{001}}{a_0^2 \cdot (1+\epsilon)^2} \cdot (\mu_P - \mu) \tag{C.8}$$

Since everything is a constant for a fixed μ, by introducing $\gamma(\mu_P)$ in this equation and calling $D_{001} = x$ we get the functional relation for a generic SE with a generic μ:

$$\boxed{\gamma_\mu(x = D_{001}) = (\gamma_0 - \gamma_\infty) \cdot e^{-B \cdot x} + \gamma_\infty + A \cdot x} \tag{C.9}$$

The fits with this function are the lines in Figure C.4-(b) and the reduced χ^2 are reported in Table C.1 showing a good agreement for all the curves, that prove the quality of such trend.

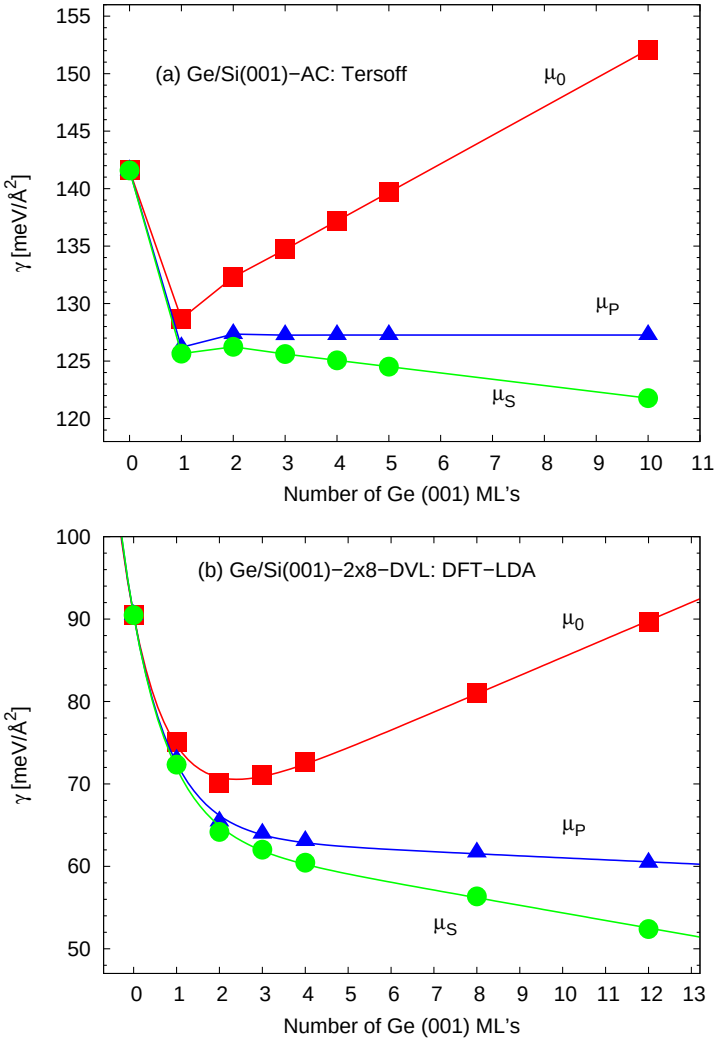

FIGURE C.4: Effect of using different CPs in the case of Ge/Si(001). (a) = Tersoff potential results for the AC cell. (b) = DFT-LDA results for the 2x8-DVL reconstruction. In (b) the lines are the interpolation with eqn (C.9), whereas in (a) they are just to guide the eye.

C.5 Effects of neglected anisotropy

As described in sec.2.4.2 at page 40, crystals have a highly anisotropic elastic response. In particular the chemical potential for a fixed in-plane-strain assumes different values for different surfaces, due to a different Poisson relaxation.
When considering surfaces other than (001), therefore, the chemical potential to use is the one strained in the direction analyzed.

In order to clarify the important role of anisotropy, our purpose here is to quantify the error introduced in the surface energy if anisotropy is neglected, that is if the $\mu_P(001)$ is used instead of the Poisson-corrected value of the CP along the analyzed direction. Let define γ_{001} the former and γ_n the latter. Here the interest is in quantifying the difference $\gamma_n - \gamma_{001}$ regardless of the exact value of the energy. Following the steps outlined to deduce eqn (C.8), this difference when the strain is applied in plane to the surface can be expressed just as a function of the chemical potential as follows:

$$\gamma_n - \gamma_{001} = -\frac{N_{Ge}}{A_0 \cdot (1+\epsilon)^2} \cdot [\mu_P(n) - \mu_P(001)] \quad \text{(C.10)}$$

$$= -\frac{2 \cdot K_3}{a_0^2 \cdot (1+\epsilon)^2} \cdot D_{001} \cdot [\mu_P(n) - \mu_P(001)] \quad \text{(C.11)}$$

This can be used to check the effect both of Ge/Si cells and for pure Ge cells containing D_{001} MLs (001) of Ge.

These trend using the Tersoff potential are reported in Figure C.5.
Panel (a) reports the values of $\mu_P(n) - \mu_P(001)$ that have already been deduced in sec.2.4.2. This shows that the chemical potential has a larger difference wrt the (001) one the larger the strain in modulus.

Since the difference in surface energy is proportional to $\Delta\mu$ this trend is present in $\Delta\gamma$ as well. This is shown in Panel (b) where eqn (C.11) is plotted for the case of $D_{001} = 1ML$, that is a single ML of Ge is present in the cell. Panel (c) shows the same trend for the case of $D_{001} = 20ML$, that is the typical thickness of a pure Ge cell to guarantee the independence of the two surfaces from each other, showing that in such cells neglecting the anisotropy can lead to misleading results. Panel (d) focuses on the difference observed at the strain-in-plane equal to -4% (the case Ge/Si) for both cell thickness.

Figure C.6 shows the results for the case of DFT-LDA in case the strain in plane is -4%. Panel (a) shows the difference in chemical potential, whereas panel (b) the difference in SE for 1 and 20 MLs (001) of Ge in the cell.

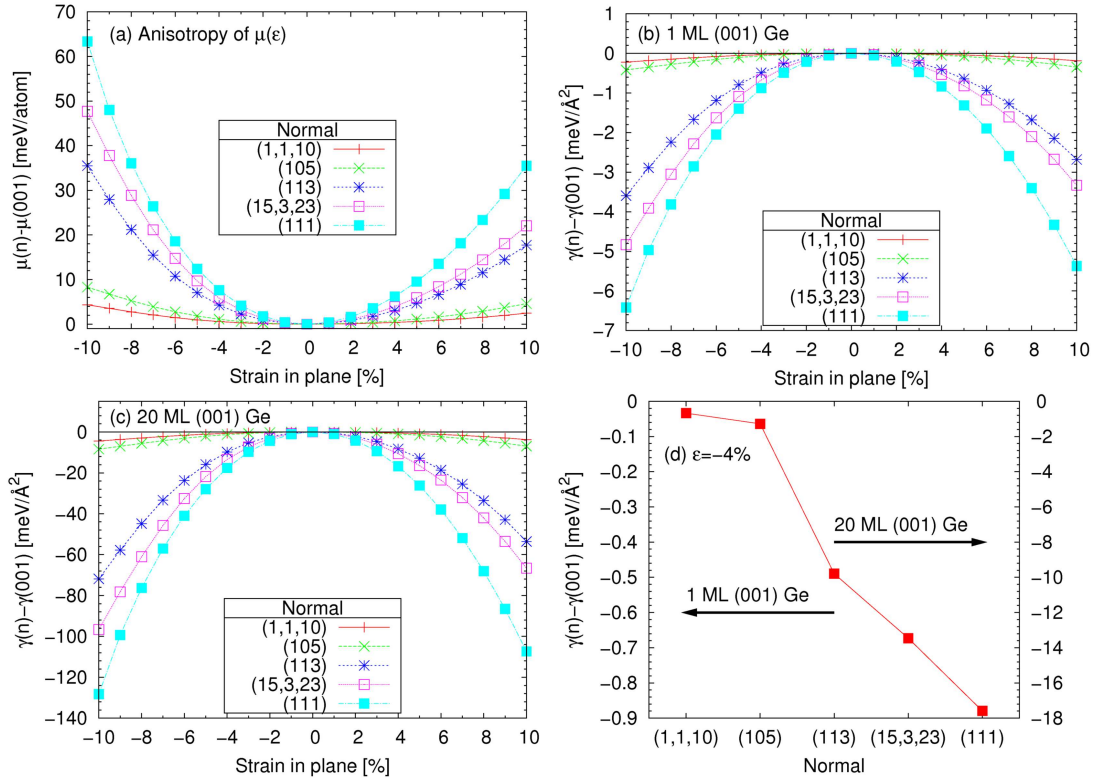

FIGURE C.5: Effect of neglecting anisotropy by using Tersoff potential. Panel (a) shows the difference of the anisotropic CP with μ_{001} computed along (001) for some directions in the stereographic triangle. Panel (b) and (c) show the difference in SE for 1 ML (001) and 20 MLs (001) Ge respectively for different strain states. Panel (d) focuses on the Ge/Si case of $\epsilon = -4\%$: left y axis refers to 1 ML Ge, the right one for 20 ML Ge.

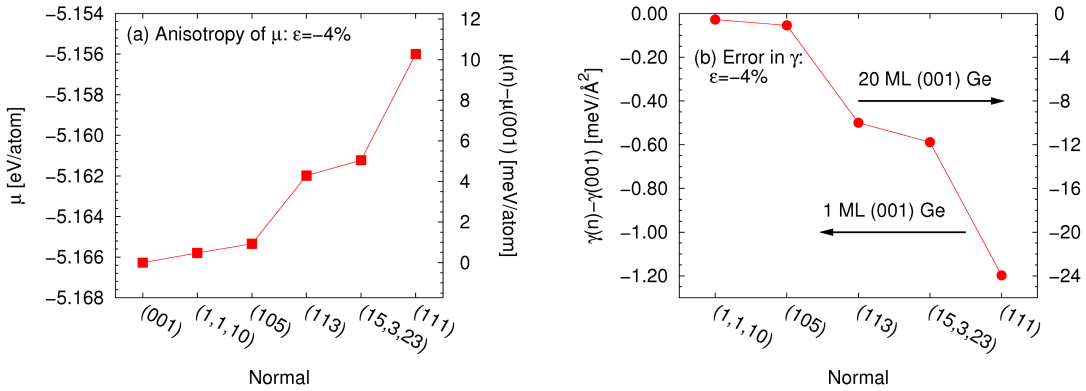

FIGURE C.6: Effect of neglecting anisotropy by using DFT-LDA approach for a biaxial strain $\epsilon = -4\%$. Panel (a) shows the chemical potential obtained (left y axis) along with the difference with the value at (001) (right y axis). Panel (b) show the difference in SE for 1 ML (001) (left y axis) and 20 MLs (001) Ge (right y axis) for these values of the chemical potential and with this strain.

In both cases we can deduce that if the anisotropy in μ_P is neglected:

1. a great error in surface energy can be obtained for cells with typical thickness used in calculations (lower value predicted)
2. the higher the number of Ge atoms (ML), the higher the error
3. the higher the strain (absolute value), the higher the error
4. typically, the steeper the surface wrt (001), the higher the error

C.5.1 Check for real reconstruction

Strictly speaking, eqn (C.11) is valid just for bulk-like (AC) cells since the relations used to derive it are so. However it turns out to be approximately valid even for a real, reconstructed surface as shown here.

Let us consider the same slab of Ge/Si(105)-RS studied in sec.5.3, page 103.
The surface energies obtained as a function of Ge epilayer thickness are reported in Figure C.7-(a) where the chemical potential used are both the Poisson-corrected $\mu_{P(105)}, \mu_{P(001)}$ and the non-Poisson-corrected $\mu_{S(105)}, \mu_{S(001)}$. This shows again that a use of μ_S leads to a monotonic decrease of the values.
In this case eqn (C.11) becomes:

$$\gamma_{105} - \gamma_{001} = - \frac{2 \cdot 1}{a_0^2 \cdot (1+\epsilon)^2} \cdot D_{001} \cdot [\mu_P(105) - \mu_P(001)] \tag{C.12}$$

This theoretical trend is plotted in panel (b) (black line) along with the real difference obtained by this reconstructed surface. As evident the deviation of the actual calculations (red points) is very close to the one predicted by the As-Cut cell.

This shows the almost general validity of the relation found and that it can be used as a check for quality of the obtained results.

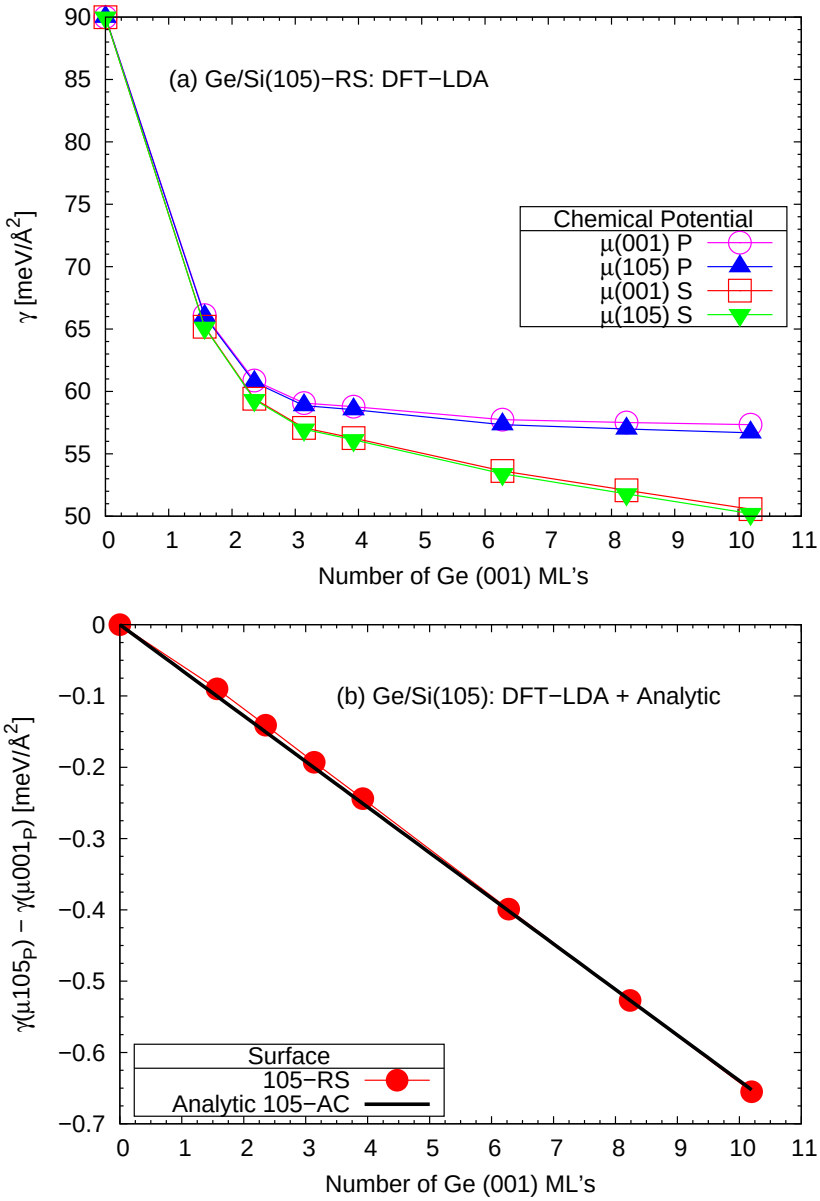

FIGURE C.7: Ge/Si(105)-RS analyzed with DFT-LDA. (a) trend with Ge coverage with different chemical potential considering or not the anisotropy (105 and 001 respectively) and considering or not the Poisson relaxation (P and S respectively). Panel (b) compares the value of eqn (C.11) for the ideal case of the AC surface with the actual values for this case. The agreement is good.

C.6 Conclusion

In this Appendix I have shown that in modelling the surface energy, the correct chemical potential for strained material must have the following properties:

1. must be strained in xy (plane direction) according to the extrenally applied strain
2. the strain state along z (normal to the surface) must be the one predicted by the Poisson relaxation
3. the directions x,y,z must be the ones of the surface, i.e. the anisotropic nature of crystals must not be neglected

Therefore, all the results of surface energy values should be computed using a chemical potential obtained following these rules (as performed in this thesis).

D

Other surfaces studied (preliminary work)

In this appendix I present some (preliminary) results, not necessarily connected to the problem of ripples, obtained during the PhD period.

I apply the methods developed in the thesis to the study additional important surfaces for the nanostructures (secs.D.1 and D.2) and show a method to take the intermixing into account by combining semiempirical calculations with a Monte Carlo approach and DFT-LDA results (sec.D.3).

D.1 (113) surface

D.1.1 Interest and motivation

As discussed in this thesis, the (113) facet is one of those appearing in the Dome structure of Ge/Si islands. Therefore the estimation of its energy is of paramount importance in assessing from an ab initio approach the surface energy of the nanoislands. In particular, its dependence on strain could help in elucidating the stability of domes with different relative extensions of the facets to predict its shape in conjunction with the elastic relaxation described in sec.2.4.3 at page 50.

Along with this, the Si(113) has been studied in the past because of its potential as a substrate for quantum wire formation[1] [170].

D.1.2 Previous works

Because of the reasons just outlined the focus at the beginning was given to the (113) surface of silicon, as in Ref.[171, 172].

The most complete treatment of this surface with the reconstructions actually observed with LEED [170] is Ref.[173]. Here the authors used a Car-Parrinello-like technique with LDA and got surface energies of Si of the order of 95-111 meV/Å^2.

This estimation of the surface energy is slightly reduced in subsequent papers by Stekolnikov et al [80, 174], where both Si ($\sim$ 87.4 meV/Å^2) and Ge surface ($\sim$ 61.7 meV/Å^2) are computed in a DFT-LDA approach. In this case all the surfaces are unstrained.

At present no study of the dependence of the surface energy as a function of Ge coverage on Si or of strain applied to the surface has been performed. The latter dependence can play an important role to check possible strain-induced surface reconstruction shift.

Here we aim to fill this gap of knowledge by adopting the same procedure as used in this thesis, i.e. by comparing DFT-LDA and Tersoff potential. For the former we adopt the same parameters described in sec.2.3 (page 36). For the k-points sampling we exploit the results in sec.5.3.3 and adopt the "bulk criterion".

D.1.3 Bulk chemical potential

The chemical potential is computed as described in Chapter 5.3.1, i.e. by properly straining a conventional 8 atoms cell.

The values for Ge in a DFT-LDA approach are reported in Fig.D.1. There panel (a) shows the trend of the energy per atom for a biaxial in-plane compression equal to -4% at different strain along z with the aim to find the chemical potential (black point). Panel (b) reports the trend of the chemical potential μ so determined for different values of biaxial strain.

[1] this was believed before the studies on the Si(1 1 10)

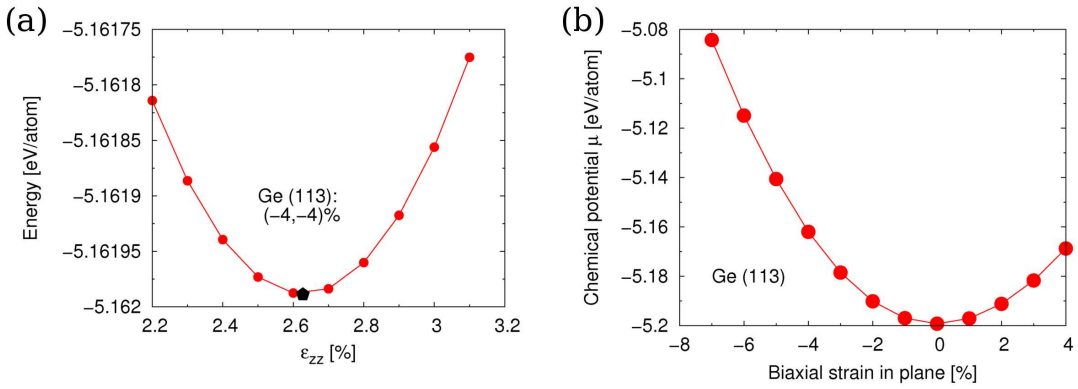

FIGURE D.1: Ge(113)-DFT-LDA: Chemical potential. In (a) we report the method to find the chemical potential (black point) by varying the strain along z for fixed values of in-plane strain (in this case equal to -4%). (b) shows the obtained values of μ for different in-plane strains.

D.1.4 Cell geometries and reconstructions

The (113) surface is a O-type one[2], so it is composed of bilayers (BL), see Fig.2.12-(d), page 59. From Tab.2.3 at page 60, we see that a single AC cell contains 44 (113) MLs. Actually this value refers also to the "missing layers"[3]. Since, however, the distance between one BL and the next one is 4 "fictitious MLs" we get that the cell contains: 44 ML / 4 (ML/BL) = 11 BLs (113).

We study the reconstructions proposed in Ref.[173] and studied also in Ref.[174], but we neglect the buckled ones. Fig.D.2 reproduces the cells used and the top view of the reconstructions that we baptise as:

- A = As Cut (AC) (not shown)
- Rec B = 3x1 dimerized model where the surface atoms rebond to create a pentagon structure (AD model, adatom-dimer)
- Rec C = 3x2 surface void, where one pentagon of the repeated cell is erased
- Rec D = 3x2-ADI "interstitialcy", where one interstitial atom creates bonds with the ones of one pentagon thus becoming 6-fold coordinated

In this case the first number (3) in the geometry refers to the [1 $\bar{1}$ 0] direction [173].
The reconstructions (b-d) are O1 type[4]. We speculate that the presence of interstitial atoms can be found more easily in type O surfaces (like this one), since the additional atom can accomodate in the space '3T' between two adjacent BLs[5].

It is noteworthy to say that in the reconstruction called "adatoms" the atoms forming the pentagons can be either added or simply rebonded depending on what layer of the BL

[2] see sec.2.5.2, page 56
[3] see discussion of this concept in sec.2.5.2
[4] i.e. the distance from one layer and the next one from the topmost ayer is 3T, T, 3T,...
[5] see Fig.2.12

the surface has been cut, i.e. if the starting AC cell is O1 or O2[6]. The starting bulk cell adopted is the one called (113)-ORTHO in Tab.2.3 at page 60.

Our results are for a cell thickness along z direction either of 2 AC cells or 3, depending on the cases. The bottom surface is either reconstructed (as in the case of 105 surface in this thesis) or kept fixed (as is the case of 1 1 10).
To specify the different cases we use the notation X-(Y)-Z where we mean that the cells contains X (113) BLs free to relax, Y (113) BLs fixed at the strain bulk position, Z (113) BLs free to relax. The case reported in Fig.D.2 are the ones with 2 cells along z called 9-(2)-9.

As done in Chapter 5, in every ab initio cell, a vacuum equal to two times the lattice constant of the cell $= 2 \cdot 5.39 \simeq 10.78$ Å(Si) and $= 2 \cdot 5.624 \simeq 11.248$ Å(Ge)

For the reciprocal space points sampling (KPOINTS) we followed the bulk criterion derived and tested in sec.5.3.3 at page 107. For the 3x2 cells (the reconstructed ones) we have values of: 3 2 1, but we also checked the trend with 3 3 1.

When dealing with Ge/Si cells, we use the same convention described in sec.2.5.5 at page 65 for the epilayer thickness, i.e. the physical distance along z between the topmost Ge atoms and the first layer of Si encountered as entering in the substrate. By exploiting eqn.(2.48) (page 66), we get:

$$1 \text{ ML } (001) = \sqrt{11} \text{ ML } (113) \tag{D.1}$$

Taking into account the missing layers as explained before, we conclude that the real thickness of 1 BL counts as 4 fictitious MLs and its thickness is expressed as follows:

$$1 \text{ BL } (113) = 4 \text{ ML}(113) = \frac{4}{\sqrt{11}} \text{ ML } (001) \simeq 1.2060 \text{ ML } (001) \tag{D.2}$$

Therefore in practice we turned into Ge the atoms in a fixed number of the topmost BLs in the cells and used he previous equation to quantify the thickness. In the cell geometry adopted (3x2) every complete BL contains 12 atoms.

[6] a O2 surface has distance from one layer and the next one from the topmost as T, 3T, T, 3T,...

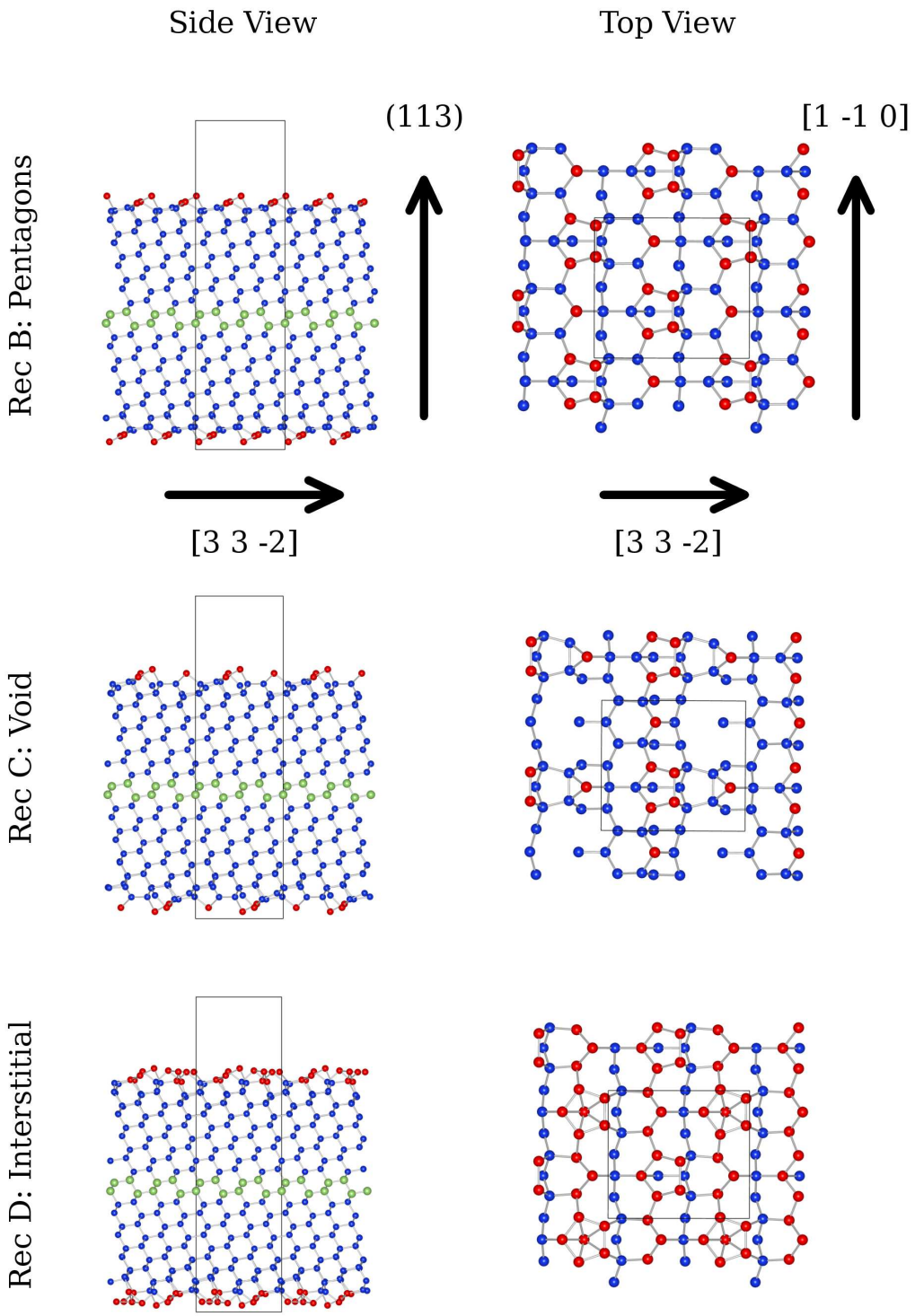

FIGURE D.2: Ge/Si(113): Reconstructions and cells. Side view and top view of the reconstructions analyzed in this work. They are the same as in Ref.[173]. The color code is the same as Fig.5.5 (page 105). The cells shown are the ones with 2 cells along z called 9-(2)-9 and refers to a Ge coverage equal to ∼1.2 ML(001) (Rec B,C) or ∼1.5 ML(001) (Rec D). Both surfaces are reconstructed and covered by Ge. From B to C is evident the missing pentagon. The interstitial atoms in D the one at the center of the pentagons at the right.

D.1.5 Comparison and check of convergence

We cannot avoid to compare our results with the ones by Stekolnikov et al [174].

We focus our attention to the as cut (AC) geometry of an unstrained Ge, for which surface Stekolnikov reports a value of surface energy equal to ~ 80.524 meV/Å^2.

We compare our data with this value in Fig.D.3-(a).
We change the thickness and position of fixed atoms (top x axis), the vacuum thickness (the first number of the bottom x axis is the thickness of vacuum expressed in units of lattice constant) and input kpoints (second number of the bottom x axis). For the last ones the values predicted by the bulk criterion are 821, since here we use a small cell in the xy plane (no reconstruction must fit here). All our cells have a complete BL at both surfaces, i.e. they are type O2 (see sec.2.5.2, page 56), whereas Stekolnikov does not mention about what surface is studied.

By comparing the data for 9-(2)-9 cells, we see that both a variation in the vacuum thickness and the kpoints density affect just slightly the data, yet the value differs from Stekolnikov's ones (Stek) for ~ 2 meV/Å^2. The presence of the fixed layers does not falsify the results as the datum 11-(0)-11 shows, where all atoms are free to relax.

Taking thicker and thicker slabs the surface energies approach the one of Stekolnikov (data of 15.5-(2)-15.5, 21-(2)-21 and 26.5-(2)-26.5), but apparently no plateau is found.

Using asymmetric slabs with the bottom surface consisting in fixed atoms in the AC positions (data of 20-(2)-0 and 29-(4)-0) reduce the value of symmetric slabs with the same thickness slightly.

The discrepancy with Stekolnikov's data can be also attributed to a different pseudopotential or a different estimation of the chemical potential, indeed he finds a Ge bulk chemical potential equal to -5.195 eV/atom, whereas ours is equal to -5.19922 eV/atom.

D.1.6 Results and discussion

Ge/Si(113)

The effects of the cell thickness may vary as a consequence of the strain induced by the reconstruction.

For this reason we perform the same preliminary study on a cell with reconstruction B (the pentagon one) for a Ge thickness equal to ~ 3.9 MLs (001) in Fig.D.3-(b). Here we get that the difference between an asymmetric cell with both surfaces reconstructed (26-(3)-4), with bottom layers fixed in the AC configuration (29-(4)-0) and for a thinner cell (9-(2)-9) for fixed kpoints (321) lies inside the 0.4 meV/Å^2 range. Within this range is also the difference caused by a different (higher) k-points sampling (331 and 441 in the same panel) and it represent therefore the error bar in our calculations.

Since in sec.5.3.4 at page 113 we established that the trend with deposition cannot be properly described by the Tersoff potential, here we study this trend in the DFT-LDA approach only.

Fig.D.3-(c) reports all the data for the three reconstructions considered with the different cell configurations written in the key. By exploiting the previous checks, in this

case the k-points are set equal to 3 2 1. It is evident that the differences revealed in panel b are hardly revealable on this scale and the symmetric thinner slab gives results that do not differ considerably from the thicker cells.

As expected[7], all the curves have a monotonic trend leading the surface energy to smaller values for Ge than for Si.

On all the coverage range analyzed the void reconstruction ("C") is the more energetic one. On the contrary the interstitial reconstruction ("D") is the most stable and from the trend no crossing with the others is expected till $\sim$ 5 MLs (001). Indeed the interstitial reconstruction is the one reproducing accurately the STM data [173] and is found to be the most stable even in previous works [174].

Ge(113) strained

The data on Ge/Si predict no coverage-induced change of reconstruction.

A change can, however, be found as induced by the strain, since the different reconstructions may have a different response to a modification of the relative position of atoms.

In order to look for a crossing, we analyzed a broad range of biaxial strain in the plane [-7%:+4%] for Ge.

The ab initio prediction of the surface energies for Ge(113) are reported in Fig.D.3-(d), where superimposed on the data are fits of quadratic function of the same type as eqn.(5.4) at page 99. These fits are not reproducing well the trend because non linear contribution are non negligible in such a broad range of strain. In these cases the maximum of the curves is for a biaxial strain of $\sim$ -1%, the preferred reconstruction being always the interstitial one. A crossing of this with the pentagon one ("B") occurs at a biaxial strain equal to -7%. Since on a Ge/Si nanostructures the strain is within the range [-4%:0], the reconstruction most likely to be osserved on a nanoisland is the interstitial one, provided that it can geometrically fit on the facets.

As discussed in sec.5.3.4, Tersoff potential can in principle give reasonable results as a function of strain. For this reason we compare our DFT-LDA results with this semiempirical approach. As Fig.D.3-(e) proves, the stability of the reconstructions is *reversed* with respect to the ab initio results: the most favoured reconstruction for ab initio (D) is even more destabilized than the unreconstructed (AC) one. This has its origin in the interstitial 6-fold coordinated atom, that induces a very high strain to the atoms in the pentagon. The perturbation is so strong that in conjunction with higher compression ($\sim -7\%, -8\%$) it can induce some bond-breaking, causing some points to be out of the trend established by the other ones. In addition to that, the maxima of the curves occur at a higher compression (around -4% or -7%).

These data suggest that the stabilization of the interstitial reconstruction can be due to charge transfer phenomena leading to a more complicated electron distribution [80] and that a description in terms of the sole strain cannot handle[8].

[7] compare the discussion at sec.2.5.5, page 65

[8] as is the case for the Ge/Si(1 1 10) analyzed in sec.5.3.6 at page 117

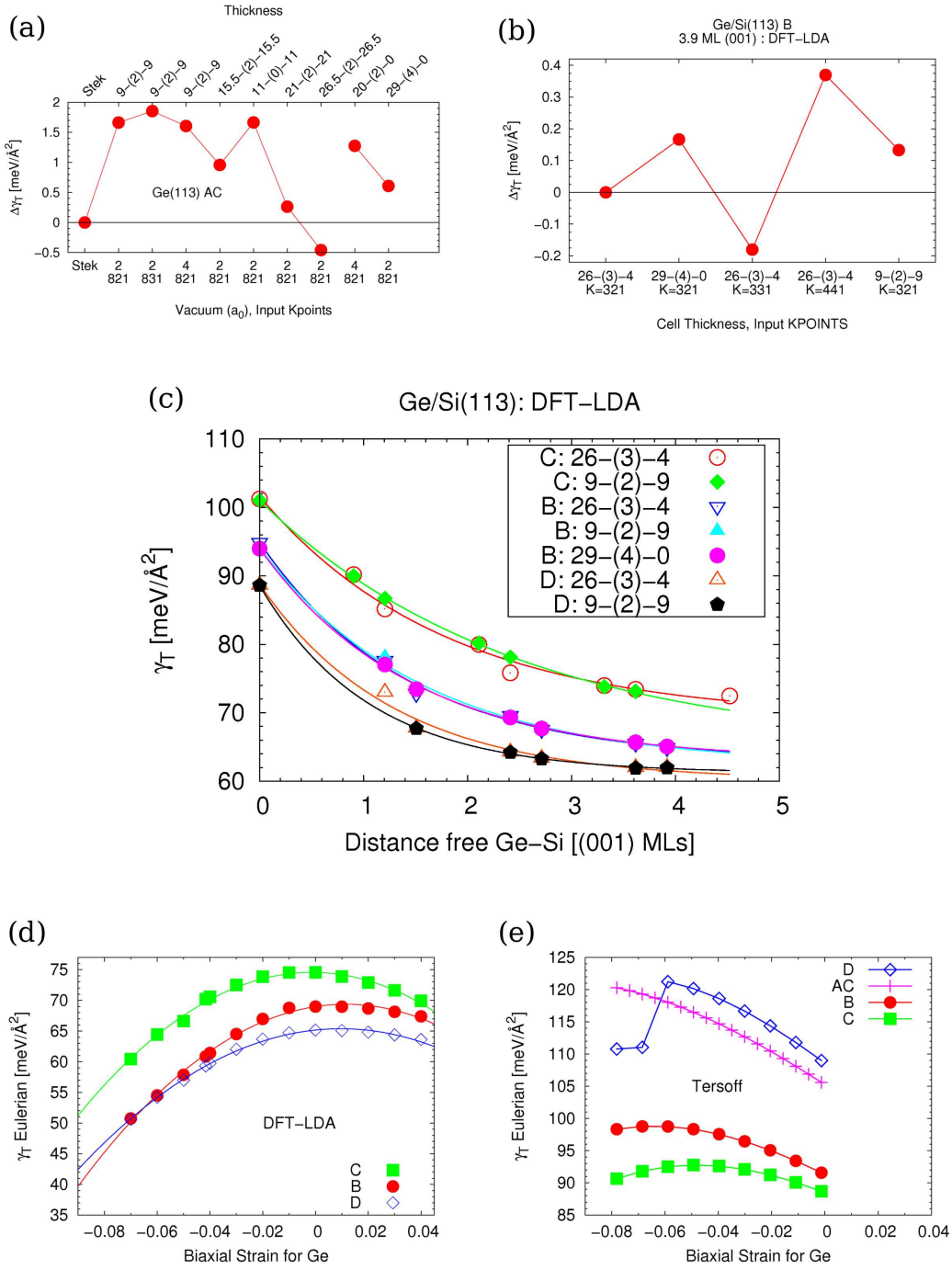

FIGURE D.3: Results. Comparison of the unreconstructed γ(Ge-113)-AC (a) for different parameters and cell geometry with the value obtained by Stekolnikov et al ('Stek') in Ref.[174]. The top x axis specifyes the geometry of the (113) BLs free-(fixed)-free from top to bottom, whereas the bottom x axis specifies the vacuum thickness (in units of Ge lattice constant) and the input kpoints. See discussion at sec.D.1.5. Panel (b) compares the results for the reconstruction B covered with 3.9 ML(001) Ge. DFT-LDA results of Ge/Si for different cell thickness and geometry are reported in panel (c), showing that the interstitial reconstruction is the most stable one. Panels (d) and (e) compare the resuts for strained pure Ge cells in the case of DFT-LDA and Tersoff potential respectively. They predict opposite stability regimes.

D.2 (001)-MxN surface

In this section we apply the methods employed in this thesis to the analysis of the "patched" reconstruction of Ge/Si(001) (also called MxN), that we mentioned in sec.2.5.3 at page 61.

We perform a systematic analysis of the surface energy in the Tersoff potential by using the Poisson-corrected chemical potential for Ge. In so doing, we get results that differ from published ones by Raiteri et al [6, 8], but our trend is actually confirmed by DFT-LDA calculations on selected structures.

D.2.1 Introduction

Experimentally, on a Ge-covered Si(001) surface a number of reconstructions appear [175].

On the clean Si substrate the topmost atoms dimerize and align to form dimer rows and lines as depicted in Fig.D.4-(a), resulting in a (2x1) reconstruction and buckling of these dimers can lead to a larger supercell, such as the p(2x2) or c(4x2). Epilayers of germanium induce a transition towards a 2xN Dimer Vacancy Lines (DVL) reconstructions, with N typically around 8-10 [175], with a geometry similar to the one shown in Fig.D.4-(b)[9]. This transition is believed to be induced by the partial relief of the compressive strain allowed by the missing dimer lines [6, 7, 176]. The same explanation is often called out to describe the transition to the MxN pattern, where "patches" of 001 terraces are separated from the others by both dimer vacancy lines and dimer row vacancies (DRV) (see Fig.D.4-(c,d))[10].

The interest in these surfaces is not strictly bound to the need of putting the experimental observations on firm theoretical bases, but it is also linked to the formation of SK islands on this important substrate for the microelectronics. Indeed it was shown [177] that the DVLs are barrier for the diffusion of adatoms on the surface. This leads to their forced accumulation on the terraces and to the more favourable nucleation of 3D mounds that eventually crystallize in {105} pyramids and huts [178].

Hence understanding the energetic stability of the different geometries for different values of M and N as a function of the Ge coverage is fundamental in predicting the expected terrace width and, therefore, the kinetics of nucleation. Another reason lays in the fact that finding the minimum energy reconstruction is important to assess the stability of the nanostructures laying upon that surface and to do this absolute numbers of surface energies are needed, that are not computed on a regular base (see e.g. Ref. [7]).

If studies on the 2xN-type reconstructions are present [76], to the best of our knowledge, no ab initio study of the MxN-type reconstructions (with M>2) has been performed, if, however, the explanation of the strain relief is the correct one, Tersoff potential should suffice to the correct description and energy ordering and evolution with coverage, if any.

Some works were already performed in this direction, both dealing with Tersoff potential directly (such as Refs.[6, 8, 179]) and by using some tight binding method [7]. However

[9] this is the case studied in chapter 5 where the 2x8-DVL reconstruction of 3ML Ge/Si was taken as a comparison to the (1 1 10) surface

[10] it is noteworthy to see that the notation commonly used is the one we adopt here, that is the reverse of the one adopted in Ref.[7] that was reported in Fig.2.13 at page 62

from their results, it appears that they used the non-Poisson corrected chemical potential for Ge or at least it is not clear. Since in Appendix C we **PROVE** that this is the one to be used, and since the cells here have different periodicities in the xy plane, a different chemical potential can lead to different values of the surface energies and therefore to a different prediction of stability, here we aim at recomputing the surface energies by considering this point.

As shown below, we arrive to different results as the published ones with different conclusions.

D.2.2 Geometry and Method

Since we want to compare our results with those in Refs.[6, 8], we use Tersoff potential as well. The speed of the calculations allows us to perform an extensive and systematic analysis of the surface energy density γ as a function of both coverage D and values of M and N. Afterwards we study the energy in a DFT-LDA approach for selected geometries to check our predictions and understandings.

In order to have a systematic and general analysis we need to find a way to create the cells in a fast and automatic way. We have seen in Chapter 5 that Tersoff potential predicts flat, untilted, dimers since it cannot handle the charge transfer. For this reason we can simply create a small number of "basic" reconstructed cells from where to get all the others needed by replicating the regions where no vacancies are found in the cell.
The basics cells are shown in Fig.D.4-(b,c,d) and are:

- 2x4-DVL $\rightarrow$ creating all the 2xN-DVL ($N \geq 4$, $\Delta N = 1$)
- 4x2-DRV $\rightarrow$ creating all the Mx2-DRV ($M \geq 4$, $\Delta M = 2$)
- 4x4-DRV-DVL $\rightarrow$ creating all the MxN ($M \geq 4$, $\Delta M = 2$ and $N \geq 4$, $\Delta N = 2$)

where the geometry of the cell compels the interval defined in parenthesis.

All the results with Tersoff are obtained with a cell 20 MLs (001) thick (equal to 5 unit cells). Ge is put just on the top surface, whereas the bottom one is unreconstructed (as cut, AC) and kept Si-terminated. As in Refs.[6, 8], no atom is kept fixed in order to have the same conditions as the paper we want to compare our results with. The lattice constant is kept fixed to the one of the silicon substrate. The bottom surface energy is computed with an AC pure Si cell and estimated to be equal to ~ 141.581 meV/Å^2.
Results with thicker cells give results in good agreement with the ones shown here, thus guaranteeing convergence. The lattice constants and the chemical potentials used are the ones reported in Tab.5.1, page 114.

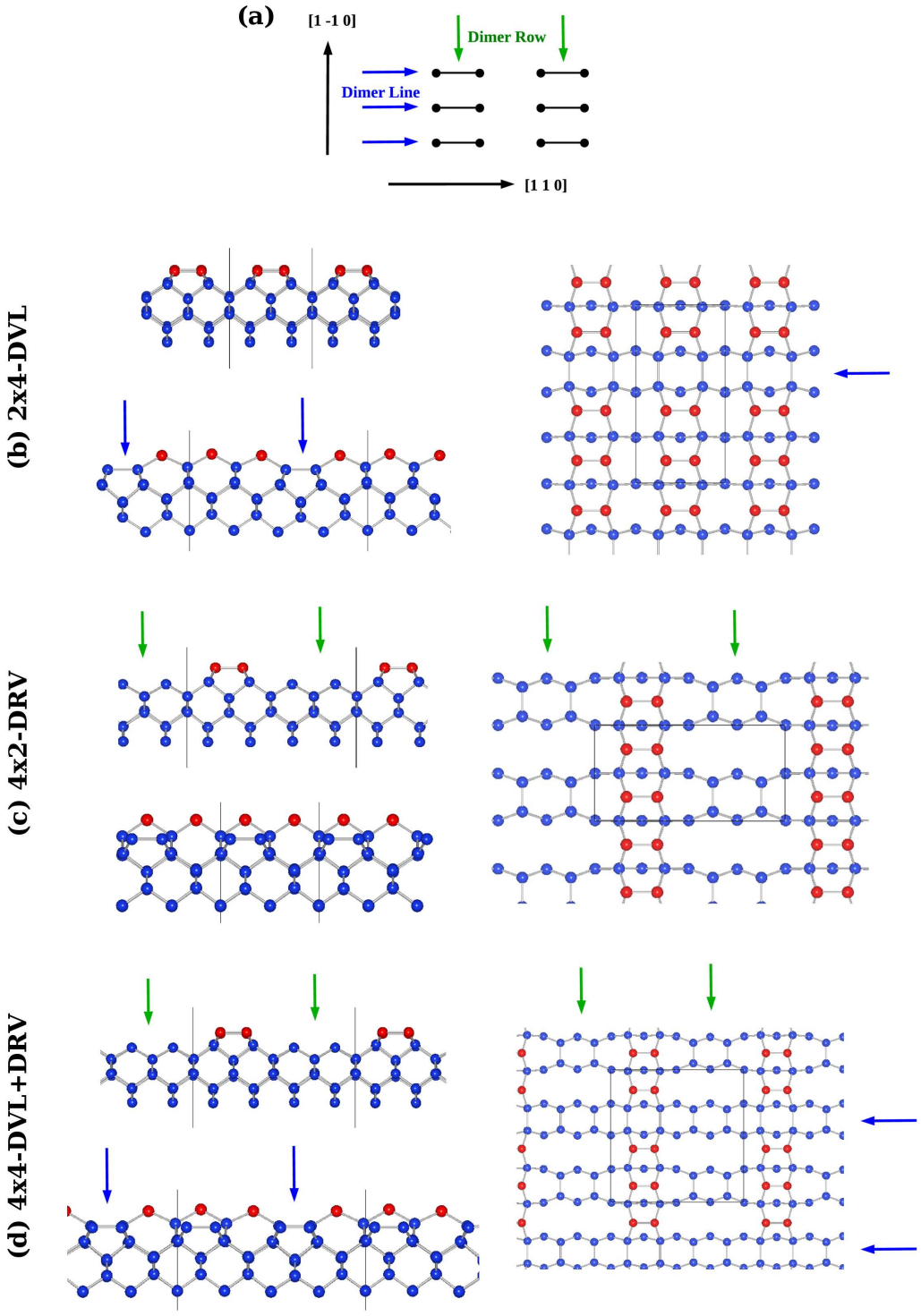

FIGURE D.4: (a) Top view of the dimers on (001) surface, where the Lines and Rows are highlighted. (b,c,d) The basic cells from whose handling all the cells are created: 2x4-DVL, 4x2-DRV and 4x4-DRV+DVL. The cells used are the ones minimized by Tersoff with 1 ML Ge and the atoms forming the topmost dimers are Ge (red atoms). In each panel the figure at the top left is a side view directed along [110], the figure at the bottom left a side view directed along $[1\bar{1}0]$, the figure at the right the top view with the same directions as panel (a). Blue arrows in (b,c,d) highlight Dimer Vacancy Lines, green arrows Dimer Row Vacancy.

D.2.3 Results for 3 ML Ge coverage: Tersoff

Fig.D.5 resumes the surface energies found in Tersoff potential with the method just described in the case of a Ge epilayer equal to 3 MLs, as in Ref.[8].

Panel (a) reports the results for 2xN-DVL if the Poisson-corrected chemical potential for Ge is used (red line) along with the data from Ref.[8] (black triangles). As evident the values obtained in the article are almost compatible with our data if the **unstrained bulk** chemical potential is used (green line).

Our doubt was, therefore, legitimate, indeed it seems that here this value is adopted. However, as proven in Appendix C, this leads to wrong results and to a different value of the surface energy if the compared cells have different periodicity in the xy plane, as is our case.

Indeed the author has confirmed that the chemical potential used here was the energy per atom of the bulk at the temperature of the experiments[11]. We speculate that the deviations of some points in Fig.D.5-(b) from our predictions could be caused by the authors' estimation of energy form a simulated annealing approach.

In the same panel, not only the absolute values are different but even the trend differs from our data.

From geometrical intuition, for a fixed value of M (as in panels and b) the effect of the DVL should be more and more negligible for larger area of surfaces (i.e. values of N) with the consequence that:

$$\lim_{N\to\infty} \gamma(MxN) = \widetilde{\gamma} \tag{D.3}$$

for a finite value of $\widetilde{\gamma}$. This happens for our data, but on the contrary the data of Raiteri et al appear to diverge for larger M (panel b).

Panels (c) and (d) make a similar analysis for fixed values of N=4 and N=6, respectively, and changing the value of M. In this case the should expect that:

$$\lim_{M\to\infty} \gamma(MxN) = \gamma(2xN) \tag{D.4}$$

as is the case for our data. The difference with Raiteri et al data is also evident, both in the values and in trends.

Our data for all the analyzed MxN reconstructions with the Poisson-corrected chemical potentials are reported in a color scale in panels (e) and (f) in 3D and 2D respectively. From these data it is evident that the reconstructions without the DRV (i.e. the 2xN-type) are preferred over any MxN type one. This result is in contrast with the published results [6, 8], where the 10x6 is the most stable one and apparently in contrast to experimental findings [8].

Following our results, we may interpret the formation of DRV and a MxN reconstruction as an "incomplete coverage" due, e.g., by kinetic limiting factors, rather than an overall surface energy minimization. It is noteworthy to remind, however, that in our calculations no estimation of the entropic term is given, that at the operating temperatures may play a role.

[11] Dr. Paolo Raiteri, private communication

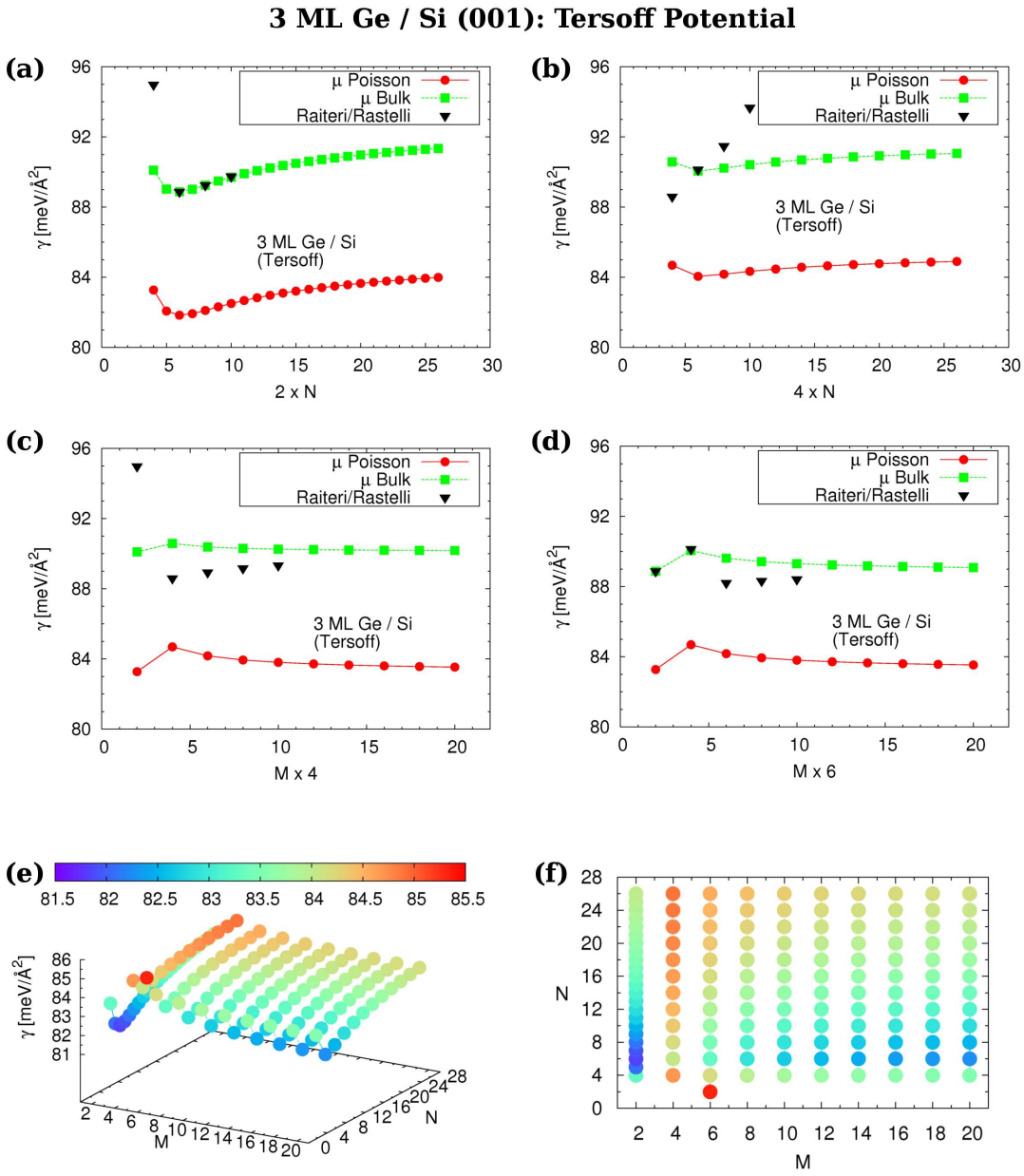

FIGURE D.5: 3 ML Ge/Si(001) Tersoff potential results. (a) Surface energy of 2xN-DVL reconstructions with the Poisson-corrected Ge chemical potential (red lines) or the unstrained bulk chemical potential (green lines) and comparison with the data published by Raiteri et al in Ref.[]. (b,c,d) Same comparison for 4xN, Mx4 and Mx6 reconstructions. It seems that the data reported in literature are comparable with the ones obtained with the incorrect bulk chemical potential. (e,f) 3D and 2D view of the values of surface energy γ for different values of M and N obtained with the Poisson-corrected Ge chemical potential. The reconstruction with DRV have higher energy than the ones with DVL alone, contrary to the explanation of DRV in terms of a better strain relieve.

D.2.4 Results for 3 ML Ge coverage: DFT-LDA

We speculate that another alternative explanation of the disagreement between experiments and our results can be due to some role played by the dimer tilting as discussed at length in sec.5.3 (page 103) in this thesis for the case of (1 1 10) surface.

To check this possibility, we study some cells in an *ab initio* approach after properly tilting the dimers in an alternate fashion as did in chapter 5. We choose the p(2x2) tilting pattern since it has already been proven to be the most stable configuration [177]. Because of the large cells, we analyze just the smaller ones.

Also in this case our cells are 20 MLs (001) thick but the bottom-most Si atoms in the AC configuration are kept fixed. The energy is minimized with the same parameters used in chapter 5 and discussed in sec.2.2. For the kpoints sampling, the bulk criterion described in sec.5.3.3 is adopted.

The relaxed cells and the data are reported in Fig.D.6.
Our DFT results for the few data 2xN-DVL nicely agree with others found in literature [76]. Panel (a) clearly shows that, as in the case of Tersoff potential, the introduction of a DRV increases the energy of the surface (at least in the small range analyzed here). The value of the 3ML Ge 2x8-DVL is the same found in chapter 5.

From panel (a) we clearly see that the insertion of a DRV (4xN reconstructions) destabilizes the surface by increasing its energy. Although this trend agrees with the Tersoff potential results, the difference is energy is much higher from the 2xN and 4xN case than the Tersoff ones.

In the relaxed geometries shown in Fig.D.6-(b,c,d) the dimer tilting pattern does not appear perturbed by the steps. This is not in contrast with what was found in the case of (1 1 10). Indeed the degree of strain relieve (i.e. expansion of the compressed Ge) is proportional to the height of the step itself. Therefore the expansion of a double-height step is roughly double to the one of a single-height step where it seems that in the latter case it is not sufficient to appreciably perturb the dimers and break their patterns.

D.2.5 Results for other coverages

So far we have established that for 3 ML Ge coverage the vacancy row-free reconstructions are favoured against the MxN for any M and N. We now turn our attention to other coverages.

Fig.D.7-(a) shows the surface energy ontained with Tersoff potential with 1,2,3 and 4 ML Ge for the case of 2xN reconstruction alone. It does not surprise to observe an oscillation of the value of the energy with deposition instead a monotonic decrease as expected since we have already shown in sec.5.3.4 that Tersoff potential cannot handle the dependence on coverage properly. Notwithstanding that, the oscillation are rather small in comparison to the non-sensical results of other published papers [169] where the surface energy was **increasing** monotonically with coverage because the chemical potential used was not the proper one.

For this incapability of handling the interfaces by Tersoff potential, the results for 1 ML Ge are not trustable. Particularly they would predict a 2xN with the largest possible N to be stable, against experimental outcomes.

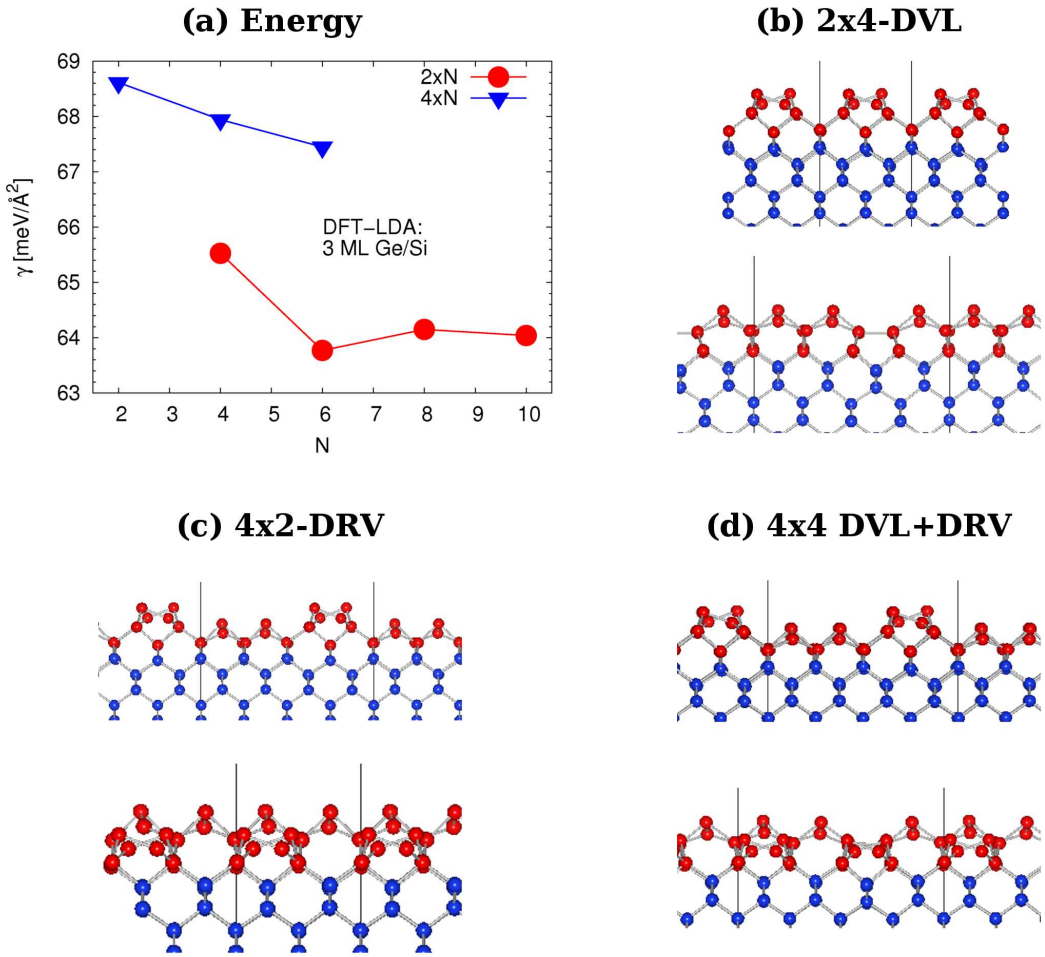

FIGURE D.6: (a) DFT-LDA results for 3 ML Ge/Si(001) for selected reconstructions. It is evident that ab initio data confirms that the insertion of a DRV causes an increase in energy (at least in the recontructions analyzed), as predicted by Tersoff potential. (b,c,d) Side view of the relaxed basic cells showing that the alternating tilting pattern is not altered by the 1 ML-deep trenches created by the reconstruction. The directions of the cells are the same as in Fig.D.4.

The safer results for 2 and 4 ML Ge come to the same conclusion of the 3 ML: the preferred reconstruction form the energetic point of view is the one without DRV. Incidentally, the results for 4 ML is almost degenerate to the case of 3 ML, meaning that we are almost at convergence.

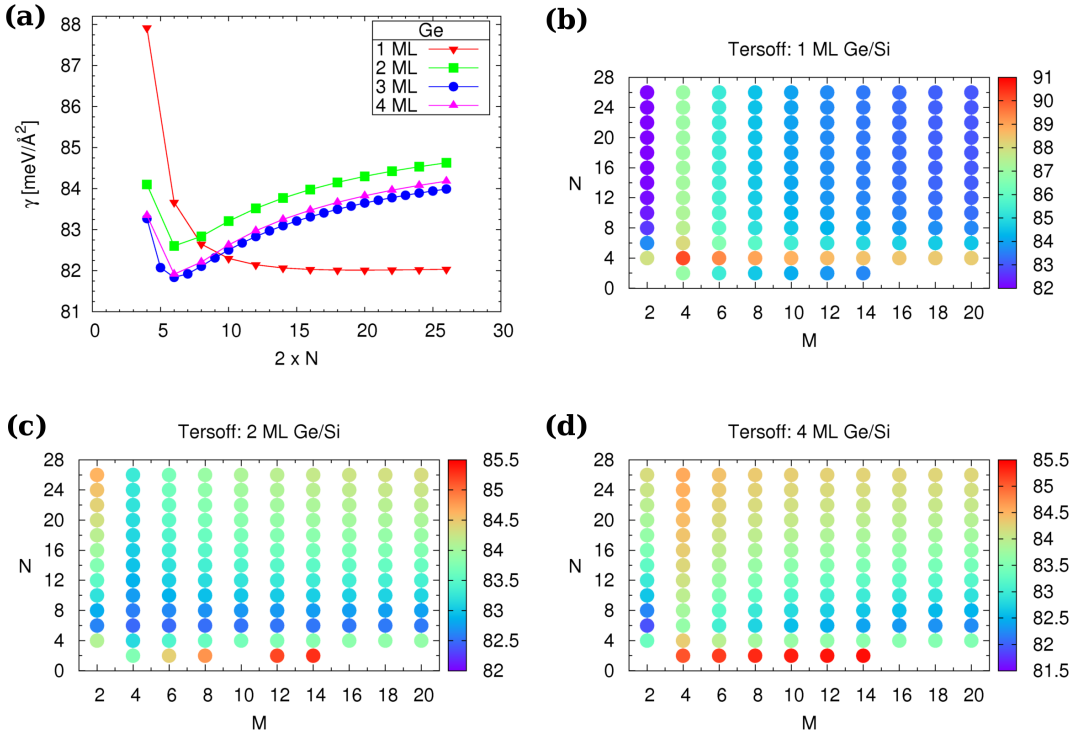

FIGURE D.7: Results of Tersoff potential for coverages other than 3 ML Ge. (a) Trend of the 2xN reconstructions for 1,2,3,4 ML Ge. The values of 3 and 4 ML are very similar, showing that 3 ML is almost at convergence. (b,c,d) 2D representation of the surface energy for 1, 2 and 4 ML Ge, respectively, to be compared with the data in Fig.D.5-(f). In every case the reconstructions with M=2 are the most stable ones.

D.2.6 Discussion and conclusions

Here we have shown that the use of the Poisson-corrected chemical potential for Ge predicts a different stability for the (001)-MxN surfaces as established in literature, leading to the conclusion that no DRV is energetically favoured.

This is not only in contrast to published results, but urges also to reconsider the interpretation of the patched-reconstruction onset. Indeed, following our results, we can rule-out the description of the onset of DVR+DVL as a way to relieve strain. This may be regarded as a result of an "incomplete" coverage of the substrate, or as a first attempt to create 2D islands as precursors for SK 3D islands. Another option could be the role played by entropic term or by kinetic factors, indeed the 2xN or MxN are observed under different experimental conditions (see discussion in Ref.[175]).

If this is the case, a prolonged annealing at a not-too-high temperature should allow the system to reach the thermodynamic minimum where no DRV are formed. To our knowledge, such an experiment is still missing.

Understanding what are the roles of the other contributions could elucidate the predictability of purely energetic approaches, but this analysis is beyond the scope of the present work.

Incidentally, the 2xN reconstruction is the one used in several published works handling first-principles methods. In one of these works [175] they use the energetics to predict the critical thickness of the WL before islanding takes place. Although the method adopted is approximated, it is noteworthy to see that the analysis of the 2xN geometry is enough to predict the value of 3-4 ML, in agreement with experimental values. If the 2xN was not the minimimum energy condition, this result should not be expected.

As Ref.[8] shows, intermixing can actually alter the ordering of the reconstructions, and this contribution is not considered in the present work.

We present a method to analyze and discuss the issue of intermixing in the next section for the case of the (1 1 10) surface.

D.2.7 Acknowledgements

Dr. Paolo Raiteri is acknowledged for useful discussion about the method and the chemical potential used in his articles.

D.3 (1 1 10) intermixed with Monte Carlo and Tersoff

D.3.1 Introduction

In chapter 3 we have shown the importance of intermixing in the elastic relaxation and hence in the overall stability. Actually intermixing can influence the surface energy term as well.

In all the calculations on surfaces presented so far in this thesis we have made the assumption that the interface Ge-Si is sharp and parallel to the free surface, with the consequence that Ge is deposited layer by layer, leading to the convention (and conversion) of coverage we have highlighted in sec.2.5.5 at page 65.

If temperature is high enough, however, the atoms can mix leading to a certain non-uniform distribution both in depth and in the xy plane. Intuitively, in the case of Ge/Si surfaces, the Ge atoms will tend to saturate the surface (since their dangling bonds have lower energy) and will preferentially take the place of Si atoms in those regions where the reconstruction leads to tensile strain.

D.3.2 System and Method

Here we want to study the effects of intermixing on the surface we have studied most in this thesis: the (1 1 10)-Db and approach the problem via a Basin-Hop Monte Carlo algorithm.

Following some ideas already present in literature in continuum models [180], we make the hypothesis that atoms of Ge can swap place with the atoms of Si inside a region of a certain depth that we fix equal to 4 MLs (001).

The generic algorithm should allow not only to accept swaps allowing a reduction of energy, but also those increasing it since atoms might have to overcome some barriers to reach the absolute minimum energy condition. Therefore the simulation should be carried out at a finite temperature T. The algorithm is therefore the following:

1. randomly chose a couple atom Ge and an atom Si in the region of intermixing and swap their position
2. relax the system and compute the internal (and surface) energy
3. the swap is accepted if a randomly chosen positive number $\aleph \in [0:1]$ is such that

$$\aleph < exp\left(-\frac{\Delta E}{kT}\right) \tag{D.5}$$

   where ΔE is the change in energy caused by the swap and k is the Boltzmann factor. This criterion automatically allows the acceptance for $\Delta E < 0$.
4. another couple of atoms is randomly chosen and the cycle starts over

Obviously the temperature T must be high enough to allow atoms overcome energetic barriers but low enough not to have a too high rate of acceptance of swap raising the overall energy.

Since this method requires several steps and attempts to reduce the surface energy to a considerable extend, it is unfeasable in an ab initio environment. Therefore here we evaluate the energy by using the Tersoff potential.

D.3.3 Results: one-shot

In order to check the efficiency of the method and to find a proper temperature to reduce the energy, we first consider the case of overall minimization of energy by taking 4 MLs (001) of Ge that can intermix with 4 MLs (001) Si underneath (corresponding to $\sim$ 20 ML 1 1 10), reproduced in Fig.D.8-(a).

We use asymmetric cells as done in sec.5.3.1, where the bottom surface is left unreconstructed (AC) and fixed, but we double the size of the cell along x direction in order to contain two dimers in a line with the aim to reveal possible intermixing in the dimers themselves. The energy E we use for the criterion of acceptance of swap is the surface energy of the top (reconstructed) surface $\gamma \cdot A$.

The surface energy γ of the top (reconstructed) surface of the cell during the swap process and the accepted swaps are reported in Fig.D.8-(b,d) for temperatures equal to 10 K and 600 K respectively, where the structures obtained in the final accepted swap (blue point) are reported in panels (c,e) respectively. As evident, the 10 K case is very effective in reducing the surface energy leading the energy from $\sim$ 82 meV/Å^2 to $\sim$ 76.5 meV/Å^2. On the contrary, in the same range of attempted swaps, the case of higher temperature (600 K) is less effective in reducing the energy leading to a final value of $\sim$ 79 meV/Å^2. This happens because the high temperature causes several swaps increasing the energy to be accepted.

The final configuration in panel (c) shows that, consistently with the expectation highlighted before, the atoms at the very surface are all Ge atoms. The atoms underneath have a peculiar distribution between Ge and Si, where the Ge atoms are more likely to be at the positions with tensile strain. No difference is noted along x direction, showing that there was no need to consider a large cell in this direction.

D.3.4 Results: Layer by layer and DFT-LDA values

The prediction just made is based on the overall minimization of the surface energy by allowing a free intermixing in a thick layer in the substrate. However, during the deposition several complex kinetic mechanisms can take place. In an attempt to model the effects of such mechanisms we can ideally find the minimum energy configuration by allowing intermixing of the topmost Ge layer with the atoms laying underneath in a thickness of 3 (001) MLs as discussed in some articles [181]. If we perform this **at every Ge ML deposited**, then some atoms intermixed in the lowest layers will be "frozen" in this configuration mimicking their impossibility to swap with atoms on the surface.

Since the (1 1 10) surface is both non-planar and reconstructed, a big effort is spent to carefully consider the addition of the (N+1)-th ML(001) Ge upon the optimized structure with N MLs Ge in order to recreate the geometry while keeping the distribution of atoms equal to the one obtained at the step before.

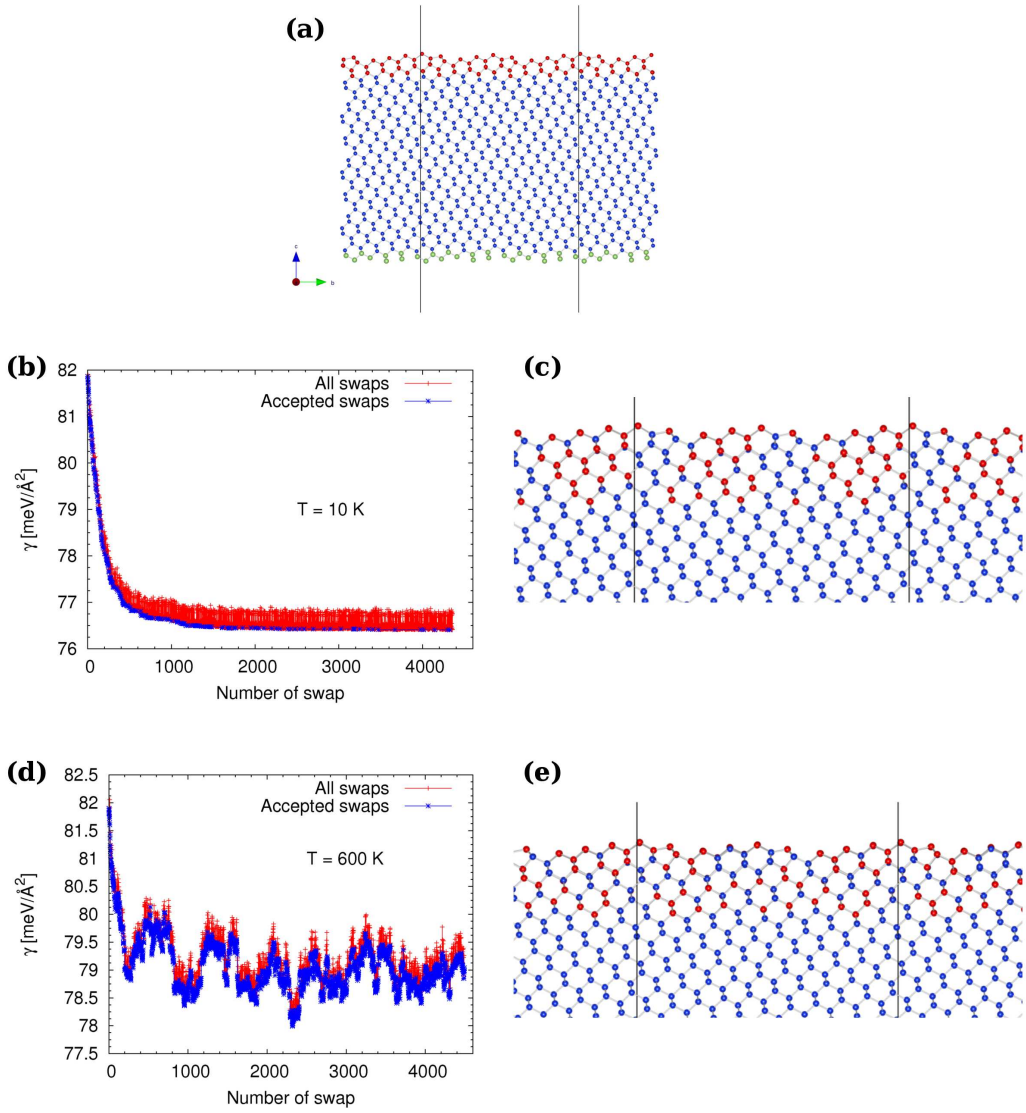

FIGURE D.8: Intermixing studied with Tersoff potential and a Monte Carlo approach for 4 ML (001) Ge. The intermixing is allowed to occur in the region of the Ge MLs with 4 ML (001) underneath. (a) initial configuration. (b,d) trend of the surface energy γ for the case of low and high temperature, respectively. Panels (c,e) show the final configurations obtained. See discussion at sec.D.3.3.

Since in the previous results no difference is found in the x direction, here we employ a cell with a single dimer along x. In this way we employ a cell with 102 ML (1 1 10) equal to the one adopted in first principles calculations in sec.5.3.1.

By exploiting the results of the 'one-shot' calculations, we use the low temperature values, and since we halve the area A, we employ a temperature equal to 5 K in eqn.(D.5).

The results are shown in Fig.D.9.
Panel (a) shows the configuration with 1 ML Ge, whereas panels (c,e,g,i) show the minimum energy condition obtained for 1,2,3,4 (001) MLs Ge, respectively. The energies in panels (b,d,f,h) show the trend as intermixing is working. The starting value of the energy in the panel with (N+1) ML is not the same as the final value of the one with N ML because the added Ge ML alters the energy of the surface.

Panel (h) shows that the final configuration with this "artificially-kinetically-hindered" intermixing phenomena is higher in energy (final value in the plateau of ~ 78.3 meV/Å^2) with respect to the previous case of energetic minimization without frozen atoms.

This suggests that the complex phenomena occurring during deposition with the consequent freezing of some atoms deep in the surface, can in fact alter the prediction of the overall intermixing within a certain thickness in the substrate.

We can estimate the effect of such a distribution of atoms in DFT-LDA approach by computing the energy of the cells with the atoms distribution found here. The energy is reported in Fig.D.10 where a comparison with the non-intermixed case is performed.

D.3.5 Discussion

Our results show that intermixing can actually lower the surface energy as predicted by strain contribution alone (from Tersoff potential), yet the surface energy of the intermixed case is higher wrt the pure one as predicted by first principles approaches. This trend is in accordance with literature results [6], both from LDA and GGA and again prove the necessity to adopt first principles calculations for the estimation of the surface energies, rather than using semiempirical potentials.

It is worth mentioning that the entropic terms are not taken into account, that, instead, can be relevant at the higher growth temperature.

In Chapter 5 intermixing for the (1 1 10) substrate is neglected because experimentally the deposition occurs at low temperature (550°C), a condition that can hinder the swaps leading to intermixing.

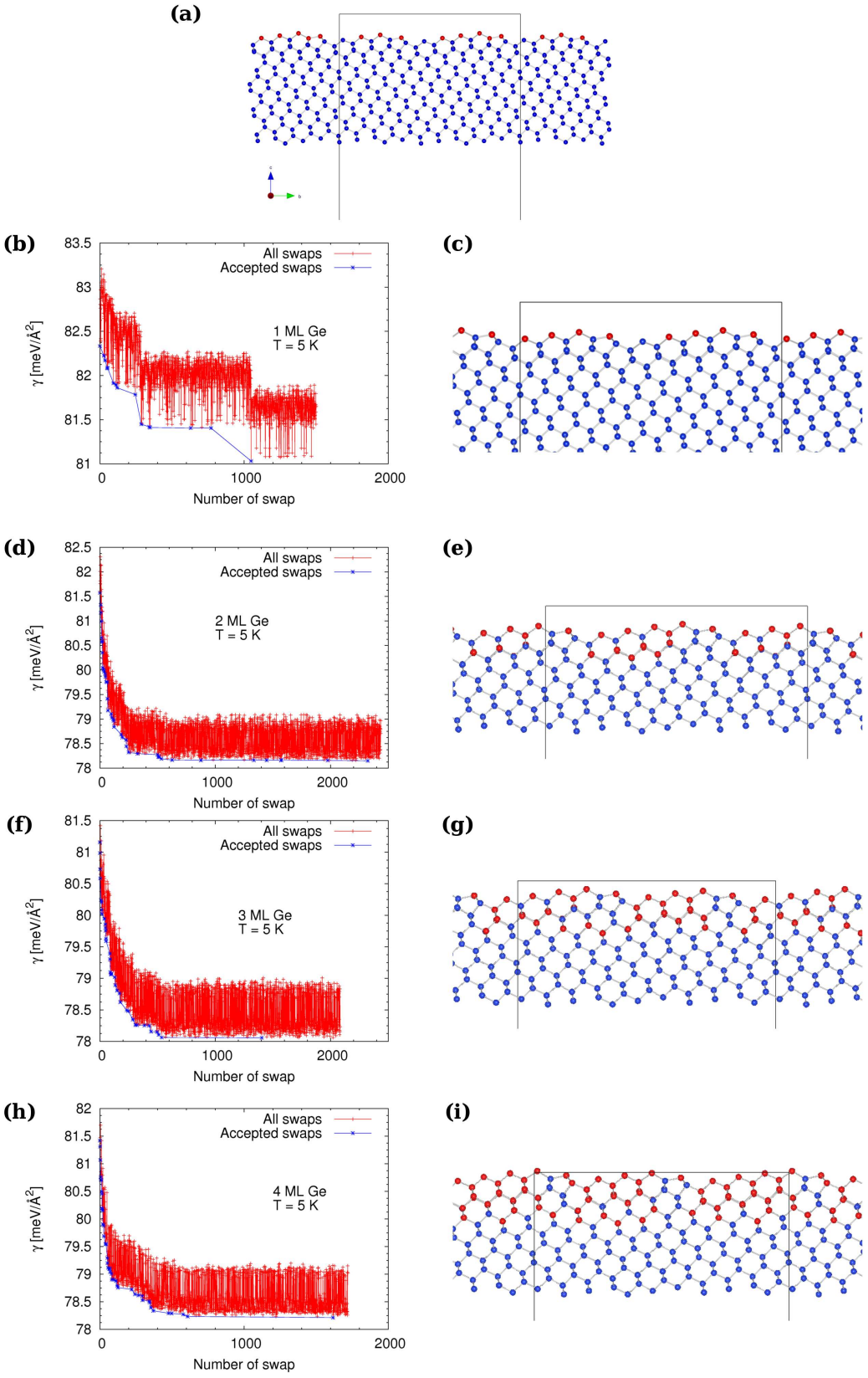

FIGURE D.9: Intermixing studied in a layer-by-layer method with Tersoff and Monte Carlo. The intermixing is allowed to occur in the region of the topmost Ge ML(001) and 3 ML (001) underneath. (a) initial configuration with 1 ML Ge. (b,d,f,h) trend of the surface energy $\gamma \cdot A$ for the case of 1,2,3,4 Ge ML (001) leading to the final distribution of species depicted in panels (c,e,g,i). See discussion at sec.D.3.4.

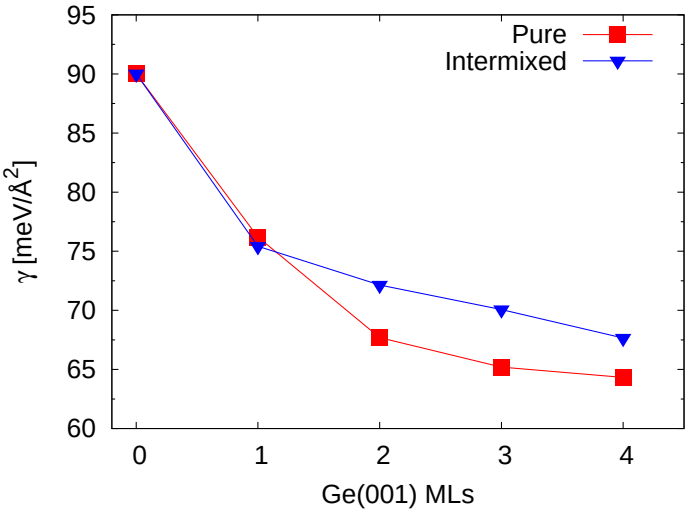

FIGURE D.10: (1 1 10)-Db Intermixed with MC and Tersoff: Results Layer by layer analyzed with DFT-LDA. Cells with 102 (1 1 10) MLs, with Ge on top non intermixed ('Pure') and intermixed. The intermixed situation has higher energy than the pure one for higher coverage.

E

Curriculum Vitæ

UPDATED on December 19, 2011.
NOTE: An updated version of the CV can be found on LinkedIn website:
http://it.linkedin.com/pub/daniele-scopece/3b/89a/b9a

E.1 Personal Information

Daniele Scopece

Department of Materials Science
University of Milano-Bicocca
Via R. Cozzi 53, 20125 – Milano – Italy
University Office Phone: +39-02-64.48.52.12

Current email: **daniele.scopece@mater.unimib.it**
Permanent: **daniele.scopece.science@gmail.com**

City and Date of Birth: Milano (Italy) – 07/07/1984
Nationality: Italian

E.2 Job Experiences

2009 Jan → 2011 Dec PhD student in Materials Science at the University of Milano-Bicocca

2010 Mar → 2010 Sep Short Term Visiting Scholar (during PhD time) at the Department of Chemical Engineering at the University of Kentucky, Lexington, KY, USA. Working with Dr. Matthew J. Beck on the project:
"Estimation of Ge/Si vicinals surface energy in a DFT-LDA approach (particularly high index ones) using the VASP code"
leading to paper number 3 in Peer Reviewed Publication section.

E.3 Education

2008 Oct: **winner** of 3-years PhD grant from the Ministry of Education of Italy (from 2009 Jan to 2011 Dec).

2008 Sep 30^{th}: **Master degree in Condensed Matter Physics**
at the University of Milano-Bicocca. Final Grade: 110/110 cum laude.
Thesis title (translated): *"Atomistic simulations of strain release in three dimensional heteroepitaxial islands"*.
Supervisors: Dr. Francesco Montalenti and prof. Leonida Miglio.
Computational thesis dealing with the simulation of InAs/GaAs islands and surfaces via a classical molecular dynamics code whose some parts were written by me (fortran language).

2006 Sep: **Bachelor Degree in Condensed Matter Physics**
at the University of Milano-Bicocca. Final Grade: 110/110 cum laude.
Thesis title (translated): *"Lifetime study of minority carriers in crystal silicon wafers via the QSSPC (Quasi Steady-State Photoconductivity) technique"*
Supervisors: Dr. Maurizio Acciarri and prof. Nice Terzi.
Experimental work.

2003 July: Scientific High School finished with maximum mark (100/100).

E.4 Languages

–} Italian: native language

–} English: very good understanding, good writing, good oral expressions

–} Spanish: good understanding, moderate writing, moderate oral expressions

E.5 Collaborations

In my research experience during PhD I have collaborated (more or less extensively) with both experimental and theoretical groups:

- Dr. Matthew J. Beck, Depart. Chem. & Materials Engineering, University of Kentucky, KY, USA
- Prof. Günther Springholz & group, Johannes Kepler University, Linz, Austria
- Prof. Friedrich Schäffler & group, Johannes Kepler University, Linz, Austria
- Dr. Armando Rastelli & group, IFW, Dresden, Germany

E.6 Publications in preparation

8. D. Scopece* *et al*, *"Ge/Si(113): strained surface energies"*, *in preparation*

7. D. Scopece* *et al*, *"Strained surface energies: What chemical potential to use?"*, *in preparation*

6. D. Scopece* *et al*, *"Strained nanoislands: Is really the steeper the more relaxed?"*, *in preparation*

5. D. Scopece* *et al*, *"On the geometrical properties of cubic lattice slabs"*, *in preparation*

E.7 Finished Peer-Reviewed Publications

4. G. Chen, D. Scopece, B. Sanduijav, D. Matei, W. Jantsch, G. Springholz, F. Schäffler and L. Miglio, *"Morphological Phase transition for pure Ge and diluted $Si_{1-x}Ge_x$ ripples on Si(1 1 10)"*, *ready for submission*
   My contribution: idea of the model and its computation leading to the theoretical figures.

3. D. Scopece*, F. Montalenti and M. J. Beck, *"Stability of Ge on Si(1 1 10) surfaces and the role of dimer tilting"*, **accepted** to Phys. Rev. B
   My contribution: entire work.

2. G. Chen, B. Sanduijav, D. Scopece, G. Springholz*, D. Matei, M. J. Beck, F. Montalenti and L. Miglio, *"Formation of Ge Nanoripples on Vicinal Si(1 1 10): From Stranski-Krastanow Seeds to a Perfectly Facetted Wetting Layer"*, *submitted to Phys. Rev. Lett.*
   My contribution: complete modeling of the system, elastic, surface and edge contributions, leading to the the theoretical predictions of Figures 3 and 4.

1. J.J. Zhang*, F. Montalenti, A. Rastelli, N. Hrauda, D. Scopece, H. Groiss, J. Stangl, F. Pezzoli, F. Schaffler, O.G. Schmidt, L. Miglio, G. Bauer,
   "Collective Shape Oscillations of SiGe Islands on Pit-Patterned Si(001) Substrates: A Coherent-Growth Strategy Enabled by Self-Regulated Intermixing",
   Phys. Rev. Let. 105, 166102 (2010).
   My contribution: modeling of the system leading to the theoretical prediction of Figure 4.
   Citations=4

E.8 Technical Skills

Programming Languages known :

- Fortran 90 and 77 : Good
- Bash shell syntax : Good
- Matlab : Moderate
- C and C++ : Moderate

Other Skills :

- Familiar with codes for Classical Molecular Dynamics and ab initio (VASP)
- Familiar with Finite Element Methods (commercial software COMSOL)
- Good knowledge of Windows and Linux operating systems
- Good knowledge of LaTeX language for writing texts
- Good knowledge of the program GIMP for image manipulation
- Good knowledge of the Office package (Word, Excell, PowerPoint)
- Good knowledge of data analysis and plots packages: Origin, Matlab (moderate knowledge), Gnuplot, vmd

E.9 Schools Attended during PhD

–) *"DFT and beyond: towards a first-principles understanding of materials properties and function"*, Hands-On DFT and beyond workshop 2011, Berlin (Germany), July 12^{th}–21^{st}, 2011

–) *"Electronic and Optical Properties of Nanoscale Materials"*, Summer School in the Physics and Chemistry of Advanced Materials (PCAM) European network of universities, Donostia–San Sebastian (Spain), July 04^{th}–07^{th}, 2011

–) *"Introduction to techniques of parallel and distributed computation"*, CILEA, Segrate, Milano (Italy), November 08^{th}–11^{th}, 2010

–) *"Chemistry and Physics of Materials for Energetics"*, Summer School in the Physics and Chemistry of Advanced Materials (PCAM) European network of universities, University of Milano-Bicocca (Italy), September 14^{th}–19^{th}, 2009

–) *"Workshop on the use of Fluidodynamics and Chemical Engineering in the Finite Element commercial code COMSOL"*, University of Bologna (Italy), February 25^{th}, 2009

E.10 Conference Contributions

- **Oral Presentation** *"From Stranski-Krastanow seeds to a perfectly facetted wetting layer: Dominant role of surface energy in the evolution of Ge nanoislands on Si(1 1 10)"* : presented by myself at the
"3^{rd} International Workshop – SemiconNano 2011",
held in Traunkirchen (Austria), September 11^{th}–16^{th}, 2011

- **Poster** *"Dominant role of the surface energy in the growth of Ge nanoislands on Si(1 1 10)"* : presented by myself at the
"18^{th} Interdisciplinary Surface Science Conference (ISSC-18)",
held at the University of Warwick, Coventry (United Kingdom),
April 04^{th}–07^{th}, 2011

- **Poster** *"Stabilizing (105) facetting of $Si_{1-x}Ge_x$ on Si(1 1 10) Interpretation by competing strains in surface and volume energies"* : presented by myself at the European School of Physics and Chemistry of Advanced Materials (PCAM): "Materials for energetics", held at the University of Milano-Bicocca, Milano (Italy),
September 14^{th} – 19^{th}, 2009.

- **Poster** *"Stabilizing (105) facetting of $Si_{1-x}Ge_x$ on Si(1 1 10): Interpretation by competing strains in surface and volume energies"* : presented by myself at the "26^{th} European Conference on Surface Science (ECOSS)",
held in Parma (Italy), August 30^{th} – September 04^{th}, 2009.

E.11 Technical Capabilities

At present my hand-made fortran software can very easily perform the following tasks:

– create a slab of cubic crystal exposing whatever surface (also any high index ones)

– create a Wulff solid laying on any surface with any number of family surfaces to be analized either by FEM or by an atomistic approach

– perform a local relaxation of atomistic structure in Tersoff semiempirical potential and test the effect of intermixing

E.12 References

- **Dr. Matthew J. Beck**, Assistant Professor at Computational Materials Science, Dept. of Chemical & Materials Engineering University of Kentucky, USA.
  beck@engr.uky.edu

- **Prof. Leonida Miglio**, full professor in Materials Science, University of Milano-Bicocca, Italy.
  leo.miglio@unimib.it ; **leo.miglio@mater.unimib.it**

- **Dr. Francesco Montalenti**, Researcher in the department of Materials Science, University of Milano-Bicocca, Italy.
  francesco.montalenti@unimib.it

F

Acknowledgements

PhD activities can be quite hard and, at times, frustrating.
However, in hindsight, it is a valuable life experience leading to the self-confidence and understanding of his own potentialities.

In the three years of my PhD I have met several people with whom I have not only worked in research, but also had fun, comparison of ideas, teachings, and also discussions...

In a word: "LIVED".

Acknowledging all of them would require an entire chapter, thus here just the most relevant are listed.

First of all my supervisor, prof. Leonida Miglio, with whom I learnt the meaning of indepedent and performing research work.
He helped me in overcoming some mutual misunderstandings arosen in everyday work in collaboration with people focused mostly on the experimental part of a work, not to mention his help in orienting the research in the right direction to addressing the results and his advises to overcome my limits.

Another support to the not-so-easy way to become a self-confident independent researcher has come from Dr. Francesco Montalenti[1].
His advises and the scientific discussions with him were useful to focus the problematics and to find the possible path to the solutions together.

[1] AKA "Franz"

I'd like to thank all the other members in Miglio group.

Roberto Bergamaschini[2] for valuable both scientific and life-based exchange of ideas, even though not always carried out in a peaceful way from both of us. I enjoyed a lot the abroad conferences we have joined together.

Francesca Boioli[3] for continuous psychological support and encouragement.

Anna Marzegalli is acknoledged for psychological support and personal advices as well.

With all of them everyday life in Milano-Bicocca has been less monotonous and boring.

The period spent at the University of Kentucky in Lexington (KY) between March and September 2010 was not less interesting and performing.

First of all a thank to Dr. Matthew J. Beck for hosting me in his group and teaching me the technical secrets of VASP and DFT on a daily basis. He is also acknowledged for "dwelling support" I needed in the first week of my staying there.

Similarly I'm also grateful to the large amount of people I met there, to both the "Lexington Little Italy" and the international friends, thanks to whom I enjoyed a lot my staying in the US and had the possibility to explore that extremely-vast country.

Psychological support and advices, along with exchange of ideas about "phylosophy of life" had with the old-date university colleague, but, above all, friend Andrea Picco[4] cannot for sure be excluded from this list. Particularly our joint experience to the discovery of the Big Apple NYC will always be vivid in my mind.

Back to Milano-Bicocca, I am grateful to Prof. Giancarlo Brivio and "Fondazione Cariplo" for continuous financial support to my missions and to my PhD period in general.

I am grateful for the support from my parents as well.

To all of them I simply say:
Thank you and Goodbye: Take Care

Daniele Scopece[5]
University of Milano-Bicocca, Italy, EU
December 19, 2011

[2] AKA "Er Bergamascini" or "BR"
[3] AKA "La Fra"
[4] AKA "Il Compagno Picco"
[5] AKA "DS"

Bibliography

[1] G. B. Stringfellow. *Rep. Prog. Phys.*, **45** : 469 , (1982).

[2] V. A. Shchukin and D. Bimberg. *Rev. Mod. Phys.*, **71** : 1125 , (1999).

[3] In D. R. Lide. *Handbook of chemistry and physics.* CRC PRESS, USA, (1998).

[4] D.J.Eaglesham and M.Cerullo. *Phys. Rev. Let.*, **64** : 1943 , (1990).

[5] A. Rastelli. PhD thesis, University of Pavia, Italy, (2002).

[6] D. B. Migas, P. Raiteri, Leo Miglio, A. Rastelli, H. von Kanel. *Phys. Rev. B*, **69** : 235318 , (2004).

[7] K. Li, D.R. Bowler, M.J. Gillan. *Surf. Sci.*, **526** : 356 , (2003).

[8] A. Rastelli, H. von Kanel, G. Albini, P. Raiteri, D. B. Migas and Leo Miglio. *Phys. Rev. Let.*, **90** : 216104 , (2003).

[9] A. Vailionis, B. Cho, G. Glass, P. Desjardins, D. G. Cahill and J. E. Greene. *Phys. Rev. Let.*, **85** : 3672 , (2000).

[10] J. Tersoff, B. J. Spencer, A. Rastelli and H. von Kanel. *Phys. Rev. Let.*, **89** : 196104 , (2002).

[11] A. Rastelli, H. Von Kanel, B. J. Spencer and J. Tersoff. *Phys. Rev. B*, **68** : 115301 , (2003).

[12] T. I. Kamins, G. Medeiros-Ribeiro, D. A. A. Ohlberg, and R. Stanley Williams. *J. Appl. Phys.*, **85** : 1159 , (1999).

[13] I. Goldfarb, P. T. Hayden, J. H. G. Owen and G. A. D. Briggs. *Phys. Rev. B*, **56** : 10459 , (1997).

[14] G. Medeiros-Ribeiro, A.M. Bratkovski, T.I. Kamins, D.A.A. Ohlberg, R.S. Williams. *Science*, **279** : 353 , (1998).

[15] G. Costantini, A. Rastelli, C. Manzano, P. Acosta-Diaz, G. Katsaros, R. Songmuang, O.G. Schmidt, H. v. Kanel, K. Kern. *J. Crystal Growth*, **278** : 38 , (2005).

[16] M. Stoffel, A. Rastelli, J. Tersoff, T. Merdzhanova, and O. G. Schmidt. *Phys. Rev. B*, **74** : 155326 , (2006).

[17] M. Brehm, H. Lichtenberger, T. Fromherz, G. Springholz. *Nanoscale Research Letters*, **6** : 70 , (2011).

[18] G. Capellini, M. de Seta, F. Evangelisti. *J. Appl. Phys.*, **93** : 291 , (2003).

[19] H. von Kanel A. Rastelli. *Surface Science Letters*, **515** : L493 , (2002).

[20] F. Montalenti, P. Raiteri, D. B. Migas, H. von Kanel, A. Rastelli, C. Manzano, G. Costantini, U. Denker, O. G. Schmidt, K. Kern , and Leo Miglio. *Phys. Rev. Let.*, **93** : 216102 , (2004).

[21] J. T. Robinson, A. Rastelli, O. Schmidt and O. D. Dubon. *Nanotechnology*, **20** : 085708 , (2009).

[22] Z. Gai, W. S. Yang, T. Sakurai, R. G. Zhao. *Phys. Rev. B*, **59** : 13009 , (1999).

[23] P. Sutter, E. Sutter, L. Vescan. *Appl. Phys. Let.*, **87** : 161916 , (2005).

[24] P. Kratzer, Q. K. K. Liu, P. Acosta-Diaz, C. Manzano, G. Costantini, R. Songmuang, A. Rastelli, O. G. Schmidt, and K. Kern. *Phys. Rev. B*, **73** : 205347 , (2006).

[25] Z. Gai, W. S. Yang, R. G. Zhao, T. Sakurai. *Phys. Rev. B*, **59** : 15230 , (1999).

[26] Z. Gai, R. G. Zhao, W. Li, Y. Fujikawa, T. Sakurai, and W. S. Yang. *Phys. Rev. B*, **64** : 125201 , (2001).

[27] D.B. Migas, S. Cereda, F. Montalenti, Leo Miglio. *Surf. Sci.*, **556** : 121 , (2004).

[28] M. Brehm, M. Grydlik, H. Lichtenberger, T. Fromherz, N. Hrauda, W. Jantsch, F. Schäffler and G. Bauer. *Appl. Phys. Let.*, **93** : 121901 , (2008).

[29] R.J. Wagner and E. Gulari. *Phys. Rev. B*, **69** : 195312 , (2004).

[30] M. Brehm, F. Montalenti, M. Grydlik, G. Vastola, H. Lichtenberger, N. Hrauda, M. J. Beck, T.Fromherz, F. Schäffler, L. Miglio, and G. Bauer. *Phys. Rev. B*, **80** : 205321 , (2009).

[31] J. J. Zhang, F. Montalenti, A. Rastelli, N. Hrauda, D. Scopece, H. Groiss, J. Stangl, F. Pezzoli, F. Schaffler, O. G. Schmidt, L. Miglio,2 and G. Bauer. *Phys. Rev. Let.*, **105** : 166102 , (2010).

[32] A. Rastellia, M. Stoffel, G. Katsaros, J. Tersoff, U. Denker, T. Merdzhanova, G.S. Kar, G. Costantini, K. Kern, H. von Kanel, O.G. Schmidt. *Microelectronics Journal*, **37** : 1471 , (2006).

[33] G. Katsaros, A. Rastelli, M. Stoffel, G. Isella, H. von Kanel, A.M. Bittner, J. Tersoff, U. Denker, O.G. Schmidt, G. Costantini, K. Kern. *Surf. Sci.*, **600** : 2608 , (2006).

[34] T.U. Schulli, M. Stoffel, A. Hesse, J. Stangl, R.T. Lechner, E. Wintersberger, M. Sztucki, T.H. Metzger, O.G. Schmidt, and G. Bauer. *Phys. Rev. B*, **71** : 035326 , (2005).

[35] G. Katsaros, G. Costantini, M. Stoffel, R. Esteban, A. M. Bittner, A. Rastelli, U. Denker, O. G. Schmidt, and K. Kern. *Phys. Rev. B*, **72** : 195320 , (2005).

[36] A. Rastelli, M. Stoffel, A. Malachias, T. Merdzhanova, G. Katsaros, K. Kern, T.H. Metger, and O.G. Schmidt. *Nanoletters*, **8** : 1404 , (2008).

[37] R. Gatti, F. Uhlik and F. Montalenti. *New J. Phys.*, **10** : 083039 , (2008).

[38] D. Digiuni, R. Gatti and F. Montalenti. *Phys. Rev. B*, **80** : 155436 , (2009).

[39] A. Rastelli, M. Kummer, and H. von Kanel. *Phys. Rev. Let.*, **87** : 256101 , (2001).

[40] E. Sutter, P. Sutter, and J. E. Bernard. *Appl. Phys. Let.*, **84** : 2262 , (2004).

[41] E. Pehlke, N. Moll, A. Kley, M. Scheffler. *Appl. Phys. A: Mater. Sci. Process*, **65** : 525 , (1997).

[42] C. M. Retford, M. Asta, M. J. Miksis, P. W. Voorhees, and E. B. Webb III. *Phys. Rev. B*, **75** : 075311 , (2007).

[43] J. Tersoff and F.K. LeGoues. *Phys. Rev. Let.*, **72** : 3570 , (1994).

[44] A. Zangwill. *Physics at surfaces (Chapter 1).* Cambridge University Press, (1987).

[45] G. Wulff. *Z. Krystallog.*, **34** : 449 , (1901).

[46] M. Holzer. PhD thesis, Simon Fraser University, (1990).

[47] H. P. Bonzel, M. Nowicki. *Phys. Rev. B*, **70** : 245430 , (2004).

[48] A. A. Stekolnikov and F. Bechstedt. *Phys. Rev. B*, **72** : 125326 , (2005).

[49] J. Tersoff. *Phys. Rev. B*, **39** : 5566 , (1989).

[50] J. Tersoff. *Phys. Rev. B*, **41** : 3248 , (1990).

[51] D. Srivastava, R. S. Taylor, and B. J. Garrison. *Journal of Vacuum Science and Technology B*, **9** : 1517 , (1991).

[52] G. Kresse and J. Furthmüller. *Phys. Rev. B*, **54** : 11169 , (1996).

[53] G. Kresse and J. Furthmüller. *Computational Materials Science*, **6** : 15 , (1996).

[54] D. Vanderbilt. *Phys. Rev. B*, **41** : 7892 , (1990).

[55] D. M. Ceperley and B. J. Adler. *Phys. Rev. Lett.*, **45** : 566 , (1980).

[56] J. P. Perdew and A. Zunger. *Phys. Rev. B*, **23** : 5048 , (1981).

[57] S. Cereda and F. Montalenti. *Phys. Rev. B*, **81** : 125439 , (2010).

[58] E. M. Liftshitz. *Theory of elasticity.* Elsevier, (1986).

[59] L. W. Wang A. J. Williamson C. Pryor, J. Kim and A. Zunger. *Jour. Appl. Phys.*, **83** : 2548 , (1998).

[60] F.D. Murnaghan. *Proc. NAS*, **30** : 244 , (1944).

[61] F. Birch. *Phys. Rev.*, **71** : 809 , (1947).

[62] D.S.Scholl and J.A.Steckel. *Density functional theory: A practical introduction.* Wiley, 2009.

[63] T. Soma. *J. Phys. F: Metal Phys.*, **4** : 2157 , (1974).

[64] P. Beauchamp L. Pizzagalli and J. Rabier. *J. Phys.: Condens. Matter*, **14** : 12681 , (2002).

[65] E. M. Fitzgerald. *Mat. Sci. Eng. B*, **124** : 8 , (2005).

[66] T. Hammerschmidt, P. Kratzer, and M. Scheffler. *Phys. Rev. B*, **75** : 235328 , (2007).

[67] M. Fearn M. A. Migliorato, A. G. Cullis and J. H. Jefferson. *Phys. Rev. B*, **65** : 115316 , (2002).

[68] R Zhu, E Pan, P W Chung, X Cai, K M Liew and A Buldum. *Semicond. Sci. Technol.*, **21** : 906 , (2006).

[69] T. Sakurai R. G. Zhao Z. Gai, W. S. Yang. *Phys. Rev. B*, **59** : 13009 , (1999).

[70] F Montalenti, A Marzegalli, G Capellini, M De Seta and Leo Miglio. *J. Phys.: Condens. Matter*, **19** : 225001 , (2007).

[71] R. Stanley Williams, G. Medeiros-Ribeiro, T. I. Kamins and D. A. A. Ohlberg. *Acc. Chem. Res.*, **32** : 425 , (1999).

[72] M. Stoffel, A. Rastelli, J. Tersoff, T. Merdzhanova, and O. G. Schmidt. *Phys. Rev. B*, **74** : 155326 , (2006).

[73] P. Kratzer T. Hammerschmidt and M. Scheffler. *Phys. Rev. B*, **77** : 235303 , (2008).

[74] R.E. napolitano, S. Liu. *Phys. Rev. B*, **70** : 214103 , (2004).

[75] P. J. Hesketh, C. Ju, S. Gowda, E. Zanoria and S. Danyluk. *J. Electrochem. Soc.*, **140** : 1080 , (1993).

[76] G. Lu, M. Cuma and F. Liu. *Phys. Rev. B*, **72** : 125415 , (2005).

[77] M. J. Beck. *"Surface and Interface Properties in Ge/Si Heteroepitaxy from First-Principles"*. PhD thesis, Northwestern University, Evanston, Illinois, USA, (2005).

[78] S. Cereda. *"Atomic-scale modeling of surface processes relevant for Si thin-film growth"*. PhD thesis, University of Milano-Bicocca, Italy, (2007).

[79] S. Cereda and F. Montalenti. *Phys. Rev. B*, **75** : 195321 , (2007).

[80] A. A. Stekolnikov, J. Furthmuller and F. Bechstedt. *Phys. Rev. B*, **68** : 205306 , (2003).

[81] P. Raiteri, D. B. Migas, L. Miglio, A. Rastelli, H. von Känel. *Phys. Rev. Lett.*, **88** : 256103 , (2002).

[82] T. Hashimoto, Y. Morikawa, Y. Fujikawa, T. Sakurai, M.G. Lagally, K. Terakura. *Surf. Sci.*, **513** : L445 , (2002).

[83] A. A. Stekolnikov, J. Furthmuller and F. Bechstedt. *Phys. Rev. B*, **67** : 195332 , (2003).

[84] Z. Gai, X. Li, R. G. Zhao and W. S. Yang. *Phys. Rev. B*, **57** : R15060 , (1998).

[85] E. Pehlke and J. Tersoff. *Phys. Rev. Lett.*, **67** : 465 , (1991).

[86] I. Berbezier and A. Ronda. *Surf. Sci. Rep.*, **64** : 47 , (2009).

[87] A. Rastelli, H. von Känel, G. Albini, P. Raiteri, D. B. Migas and L. Miglio. *Phys. Rev. Let.*, **91** : 229901 .

[88] D. B. Migas, S. Cereda, F. Montalenti, L. Miglio. *Surf. Sci.*, **556** : 121 , (2004).

[89] C. B. Duke. *Chem. Rev.*, **96** : 1237 , (1996).

[90] R.T. Fu, K.Esfarjani, Y. Hashi, J. Wu, X. Sun and Y. Kawazoe. *Sci. Rep. RITU*, **A44** : 77 , (1997).

[91] A. A. Baski, S.C. Erwin, L.J. Whitman. *Surf. Sci.*, **392** : 69 , (1997).

[92] V. A. Shchukin, N. N. Ledentsov, P. S. Kop'ev and D. Bimberg. *Phys. Rev. Lett.*, **75** : 2968 , (1995).

[93] G. Lu and F. Liu. *Phys. Rev. Lett.*, **94** : 176103 , (2005).

[94] P. Muller and R. Kern. *Appl. Surf. Sci.*, **102** : 6 , (1996).

[95] V. G. Dubrovskii, G. E. Cirlin, and V. M. Ustinov. *Phys. Rev. B*, **68** : 075409 , (2003).

[96] G. Vastola. PhD thesis, Univ. of Milano-Bicocca, 2008.

[97] J. J. Zhang, F. Montalenti, A. Rastelli, N. Hrauda, D. Scopece, H. Groiss, J. Stangl, F. Pezzoli, F. Schaffler, O.G. Schmidt, L. Miglio, and G. Bauer. *Phys. Rev. Let.*, **105** : 166102 , (2010)– and supplementary material at http://link.aps.org/supplemental/10.1103/PhysRevLett.105.166102.

[98] V. Jovanovic *et al. IEEE Electron Device Lett.*, **31** : 1083 , (2010).

[99] G. Katsaros, P. Spathis, M. Stoffel, F. Fournel, M. Mongillo, V. Bouchiat, F. Lefloch, A. Rastelli, O. G. Schmidt and S. De Franceschi. *Nature Nanotechn.*, **5** : 458 , (2010).

[100] D. Grützmacher, T. Fromherz, C. Dais, J. Stangl, E. Müller, Y. Ekinci, H. H. Solak, H. Sigg, R. T. Lechner, E. Wintersberger, S. Birner, V. Holy, and G. Bauer. *Nano Lett.*, **7** : 3150 , (2007).

[101] J. J. Zhang, M. Stoffel, A. Rastelli, O. G. Schmidt, V. Jovanovic, L. K. Nanver and G. Bauer. *Appl. Phys. Let.*, **91** : 173115 , (2007).

[102] J. Zhang, A. Rastelli, O. G. Schmidt and G. Bauer. *Appl. Phys. Lett.*, **97** : 203103 , (2010).

[103] G. Vastola, F. Montalenti and L. Miglio. *J. Phys.: Cond. Mat.*, **20** : 454217 , (2008).

[104] H. Hu, H. J. Gao and F. Liu. *Phys. Rev. Let.*, **101** : 216102 , (2008).

[105] F. M. Ross, J. Tersoff and R. M. Tromp. *Phys. Rev. Let.*, **80** : 984 , (1998).

[106] A. Rastelli, M. Stoffel, U. Denker, T. Merdzhanova and O. G. Schmidt. *Phys. Status Solidi A*, **203** : 3506 , (2006).

[107] F. K. LeGoues, M. C. Reuter, J. Tersoff, M. Hammar, and R. M. Tromp. *Phys. Rev. Let.*, **73** : 300 , (1994).

[108] A. Marzegalli, V. A. Zinovyev, F. Montalenti, A. Rastelli, M. Stoffel, T. Merdzhanova, O. G. Schmidt and L. Miglio. *Phys. Rev. Let.*, **99** : 235505 , (2007).

[109] G. Chen, H. Lichtenberger, G. Bauer, W. Jantsch and F. Schäffler. *Phys. Rev. B*, **74** : 035302 , (2006).

[110] M. Stoffel, A. Rastelli, J. Stangl, T. Merdzhanova, G. Bauer and O. G. Schmidt. *Phys. Rev. B*, **75** : 113307 , (2007).

[111] J. Tersoff. *Appl. Phys. Lett.*, **83** : 353 , (2003).

[112] G. Biasiol, A. Gustafsson, K. Leifer, and E. Kapon. *Phys. Rev. B*, **65** : 205306 , (2002).

[113] C.V. Ciobanu, F.-C. Chuang, D.E. Lytle. *Appl. Phys. Lett.*, **91** : 171909 , (2007).

[114] J. tersoff and R.M. Tromp. *Phys. Rev. Lett.*, **70** : 2782 , (1993).

[115] F. Montalenti V.A. Zinovyev, G. Vastola and L. Miglio. *Surf. Sci.*, **600** : 4777 , (2006).

[116] V.M. Kaganer, K.H. Ploog. *Solid State Communication*, **117** : 337 , (2001).

[117] V.B. Shenoy, L.B. Freund. *J. of the Mechanics and Physics Society*, **50** : 1817 , (2002).

[118] V.B. Shenoy, C.V. Ciobanu and L.B. Freund. *Appl. Phys. Lett.*, **81** : 364 , (2002).

[119] D.J. Chadi. *Phys. Rev. Lett.*, **59** : 1691 , (1987).

[120] S. Somasi, B. Khomami, R. Lovett. *J. Phys. Chem. B*, **108** : 19721 , (2004).

[121] M.B. Webb. *Surf. Sci.*, **299** : 454 , (1994).

[122] J. Myslivecek, C. Schelling, F. Schäffler, G. Springholz, P. Smilauer, J. Krug, B. Voigtländer. *Surf. Sci.*, **520** : 193 , (2002).

[123] K. Cho, J.D. Joannopoulos and A.N. Berker. *Phys. Rev. B*, **53** : 1002 , (1996).

[124] J. Wang, D.A. Drabold, A. Rockett. *Appl. Phys. Lett.*, **66** : 1954 , (1995).

[125] P. Politi, A. Ponchet, J. Villain. *ArXiv:cond-mat*, page 9906289v1 , (1999).

[126] H.-C. Jeong, E.D. Williams. *Surf. Sci. Rep.*, **34** : 171 , (1999).

[127] C. Schelling, M. Muhlberger, G. Springholz and F. Schaffler. *Phys. Rev. B*, **64** : R041301 , (2001).

[128] S.N. Filimonov and B. Voigtländer. *Surf. Sci.*, **549** : 31 , (2004).

[129] A. Ronda, I. Berbezier, A. Pascale, A. Portavoce, F. Volpi. *Materials Science and Engineering B*, **101** : 95 , (2003).

[130] F. Montalenti S. Cereda and Leo Miglio. *Surf. Sci.*, **591** : 23 , (2005).

[131] B. J. Spencer and J. Tersoff. *Appl. Phys. Lett.*, **96** : 073114 , (2010).

[132] Y. H. Xie, G. H. Gilmer, C. Roland, P. J. Silverman, S. K. Buratto, J. Y. Cheng, E. A. Fitzgerald, A. R. Kortan, S. Schuppler, M. A. Marcus and P. H. Citrin. *Phys. Rev. Lett.*, **73** : 3006 , (1994).

[133] S.R. Schofield, M.W. Radny and P.V. Smith. *Phys. Rev. B*, **62** : 10199 , (2000).

[134] C. J. Moore, C. M. Retford, M. J. Beck, M. Asta, M. J. Miksis, and P. W. Voorhees. *Phys. Rev. Let.*, **96** : 126101 , (2006).

[135] B. Sanduijav, D. Matei, G. Chen and G. Springholz. *Phys. Rev. B*, **80** : 125329 , (2009).

[136] Z. Zhong, A. Halilovic, M. Muhlberger, F. Schaffler and G. Bauer. *J. Appl. Phys.*, **93** : 6258 , (2003).

[137] D. Matei, B. Sanduijav, G. Chen, G. Hesser, G. Springholz. *J. Cryst. Growth*, **311** : 2220 , (2009).

[138] F. Watanabe, D. G. Cahill and J. E. Greene. *Phys. Rev. Lett.*, **94** : 066101 , (2005).

[139] I. Berbezier and A. Ronda. *Phys. Rev. B*, **75** : 195407 , (2007).

[140] L. Persichetti, A. Sgarlata, M. Fanfoni and A. Balzarotti. *Phys. Rev. B*, **82** : 121309(R) , (2010).

[141] V. A. Shchukin and D. Bimberg. *Rev. Mod. Phys.*, **71** : 1125 , (1999).

[142] I. Berbezier, A. Ronda, F. Volpi, A. Portavoce. *Surf. Sci.*, **531** : 231 , (2003).

[143] P. D. Szkutnik, A. Sgarlata, A. Balzarotti, N. Motta, A. Ronda and I. Berbezier. *Phys. Rev. B*, **75** : 033305 , (2007).

[144] A. A. Baski, S. C. Erwin and L. J. Whitman. *Surf. Sci.*, **392** : 69 , (1997).

[145] Y. Fujikawa, K. Akiyama, T. Nagao, T. Sakurai, M. G. Lagally, T. Hashimoto, Y. Morikawa and K. Terakura. *Phys. Rev. Lett.*, **88** : 176101 , (2002).

[146] F. M. Ross, R. M. Tromp, M. C. Reuter. *Science*, **286** : 1931 , (1998).

[147] O. G. Schmidt, U. Denker, S. Christiansen and F. Ernst. *Appl. Phys. Lett.*, **81** : 2614 , (2002).

[148] M. J. Beck. PhD thesis, Northwestern University, Evanston, Illinois, USA, 2005.

[149] K. Momma and F. Izumi. *J. Appl. Crystallogr.*, **41** : 653 , (2008).

[150] M. J. Beck, A. van de Walle and M. Asta. *Phys. Rev. B*, **70** : 205337 , (2004).

[151] L. Persichetti, A. Sgarlata, M. Fanfoni and A. Balzarotti. *Phys. Rev. Lett.*, **104** : 036104 , (2010).

[152] G. Chen, E. Wintersberger, G. Vastola, H. Groiss, J. Stangl, W. Jantsch, and F. Schäffler. *Appl. Phys. Lett.*, **96** : 103107 , (2010).

[153] A. Ronda, M. Abdallah, J. M. Gay, J. Stettner, I. Berbezier. *Appl. Surf. Sci.*, **162** : 576 , (2000).

[154] J. Tersoff. *Phys. Rev. B*, **43** : 9377 , (1991).

[155] A. P. Smith, J. K. Wiggs, H. Jonsson, H. Yan, L. R. Corrales, P. Nachtigall and K. D. C. Jordan. *J. Chem. Phys.*, **102** : 1044 , (1995).

[156] J. Cai and J.-S. Wang. *Phys. Rev. B*, **64** : 035402 , (2001).

[157] P. Boguslawski, Q-M Zhang, Z. Zhang and J. Bernholc. *Phys. Rev. Let.*, **72** : 3694 , (1994).

[158] U. Denker, H. Sigg, O.G. Schmidt. *Appl. Surf. Sci.*, **224** : 127 , (2004).

[159] U. Denker, H. Sigg, O.G. Schmidt. *Materials Science and Engineering B*, **101** : 89 , (2003).

[160] G. Chen, E. Wintersberger, G. Vastola, H. Groiss, J. Stangl, W. Jantsch and F. Schäffler. *Appl. Phys. Lett.*, **96** : 103107 , (2010).

[161] L. Persichetti, A. Sgarlata, M. Fanfoni, and A. Balzarotti. *Phys. Rev. Lett.*, **106** : 055503 , (2010).

[162] Zhenyang Zhong, Hua Gong, Yingjie Ma, Yongliang Fan and Zuimin Jiang. *Nanoscale Research Lett.*, **6** : 322 , (2011).

[163] U. Denker, A. Rastelli, M. Stoffel, J. Tersoff, G. Katsaros, G. Costantini, K. Kern, N. Y. Jin-Phillipp, D. E. Jesson and O. G. Schmidt. *Phys. Rev. Lett.*, **94** : 216103 , (2005).

[164] A. Rastelli, M. Stoffel, J. Tersoff, G. S. Kar and O. G. Schmidt . *Phys. Rev. Lett.*, **95** : 026103 , (2005).

[165] T. Merdzhanova, S. Kiravittaya, A. Rastelli, M. Stoffel, U. Denker and O. G. Schmidt. *Phys. Rev. Lett.*, **96** : 226103 , (2006).

[166] Hidong Kim, Huiting Li, Jae M. Seo. *Surf. Sci.*, **602** : 2563 , (2008).

[167] J. Knall and J.B. Pethica. *Surf. Sci.*, **265** : 156 , (1992).

[168] S. C. Jain and W. Hayes. *Semicond. Sci. Technol.*, **6** : 547 , (1991).

[169] Feng Liu and M. G. Lagally. "Interplay of Stress, Structure and Stoichiometry in Ge-Covered Si(001)". *Phys. Rev. Lett.*, **76** : 3156 , (1996).

[170] G.P. Srivastava. *Rep. Prog. Phys.*, **60** : 561 , (1997).

[171] J. Todd J. Knall, J. Pethica and J.H. Wilson. *Phys. Rev. Lett.*, **66** : 1733 , (1991).

[172] D. Bird *et* al. *Phys. Rev. Lett.*, **69** : 3785 , (1992).

[173] J. Dabrowski *et al. Phys. Rev. Lett.*, **73** : 1660 , (1994).

[174] J. Furthmuller A.A. Stekolnikov and F. Bechstedt. *Phys. Rev. B*, **67** : 195332 , (2003).

[175] K. Varga, L.G. Wang, S.T. Pantelides, Z. Zhang. *Surf. Sci. Lett.*, **562** : 225 , (2004).

[176] J. Tersoff. *Phys. Rev. B*, **45** : 8833 , (1992).

[177] L. Huang, G.-H. Lu, F. Liu, X.G. Gong. *Surf. Sci.*, **601** : 3067 , (2007).

[178] I. Goldfarb, J.H.G. Owen, P.T. Hayden, D.R. Bowler, K. Miki, G.A.D. Briggs. *J. Vac. Sci. Tec. A*, **16** : 1938 , (1998).

[179] C.V. Ciobanu, D.T. Tambe, V.B. Shenoy. *Surf. Sci.*, **556** : 171 , (2004).

[180] Yuhai Tu and J. Tersoff. *Phys. Rev. Lett.*, **93** : 216101 , (2004).

[181] H.W. Yeom, M. Sasaki, S. Suzuki, S. Sato, S. Hosoi, M. Iwabuchi, K. Higashiyama, H. Fukutani, M. Nakamura, T. Abukawa, S. Kono. *Surf. Sci. Let.*, **381** : 533 , (1997).